Synthesis and Characterization of Lithium-Manganese-Oxide Electrodes for Lithium Battery Applications

---

Margaretha Hendrina Rossouw

A Dissertation submitted to the Faculty of Science,

University of Cape Town,

in fulfilment of the requirements for the

Degree Master in Science

Pretoria 1993

DECLARATION

I declare that this thesis is my own unaided work. It is being submitted for the degree of Master of Science at the University of Cape Town, South Africa. It has not been submitted before for any degree or examination in any other tertiary institution.

Signed on this 5th day of November 1993

Signed by candidate

ACKNOWLEDGEMENTS

I would like to thank my supervisors Prof L R Nassimbeni and especially Dr M M Thackeray for the many useful discussions held and the assistance and encouragement given.

Dr A W Paterson, Director of the Division for Materials Science and Technology (Mattek) at CSIR, is thanked for the permission to use the research undertaken at CSIR for this dissertation. Financial assistance from CSIR is gratefully acknowledged.

A special word of thanks goes to my colleagues at Mattek and in the Battery Technology Unit, in particular, Dave Liles for useful discussions on the structural aspects of the materials, Monika Schatz for undertaking the atomic absorption analyses, and Piet Terblanche for modifying certain computer programmes to suit some of my requirements.

The contribution from Dr W I F David and Dr R M Ibberson of the Rutherford Appleton Laboratory (U.K.) in collecting and refining the neutron diffraction data of several samples is greatly appreciated.

Ingrid Nänni at the Chemistry Department at the University of Cape Town for performing the thermal analyses is also thanked.

Finally, I want to let my parents know that their constant enquiries as to the status of this dissertation can finally be put to rest.

CONTENTS

PUBLICATIONS

Sections of this dissertation, and other related research obtained during the course of the project, have been published or presented at conferences. The novelty of certain synthesis routes and structures of the reaction products have been patented.

A. INTERNATIONAL JOURNALS

1. M H Rossouw, A de Kock, L A de Picciotto, M M Thackeray, W I F David and R M Ibberson, "Structural Aspects of Lithium-Manganese-Oxide Electrodes for Rechargeable Lithium Batteries". *Materials Research Bulletin*, **25**, 173-182, 1990.

2. A de Kock, M H Rossouw, L A de Picciotto, M M Thackeray, W I F David and R M Ibberson, " Defect Spinels in the System $Li_2O.yMnO_2$ ($y > 2.5$): A Neutron-Diffraction Study and Electrochemical Characterization of $Li_2Mn_4O_9$". *Materials Research Bulletin*, **25**, 657-664, 1990.

3. M H Rossouw and M M Thackeray, "Lithium Manganese Oxides from Li_2MnO_3 for Rechargeable Lithium Battery Applications". *Materials Research Bulletin*, **26**, 463-473, 1991.

4. M H Rossouw, D C Liles, M M Thackeray, W I F David and S Hull, "Alpha Manganese Dioxide for Lithium Batteries: A Structural and Electrochemical Study". *Materials Research Bulletin*, **27**, 221-230, 1992.

5. M M Thackeray, A de Kock, M H Rossouw, D Liles, R Bittihn and D Hoge, "Spinel Electrodes from the Li-Mn-O System for Rechargeable Lithium Battery Applications". *Journal of the Electrochemical Society*, **139**, 363-366, 1992.

6. M H Rossouw, A de Kock, D C Liles, R J Gummow and M M Thackeray, "Synthesis of Highly-Crystalline Ramsdellite-MnO_2 and Its Lithiated Derivative

$Li_{0.9}MnO_2$". *Journal of Materials Chemistry*, **2**, 1211, 1992.

7. M M Thackeray, M H Rossouw, A de Kock, A P de la Harpe, R G Gummow, K Pearce and D C Liles, "The Versatility of MnO_2 for Lithium Battery Applications". *Journal of Power Sources*, **43-44**, 289-300, 1993.

8. M M Thackeray, M H Rossouw, R J Gummow, D C Liles, K Pearce, A de Kock, W I F David and S Hull, "Ramsdellite-MnO_2 for Lithium Batteries: The Ramsdellite to Spinel Transformation". *Electrochimica Acta*, **38**, 1259-1267, 1993.

9. M H Rossouw, D C Liles and M M Thackeray, "Synthesis and Structural Characterization of a Novel Layered Lithium Manganese Oxide $Li_{0.36}Mn_{0.91}O_2$ and Its Lithiated Derivative $Li_{1.09}Mn_{0.91}O_2$". *Journal of Solid State Chemistry*, in press.

B. CONFERENCES

1. M H Rossouw, A de Kock, L A de Picciotto, M J Kelly and M M Thackeray, "Spinels in the System $Li_2O.yMnO_2$ ($2.5 \leq y \leq 4.0$): Structural and Electrochemical Characterization". *Inorganic '90*, South African Chemical Institute, Golden Gate, January 16-19, 1990.

2. M M Thackeray, A de Kock, M H Rossouw, D C Liles, R Bittihn and D Hoge, "Spinel Electrodes $Li_2O.yMnO_2$ ($y \geq 2.5$) for Rechargeable Lithium Battery Applications". *178th Meeting of the Electrochem. Soc.*, Seattle, Washington, October 14-19, 1990.

3. M H Rossouw and M M Thackeray, " Lithium Manganese Oxides from Li_2MnO_3 for Battery Applications". *South African Chemical Institute 31st Convention*, Rhodes University, Grahamstown, June 24-27, 1991.

4. M M Thackeray, M H Rossouw, A de Kock, A de la Harpe, R J Gummow, K Pearce and D C Liles, "The Versatility of MnO_2 for Lithium Battery Applications". *6th International Meeting on Lithium Batteries*, Münster, Germany, May 11-15, 1992.

5. D C Liles, M H Rossouw and M M Thackeray, "Modifications to the Structure of the Ramsdellite Form of Manganese Dioxide on Lithiation". *SA Crystallographic Society Meeting*, Rand Afrikaans University, Johannesburg, August 11, 1992.

C. PATENTS

1. M M Thackeray and M H Rossouw, "Lithium-Manganese-Oxide". *SA Patent* 90/5974, *US Patent* 5153081.

2. M H Rossouw and M M Thackeray, "Alpha Manganese Dioxide". *SA Patent* 91/2329, *US Patent* 5166012.

3. M M Thackeray and M H Rossouw, "Ramsdellite". *SA Patent* 92/3284.

Chapter 1

Introduction

ABSTRACT: As the electronics industry moves more towards portable equipment the demand for batteries, especially rechargeable batteries, is increasing. Lithium batteries have several advantages over other competitive systems. Coupled with the inexpensive and environmentally friendly manganese dioxide, Li/MnO_2 batteries are being used extensively for powering a range of devices, but particular electronic systems. This chapter briefly evaluates lithium batteries and the applications of manganese dioxide as an electrode material. An overview of the contents of this dissertation is given.

1.1 Applications of Manganese Dioxides

Manganese (di)oxides are employed in a variety of applications, of which the application as an active battery material is only one. Other applications include sensors, ion-exchange materials, catalysts and pigments.

It is proposed that major progress in most scientific fields occurs in a stepwise manner. Breakthroughs which revolutionise technology occur every five to ten years. After such a breakthrough, there are extended periods during which fundamental research investigating the underlying phenomena leads to better understanding and gradual improvement of the new technology. During such periods, it may appear that a field or even the whole of the specific technology is relatively mature. This is, however, a misconception because history teaches us that fields which appear mature are suddenly revitalized by a major discovery.

This can also be applied to the progress made in the battery field, and more specifically, the progress made in the manganese (di)oxide research effort. Research on the synthesis of manganese dioxides continues to evoke considerable interest. This is mainly due to the ever increasing demand in the battery industry for a superior cathode material. Increasing importance is given to the chemical synthesis of the dioxides as a substitute for the relatively expensive electrolytically synthesized dioxides which are almost exclusively used at present for high quality zinc cells.

MnO_2 has been used mainly as an active cathode material for dry (zinc) batteries since 1860. MnO_2 is the most suitable material for cathodes in such cells, from both a resource and economical stand point (Ikeda, 1983). The principle MnO_2 used in zinc cells in the earlier days were natural ores (NMD). Synthetic MnO_2 materials were added to improve the capacity of certain cells. Today NMD is mainly used as a "filler material" in inexpensive Leclanché cells. The Leclanché system is the standard flashlight battery with a mixed electrolyte of NH_4Cl and $ZnCl_2$. The alkaline cell uses a KOH electrolyte. The systems differ primarily in rate capability. For high-rate applications, the alkaline cell is clearly better and sets the standard. The Leclanché cell performs well on lower rate applications and is the least expensive. The $ZnCl_2$ cell is intermediate in cost and approaches alkaline cell performance in all but high-rate applications. At low-rate discharges, they all have the same energy density. The lithium cell offers several advantages over the Zn-MnO_2 systems (Brodd, 1985).

Studies on lithium cells started around the 1960s, supported by NASA and DOD in the USA, in order to develop high power density batteries for space and military use. At that time, alkaline metals such as Li, Na, Al and Mg were being examined as prospective anode materials from the stand point of the electrode potential and the electrochemical equivalent. Halogenides, sulphides and oxides of transition metals were examined as possible active cathode materials (Ikeda, 1983).

Manganese dioxide, which has been used for a long time as an active cathode material in zinc cells, is well characterized and is known as an economical material. MnO_2 thus received renewed interest with the developments in the lithium battery field.

Before looking at the development of MnO_2 in the battery field, a look at the lithium battery market and the battery market in general is needed.

The boom in take-along (portable) electronic gadgets, for example, cellular phones, personal organisers, tape and compact-disc machines and "smart" credit cards, has been accelerating the demand for compact longer-life batteries. Battery technology, traditionally, has been notoriously slow at yielding dramatic performance gains. Now, recent advances in metal alloys, carbon materials, and polymers are finally moving higher-energy batteries out of the laboratories and into products and stores (Krause, 1993).

The latest developments include:

- The zinc-air designs. These batteries can power a notebook computer for 8 h, four times longer than nickel-cadmium designs.

- Nickel metal-hydride batteries. Already in electronic products, these rechargeable batteries, despite some drawbacks, are challenging nickel-cadmium.

- Nickel-zinc batteries. These batteries could challenge older technologies and new nickel-hydride designs.

- Lithium batteries. Rechargeable lithium-ion designs, safer than earlier systems, power for example a new camcorder. Flexible solid-state lithium-polymer batteries are just emerging from the laboratories.

Table 1.1 compares some of the older battery technologies with newer systems. Performance comparisons are made, for example, in terms of energy density, by weight as watt-hours/kilogram (Wh/kg) and by volume as watt-hours/litre (Wh/*l*). Where AA sizes were available the table also compares energy capacity (how long a given current can be drawn before a cell is totally discharged) in milliamperes hour (mAh).

Table 1.1

Comparing Power Packages (Krause, 1993)

	Voltage (Nominal)	Peak Power	Recharge Cycles	Self Discharge	Capacity (mAh)	Energy Density (Wh/kg)	Energy Density (Wh/dm^3)
Nickel- Cadmium	1.2	High	500	Moderate	800	55	130
Lead-~~air~~ acid	2.0	Moderate	200	Low-moderate	N/A	35	90
Zinc-air	1.2	Low-moderate	50-75	Low	N/A	135	150
Nickel Metal-hydride	1.2	Moderate	500	High	1150	70	175
Nickel-zinc	1.6	Moderate-high	100-500	Moderate	450	70	120
Lithium/MnO_2	2.8	Low-moderate	>200	Low	750	130	310
Lithium-ion ($C\text{-}Li^+/Li_xCoO_2$)	3.6	Low-moderate	>200	Moderate	830	115	250
Lithium polymer (V_6O_{13})	3.2	Low-moderate	>200	Low	N/A	175	350
Alkaline (Zinc-MnO_2)	1.5	Low-moderate	N/A	Low	2300	130	300
Lithium/iron sulphide	1.6	High	N/A	Low	2400	130	385

1.2 Lithium Batteries

1.2.1 The Versatility of Lithium Batteries

Many consumers of lithium batteries are unaware of the range of available cell sizes, types, and more importantly, performance features. In nearly every category - cell voltage, shape, current capability, capacity, price - options abound. Cell voltages range from 1.4 V to 3.9 V, current capabilities vary from 1 μA to greater than 10 A, and capacities range from 10 mAh to 10000 Ah (Brookman, 1984). In many respects, lithium batteries seem to be the ideal portable power source. They are light, store a lot of energy, and have a long shelf life. But they also have two major drawbacks: their voltage and cost (Bahniuk, 1989).

The feasibility of insertion-compound electrodes for non-aqueous secondary (rechargeable) batteries of high specific energy and power was first demonstrated with the Li/Li_xTiS_2 cell in 1976. Lithium was reversibly inserted into and extracted from a TiS_2 cathode, Li_xTiS_2, over the compositional range $0 \leq x \leq 1$; over most of this range a cell voltage in excess of 2 V was maintained at current densities of 1 mA/cm^2 to 10 mA/cm^2. However, difficulties with practical non-aqueous electrolytes and reversible deposition at the lithium anode have restricted commercial Li/Li_xTiS_2 cell to button size units (Mizushima, 1981).

Since 1976, many insertion compounds that can accommodate lithium have been explored. The materials studied include transition metal sulphides such as MoS_2 and $NiPS_3$, oxides such as V_2O_5 and MoO_3, and the oxyhalide FeOCl. In addition to these layered compounds, the oxide V_6O_{13} has also been investigated extensively as an insertion electrode for lithium polymer electrolyte cells (Mizushima, 1981).

The theoretical energy densities and reversible cell potentials of some lithium battery systems are given in Table 1.2. A battery system having a high specific energy depends upon a large difference in the electronegativity of the anode and the cathode materials.

Table 1.2
Theoretical Energy Densities and Reversible Cell Potential of Lithium Battery Systems (Gabano, 1983)

Battery Couple	Open-Circuit Voltage	Nominal Operating Voltage	Energy Density (Wh/kg)	Energy Density (Wh/dm^3)
Li/F_2	6.05	*	6254	6443
Li/Cl_2	3.98	*	2516	2986
$Li/SOCl_2$	3.66	*	1477	2005
Li/CuF_2	3.54	3.5	1644	3796
Li/V_2O_5	3.50		497	1397
Li/MnO_2	3.50	3.0-2.9	1000	3097
$Li/Ag_2Cr_2O_4$	3.31	3.0	513	2088
Li/I_2	3.10	3.1-2.6	-	-
$Li/CuCl_2$	3.07	2.8	1110	2505
Li/SO_2	2.91		1098	1353
Li/CF_x	2.82-3.3	2.85	1992	2653
Li/I_2	2.77	2.8	556	1920
Li/MoO_3	2.75	2.8	488	1688
Li/TiS_2	2.45		552	1374
Li/CuO	2.24	2.1[a]	1285	3140
Li/S	2.18	1.5	2550	2826
Li/CuS	2.12		557	1683
Li/Bi_2O_3	2.04	1.5[a]	646	2478
$Li/Bi_2Pb_2O_5$	2.00	1.5	546	2318
Li/PbI_2	1.87	1.5	211	997
Li/FeS_2	1.75		1273	2474
Li/Cu_2S	1.74	1.5	539	1714
$Li/LiCoO_2$ [a]		4.0	1095	
Li/MoO_3 [a]		2.4	550	
Li/V_6O_{13} [a]		2.3	430	
Li/Cr_3O_8 [a]		3.0	985	

[a] from Abraham (1983)
* data not available

Lithium possesses the lowest electronegativity of all existing metals. The effect of the equivalent weight of cell reactants on the specific energy density is illustrated in Fig. 1.1.

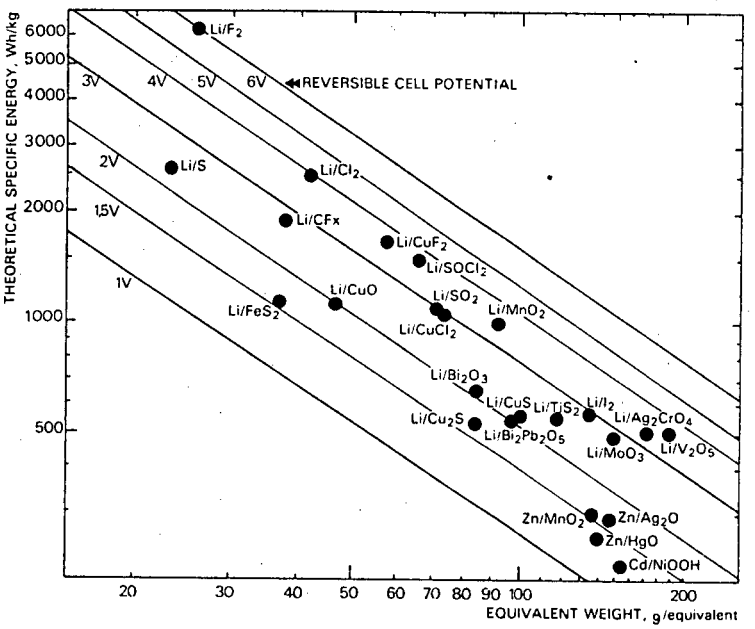

Fig. 1.1 Effect of the difference of electronegativity between anode and cathode (as reflected by the cell reversible voltage) and of the equivalent weight on the theoretical specific energy on weight basis of various electro-chemical systems (Gabano, 1983).

Primary batteries based on lithium couples offer the ideal combination of high capacity with a very low self-discharge rate - typically 1 % per year. They offer between two and four times the density of standard alkaline manganese systems and, in addition to their flat discharge characteristic and wide temperature range, also feature a non-caustic organic electrolyte and a zero-pressure system (Batley, 1986). Examples of primary lithium batteries that are already commercially available, are Li/CuO, Li/I_2, Li/SO_2 and Li/MnO_2.

There are several different groups of lithium batteries. The type of cathode and electrolyte determines their classification. The two basic groups are solid and liquid

electrolyte. These further divide into solid and liquid cathode. Additional classifications can be made by subdividing the batteries by chemistry (SO_2, CuO, etc.) or construction (coin, bobbin, or spiral). The reason for the multiple classifications is that the cathode, electrolyte, and construction determine battery output qualities. Two batteries constructed differently but with the same chemistry will have the same output voltage. However, they will have different discharge curves (Bahniuk, 1989).

Comparison of electrochemical performances of lithium cells with others is generally made in their practical (delivered) energy density on a weight or volume basis. It must, however, include their operating voltage; moreover, the cell design and internal technology have to be defined as these parameters strongly affect the specific performances of the systems. Fig. 1.2 shows the discharge characteristics of some low and high voltage lithium battery systems together with some conventional ones.

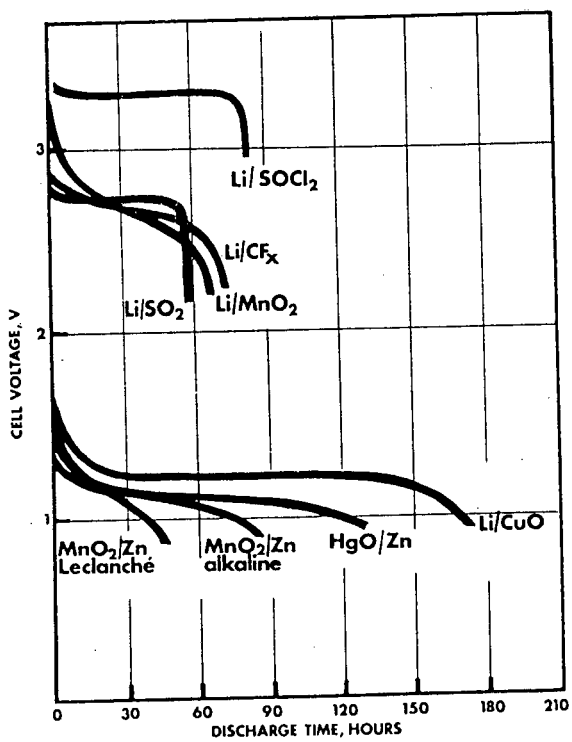

Fig. 1.2 Discharge characteristics of AA size non-aqueous solid and liquid lithium cells under 20 mA continuous drain, compared to those for conventional cells (Gabano, 1983).

1.2.2 Rechargeable Lithium-Metal Oxide Systems

A large negative free energy change for a reaction

$$xA + MX_n \rightarrow A_xMX_n \qquad (1.1)$$

is expected when A is highly electropositive, MX_n contains a metal atom M in a high oxidation state, and X is highly electronegative. Therefore, for a higher cell voltage, lithium is preferable to sodium, and oxides are preferable to sulphides. Moreover, a higher oxidation state of M is more likely to be thermodynamically stable as an oxide than a sulphide.

(a) Rutile-Related Structures

Several rutile-related metal dioxides have been evaluated in an attempt to correlate crystal and electronic structural relationships with electrochemical activity in lithium cells. Among these are RuO_2, WO_2, MoO_2, IrO_2 and OsO_2. In general, they are characterized by relatively low potentials vs Li, i.e. 1 V to 2 V. They have also shown substantial irreversibility upon extended cycling (Abraham, 1983). MoO_2 is used as an active component of electrodes for secondary lithium batteries and is under commercial development.

These dioxides exhibit a range of possibly important parameters for lithium incorporation, such as the size of vacancies available to lithium and its diffusion pathway, electronic conductivity, and various crystallographic distortions (Murphy, 1978).

(b) Layered Transition Metal-Lithium Oxides

Layered structures, in general, are able to accommodate ions of different sizes because of the ease of interlayer separation.

Among the transition metal-lithium oxides, $LiMO_2$, where M = Co, V, Cr, Ni and Fe, several have been identified as potentially useful. $LiCoO_2$ exhibited very high cell voltages with open-circuit-voltages lying in the range 3.9 V to 4.7 V for $0.07 < x < 1$ in Li_xCoO_2 (Abraham, 1983).

As a result of the very high cell voltage (in the 3.5 V to 4 V range), Li_xNiO_2 and Li_xCoO_2 are very promising for applications in secondary lithium battery systems. Moreover, they allow the use of recently developed carbon-lithium negative electrodes which exhibit a better cyclability than the lithium anode. The major disadvantage of the Li_xCoO_2 system is that the cell voltage may be too high as it is out of the electrochemical window of most electrolytes (Delmas, 1992).

(c) **Spinels** (Goodenough, 1989)

Lithium diffusion within the host may be one-dimensional (1D), two-dimensional (2D) or three-dimensional (3D). Transport across the electrode/electrolyte interface is easier for 3D than for 2D or 1D diffusion in the host; moreover, co-intercalation of unwanted species occurs into the layered hosts, but not into the 3D hosts. The $[B_2]X_4$ framework of an $A[B_2]X_4$ spinel may be considered as a host providing 3D diffusion of guest species in a close-packed anion array.

A good example is the manganese spinel framework, $[Mn_2]O_4$. Although λ-MnO_2 and $Li[Mn_2]O_4$ are promising cathode materials for a lithium cell, low Li^+-ion mobilities restrict their use to low-power applications. Other oxospinels that have been investigated include $Li[Ti_2]O_4$ and $Li[V_2]O_4$.

(d) **Other Metal Oxides** (Abraham, 1983)

Several vanadium oxides with perovskite-type structures have received considerable attention. V_2O_3, V_6O_{13}, V_3O_4, V_4O_9 and VO_2(B) react reversibly with Li to varying extents. The best material among them is V_6O_{13}. Some Fe substituted oxides, e.g. FeV_3O_8 and $Fe_{0.13}V_{0.87}O_{2.17}$, were also reported, but they offered no advantage over V_6O_{13}.

The chromium oxides have been investigated briefly. These are Cr_2O_5, Cr_3O_8 and CrO_x-graphite. They show high lithium utilization, ~ 1.4 e^-/Cr and high cell voltages, ~ 3 V. A potential disadvantage is the instability of the organic electrolytes because of the high oxidizing power of chromium oxides and very high voltages required for cell charging.

MoO_3 was one of the earliest materials investigated for use in rechargeable Li cells. Other Mo oxides that received attention include Mo_4O_{11}, Mo_8O_{23}, Mo_9O_{26} and $Mo_{17}O_{47}$. These materials undergo irreversible structural changes on deep discharge.

1.2.3 New Developments

Lithium batteries, in general, have the flattest discharge profiles at high voltage of any battery technology. Thus, they will deliver more energy for a longer time than most other types of batteries. Lithium batteries also have a wide operating temperature range. Many lithium batteries operate over a temperature range of -40°C to 70°C (Bahniuk, 1989).

(a) Anode

In 1985, Moli Energy Ltd. commercialized one of the first lithium rechargeable batteries, the Li/MoS_2 battery. This battery had a venting problem and was subsequently withdrawn from the market. A problem with the recharging of lithium batteries is that lithium dendrites form on the anode. Lithium creates a mossy, granular surface that ultimately causes dendrite formation that can cause a cell to short circuit (Krause, 1993).

One way around the problem is to use alloys, such as lithium-aluminum compounds, that reduce dendrite growth. A different technology, "lithium-ion" systems, avoid the use of metallic lithium or lithium alloys as anode materials. In these systems the cell is loaded in the discharged state in which lithium is initially contained in the host structure of the discharged cathode. The cells use special forms of carbon as the anode. Lithium ions are inserted into the carbon molecular structure. This concept has been labelled the swing concept and the rocking chair concept (Krause, 1993), because the lithium shuttles or

"rocks" between the electrodes as the cell is charged and discharged. In a practical rocking chair cell it is necessary to ensure that one of the electrodes is loaded with sufficient lithium prior to cell assembly (Dahn, 1991).

The disadvantage of the lithium-ion system is that the carbon does not contribute to the electrochemical reaction and thus a reduced cell voltage and more cell weight are the price to pay for a 'safer' battery. Sony Corporation has recently commercialized a "lithium-ion" cell that uses a lithium-cobalt-oxide cathode.

(b) Electrolyte

Another promising technology is the use of polymer electrolytes in a solid-state lithium cell. The challenge has been to make these cells work at room temperature. This technology is in the process of being commercialized. The cathode that has been used in initial studies, is a vanadium-oxide composite material.

(c) Improving Current Technologies

Another trend is to improve older battery technologies. Better nickel-cadmium batteries have emerged in the last 5 years. In addition, the energy density of sealed lead-acid batteries is improving. Rechargeable alkaline manganese dioxide batteries can pack twice the energy of nickel-cadmium batteries and are environmentally friendly, but can only deliver 40 to 50 cycles.

Amongst the emerging 4 V lithium battery technologies Li_xCoO_2 exhibits a better reversibility and a higher cell voltage than the Li_xNiO_2 system. However, the high voltage of the Li_xCoO_2 system may be too high as it is out of the electrochemical window of most electrolytes. The slightly lower cell voltage obtained using Li_xNiO_2 as cathode is more convenient, but some structural rearrangements that occur at low lithium contents and the difficulty of making an ideally-layered $LiNiO_2$ structure limits the utility of this electrode material. Therefore, the use of the solid solution between these two electrode types is a possible way to optimize 4 V lithium cells (Delmas, 1992).

For $y = 0.5$ in $LiCo_yNi_{1-y}O_2$, the compound is easier to prepare than $LiNiO_2$ but has almost the same voltage profile. In addition, nickel is less expensive than cobalt and is more abundant, so $LiCo_yNi_{1-y}O_2$ is more useful than $LiCoO_2$. By extending this concept, it can be argued that the solid solutions $Li_xMn_yNi_{1-y}O_2$ should be investigated since the cost of manganese is about one tenth that of nickel (Rossen, 1992).

1.3 Manganese Dioxide

Li/MnO_2 was the first solid-cathode 3 V lithium system to be manufactured commercially using inexpensive materials which makes it suitable for low-drain long-life mass-production applications. These cells operate over a temperature range from -20°C to +55°C (Ewing, 1982).

Manganese dioxide has a high energy density, is inexpensive and creates no environmental problems. As γ-MnO_2 is well characterized as an active material in zinc cells, it was used as a starting point in the development of the Li/MnO_2 cell.

The γ-MnO_2 phase, which is generally prepared electrolytically (EMD), has a structure which can be described as an intergrowth of rutile and ramsdellite type structures. The γ-MnO_2 electrode must be heat-treated, typically to 400°C, before use to remove surface and occluded water; heat-treatment increases the concentration of the rutile component in the structure. During the discharge of cells, lithium ions are inserted into the γ-MnO_2 structure with a concomitant reduction of the manganese cations from +4 to +3. EMD can operate as a rechargeable electrode over a limited range of x in Li_xMnO_2 ($0 < x < 1$); heat-treatment tends to reduce the rechargeability because the rutile component in the structure increases and also because Li^+-ion insertion takes place more easily into the [2x1] ramsdellite channels, rather than the [1x1] rutile channels.

The advent of lithium battery technology has led to the investigation of many of the polymorphs of manganese dioxide as possible materials for rechargeable cells. The

research emphasis has moved away from γ-MnO_2 which used to be the conventional material. These "new" materials are summarized in Table 1.3.

Table 1.3
Examples of MnO_2 Materials

Material	Structure-Type	Packing	Features	Ref.
α-MnO_2	Hollandite	hcp	Framework, [2x2] channels	a
ß-MnO_2	Rutile	hcp	[1x1] channels	b
γ-MnO_2	Ramsdellite/Rutile	hcp	Intergrown [1x2] and [1x1] channels	c
R-MnO_2	Ramsdellite	hcp	[1x2] channels	d
δ'-MnO_2	Layered	-	Sheets of MnO_6 octahedra with intermediate layers of H_2O and stabilizing cations	e
λ-MnO_2	Spinel	ccp	3-dimensional network of channels	f

Ref. a Ohzuku, 1991; Lubin, 1991a; Rossouw, 1992a; Humbert, 1992
Ref. b Uedaira, 1985; Rossouw, unpublished results
Ref. c Ohzuku, 1989b and 1990
Ref. d Rossouw, 1992b; Thackeray, 1992b and 1993a
Ref. e Rossouw, 1991 and 1993; Lubin, 1991a and 1991b; Ohzuku, 1992
Ref. f Hunter, 1981a, 1981b and 1985; Thackeray, 1992a; Tarascon, 1991a; Manev, 1992a.

These materials have been made in pure form or stabilized with lithium. The best known lithium-stabilized materials are the defect spinel $Li_2Mn_4O_9$ (De Kock, 1990) and the so-called "CDMO" (an acronym used by Sanyo Electrical Co. for Composite Dimensional Manganese Oxide) materials (Furukawa, 1987a, 1987b, 1988 and 1992; Nohma, 1989,

1990, 1991 and 1992; Ohzuku, 1989a; Li, 1991a and 1991b). The "CDMO" and $LiMn_2O_4$ materials have received the most attention over the last 5 to 6 years. The versatility of the structures of these polymorphs of MnO_2 is discussed in more detail in Chapter 2.

1.4 Outline of Research

Novel, or modified, manganese oxides have been synthesized and evaluated as potential cathode materials in rechargeable lithium cells.

The initial idea was to synthesize a novel layered Li-Mn-O structure by inserting manganese into the layered rock salt phase Li_2MnO_3. Limited success was achieved with this approach and this concept was soon revised to encompass the acid-leaching of the lithium oxide component from stable lithium-manganese-oxide compounds, i.e. Li_2MnO_3 and $LiMn_2O_4$, to yield novel manganese oxides.

Li_2MnO_3 has a layered structure in which lithium layers alternate with layers consisting of both lithium and manganese cations. In layered notation Li_2MnO_3 can be written as $Li(Li_{0.33}Mn_{0.67})O_2$ by analogy to the well-known layered compounds $LiCoO_2$ and $LiNiO_2$. It was envisaged that by extracting some lithium oxide from Li_2MnO_3 a novel layered Li-Mn-O compound in which lithium layers alternate with manganese layers, could be formed. Attempts were made to extract Li_2O from Li_2MnO_3 (which can also be written as $Li_2O \bullet MnO_2$) by acid-treatment. This approach lead to novel layered manganese-oxide phases that could be characterized by the general formula $A_{2-x}MnO_{3-x/2}$ (A = H, Li; $0 \leq x \leq 2$).

By increasing the reaction temperature and by refluxing Li_2MnO_3 in H_2SO_4 it was discovered that a highly crystalline α-MnO_2 phase with a hollandite-type structure, with no foreign stabilizing cations in the structure, could be synthesized.

The concept of removing lithium from lithium-manganese-oxides by acid-leaching was

extended to the family of spinel compounds, $Li_xMn_{2-z}O_4$ ($0 \leq x \leq 1.33$; $0 \leq z \leq 0.33$). At room temperature this process leads to the formation of λ-MnO_2, whereas, at elevated temperatures (40°C to 100°C), it was discovered that an essentially pure and highly crystalline ramsdellite-MnO_2 could be synthesized.

This dissertation describes in broad terms the synthesis, structural characterization and electrochemical evaluation of these novel or structurally-modified manganese dioxides and lithium-manganese-oxide phases. It emphasizes the versatility of the lithium-manganese-oxide system and the application of these materials in room temperature lithium cells.

Chapter 2

A Review of MnO_2 and Li-Mn-O Structures

ABSTRACT: The basic crystal structures of the manganese (di)oxides are discussed in this chapter. These include the one-dimensional tunnel structures pyrolusite, ramsdellite, nsutite and hollandite. The rock salt phase Li_2MnO_3 and the δ-MnO_2 family (the phyllomanganates of the birnessite and the buserite group) are discussed as examples of the two-dimensional layered structures. Under the three-dimensional structures, the spinel phases, $Li_xMn_{2-z}O_4$ ($0 \leq x \leq 1.33$ and $0 \leq z \leq 0.33$), are the best known.

2.1 Introduction

2.1.1 Historical Background

MnO_2 is one of many chemical compounds which crystallize in two or more forms. Before the use of X-ray methods to study crystalline materials, the various natural forms of MnO_2 were differentiated by physical appearance (texture, colour, etc.). The names that used to be applied to the principle MnO_2 minerals were pyrolusite, psilomelane, polianite and wad (McMurdie, 1944).

The name pyrolusite was retained for the tetragonal form of MnO_2, while the orthorhombic form was named ramsdellite. What had formerly been called psilomelane was divided into several minerals. Psilomelane was retained as the name for a hydrous barium manganate, and a new name, cryptomelane was proposed for a common

anhydrous potash-bearing manganese dioxide. Cryptomelane occurs in several natural ores which are, or have been, used in dry cells, and it is a constituent of many artificial oxides. γ-MnO_2 has been found to occur naturally in several places (McMurdie, 1944).

In the course of an investigation on methods of preparing artificial manganese dioxide for use in dry cells, it became apparent that a method was needed for classifying the many oxides which were being examined, and which differed so markedly in colour, hardness, apparent density, and chemical reactivity. The obvious classification required was one based on crystal structure, though it was realized that even within one crystal species there would be secondary modifications not easily identified by X-ray or electron diffraction methods (Cole, 1947).

In natural environments manganese occurs in the Mn^{2+}, Mn^{3+} and Mn^{4+} oxidation states. All three valencies form a large number of oxide minerals, ranging from the simple manganosite (MnO), partridgite (Mn_2O_3) and pyrolusite (MnO_2) to complex mixed valence oxides such as birnessite ($(Ca,Na)(Mn^{2+},Mn^{4+})_7O_{14}\cdot H_2O$) and todorokite ($(Na,Ca,K,Ba,Mn^{2+})_2Mn_5O_{12}\cdot 3H_2O$) (Sherman, 1984).

2.1.2 Basic Structures

In the crystal structures of the manganese oxides, manganese cations are octahedrally coordinated by oxygen anions; the resulting [MnO_6] polyhedra are linked by either edge or corner sharing to form infinite chain, sheet, and three-dimensional units (Turner, 1981; Sherman, 1984).

Amongst the possible ways of stacking [MnO_6] octahedra, MnO_2 has been reported to possess structures in which the oxygen layers are hexagonally-close-packed. Furthermore [MnO_6] octahedra always form straight chains, either single (ß-MnO_2, pyrolusite), double (γ-MnO_2, ramsdellite and α-MnO_2) or a mixture of the two (electrolytic manganese dioxide). Reasons for the hexagonally-close-packed (*hcp*) oxygen packing and the straight chains are not very clear and MnO_2 could conceivably exist also with cubic-close-packed (*ccp*) oxygen layers as well as kinked chains of octahedra. The most distinctive feature

of MnO_2 amongst the other MX_2 compounds is the existence of a structure in which there are double chains of occupied octahedra. These straight chains can all be parallel to each other (ramsdellite) or be stabilized by large cations in two perpendicular planes (hollandite) (Voinov, 1982).

The known crystal structures fall into two broad categories: chain or tunnel structures, and layer or sheet structures. The tunnel structure-types all contain infinite chains of edge-shared [MnO_6] octahedra, one to three octahedra wide in the simple cases, which are linked by corner sharing to adjacent chains, and extend in one unique crystallographic axis for each type. The similarity of widths of the tunnels in one dimension theoretically permits domain intergrowths of two or more of the phases (Burns, 1980).

Pyrolusite has the simplest structure, with single chains of [MnO_6] octahedra on each side of a central tunnel (Fig. 2.1a). This arrangement can be represented in shorthand notation as a tunnel of size [1x1]. Pyrolusite intergrows with manganese octahedral chains of greater width by sharing a common single-chain width. The intergrown material is called nsutite (Fig. 2.1c). Hollandite has a [2x2] structure with large cations such as barium, potassium, sodium, or strontium fitting in the centre of the tunnel (Fig. 2.1d). Romanéchite has a [2x3] structure with room for two chains of large cations and water molecules in its centre (Fig. 2.1e) (Turner, 1981).

Most forms of MnO_2 are non-stoichiometric, due to several effects, which can be combined: (i) partial substitution of O^{2-} by OH^-, associated with partial Mn^{3+} content, (ii) presence of structural water, (iii) presence of other metallic cations. The latter are essential components of the α- and δ-forms and of psilomelane, which also correspond to the most open structures (wide tunnels in hollandite and in psilomelane, layered structure in the δ-family) (Strobel, 1986).

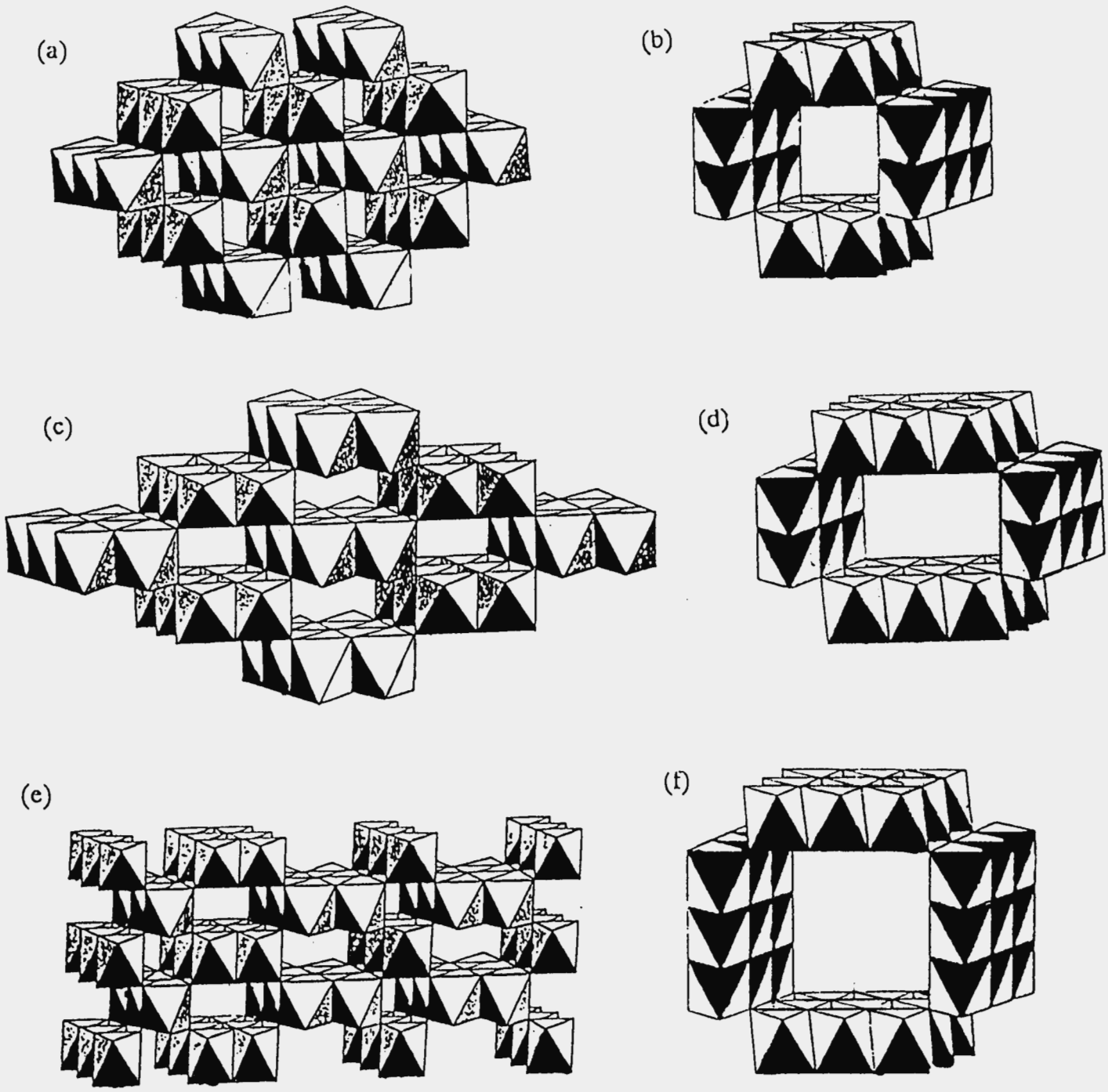

Fig. 2.1 Diagram of the various manganese oxide tunnel (1-dimensional) structures: (a) [1x1], pyrolusite; (b) [2x1], ramsdellite, (c) [1x1] + [2x1], nsutite, (d) [2x2], hollandite, (e) [2x3], romanéchite, and (f) [3x3], a common member of the todorokite family.

α-, δ- and psilomelane are actually ternary compounds and should strictly be called manganates. The family of δ-MnO_2 compounds are commonly called phyllomanganates in view of their lamellar structure. The terms η- and ρ-MnO_2 encountered in earlier work have now been discarded. The ϵ-MnO_2 label has been used by different authors for several structurally different compounds and has been proposed for a hexagonal phase, macroscopically similar to γ-MnO_2. This phase is also denoted *hc*-MnO_2 (Strobel, 1986).

2.1.3 MnO_2 as an Insertion Electrode

Several materials, with different structures, have been evaluated in an attempt to correlate crystal and electronic structural relationships with electrochemical activity in lithium cells. In order to assess the feasibility of MnO_2, and thus the most viable structural arrangement, as an insertion electrode, a look at the basic requirements for insertion electrodes seems appropriate (Murphy, 1979):

- Large free energy of reaction, ΔG, affording a high cell voltage.

- Wide compositional range, resulting in a high cell capacity.

- High diffusivity of the guest species in the host, allowing high power densities.

- Minimal structural change as a function of composition, resulting in a reversible reaction.

- Good electronic conductivity to minimize resistive heat generation and eliminate the need for a conductive additive to the electrode.

- Low solubility in the electrolyte to prevent self-discharge, and for structural stability.

Most of the oxides used as positive electrodes have close-packed oxygen arrays or are considered as derivatives of the ReO_3 structure type by crystallographic shears. Three main types of materials with oxygen close packing are considered as insertion electrode materials: layered oxides, spinel and rutile derivatives (Delmas, 1989).

A good intercalation electrode material must have a large domain of accessible concentration of alkali metal and must exhibit a high mixed conductivity (ionic and electronic). Several cation distributions lead to the layered, spinel and rutile structures. Within the rutile structure the connected vacant sites form parallel tunnels. In the spinel structure the tunnels occupied by the alkali ions are three dimensionally interconnected, leading to isotropic lithium diffusion. The most interesting case is that of layered materials in which the ordered cation distribution in one plane out of two favours high diffusion kinetics for the intercalated alkali metal. Moreover, such a structure allows for easy relaxation of the mechanical constraints resulting from the intercalation and good electronic conductivity within the MO_2 layers (Delmas, 1989)

Host lattices with a framework structure (three-dimensional systems) intercalate only metal ions and protons. Host lattices with layered (two-dimensional) and chain (one-dimensional) structures may take up metal ions as well as molecular ions; both cation types can be solvated by neutral molecules via cation dipole interaction. Layered structures can thus intercalate, besides metal ions, a large variety of species of different size and geometry with expansion of the lattice perpendicular to the layered planes (Schöllhorn, 1980).

The MnO_2 materials can be divided into

- one-dimensional structures which include the tunnel structures resembling the rutile derivatives;

- two-dimensional structures which consist of the layered materials with a close-packed oxygen array; and

- three-dimensional structures which include the spinel framework that has a cubic-close-packed oxygen array.

Diagrams of the different structures are represented in Figs. 2.1 and 2.2.

(a)

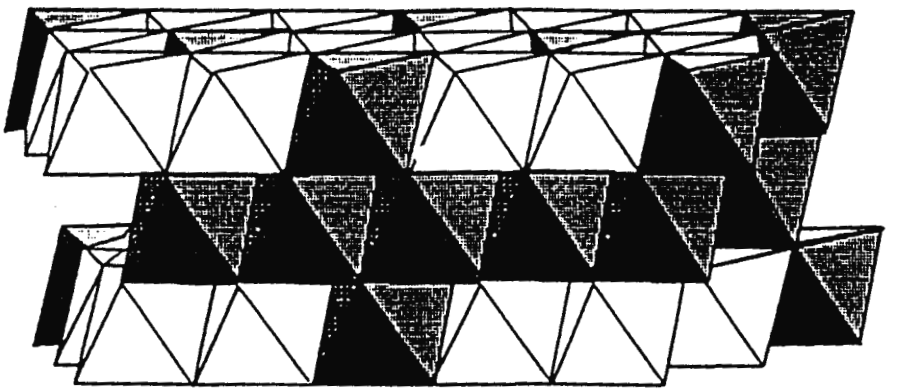

(b)

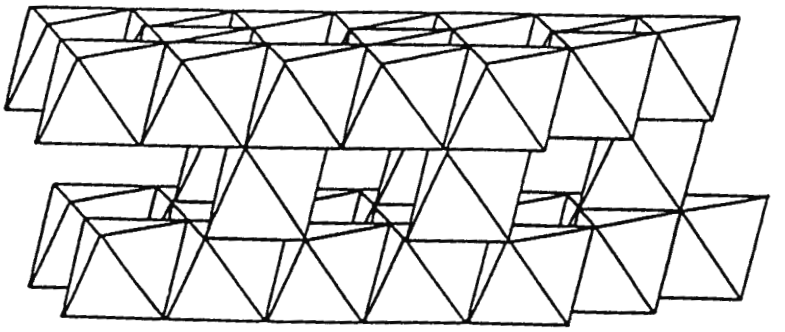

Fig. 2.2 Diagram of (a) the layered (2-dimensional) phase Li_2MnO_3, and (b) the framework (3-dimensional) phase of defect spinel λ-MnO_2.

Contrary to all other alkali or alkaline-earth ions, Li^+ has nearly the same ionic radius as Mn^{4+}, so that both can occupy similar sites in oxygen 3-dimensional frameworks. Very stable structures such as spinel ($Li_4Mn_5O_{12}$) or ordered rock salt superstructures (Li_2MnO_3) are then possible. These compounds are thermally stable and can even form in some low temperature aqueous reactions (Strobel, 1986).

2.1.4 The Li-Mn-O Phase Diagram

As many of these lithium-manganese-oxides and manganese (di)oxides with spinel and rock salt-type structures are of interest for application in lithium battery systems a look at the Li-Mn-O phase diagram is appropriate.

An isothermal cross-section of the pseudo-ternary Li-Mn-O phase diagram at 25°C is shown in Fig. 2.3 (Thackeray, 1992a). Mole fractions of the components were used.

Stoichiometric and defect spinel phases in the Li-Mn-O system are defined by the $Mn_3O_4 \bullet Li_4Mn_5O_{12} \bullet \lambda\text{-}MnO_2$ triangle. Stoichiometric spinel phases are represented by the general formula $Li_xMn_{3-x}O_4$ ($0 \leq x \leq 1.33$); they lie on the tie-line from Mn_3O_4 ($x = 0$) to $Li_4Mn_5O_{12}$ ($x = 1.33$).

Manganese defect oxide spinels, $Mn_{3-x}O_4$ ($0 < x \leq 1$), are located between Mn_3O_4 and $\lambda\text{-}MnO_2$. Lithium defect manganese-oxide spinels, represented by the general formula $Li_2O \bullet yMnO_2$ ($y > 2.5$), lie on the tie line between $Li_4Mn_5O_{12}$ and $\lambda\text{-}MnO_2$; this line also defines a constant valence of 4+ for the manganese ion.

Phases with a rock salt stoichiometry ($Li_zMn_{3-z}O_3$, $0 \leq z \leq 2$) are located on the tie line from MnO ($z = 0$) to Li_2MnO_3 ($z = 2$).

Lithium insertion reactions with spinel electrodes follow the dotted lines that converge at the Li apex of the Li-Mn-O triangle; the dotted lines represent the change in composition of the electrode from a spinel- to a rock salt stoichiometry.

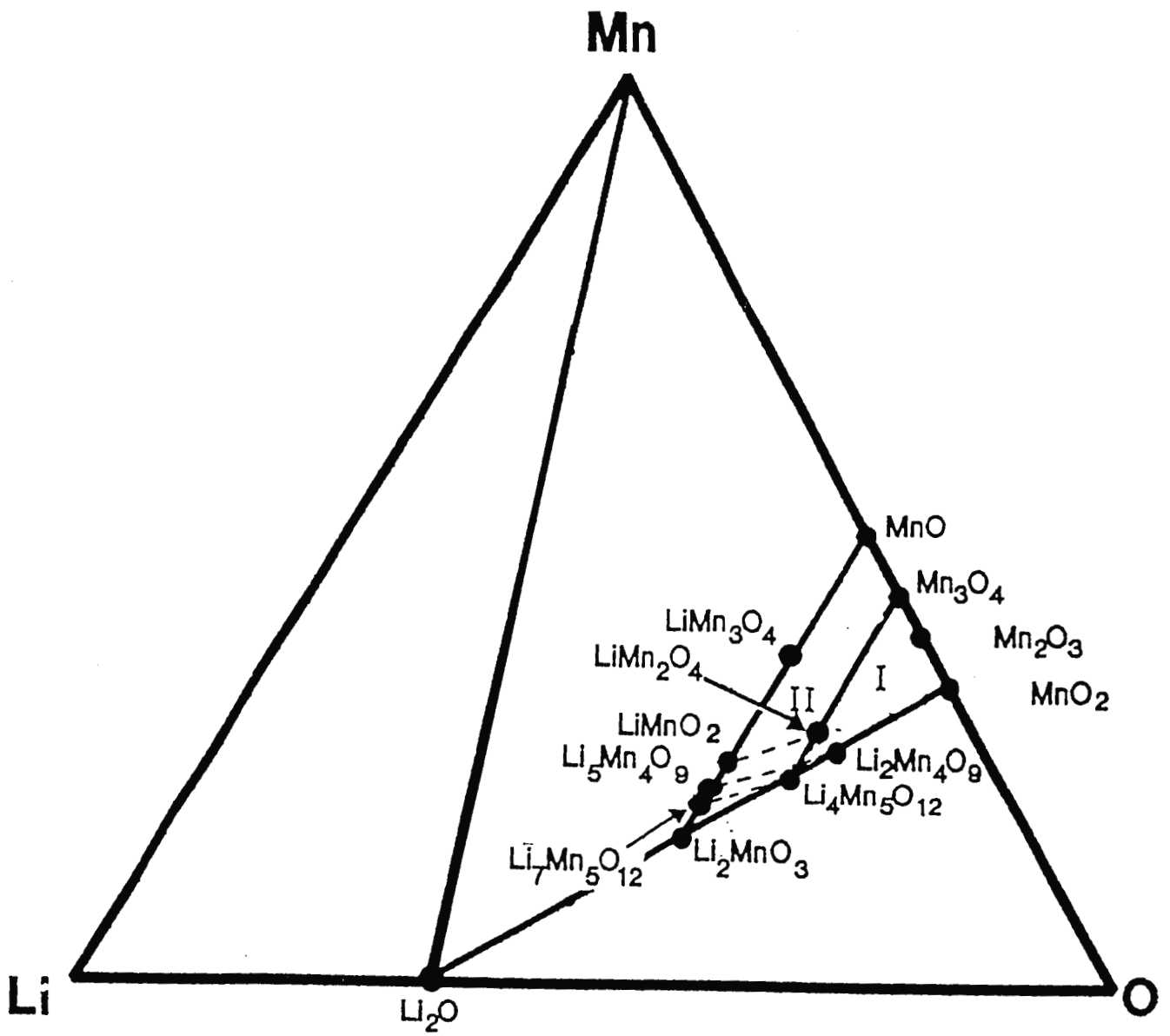

Fig. 2.3 An isothermal cross section of the Li-Mn-O phase (mole fractions) diagram at 20°C. Areas I and II represent regions of defect spinel and defect rock salt phases, respectively (Thackeray, 1992a).

2.2 Tunnel Structures

2.2.1 Pyrolusite (ß-MnO_2)

Pyrolusite was designated ß-MnO_2 by Dubois (Delano, 1950). Pyrolusite has been the only form of manganese dioxide which has been synthesized, and for which relatively unequivocal preparation, structure, and properties were known to earlier researchers. This compound occurs widely in nature (Moore, 1950).

The structure is well established as tetragonal (rutile group) with a = 4.38 Å and c = 2.86 Å. The unit cell contains two MnO_2 formula units, but is usually oxygen deficient (Moore, 1950; Levason, 1972). The rutile structure of ß-MnO_2 possesses the tetragonal space group $P4_2/mnm$ with octahedral site Mn^{4+} ions at positions 2*a* and O^{2-} at positions 4*f*. The 4*f* coordinates x,x,0; -x,-x,0; ½+x,½-x,½; ½-x,½+x,½ contain the variable positional parameter x, which permits distortion of the occupied octahedral sites to orthorhombic point symmetry (David, 1984).

Pyrolusite (ß-MnO_2) is pivotal in descriptions of all manganese oxides. It is isostructural with rutile (TiO_2), in which each cation is surrounded by six oxygen atoms located at the vertices of a distorted octahedron with Mn at the centre. Each [MnO_6] octahedron shares two opposite edges with adjacent [MnO_6] octahedra to form single chains running parallel to the *c*-axis (Fig. 2.1a). These single chains are cross-linked to adjacent chains by corner sharing of oxygen atoms of adjacent [MnO_6] octahedra (Goodenough, 1984; David, 1984; Burns, 1985). All [MnO_6] octahedra are equivalent in ß-MnO_2, and the average Mn-O distance is 1.88 Å. The interatomic distances between adjacent Mn^{4+} cations across the shared edges of the single chains of [MnO_6] octahedra is 2.87 Å, which corresponds to the unit cell *c*-dimension of pyrolusite and many other MnO_2 polymorphs. The single chains of linked [MnO_6] octahedra also define the [1x1] tunnels which, in the ß-MnO_2 structure, are not extended cavities but, instead, correspond to linear arrays of unoccupied octahedra (Burns, 1985).

The anion arrangement is essentially that of tetragonal close packing, which is easily derived from hexagonal-close-packing by a rotation of the *c*-axis strings of edge-shared octahedra. A distortion of the octahedra from cubic to orthorhombic symmetry, which screens the strong electrostatic repulsion between M ions of a string, perturbs the tetragonal close packing of the anions (Goodenough, 1984; David, 1984).

The pyrolusite structure can also be described in terms of a close packed lattice of large O^{2-} anions, which approximate hexagonal-close-packed (*hcp*) layers of large oxygen spheres. In an undistorted *hcp* lattice, there are two tetrahedral and one octahedral interstices per packing O^{2-} anion. In the ideal structure the small tetravalent cations occupy one half of the octahedral sites in a linear array parallel to the *c*-axis. The other half of the unfilled octahedral sites also form linear arrays alternating with the filled octahedral sites along the *c*-axis (Voinov, 1982; Burns, 1985). However, the *hcp* layers of oxygen anions are puckered in the rutile structure, and such an array was described as a primitive-tetragonal-packed (*ptp*) lattice. In the *ptp* lattice, the number of unfilled octahedral sites is doubled and they are strongly distorted compared to those in the *hcp* lattice. These distorted sites are all located in the columns of square cross section in the (0 0 1) projections of the rutile structure (Burns, 1985).

In reality the ideal rutile structure is never met and the $[MnO_6]$ octahedra are distorted in such a way that three coplanar 120° Mn^{4+}-O bonds are preferred to the one 90° and the two 135° angles that would exist if all octahedra were regular. The result appears as a lattice expansion in the *c*-direction and a contraction in the other two (Voinov, 1982).

For each MnO_2 unit there are four empty tetrahedra but these are not all equivalent. Half of the tetrahedra share two faces with two Mn^{4+} occupied octahedra. The other half share only one face with a Mn^{4+} occupied octahedron. Because of cation-cation repulsion, occupied tetrahedra tend not to share any faces at all. If tetrahedra sharing two faces with occupied octahedra are discarded as possible insertion sites, the 3-dimensional array of tetrahedra will only be half occupied giving a maximum insertion amount of 0.5 atoms per MnO_2 (Voinov, 1982). In rutile, intercalation is unfavourable because all possible sites for Li share faces with $[MnO_6]$ units (Murphy, 1991).

Diffusion from tetrahedron to tetrahedron in the *c*-direction takes particles through empty octahedra. Diffusion in other directions is impeded by the fact that it involves transit through the very unfavourable tetrahedral positions that are sharing two faces with occupied octahedra. The poor performance of ß-MnO_2 as a cathode material is due to the fact that even tetrahedra sharing only one face with occupied octahedra are not "good" insertion sites and therefore constitute obstacles to fast diffusion (Voinov, 1982). The limiting composition of $Li_{0.2}MnO_2$ was obtained by chemically lithiating rutile-MnO_2 with *n*-butyllithium (Murphy, 1978).

Primitive-tetragonal anion packing is midway between cubic- and hexagonal-close-packing, so introduction of Li^+ ions could induce a transformation to either hexagonal- or cubic-close packing. However, the electrostatic interactions between cations in face-shared sites is greater on transformation to hexagonal-close-packing, so the transformation to cubic-close-packing of the anions is favoured. Cations in half the *c*-axis chains remain fixed. Cations in the remaining *c*-axis chains are cooperatively displaced to neighbouring, distorted octahedral sites. A diffusionless readjustment of the anion array to give regular octahedra about the manganese, but without shared faces, gives the $[Mn_2]O_4$ spinel framework (Goodenough, 1984; David, 1984).

The density of ß-MnO_2 is 5.2 g/cm^3, making ß-MnO_2 the most compact form of manganese dioxide (Ohzuku, 1988).

2.2.2 Ramsdellite (R-MnO_2)

The structure determination of the mineral ramsdellite gave the symmetry as orthorhombic and the cell dimensions as a = 4.533 Å, b = 9.27 Å and c = 2.866 Å. Possible space groups are Pnam (D_{2h}^{16}) and Pna2$_1$ (C_{2v}^{9}). Each manganese atom is surrounded by six oxygen atoms distributed at the corners of an octahedron with an average Mn-O distance of 1.89 Å. Each oxygen atom is surrounded by three manganese atoms. The oxygen octahedra are linked together by sharing edges, thus producing double strings running in the *c*-direction (Fig. 2.1b); in pyrolusite these are single chains (Fig. 2.1a). By sharing corners the octahedra are further linked together to complete the

structure (Byström, 1949).

The mineral ramsdellite and γ-MnO_2 have a double-octahedral chain structure. It is essentially the ramsdellite structure, except that the short O-O contacts of 2.65 Å have lengthened to the normal value of 3.34 Å in ramsdellite (Bursill, 1979).

Ramsdellite changes to pyrolusite above 250°C. In view of the earlier failures to synthesize ramsdellite, it is necessary to reserve judgement on the identity and characterization of this substance (Moore, 1950; Fleischer, 1962).

The really striking feature of the ramsdellite structure is that there are, per MnO_2, four different tetrahedral sites. These share respectively 3, 2, 1 and 0 faces with occupied octahedra. It is likely that inserted particles will be most stable in the last type of tetrahedron yielding a theoretical maximum insertion amount of one atom per MnO_2. These favoured sites are lined up parallel to the MnO_6 double chains and diffusion in this direction occurs from one tetrahedron through an empty octahedron into another tetrahedron. Diffusion in the other direction is impeded by the fact that it involves transit through the very unfavourable tetrahedral positions that share two faces with occupied octahedra (Voinov, 1982).

In the ideal ramsdellite structure all the oxygens are not equivalent. Half of them are in the same surroundings as in the rutile structure and the same type of distortion will ensue. The other half of the oxygen atoms are not located in the same plane as their three nearest Mn^{4+}. As a consequence the [MnO_6] octahedra will be further distorted in such a way as to bring these oxygens toward the plane defined by their closest Mn^{4+}. This distortion increases the size of the favoured tetrahedron and also of the trigonal position through which diffusion in the *c*-direction occurs. Therefore, the diaspore/ramsdellite structure is not only favoured because it has tetrahedra sharing no faces with other occupied sites but also, and specially in the case of lithium insertion, because of lattice distortions favouring diffusion from one site to the other (Voinov, 1982).

The density of ramsdellite is calculated to be 4.8 g/cm^3, which is 0.4 g/cm^3 smaller than

that of ß-MnO_2 (Ohzuku, 1988).

2.2.3 Nsutite (γ-MnO_2)

Pyrolusite intergrows with manganese octahedral chains of greater width by sharing a common single-chain width as can be seen in Fig. 2.1c. The intergrown material is called nsutite (Turner, 1981).

Both ramsdellite and pyrolusite contain well-defined structural units. For pyrolusite the unit is a infinite chain of [MnO_6] octahedra, each octahedron sharing two opposite edges with its neighbours, while neighbouring chains merely share corners. In ramsdellite units consisting of two such chains exist, each octahedron sharing two edges with those of the other chain (Byström, 1949). Neighbouring units share corners only and are termed double chains (de Wolff, 1959).

The chains run in the *c*-direction for both minerals, i.e pyrolusite and ramsdellite. Viewed in this direction, the outline of the units is a rhomb for the single chain, and roughly a parallelogram for the double chain. γ-MnO_2 is an intergrowth structure with microdomains of ß-MnO_2 in a matrix of ramsdellite MnO_2 (de Wolff, 1959).

γ-MnO_2 contains irregular intergrowths of pyrolusite [1x1] and ramsdellite [1x2] units. The ratio of [1x1] rutile tunnels to [1x2] ramsdellite tunnels for the intergrowth structure of γ-MnO_2 was found to be as high as 46.2 % when extended X-ray absorption fine structure (EXAFS) was used to study the polymorphs (Li, 1988). The alternating *c*-axis chain segments of the basic single and double octahedral chains are random, so that regular periodicity or superstructure may not be apparent. Such lattice disorder causes nsutites and synthetic γ-MnO_2 phases to have extensive defects and vacancies, and to be non-stoichiometric and impure. These factors, together with the small crystallite sizes of natural and synthetic phases therefore give rise to a variety of powder X-ray diffraction lines, as well as the frequently observed asymmetric and selective line broadening for nsutites (Burns, 1980).

γ-MnO_2 is used as a collective name for a series of phases, characterized mainly by their diffraction patterns. The poorest patterns consist of a strong diffuse background with some lines, the greater part of which happen to match certain lines of pyrolusite. The most line-rich patterns, on the contrary, show a remarkable resemblance with the pattern of a rare MnO_2 mineral called ramsdellite. γ-MnO_2 is usually identified by a powder X-ray diffraction pattern containing only four typical and rather broad, lines at $d \approx 4.00$ Å, 2.41 Å, 2.13 Å and 1.63 Å (Delano, 1950; de Wolff, 1959).

In addition to the ores, a considerable number of artificially prepared manganese oxides are available. These are employed largely by mixing them in various proportions with the natural ores in order to obtain certain desired characteristics in the electrochemical cells (McMurdie, 1944).

There are two kinds of γ-MnO_2, i.e. natural ore (NMD) and synthetic MnO_2 produced by chemical (CMD) or electrolytic (EMD) processes (Ikeda, 1983). The synthetic oxides are made by various processes and from various raw materials. Both the natural and the synthetic oxides vary widely in properties such as mineral content, acidity, crystal size and shape, and in impurities. Chemical analysis alone will not indicate whether or not an oxide is suitable for use in electrochemical cells (McMurdie, 1944).

Battery active γ-MnO_2 is prepared by either electrolysis or by aqueous redox chemistry. Wet methods of preparing manganese dioxide may be classified as (i) oxidation of Mn^{2+} ions in an acid solution, (ii) electrochemical oxidation of Mn^{2+} ions in an acid electrolyte, (iii) reduction of Mn^{7+} ions with a reducing agent in an acid or neutral solution, and (iv) hydrolysis of Mn^{4+} ions in an acid solution.

(a) Natural Manganese Dioxide (NMD)

Prior to World War I the principle manganese dioxide used by the dry battery industry was Caucasian ore assaying 80 to 85% manganese dioxide and composed largely of pyrolusite. Among the most promising new ores found after the imports from Caucasus were cut off during World War I, was the Montana ore, assaying 70 to 75% manganese

dioxide. In the early 1920s a new ore from the African Gold Coast (Ghana) was found and became the most important battery ore. The grade is high, usually 84 to 87% manganese dioxide (McMurdie, 1944; Delano, 1950).

(b) Chemical Manganese Dioxide (CMD)

FARADISER WS of Sedema Ltd located in Belgium, is produced from $MnCO_3$ (as an intermediate) by dry oxidation in hot air, repeated leaching of the product with sulphuric acid and finally by oxidation using $NaClO_3$ (Giovanoli, 1990).

(c) Electrolytic Manganese Dioxide (EMD)

EMD is usually manufactured by anodic oxidation of manganous sulphate at inert anode substrates such as titanium or graphite in hot sulphuric acid. The EMD is formed as a deposit on the anode during electrolysis. The deposit is allowed to grow to about one to two inches before harvest. In other words, different portions of the deposit are retained in the electrolyte for different periods of time, which may vary from days to weeks, depending on the electrolytic conditions. While the majority of EMD produced is the γ-variety, ß-phase material is present occasionally. The γ-deposit is bright and hard, and performs well in dry cells. The ß-phase, on the other hand, appears to be dull and gives a poor discharge life. The ß-phase seems to be enriched at the side of the deposit facing the anode. This side, which often gives a porous, sponge-like structure, stays longer in the electrolyte. It appears that EMD "betafication" starts at surfaces by forming ß-MnO_2 nuclei. The nuclei grow into the core of EMD particles to complete the phase transformation. The formation of nuclei and the growth of ß-MnO_2 may be assisted by Mn^{II} in the electrolyte and protons in the EMD lattice (Kao, 1988).

EMD consists mainly of carbonic manganese ore and MnO_2. The crystal structure of EMD is called γ-MnO_2 and has great porosity. From an electrochemical point of view, it has high depolarizing characteristics and is mainly used as the cathodic material for high performance zinc batteries (Ikeda, 1983). EMD contains on average 3.0 % water, while CMD contains 3.5 %.

2.2.4 Hollandite (α-MnO_2)

The name α-MnO_2 is a general term that includes isostructural minerals and synthetic manganese oxides of the hollandite group (Burns, 1980; Bayer, 1966).

The members of the hollandite group can be considered as having the α-MnO_2 structure, for which the idealised unit cell can be written $V_2Mn_8O_{16}$, where V denotes vacant structural sites. Filling of the vacancies by divalent or monovalent cations, which in the hollandite group are large 8-coordinated cations in natural materials, is compensated electrostatically by a valence shift in the manganese ions as indicated in the formula $(V_{2-x}A_x)_x(Mn^{4+}{}_{8-x}Mn^{2+}{}_x)_8O_{16}$ where A is Ba^{2+} in hollandite, Pb^{2+} in coronadite, K^+ in cryptomelane, and possibly also NH_4^+, or H_2O. Vacancies can also occur to a small extent in 6-coordinated (Mn^{4+},Mn^{2+}) positions, and OH^- can substitute for O^{2-} (Byström, 1950; Frondel, 1960; Bursill, 1979; Fanchon, 1991).

The structure is usually stabilized by large alkali or alkaline earth ions in the tunnels (Buser, 1954; Bayer, 1966; Giovanoli, 1980; Turner, 1981). These large cations were believed to be necessary to prevent the structure from collapsing. But it has also been reported that the compound can be stable without any foreign cations (Butler, 1952). They used $MnSO_4$ and $(NH_4)_2S_2O_8$ which gave a material having the same structure as cryptomelane, although potassium could only be present in minute traces. They did not consider the possibility that the ammonium ion may replace the potassium in the cryptomelane structure. This seems to be a common mistake, because Parida et al (1981) also stated that the α-MnO_2 prepared from $MnSO_4$ and NH_4HCO_3 does not contain any alkali metal ion belonging to the category consisting of K^+, Na^+ or NH_4^+. The tunnel sites unoccupied by potassium in a hollandite prepared in a aqueous medium are occupied by water molecules. Attempts to remove all uni- or divalent ions from α-MnO_2 result in structure collapse and conversion into the γ-form (Strobel, 1986).

Giovanoli (1980) stated that the members of the cryptomelane-hollandite group can only and exclusively exist if an appropriate cation of ca. 1.4 Å ionic radius sits in the tectomanganate framework, thus forming tunnels. These tunnels do not exist a priori and

are then empty or filled with water molecules.

In general, the hollandite structure, $A_xB_8O_{16}$, consists of double chains of edge-sharing B-O octahedra that corner share with other double chains to form a framework structure containing large [2x2] tunnels. The generic hollandite structure has tetragonal space group I4/m with a *c*-axis of the order of 3 Å. Hollandites are constituted by a framework of $[(B,B')O_6]$ octahedra providing tunnels of square cross-section running along the *c*-axis (Byström, 1950). A diagrammatic presentation of the ideal hollandite structure is shown in Fig. 2.1d.

A tunnel can be viewed as a string of cavities large enough to accommodate the A cations. The distance between cavity centres is equal to the *c*-cell parameter. The tunnel sites are only partially occupied and it is believed that the A cations can move within the tunnels. Hollandites would thus be a perfect realization of one-dimensional ionic conductors. Two adjacent cavities are separated by a bottle-neck formed of four oxygen atoms (Fanchon, 1991).

Hollandite has a very open structure and it is sometimes thought that diffusion within this structure is very fast. Because some of the oxygen layers are incomplete, such a structure has only three kinds of tetrahedra sharing respectively 3, 2 and 1 face with occupied octahedra. The most favoured site (a tetrahedron sharing no faces) is absent. Hollandite also has less sites sharing only one face than rutile (Voinov, 1982).

Most hollandites have tetragonal symmetry, but the unit cell can also be pseudo-tetragonal (or monoclinic; space group I2/m, C2/m). The symmetry of the compounds depend on the ratio of the average ionic radius of the octahedral cations to that of the tunnel cations. Structures in which this ratio is >0.48 distort, because the columns of B-O octahedra twist to decrease the volume of the tunnel, and thereby lower the symmetry from tetragonal to monoclinic. The position occupied by the tunnel cation is determined primarily by the size of the cation. The tunnel cations fit into cavities that are formed by eight O atoms at the corners of a distorted prism. A tunnel cavity contains one of the A cations, or H_2O, or it can be empty. The cation can occupy the special position at the

centre of the cavity or be displaced along the tunnel toward four of the surrounding O atoms. Relatively small cations displace from the special position to more stable sites that are at the sum of the ionic radii of the nearest oxygen atoms (Post, 1982).

The different methods described in the literature for preparing α-MnO_2 are consistent in that they either involve the reduction of permanganate with reducing agents such as H_2O_2 or HCl, or the oxidation of a Mn^{2+}-salt with an oxidizing agent such as $KClO_3$, O_3 or $(NH_4)_2S_2O_8$ (Tsuji, 1984; Parida, 1981; Fernandes, 1983). It has also been found that the presence of sulphate ions seems to influence the formation of α-MnO_2 (Fernandes, 1983).

Cryptomelane forms very easily and very often, e.g. in preparations starting from $KMnO_4$, and has been used as a depolarizer and as a catalyst (Wadsley, 1951). The potassium content is variable, but never exceeds the amount required to fill approximately 50 % of the potassium sites in the lattice (McKenzie, 1971). Many preparations of widely different alkaline content give pure cryptomelane patterns; $K_2Mn_8O_{16}$ is thus only one member of a series of definite space lattice arrangements, but indefinite chemical compositions. In all these compounds the alkali is chemically bound and partly water insoluble (Delano, 1950); no transformation of cryptomelane to pyrolusite or ramsdellite has been found.

2.2.5 Romanéchite (Psilomelane)

The name psilomelane was used to refer to any hard, botryoidal manganese oxide, regardless of composition or density, until the term had practically come to mean any hard, unidentified manganese oxide, soft samples being referred to as wad. The data in the literature on psilomelane therefore refer in part to cryptomelane, hollandite, coronadite, and lithiophorite, and probably other minerals as well (Fleischer, 1960). Hollandite and romanéchite, two of the more common psilomelane oxides, occur in sediments, weathered outcrops, the supergene zone of Mn and base metal ore deposits, and metamorphosed Mn deposits (Turner, 1979).

Psilomelane has also been used as a mineral name, but the Commission of New Mineral Names voted on 25 August 1969 to make romanéchite the name for the specific mineral and psilomelane as the general name (Turner, 1979).

Romanéchite is one of several naturally occurring manganese oxides with a tunnel structure. The formula is $(Ba,H_2O)_2Mn_5O_{10}$ with Ba/H_2O approximately 1/2. Its structure is closely related to those of hollandite and todorokite and to their many derivative structures. The romanéchite structure consists of double and triple chains of edge-sharing $[MnO_6]$ octahedra that share corners to produce a framework containing large rectangular-shaped tunnels running in the direction of the *b*-axis, measuring two by three [2x3] octahedra on an edge as shown in Fig. 2.1e. The tunnels are occupied by a double row of barium ions and water molecules which are crystallographically indistinguishable. It is considered probable that each tunnel contains an ordered sequence of barium ions and water molecules which, however, are disordered in the structure as a whole. The charges of the tunnel cations are offset by substitution of lower-valence cations in the octahedral sites. By comparison, the hollandite structure is constructed of double octahedral chains and todorokite of triple chains resulting in frameworks with [2x2] and [3x3] square tunnels, respectively (Wadsley, 1953; Turner, 1979, 1981 and 1988).

There is a marked resemblance between the chemical composition of romanéchite and hollandite, the only significant difference being the water present in the former. In hollandite the Ba ions are situated in a single row in tunnels formed by double strings of $[MnO_6]$ octahedra linked in a square array by sharing corners, and elongated in the *b*-axis (monoclinic symmetry axis) direction. The Ba positions are only half filled. Romanéchite is converted to hollandite on heating to 550°C. Since most of the water is expelled at this temperature, the double rows in the tunnels will now consist mainly of Ba ions. The creation of so many vacant sites will doubtless lead to structural instability, and the formation of a single hollandite-type row of Ba ions and vacant sites for each tunnel may readily be visualised. The tunnels of linked $[MnO_6]$ octahedra would then collapse to those of hollandite by the rearrangement of the treble strings into double strings (Wadsley, 1953).

High-resolution transmission electron microscopy (HRTEM) has shown that coherent intergrowths occur between hollandite and romanéchite. These intergrowths may account for (i) the reported range in compositions between different hollandites and romanéchites, and (ii) the variable and problematical X-ray patterns obtained from romanéchite samples (Turner, 1979).

Romanéchite crystallizes in the monoclinic system, space group A2/m, with a = 9.56 Å, b = 2.88 Å, c = 13.85 Å and ß = 92°30′ (Wadsley, 1953). Romanéchite has also been refined to orthorhombic symmetry with a = 9.1 Å, b = 13.7 Å and c = 2.86 Å. Possible formulae are $H_4(Ba,Mn)_2Mn_8O_{20}$ with Ba/Mn close to 1, $BaR_9O_{18}\cdot 2H_2O$ (R = Mn^{4+}, Mn^{2+}, Co^{2+}, etc.) or $BaMn^{II}Mn^{IV}{}_8O_{16}(OH)_4$ (Fleischer, 1960). Another report refined the orthorhombic symmetry with space group P222, and dimensions a = 9.45 Å, b = 13.90 Å and c = 5.72 Å. Two molecules of $A_3X_6Mn_8O_{16}$ per unit cell, where A represents Ba^{2+}, Mn^{2+}, Al^{3+}, Fe^{3+}, Si^{4+} etc., and X represents O^{2-} and OH^- (Mukherjee, 1965).

2.2.6 Todorokite

The name todorokite was recommended to be universally adopted for the predominant manganese oxide mineral accommodating divalent cations of nickel and copper in marine magniferous concretions (Burns, 1983). Todorokite has been found as a product of terrestrial weathering in sedimentary manganese ore, in deep-sea iron and manganese nodules and crusts. It is considered as an important source of Ni, Co, Zn, Cu, Mg in marine manganese nodules (Chukhrov, 1979; Turner, 1979).

Todorokite is a hydrated Na-, Ca-, K-, Mg-bearing manganese oxide with characteristic powder X-ray diffraction lines at about 9.6 Å, 4.8 Å and 2.42 Å (Post, 1988).

Selected area electron diffraction (SAD) has shown that todorokite occurs in the form of lathes with a basal face (0 0 1). A study of SAD-patterns has revealed that besides the todorokite having a = 9.75 Å, b = 2.84 Å and c = 9.59 Å found in many deposits, species with a = 14.6 Å and 24.38 Å occur in the natural environment. Thus, todorokite species may be characterized by unit cells having different parameters a which are

divisible by 4.88 Å. The variations of the *a* parameter and the formation of the todorokite superstructures can probably be attributed to certain differences in their composition and the environment of their crystallization (Chukhrov, 1979).

Although [3x3] dimensional tunnels predominate in todorokite, occasional tunnels with [3x2], [3x4], [3x5], [3x8] and higher dimensions were observed in crystals from both terrestrial and manganese nodule deposits (Burns, 1983).

The unit cell nominally has six Mn and twelve O atoms constituting the octahedral framework, along with the tunnel cations and water molecules. Rietveld refinements, using X-ray powder data, of todorokite have confirmed the basic [3x3] tunnel structure. The basic [3x3] structure is represented in Fig. 2.1f. Fourier-difference maps reveal a major tunnel water and/or cation position at (0.37, 0, 0.35), along with other sites near (0.70, ½, 0.38) and (½, ½, ½). Structure-energy calculations suggest that cations such as Na and Ca reside near (½, ½, ½), where they are octahedrally coordinated by water molecules occupying the other two tunnel positions (Post, 1988).

Todorokite and psilomelane both contain essential Mn^{2+} ions, and in psilomelane these divalent cations are located in specific positions in the triple chains of edge-shared octahedra. The Mn^{2+}, Mg^{2+}, Ni^{2+}, etc. might also be located in analogous sites in todorokite. The larger Ca^{2+}, Na^{+}, K^{+}, Ba^{2+}, etc. ions and H_2O molecules were envisaged to occupy large tunnels in a psilomelane-like tectomanganate structure (Burns, 1983).

Chemical analysis of todorokites in continental deposits show that manganese is present in two oxidation states, and that Mn^{II}/Mn^{IV} ratios fall in the range 0.15 - 0.23. Significant amounts of Mg are also present, suggesting that relatively small divalent Mg^{2+} and Mn^{2+} ions are essential constituents of todorokite. The analyses show that Ca^{2+}, Na^{+} and to lesser extends K^{+}, Ba^{2+}, Ag^{+} and Zn^{2+}, are also common constituents. Several chemical formulae have been proposed for todorokite, including according to Burns (1983), $(Ca,Na,K,Ba,Ag)(Mg,Mn^{2+},Zn)Mn^{4+}{}_5O_{12}\cdot 3H_2O$.

2.3 Spinel Structures

Spinels are crystalline compounds with the general formula AB_2X_4, where A,B = metal cations and X = O^{2-}, S^{2-}, Se^{2-}, isomorphous with the mineral spinel $MgAl_2O_4$. A projection of the spinel structure is given in Fig. 2.4 (West, 1984). Unit cell contents are eight formula units (Z = 8), corresponding to $Mg_8Al_{16}O_{32}$.

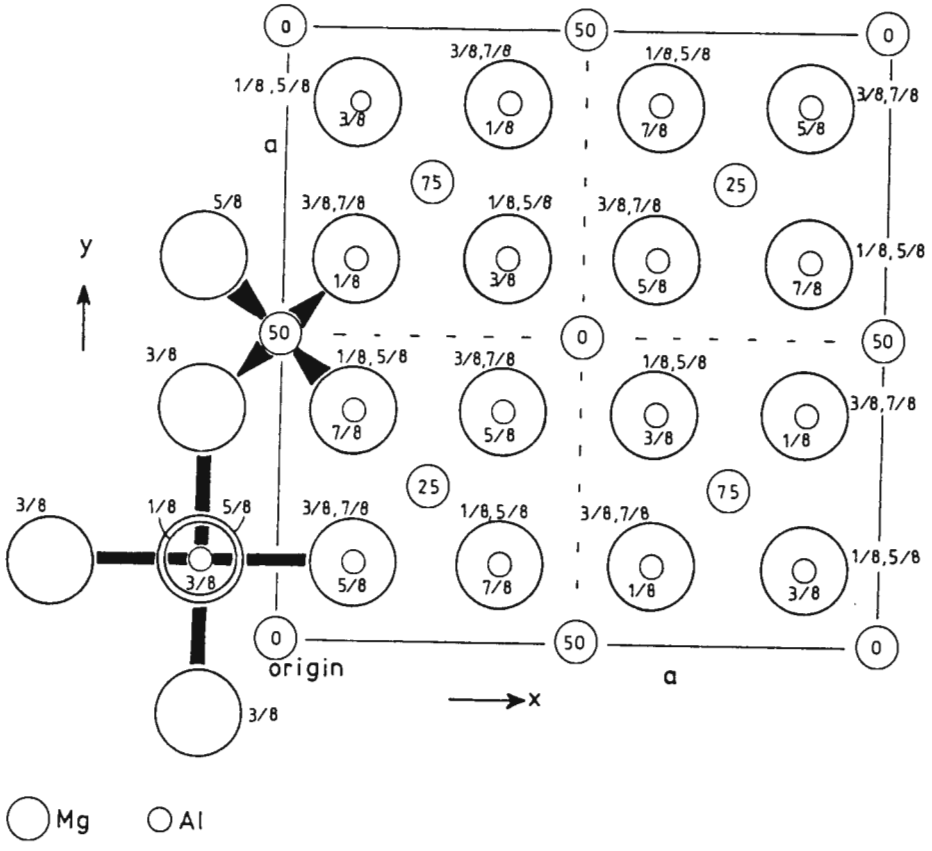

Fig. 2.4 Projection of the spinel structure (West, 1984).

A good review on spinels and in particular $Li[Mn_2]O_4$ is given by J B Goodenough (1984). The structure of the defect spinel λ-MnO_2 is shown in Fig. 2.2b.

The $[B_2]X_4$ framework of the $A[B_2]X_4$ spinels offers a three-dimensional interstitial space within a close-packed anion array. A cubic $A[B_2]X_4$ spinel (lattice parameter a) contains eight formula AB_2X_4 units and has its close-packed array of anions X located at the 32e positions of space group Fd3m (O_h^7). The B cations occupy the half of the octahedral

sites designated 16d, and the A cations the eighth of the tetrahedral sites designated 8a. The empty 16c octahedral sites form an interconnected three-dimensional array of edge-shared sites identical to the 16d array, but shifted by ($a/2$, $a/2$, $a/2$). Each 16c site shares edges with six other 16c sites forming intersecting <1 1 0> chains; it also shares common faces with two 8*a* tetrahedral sites on opposite sides along a <1 1 1> axis.

If the B cations have a strong octahedral-site preference, the lithium spinels LiB_2O_4 are normal, which means that the Li^+ ions occupy the A sites and have access to the interstitial 16c sites. A known example is $Li[Mn_2]O_4$. It has a mixed B-site valence and is therefore a good electronic conductor.

Manganese is stable in octahedral sites as Mn^{2+}, Mn^{3+} and Mn^{4+}. The presence of Mn^{3+} may lead to cooperative Jahn-Teller distortions or to a disproportionation reaction. A cooperative Jahn-Teller distortion generally leads to a site distortion from cubic to either tetragonal or orthorhombic symmetry; a cooperative disproportionation reaction results in a dilation of the Mn^{2+} sites and a contraction of the Mn^{4+} sites that leaves the site symmetry cubic, but changes the translation symmetry of the site potential.

In the insertion/extraction reactions with manganospinels cooperative Jahn-Teller distortions are associated with bulk Mn^{3+}-ion concentrations in excess of a critical value, and surface-disproportionation reactions are found in the system $Li_{1-x}[Mn_2]O_4$ at low pH.

The cubic spinel $Li^+[Mn^{3+}Mn^{4+}]O_4$ has only Li^+ ions in the 3-dimensional interstitial space of the $[Mn_2]O_4$ spinel framework. The fact that $Li[Mn_2]O_4$ is cubic at room temperature whereas $LiMn_3O_4$ is tetragonal (c/a = 1.05) simply shows that the critical concentration of octahedral-site Mn^{3+} ions for a cooperative Jahn-Teller distortion is about one per formula unit and depends on the counter cations that are present. Insertion of Li into the $LiMn_2O_4$ structure produces a tetragonal distortion of the cubic structure. Li^+ ions are nearly randomly distributed over the interstitial 16c and 8a positions. Neutron diffraction data from a chemically lithiated $Li_2[Mn_2]O_4$ confirms ordering of Mn^{3+} ions on the 16d sites, but also a nearly statistical distribution of Li^+ on both 8a and 16c sites. The coexistence of 8a and 16c Li^+ ions promises ready ion

exchange between 8a and 16c positions, a requirement for fast Li^+-ion conduction.

$LiMn_2O_4$ forms whenever Li_2CO_3, or LiOH, and any oxide of manganese are taken in a 1/2 ratio of Li/Mn, and heated at 800°C to 900 °C in air. The product $LiMn_2O_4$ contains equal amounts of Mn^{3+} and Mn^{4+}. Using an excess Li in the reaction leads to the formation of a mixture of $LiMn_2O_4$ and Li_2MnO_3 (a red material), while an excess Mn leads to a mixture containing Mn_2O_3 in addition to the $LiMn_2O_4$. Other lithium or manganese compounds can be used as starting materials provided they decompose under the reaction conditions used (Hunter, 1981a and 1981b).

Due to the multiple oxidation states of Mn and the compositional possibilities of the spinel structure, the carbonate precursor method may be used to prepare cation-deficient spinel-related phases containing Mn in high oxidation states. Spinels so prepared can be defined by the system $Li_2O \cdot yMnO_2$ ($y \geq 2.5$). Spinel phases of composition $Li_4Mn_5O_{12}$ ($y = 2.5$), $Li_2Mn_3O_7$ ($y = 3$), $Li_4Mn_7O_{16}$ ($y = 3.5$) and $Li_2Mn_4O_9$ ($y = 4$), have been prepared mainly by solid reaction of $MnCO_3$ and Li_2CO_3 at $\leq$ 400°C (Nagaura, 1987; Rossouw, 1990; de Kock, 1990; Macklin, 1991; Manev, 1992a and 1992b; Thackeray, 1992a).

2.4 Layered Structures

2.4.1 The Rock Salt Structure of Li_2MnO_3

For the Li_2MO_3 composition the layered structure results from a peculiar Li^+-Mn^{4+} distribution as shown by the crystallographic formula $Li(Li_{0.33}M_{0.67})O_2$ (Delmas, 1989).

Li_2MnO_3 is known to crystallize in the Li_2SnO_3-type structure, an ordered rock salt superstructure with cationic (1 1 1) planes alternatively occupied by Li and by ($LiSn_2$) layers (Lang, 1966). There is some confusion in the literature about the actual cell symmetry of Li_2MnO_3; given as orthorhombic (Lang, 1966) or monoclinic C2/c (Riou,

1992), but cubic and hexagonal forms have also been reported (Riou, 1992). Single crystal structure determination of Li_2MnO_3 has recently shown that the cell is a $Z = 4$ cell with C2/m space group. Refined cell parameters at 25°C are $a = 4.937(1)$ Å, $b = 8.532(1)$ Å, $c = 5.030(2)$ Å, ß = 109.46(3)° (Strobel, 1988).

In the Li_2SnO_3 structure, tetravalent cations lie in layers, forming a honeycomb planar sublattice for complete (LiM_2^{4+}) ordering, separated by O, Li and O layers (Strobel, 1988).

The layered structure of Li_2MnO_3 is presented in Fig. 2.2a.

2.4.2 Phyllomanganates

Syntheses carried out in alkali medium give layered products with formula $A_xMnO_{2\pm y}\bullet zH_2O$, containing alkali cations A. This family of compounds is characterized by (i) a layered texture and structure (when known), hence the name phyllomanganates, (ii) usually poor crystallinity (the powder X-ray diffraction pattern frequently consists of only two to four broad lines), (iii) variable composition and ion-exchange properties with various univalent or divalent cations A. Evidence of layer structures containing CdI_2-like MnO_2 layers, in which a fraction of octahedral Mn sites are vacant, and interlayer A-cation and water sites, has been found. The general formula is $[Mn^{4+}_{n-1}O_{2n}]A\bullet zH_2O$ where $1/n$ is the fraction of Mn vacancies and [...] is the layer content (Strobel, 1987).

Natural δ-MnO_2 or "manganous manganite" was first described under the name birnessite. The four lines recorded in the X-ray diffraction pattern are probably orders of (0 0 *l*), from a layer-structure. Possibly the Ca, Mg and alkalis occupy vacant lattice sites, analogous to the relationship of the hollandite group of minerals to α-MnO_2, and the general formula can be written (Ca, Mg, Na_2, $K_2)_x(Mn^{4+}, Mn^{2+})(O, OH)_2$ where x may be compensated by variation in the Mn^{4+}/Mn^{2+} or O/OH ratios (Frondel, 1960).

Phyllomanganates occur in nature and have been named the birnessite group (7Å-phyllomanganates) and the buserite group (10Å-phyllomanganates). The buserites are

hydrates of the birnessites and can be produced out of them. Rehydration does not occur. The manganates appear in terms of X-ray diffraction as near-amorphous. Two weak and broad peaks near 2.4 Å and 1.4 Å appear, which are the Mn-Mn distances in the tetrameric unit (Giovanoli, 1980).

A compound of manganese dioxide with prominent lines around d_{hkl} = 7.3 Å, 3.6 Å, 2.45 Å and 1.41 Å, frequently has been obtained by precipitation under oxidizing conditions from strongly alkaline solutions. The powder X-ray diffraction patterns of δ-MnO_2 typically contain two broad and diffuse lines at about 2.40 Å and 1.42 Å with or without the presence of the lines at 7.0 Å to 7.2 Å and 3.5 Å to 3.6 Å which are the diagnostic basal plane reflections from the layer lattice of the mineral birnessite (Parida, 1981). McMurdie proposed the name δ-MnO_2 for a material giving an X-ray pattern with only two diffuse lines at 2.4 Å and 1.4 Å (Delano, 1950).

Numerous synthetic phyllomanganates have been reported, with various A cations and compositions. Correlating their chemical composition to a structural formula is difficult; (i) single crystals usually cannot be obtained, (ii) their average manganese oxidation state is generally lower than four, so that a fraction of Mn can occupy interlayer sites as Mn^{2+} (as in Mn_5O_8); the presence of either Mn^{3+} or OH^- (or both) has been conjectured in order to ensure electrical neutrality (Strobel, 1987).

Their structure has been described as infinite two-dimensional sheets of edge-shared [MnO_6] octahedra separated by 7 Å and 10 Å, respectively. Intermediate layers may contain sheets of H_2O, or OH^- anions bonded to the [MnO_6] layers by other cations, such as Zn^{2+}, Cd^{2+}, Mn^{2+}, Na^+, etc. The layered structure and the presence of Mn^{4+} vacancies facilitate ion exchange or chemisorption processes which allow the introduction of other ions into the lattice (Yao, 1987; Strouff, 1988). Cation vacancies may exist in the sheets of edge-shared [MnO_6] octahedra, and these Mn^{4+} vacancies may or may not be ordered. Stacking disorder between octahedral layers, variable arrangements of vacancies in the sheets of edge-shared [MnO_6] octahedra, and different cations adjacent to these vacancies are characteristic features of tetravalent manganese oxides with layer structures such as the polytypes of buserite, birnessite and δ-MnO_2 (or vernadite) (Burns,

1980).

NOTE: Disagreement exists on the usage of the term δ-MnO_2:

- It has been used as an alternative name for birnessite (manganous-manganite), the natural occurring, polycrystalline oxide of tetravalent manganese. The foreign cations such as sodium, calcium and potassium are non-essential (McKenzie, 1971).

- Birnessite is a layered form of MnO_2 usually termed δ-MnO_2, which contains sodium ions (Clearfield, 1988).

- Manganous manganite with a O/Mn ratio > 1.9 is δ-MnO_2; its X-ray diffraction patterns have no basal reflections. The designation Mn^{II}-manganite is retained for samples with a O/Mn ratio of 1.7 -1.9, which show X-ray patterns with basal reflections indicating a double-layer structure (Buser, 1954).

- The term δ-MnO_2 should be reserved for the phase with *d*-spacings only at 2.40 Å and 1.42 Å corresponding to diffraction of X-rays from the (10 $\bar{1}$ 0) and (11 $\bar{2}$ 0) planes of hexagonally close-packed oxygens containing manganese ions in octahedral coordination. δ-MnO_2 is generally considered to be a fine-grained disordered birnessite (Bach, 1991).

- The names δ-MnO_2 and manganous manganite designate compounds of alkali and manganese oxides in variable proportion and, therefore, are incorrectly chosen (Giovanoli, 1980).

2.5 "CDMO"

In 1987 the so-called "Composite Dimensional Manganese Oxide" ("CDMO") was patented by Sanyo Electric Co., Ltd., mainly for application in rechargeable lithium cells (Furukawa, 1987a).

CMD was found to have better rechargeability than EMD and NMD. But the rechargeability of CMD, whose structure is a γ/ß-type, was insufficient. In γ/ß-MnO_2, an expansion of the crystal lattice occurs when lithium ions are inserted into its crystal structure. However, the degree of expansion does not increase much after a large initial change at a quite low depth of discharge. The possibility of having lithium in the manganese dioxide structure beforehand was investigated to see if the rechargeability could be improved (Furukawa, 1987b; Nohma, 1989).

The original "CDMO" was prepared by mixing LiOH and MnO_2 in a Li/Mn ratio of 3/7, and then heat-treated at 375°C for 20 hours. It was labelled LiOH•MnO_2 and the structure claimed to be MnO_2 and Li_2MnO_3 (See Fig. 2.5). Typical surface area is 58 m^2/g (Furukawa, 1987b).

By reacting CMD and $LiNO_3$ in the presence of HNO_3, the formation of a $LiMn_3O_6$ compound (Yoshio, 1989, 1990, and 1991) and a single phase Li_xMnO_2 material (Li, 1991a and 1991b) have been claimed.

The reversibility of MnO_2 modified by reaction with lithiation agents broadly changes with (i) the nature of the Li compound, (ii) the concentration of the Li compound, (iii) nature and pre-treatment of MnO_2, and (iv) the reaction temperature. The superiority of the material prepared at 370°C from CMD (pre-treated with HNO_3) and $LiNO_3$ (7/3 ratio) was established (Li, 1991b).

Controversy about the structure of the composite electrodes exists. Thackeray (Rossouw,

1990) pointed out that the lithium manganese composite oxide of "CDMO" is mainly a lithiated γ-MnO_2 structure, stabilized by domains of spinel, e.g. $Li_2Mn_4O_9$. Yoshio (Nakamura, 1992) did not identify the spinel component; they interpreted the structure of CDMO as being predominantly comprised of the lithiated γ-MnO_2 phase of composition $Li_{0.3}MnO_2$. They did, however, confirm that Sanyo's "CDMO" (Nohma, 1989 and 1990) contains the spinel component.

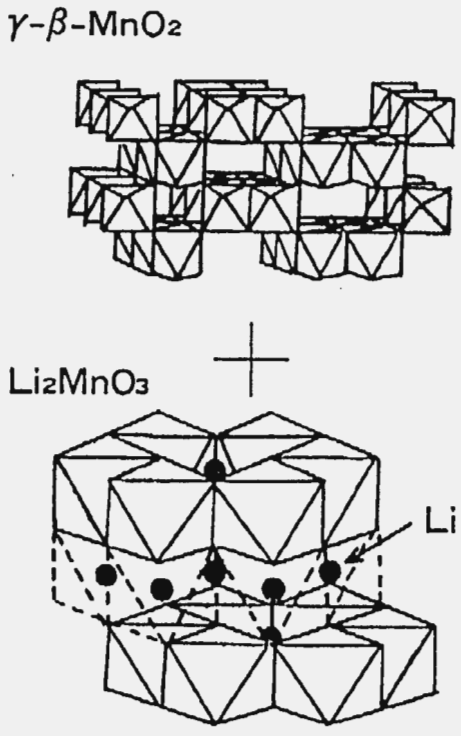

Fig. 2.5 The proposed structure/composition of CDMO (Nohma, 1990).

Chapter 3

Experimental Techniques

ABSTRACT: A number of experimental techniques were used throughout this investigation to study and characterize the materials. The structures were characterized by powder X-ray diffraction and neutron diffraction. Phase transformations were studied by various thermal techniques, and several electrochemical methods were used to examine the electrochemical reactions. The general principles and the instrumentation will be presented briefly in this chapter. A literature review of the physical properties which play a role in the electrochemical activity is given.

Part I - Structural Characterization

3.1 Powder X-ray Diffraction

3.1.1 Historical Background

A powder X-ray diffraction pattern is a set of lines or peaks, each of different intensity and position (*d*-spacing or Bragg angle, θ) on a length of chart paper. For a given substance the line positions are essentially fixed and are characteristic of the unit cell of that substance. The peak intensities, that contain information on the atomic positions within the unit cell, may vary somewhat from sample to sample, depending on the method of sample preparation and the instrumental conditions.

X-rays were discovered in 1895 by the German physicist Wilhelm Conrad Röntgen. X-rays are produced when high-energy electron beams (30 keV to 100 keV) strike a metal

target.

It was proposed in the 1890s that crystals were composed of atoms arranged like closely packed spheres. After it was realised that X-rays have wavelengths in the order of 100 pm, the German physicist Max Theodor Felix von Laue suggested in 1912 that crystals could serve as gratings for the diffraction of X-rays.

At the same time the English physicist Sir William Henry Bragg and his son Sir (William) Lawrence Bragg were experimenting with X-rays having a narrow range of wavelengths.

3.1.2 The Bragg Equation

X-rays are a form of electromagnetic radiation of similar wavelength as the interatomic distance in crystals, and can therefore be diffracted by planes of atoms. The ability to scatter X-rays depends on the number of electrons in an atom. Furthermore, since the atoms in a crystal are lined up in planes, each plane can diffract X-rays. The Braggs found that the X-rays were diffracted only at certain angles that depended on the wavelength and the interplanar spacings.

X-rays impinge on the crystal at an angle θ (Fig. 3.1). The incident X-rays of wavelength λ are reflected specularly (as if by a mirror), the angle of incidence being equal to the angle of reflection. A small part of the beam is reflected from surface atoms as from point A. Some of the beam will penetrate to lower planes and will be reflected. Constructive interference of the beam at RR' occurs only if the difference in distances travelled by the two beams is an integral number of wavelengths, that is, only if the path IAR differs from that of $I'BR'$ by a whole number of wavelengths. Otherwise no diffraction will be observed.

The necessary condition for reinforcement is, therefore, that the distance $BC + CD$ be equal to an integral number of wavelengths ($n\lambda$). Thus, $\sin\theta = CD/d$ or $CD = d \sin\theta$ and $BC = d \sin\theta$.

This condition requires that (Bragg's law)

$$n\lambda = 2d \sin \theta \tag{3.1}$$

Homogeneous X-rays of fixed λ are usually used and for a given set of lattice planes d is fixed. Whether a diffraction maximum is found depends on θ, known as the glancing angle or angle of incidence.

When Bragg's Law is satisfied, the reflected beams are in phase and interfere constructively. At angles of incidence other than the Bragg angle, reflected beams are out of phase and destructive interference or cancellation occurs.

The integer n expresses the order of the reflection; since an nth order reflection from an (h k l) plane can be considered as a first order reflection from a (nh nk nl) plane, it is customary to set $n = 1$. Each plane in a crystal is defined by its Miller indices hkl.

Miller indices of a plane are the reciprocals of the intercepts which the plane makes with the crystallographic axes. For example, if a plane intercepts the crystallographic axes at a/h, b/k, c/l then the Miller indices of that plane is h k l. If a plane is parallel to a crystallographic axis, then the Miller index for that direction will be 0.

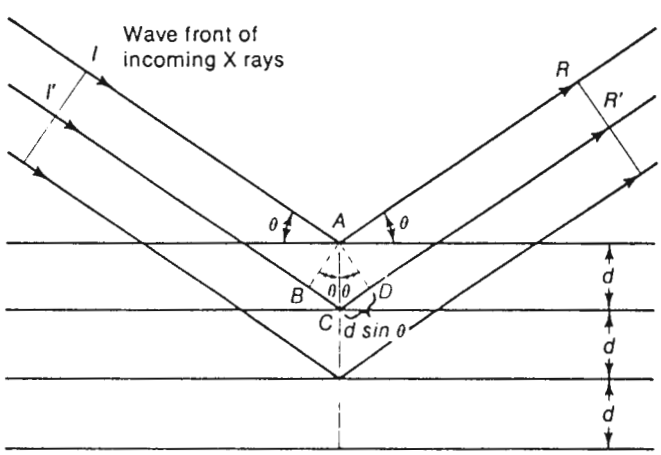

Fig. 3.1 Diffraction of X-rays from the planes of a crystal.

3.1.3 The Powder Method

Single crystal X-ray diffraction is a very powerful method for the determination of crystal structures and has been used to resolve extremely complex systems. Its application, however, is limited by the availability of single crystals. When single crystals are not available, the material is ground down to a powder which then presents all possible orientations to a collimated X-ray beam consisting primarily of Kα radiation.

When reduced to bare essentials, the X-ray diffraction experiment requires an X-ray source, the sample under investigation and a detector to pick up the diffracted beams. Within this broad framework, there are three variables which govern the different X-ray techniques:

- radiation: monochromatic or of variable λ;
- sample: single crystal, powder or a solid piece;
- detector: radiation counter or photographic film.

A monochromatic beam of X-rays strikes a finely powdered sample that, ideally, has crystals randomly arranged in every possible orientation. In such a powder sample, the various lattice planes are also present in every possible orientation. For each set of planes, therefore, at least some crystals must be orientated at the Bragg angle, θ, to the incident beam and thus, diffraction occurs for these crystals and planes. The diffracted beams may be detected by using a movable detector.

The most commonly used powder X-ray instrument is the powder diffractometer. It has a proportional, scintillation or Geiger counter as the detector which is connected to a chart recorder or sometimes to a means of digital output. In normal use the counter is set to scan over a range of 2θ values at a constant angular velocity. Usually the 10 to 80°2θ range is sufficient to cover the most useful part of the powder pattern.

3.1.4 Applications

A powder pattern has three main features that may be measured quantitatively. In decreasing order of relative importance, these are (i) *d*-spacings, (ii) intensities, and (iii) line profiles.

It is by no means a straightforward exercise to obtain reliable powder X-ray intensity data. Sample preparation is very important as it may be difficult if not impossible to avoid preferred orientation of crystals within the powder specimen. Intensities are normally measured as peak heights or peak areas at slow scanning speeds.

For certain specialized applications, the shape of the peaks may yield valuable information. Peaks have a finite width, but extra broadening may occur if stresses are present in the crystals, or the size of the crystals is less than about 2000 Å diameter.

(a) Phase Identification

The most important use of the powder method is in the qualitative identification of crystalline phases or compounds. Powder diffraction tells which crystalline compounds or phases are present, but gives no direct information about their chemical constitution.

Each crystalline phase has a characteristic powder pattern which can be used as a fingerprint for identification purposes. There are two main factors that determine powder patterns: (i) the size and shape of the unit cell, and (ii) the atomic number and position of the various atoms in the cell. The normal practice in using powder patterns for identification purposes is to pay most attention to the *d*-spacings but, at the same time, check that the intensities are roughly correct. The *d*-spacings should be reproducible from sample to sample unless impurities are present to form a solid solution or the material is in some stressed, disordered or metastable condition.

(b) Quantitative Phase Analysis

The amount of a particular crystalline phase in a mixture can be determined, but the process is tedious and prone to errors. It is necessary to add an internal standard, which is a well-crystallized phase, to the sample in a closely controlled amount. A line in the powder pattern of the phase of interest is selected and its intensity is compared with that of the internal standard. The amount of the phase present can be determined by interpolation from a previously constructed calibration graph of intensity against composition.

(c) Unit Cell Parameters

The position of the reflection, given by the angle of incidence of the beam, and generally expressed in 2θ, can be related to the interplanar d-spacing according to Bragg's Law. The interplanar spacings of a crystal are related to the indices of the plane and to the lattice constants. For three simple cases, the expressions are:

Cubic : $$\frac{1}{d^2} = \frac{h^2 + k^2 + l^2}{a^2} \qquad (3.2)$$

Tetragonal : $$\frac{1}{d^2} = \frac{h^2 + k^2}{a^2} + \frac{l^2}{c^2} \qquad (3.3)$$

Orthorhombic : $$\frac{1}{d^2} = \frac{h^2}{a^2} + \frac{k^2}{b^2} + \frac{l^2}{c^2} \qquad (3.4)$$

The position and number of reflections thus give information on the shape and size of the unit cell.

(d) Solid Solution Parameters

The lattice parameters of a solid solution series often show a small but detectable variation with composition.

(e) Crystal Structure Determination

Crystal structures are solved by analysing the intensities of the diffracted X-ray beams. The relative intensities of the reflections can be used to determine the position of the individual atoms within the unit cell. Several factors affect the relative intensity, which will be discussed briefly.

(i) Structure Factor

The structure factor, F, is basically an expression for the wave scattered by the atoms in a plane (*h k l*) within the unit cell, and is specific to a given structure. The determination of a crystal structure by X-ray powder diffraction depends mainly on this term.

X-ray scattering is caused by the electrons in an atom and each different type of atom thus has a different ability to scatter X-rays. Furthermore, because the electron distribution can be "smeared out" unsymmetrically under the influence of adjoining atoms, the ability of an atom to scatter X-rays depends on the space group of the crystal structure. The scattered intensity is the sum of the individual intensities. The scattering factor, *f*, of an atom is proportional to its atomic number, *Z*, or, more strictly, to the number of electrons possessed by that atom; it decreases as θ increases because the electron distribution around the nucleus gives rise to a phase difference. Atomic scattering factors have been tabulated for all the space groups in the *International Tables for X-ray Crystallography* (Vols. 1-5), Birmingham, England, Kynoch Press, 1952. They are tabulated against (sin θ/ λ) to include both angle and the X-ray wavelength.

It is the amplitude of all the superimposed waves that is related to the intensity and, when the contribution of each atom in the unit cell is added, the structure factor, F_{hkl}, is obtained:

$$F_{hkl} = \sum_{j=1}^{N} f_j \exp[2\pi i(hx_j + ky_j + lz_j)] \qquad (3.5)$$

where N is the total number of atoms contained in the unit cell. The intensity is proportional to the amplitude squared.

Two consequences of the dependence of scattering factors on sin θ/λ and atomic numbers are as follows. First, the powder patterns of most materials contain only weak lines at high angles, because atoms scatter weakly at high angles. Second, in crystal determinations using X-rays, it is difficult to locate light atoms because their diffracted radiation is so weak.

(ii) Multiplicity Factor

The multiplicity factor depends on the symmetry of the crystal, and expresses the number of planes with the same *d*-spacing but with different Miller indices. Multiplicity is thus the number of reflections that contribute to an observed powder line.

(iii) Temperature Factor

Thermal vibrations of atoms decrease the intensities of diffracted beams and increase background scatter. The relative intensity is decreased by the thermal vibrations since the vibrations displaces the atoms from an ideal plane; the effect increases at high temperature and at high θ-angles.

The temperature factor is given by the quantity e^{-2M}, where M depends on the average displacement, $\bar{u}$, of the atom and the angle θ:

$$M = 2\pi^2 (\overline{u}^2/d^2) = 8\pi^2\overline{u}^2 (\sin \theta/ \lambda)^2 = B (\sin \theta/ \lambda)^2 \quad (3.6)$$

B is the isotropic temperature factor, and is generally expressed in $Å^2$; λ is the radiation wavelength in Å.

(iv) Polarization Factor

The polarization factor expresses the angular dependence of intensity scattered by electrons and is derived from the Thomson equation:

$$I_P = I_o K/r^2 [(1 + \cos \theta)/2] \quad (3.7)$$

where I_P = intensity at point P
I_o = intensity of the incident beam
K = constant

The expression $[(1 + \cos \theta)/2]$ is known as the polarization factor. It is derived from the fact that the incident beam is unpolarised and can be divided into two polarised components, whose scattered intensities differ and vary with θ.

(v) Lorentz Factor

The Lorentz factor is a geometric factor that depends on the particular instrument used and varies with θ. It causes some diffraction to be observed at angles that differ slightly from the Bragg angle θ. It is given by the expression:

$$L = (4 \sin^2\theta \cdot \cos\theta)^{-1} \quad (3.8)$$

The Lorentz factor and the polarization factor are usually combined to give:

$$L^P = (1 + \cos^2 2\theta)/(\sin^2\theta \cdot \cos\theta) \quad (3.9)$$

(vi) Absorption Factor

The absorption factor takes into account the absorption of X-rays by the sample and depends on the form of the sample and geometry of the instrument.

(vii) Preferred Orientation

If the crystal arrangement is not random, then preferred orientation exists and can introduce errors into the measured intensities. The object of sample preparation is thus to obtain a sample which contains a random arrangement of crystal orientations.

(viii) Extinction

Crystals that are nearly perfect have a reduced diffracting power. This factor is unimportant in powders.

Structural analyses are generally obtained by comparing the normalised calculated and observed intensities of possible models. During structure refinements by least-square methods, site occupancies, fractional coordinates and temperature factors are varied until the best fit between calculated and observed intensities is obtained.

The reliability of the fit between observed and calculated intensity data is measured by the general reliability factor R:

$$R = \frac{\Sigma (I_{obs} - I_{calc})}{\Sigma I_{obs}} \qquad (3.10)$$

where I_{obs} = observed intensity

I_{calc} = calculated intensity

(f) Particle Size Determination

If the average crystal size in a powder is below a certain limit (2000 Å diameter), additional broadening of diffracted X-ray beams occur. From measurement of this extra broadening an average particle size may be obtained.

(g) Short Range Order in Non-Crystalline Solids

Crystalline solids give diffraction patterns that have a number of sharp lines. Non-crystalline solids, e.g. glasses and gels, give diffraction patterns that have a small number of very broad humps.

(h) Crystal Defects and Disorder

Certain types of defect and disorder that occur in crystalline solids may be detected by a variety of diffraction effects.

3.1.5 Facilities

Powder X-ray diffraction data at CSIR were collected on an automated Rigaku diffractometer. The beam of CuKα radiation was monochromated with a graphite single crystal.

A method for powder X-ray diffraction was first developed by Debye and Scherrer in 1916. The Debye-Sherrer camera consists of a cylindrical chamber into which the incident beam is introduced through a collimator. The sample is placed in the cylindrical axis. A film, situated in the internal edge of the cylinder, is used to detect the diffracted X-rays.

Several other cameras now exist, amongst which a widely used version of the Guiner camera. The Guiner camera can be described as a focusing camera with a focusing monochromator, and has the advantage of a better resolution than the Debye-Scherrer

camera.

In this investigation a conventional flat-plate diffractometer was used. Commercial diffractometers were developed in the late 1940s. The geometry of the diffractometer is basically identical to that of the Debye-Scherrer camera; the photographic film is substituted by an electronic counter. A diagram of the diffractometer assembly is shown in Fig. 3.2.

The beam originates from the X-ray source S, placed on the diffractometer circle, and passes through a series of slits (a, A, b) before it reaches the sample C. The sample is mounted on a glass disc, and must be absolutely flat in order to get maximum precision. The component H, which holds the sample in position, rotates about the axis O, forming an angle θ with the incident beam.

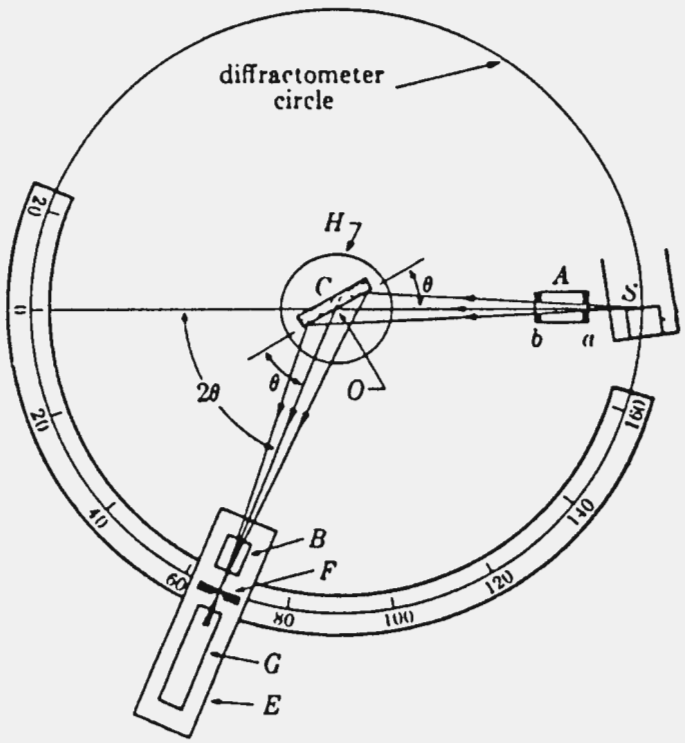

Fig. 3.2 The diffractometer assembly.

During operation the components H and E rotate simultaneously. E must rotate in order to allow the detector to scan the full range of 2θ-values, while H rotates in order to ensure good focusing conditions. Focusing is obtained by maintaining the source S, the receiving slit F and the sample on the focusing circle (Fig. 3.3). This is achieved by rotating the sample about the axis O.

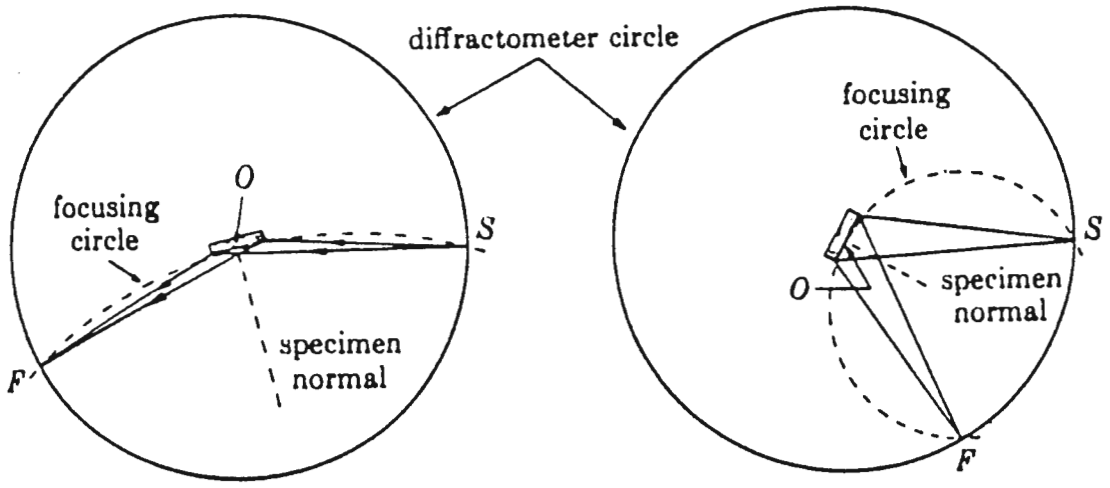

Fig. 3.3 The focusing circle.

The slits A and B are known as Sollier slits, and consists of several long, thin metal plates, parallel to the plane of the diffractometer circle. The slits eliminate to a large extent X-rays which diverge excessively from the plane. Slits a and b, which are situated immediately before and after the Sollier slit A, define the divergence of the beam. The detector G is generally a proportional or a scintillation counter.

A filter is usually placed before the receiving slit F in order to cut out the K_β line and decrease the background radiation. In modern diffractometers, a monochromator is used instead of a filter and is situated between the receiving slit and the detector. Monochromation is usually achieved from a single crystal.

The major advantage of a diffractometer over a camera is that with the former both the position and the relative intensity of the reflection are obtained simultaneously.

3.2 Neutron Diffraction

3.2.1 Background

Neutrons are particularly useful because they interact with unpaired electron magnetic moments and with the nuclear magnetic moments.

Neutron powder data is greatly superior for intercalation compounds of Li because ^{7}Li has a large neutron scattering cross-section, whereas Li contributes little to the X-ray intensities. In addition, because the shape of neutron diffraction peaks is better defined than those with X-rays the entire peak profile may be refined, and the long absorption length of neutrons alleviates corrections necessary with X-rays.

The characteristics of neutron diffraction make it both different and complementary of more conventional radiations (e.g. X-ray and electrons) in studies condensed matter; two of its properties are particular well suited to investigate the behaviour of materials held in complex environments. The first is penetrability: a beam of thermal neutrons can usually get through centimetres of matter while X-ray beams probe only a few microns below the surface of the same material. Another useful property is the almost random variation of its interaction with the elements of the periodic table: as a consequence, neutron diffraction "sees" light atoms, which are usually the most affected by chemical and/or structural transformations, as well as heavier atoms.

3.2.2 Time of Flight Analysis

The neutron source gives a continuous spectrum of radiation without the intense characteristic peaks that are present in X-ray spectra. In order to have monochromatic neutrons it is necessary to select a particular wavelength for use and by some means filter out the remainder. Most of the available neutron energy is wasted, and the beam that is used is weak and not particularly monochromatic.

The method of "pulsed source with time of flight analysis" uses the entire neutron spectrum (variable wavelength, λ) with a fixed diffraction angle, θ. By using a pulsed source, the diffracted radiation is separated according to its time of flight and, hence, according to its wavelength. The fundamental law of diffraction is Bragg's Law, $n\lambda = 2d \sin\theta$. In the time of flight (TOF) method, λ and d are the variables at fixed θ.

3.2.3 Facilities

Time of flight (TOF) neutron diffraction data were collected at the ISIS facility of the Rutherford Appleton Laboratory (UK) either on the POLARIS diffractometer or high resolution powder diffractometer (HRPD). Peak shape was defined by a double-decay exponential, convoluted with a Voigt function. Neutron scattering amplitudes used in the refinements were,

b(Li)	=	-0.203×10^{-12} cm
b(Mn)	=	-0.373×10^{-12} cm
b(H)	=	-0.374×10^{-12} cm
b(O)	=	0.5804×10^{-12} cm

In TOF methods a white beam of neutrons is used; the diffraction pattern is obtained as a function of the time-of-flight of the neutrons in microseconds. This TOF is related directly to the interplanar d-spacings of the crystal lattice according to the expression:

$$d = t(505.556L \sin\theta)^{-1} \qquad (3.11)$$

where t = time-of-flight of neutrons (μs)

L = distance of neutron source to the detector (m)

θ = Bragg diffraction angle, which is kept constant in TOF methods

(For HRPD, L = 96.050 m and 2θ = 168.329°)

Part II - Electrochemical Evaluation

3.3 Galvanostatic Testing and Cell Cycling

3.3.1 General Principles

Galvanostatic reduction and oxidation at constant current yields quantitative information on phase changes and intermediate stages, provided equilibrium potential is maintained and side reactions are excluded. The shape of the electrochemical cell voltage vs the composition of the intercalation electrode is technologically important and scientifically informative. For a binary system the free energy (cell voltage) is constant over a two-phase region and varies smoothly in a single-phase region (Murphy, 1991).

The general chemical concepts that translate into important parameters for batteries based on intercalation reactions include (Murphy, 1991):

- The free energy of reaction determines the cell voltage, $E = \Delta G/nF$.
- The stoichiometry of the intercalant determines the capacity of the cell.
- The rate of the intercalation reaction determines the power that a cell can deliver.

The potential of an electrochemical cell, E, is given by the Nernst equation:

$$E = E_o - \frac{RT}{nF} \ln \frac{[Ox]}{[Rcd]} \qquad (3.12)$$

where E_o = standard electrode potential (V)

R = kN

k = Boltzmann's constant
N = Avogadro's constant
T = temperature (K)
n = number of electrons
[Ox] = concentration of oxidized species
[Red] = concentration of reduced species

The Nernst potential E is measured when the system is at equilibrium and corresponds to the open-circuit voltage (OCV) of the cell.

Although the OCV curve is useful to determine thermodynamic data and to investigate the reaction mechanism, it does not entirely reflect the behaviour of a cell under load, i.e., the conditions in which a battery is used.

The galvanostatic (constant current) discharge curve provides information on the operating voltage and efficiency of a cell when discharged at a given current density. The OCV, measured at equilibrium, is a thermodynamic value and can be calculated according to the Nernst equation. The voltage of an electrochemical cell is lower when discharged at a finite current rate and higher when charged at a finite rate, compered to the OCV curve. The voltage drop on discharge is due to polarisation.

Polarisation can be divided into three broad categories:

(i) activation polarisation, i.e., the energy necessary to initiate the electron transfer reaction;

(ii) concentration polarisation due to the changes in the concentrations of the reactants in the electrodes and the electrolyte. These changes counter diffusion which would lead to a uniform concentration within the electrolyte and the electrode-electrolyte interface;

(iii) resistance polarisation due to the finite electronic conductivity of the

electrodes and the electrolyte, the changes in the concentration of the electrochemically active species within the electrolyte, and the formation of solid products at the electrode surface.

At the beginning of the cell discharge, the voltage drops at an uniform rate which is a function of the current density, i.e., the discharge rate. Once the effects of polarisation for a particular system become predominant, a voltage plateau is observed. This potential is termed the operating voltage of the cell. After a certain time the potential drops. Beyond this point, often termed the knee of the curve, very little useful energy can be obtained from the system. The length of the voltage plateau depends on the discharge rate.

It is generally accepted that the efficiency of an electrochemical cell at different rates of discharge largely depends on the chemical reactions involved and the cell geometry. Since these two factors cannot be separated easily, great care must be exercised when comparing the performance of different systems.

3.3.2 Cell Components

The cell arrangement as used at CSIR will be discussed here. Basically a "flooded-cell" concept is used for cell cycling, galvanostatic discharge curves and determination of open-circuit-voltage curves.

(a) Electrolyte

The electrolyte consisted of 1M $LiClO_4$ dissolved in the mixed solvent of propylene carbonate (PC) and 1,2-dimethoxyethane (DME), 1:1 v/v. It was prepared and stored in the argon filled glovebox.

$LiClO_4$ was dried overnight in the drying oven (80°C to 90 °C). It was then dried under vacuum at 220°C (m.p. 236°C). The dried salt was transferred to the glovebox where it

was crushed and stored.

PC was allowed to equilibrate, for at least 48 hours, over 4 Å molecular sieves which were dried under vacuum at 300°C. The solvent was then transferred to a clean dry flask. The solvent was distilled under vacuum at a vapour pressure of 100°C to 110 °C. The distilled solvent was then transferred to the glovebox where it was stored.

The DME was refluxed over sodium for six hours. The appearance of a deep blue colour upon addition of a few crystals of benzophenone indicated that the solvent was dry. It was then distilled at a vapour temperature of 81°C to 84 °C at atmospheric pressure. The system was protected against humidity with a silica gel drying tube during the entire process. The distilled solvent was transferred to the glovebox immediately, where it was stored over sodium.

(b) Anode

Lithium foil was pressed onto a stainless steel current collector and employed as the anode. The current collector was cut out of stainless steel gauze in a rectangular shape 7 cm x 2 cm.

(b) Cathode

For the cathode, 80 wt% lithium-manganese-oxide material was mixed with 20 wt% teflonized acetylene black (TAB) using hexane as solvent. The TAB was premixed in a 1:2 mass ratio of teflon and acetylene black in a hexane medium and stored in the drying oven (90°C to 100°C). The cathode mix was allowed to dry in the drying oven, before some of it was pressed on the current collector. Typical pressures used are 10 MPa and 20 MPa. The stainless steel current collector consisted of a round disc (diameter 10 mm) spotwelded to a 50 mm stainless steel wire. The cathodes were used in the cells without any further treatment.

(d) Separator

The separator was placed around either the anode or the cathode as a sleeve. It consisted of a microporous membrane made from "Celgard" polypropylene obtained from Hoechst Celanese Corporation in the U.S.A. These thin, opaque membranes have submicron porosity, dimensional stability and have excellent resistance to acids, bases and most chemicals.

3.3.3 Cell Holder and Assembly

The flooded experimental cell consisted of two glass parts. The bottom part consisted of a 12 cm glass tube (diameter 4 cm), of which the bottom 3 cm was tapered to form a flat rectangular pocket. The electrodes fitted into this pocket. A schematic design is presented in Fig. 3.4.

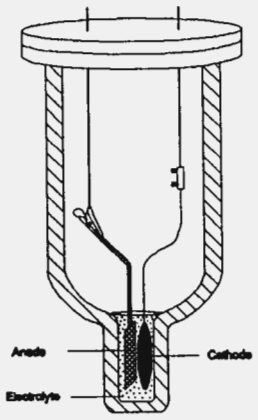

Fig. 3.4 Schematic presentation of the "flooded-cell".

The top part consisted of a flat glass lid through which two metal wires penetrated. To the one wire a crocodile clip was attached onto which the anode was clipped. On the other wire a electric screw connector was attached. The stainless steel wire of the cathode was screwed onto this connector.

The cell was assembled in the glovebox. The separator, in the form of a sleeve, was put

around one of the electrodes. The anode is folded around the cathode and the lower and upper parts of the cell holder put together. Only the small pocket in the bottom of the cell holder was filled with electrolyte before the cell holder was finally sealed with vacuum grease.

3.3.4 Facilities

Discharge and cycling were continuously monitored using an automated cell-cycler, designed at CSIR, connected to a personal computer for data collection.

3.4 Cyclic Voltammetry

3.4.1 General Principles

Cyclic voltammetric studies provide qualitative data on the reversibility of the reaction. In the cyclic voltammetry experiment a potential, applied between the working- and the counter electrode, is varied linearly as a function of time. The current resulting from a redox reaction is measured. A current-voltage curve, i.e. the voltammogram, is thus recorded.

On a negative (cathodic, reduction) scan, the current varies very little until the applied voltage reaches the value of an electrochemical reduction potential of the system observed. At this value, the electro-active species at the surface of the working electrode will be reduced. This results in a rapid increase of the current. The current is controlled by the electron-transfer rate constant, which is a function of the potential, and the movement of electro-active material towards the electrode surface. The electron-transfer rate is responsible for the initial sharp rise of the current.

As the electro-active species in the vicinity of the working electrode is depleted, the process becomes diffusion-controlled, but its rate depends on the diffusion of the electro-

active species through the unstirred electrolyte. The current will then be proportional to the slope of the profile describing concentration versus distance from the electrode.

The scan direction is then reversed. Diffusion-limited reduction continues until the electrochemical oxidation potential is reached. At this point oxidation may occur. The reduced species, accumulated near the working electrode in the course of the negative scan, is oxidised, causing a rise of the anodic current. Once the reduced species close to the electrode is exhausted, the current decreases.

For a fully reversible electrochemical system, the separation between the reduction and the oxidation peak depends on the number of electrons transferred. The reduction peak current equals the cathodic peak current.

An electrochemically reversible system is defined as a reaction that is sufficiently fast to maintain equilibrium between the oxidised and the reduced species at the electrode surface. Slow electron transfer or slow diffusion may result in "irreversibility". In this case an increase in the peak separation is observed when the scan rate is increased.

Cyclic voltammetry yields considerable information about an electrochemical system: reversibility, number of electrons involved, reaction kinetics, etc.

A qualitative analysis of the cyclic voltammograms of intercalation processes yields the following information:

- number of processes involved
- oxidation/reduction potentials for each process
- reversibility of each process
- fate of the reacted species; appearance of new processes, reversibility, etc.

- qualitative assessment of the diffusion rates by varying the scan rates

- relative diffusion rates; comparison of different processes within the same system.

3.4.2 Instrumentation

The instrumentation required for cyclic voltammetry comprises a waveform generator, a potentiostat, a current-to-voltage converter and an XY plotter. The generator produces a triangular excitation signal which is transmitted to the electrochemical cell via the potentiostat. The potentiostat has the function of controlling the working-electrode potential during the reaction. The current-to-voltage converter measures the current. The voltammogram is finally displayed on the XY recorder.

A three-electrode cell assembly is used: a working electrode, a reference electrode and a counter electrode. A potential is applied between the working electrode and the counter electrode. The voltage is measured between the working electrode and the reference electrode, through which practically no current flows.

3.4.3 Cell Components

Lithium foil pressed on a stainless steel disc was used for the reference electrode and the counter electrode. The working electrode consisted of the active material, with approximately 20 wt% teflonized acetylene black, pressed onto a stainless steel disc. 1M $LiClO_4$ in PC:DME (1:1 v/v) was used as the electrolyte. Cell assembly was carried out in the glovebox.

3.4.4 Test Facilities at CSIR

A Princeton Applied Research (P.A.R.) potentiostat (Model 173) linked to a P.A.R. Universal Programmer (Model 175) was used to control the voltage.

Part III - Thermal Analysis

Thermal analysis may be defined as the measurement of physical and chemical properties of materials as a function of temperature. In practice, however, the term thermal analysis is used to cover certain specific properties only. These are enthalpy, heat capacity, mass and coefficient of thermal expansion. In thermal methods of analysis, either temperature change is measured or the temperature is manipulated to produce the measured parameter. Thermogravimetric analysis (TGA), differential thermal analysis (DTA), and differential scanning calorimetry (DSC) are the three major methods that use temperature change as the independent variable.

A fourth thermal analysis technique is dilatometry, in which the change in linear dimension of a sample as a function of temperature is recorded.

Since thermal analyses are usually run under conditions of constant pressure, the underlying equation is the Gibbs-Helmholtz expression:

$$\Delta G = \Delta H - T\Delta S \tag{3.13}$$

where G = the free energy of the system
H = the enthalpy of the system
S = the entropy of the system
T = the temperature in K

3.5 Thermogravimetry

Thermogravimetry involves measuring the mass of a sample as its temperature is increased. A plot of mass versus temperature permits evaluation of thermal stabilities, rates of reaction, reaction processes, and sample composition.

Suitable samples for thermogravimetric analysis (TGA) are solids that undergo one of the two general types of reaction:

$$\text{Reactant(s)} \rightarrow \text{Product(s)} + \text{Gas} \quad (3.14)$$

$$\text{Gas} + \text{Reactant(s)} \rightarrow \text{Product(s)} \quad (3.15)$$

$$\text{Gas} + \text{Reactant(s)} \rightarrow \text{Product(s)} + \text{Gas 2} \quad (3.16)$$

The first process involves a mass loss, whereas the second involves a mass gain. In the third process either mass gain or mass loss can occur, depending on the process.

In a simple thermogram there are two points of major interest to the analytical chemist. The first is the general shape of the thermogram and the particular temperatures at which changes in mass occur. These temperatures are dependent on the heating rate, the nature of the solid and the atmosphere above the sample.

The second major feature of the curve (the magnitudes of the mass changes observed) has found much more use, because it is independent of the many factors that affect the shape of the thermogram. Mass changes are directly related to the specific stoichiometries of the reactions occurring, generally independent of the temperature, but dependent on certain experimental conditions (discussed later). Consequently, precise quantitative analysis of samples whose qualitative composition is known can be made, or else the composition of novel compounds can be deduced.

TGA instrumentation should include several basic components in order to provide the flexibility necessary for the production of useful analytical data. These components are (a) a balance, (b) a heating device, (c) a unit for temperature measurement and control, (d) a means of automatically recording the mass and temperature changes, and (e) a system to control the atmosphere around the sample.

In virtually all TGA analyses, the mass is monitored as the temperature is increased;

accurate measurements under decreasing temperature are difficult and tend to yield no additional information.

A reaction occurs when ΔG for the process becomes zero or negative, and its start is indicated when the mass deviates from the initial plateau. When the reaction stops, a new plateau is reached. The temperatures at which the reaction appears to start and end, as well as the shape of the curve, depend of the heating rate, heat of reaction, furnace atmosphere, amount of sample, nature of sample container, particle size, packing of the sample, to name a few.

The major use of TGA is in the precise determination of mass changes for several sequential reactions.

3.6 Differential Thermal Analysis

Differential thermal analysis (DTA) is the monitoring of the difference in temperature between a sample and a reference compound as a function of temperature. These data can be used to study heats of reaction, kinetics, phase transitions, thermal stabilities, sample composition and purity, critical points, and phase diagrams.

Differences in temperature between the sample and an inert reference substance will be observed when changes that involve a finite heat of reaction, such as chemical reactions, phase changes, or structural changes, occur in the sample. If ΔH is positive (endothermic reaction), the temperature of the sample will lag behind that of the reference. If ΔH is negative (exothermic reaction), then the temperature of the sample will exceed that of the reference. DTA is more widely applicable than TGA because it is not limited to reactions in which a change in mass occurs. If a measurable change in heat capacity accompanies the process, a change in the position of the baseline will be noted.

DTA heating curves are useful both qualitatively and quantitatively. The positions and

shapes of the peaks can be used to determine the composition of the sample. The area under the peak is proportional to the heat of reaction and the amount of material present:

$$\Delta H = k \bullet \text{area}$$

but the constant k is a function of temperature.

Implementing DTA requires the following components: (a) a circuit for measuring differences in temperature, (b) a heating device and temperature-control unit, (c) an amplifying and recording apparatus, and (d) an atmospheric control device.

3.7 Differential Scanning Calorimetry

Measurement of the differential power (heat input) necessary to keep a sample and a reference substance isothermal as temperature is changed (scanned) linearly is the basis of differential scanning calorimetry (DSC).

In DTA, reactions are observed by measuring the deviation of the sample temperature from that of the reference material. This deviation causes thermal fluxes which complicate the theoretical description of the curves and decrease the sensitivity. It would be advantageous to keep the sample and the reference at the same temperature and to measure the rate of heat flow into each that was necessary to maintain the constant temperature. This is achieved by placing separate heating elements in the sample and reference chambers; the rate of heating these elements can be controlled and measured as desired. This is the basis of DSC.

DSC plots are graphs of the differential rate of heating (in J/sec) versus temperature. The area under the peak is directly proportional to the heat evolved or absorbed by the reaction, and the height of the curve is directly proportional to the rate of the reaction

at all temperatures.

3.8 Facilities

For the TGA and DSC experiments a Perkin-Elmer System 7 Analyser at the University of Cape Town was used. A facility to monitor gas flow and to change the reaction medium was available. DTA experiments were undertaken at the Division of Energy Technology at CSIR on a Du Pont Instruments 1090 Thermal Analyser. Samples were heated in air.

Part IV - Physical Properties

No single physicochemical property is sufficient to predict MnO_2 battery activity (Anderson, 1992). An overview of the physical properties, and their measurement, that may have an influence on the battery activity is given here.

Although no significant attempt was made to determine the physical properties of the manganese oxides, several of these properties are important when considering the application of these materials for battery application. Nevertheless, a brief account of some of the most important physical properties is provided in this section.

3.9 Review on Physical Properties

3.9.1 Density

As a general rule higher density EMD permits more energy density to be incorporated in a standardized cell volume, other factors being about the same. As manufacturers switched to metal anodes and low potassium content deposition baths, the observed density by helium displacement came to a fairly standard 4.47 g/cm^3. Any significant

content of potassium-containing cryptomelane in the EMD will lower the average density significantly since the density of cryptomelane is about 4.0 g/cm^3 (Schumm, 1990).

3.9.2 Porosity / Block Density

Porosity is represented by surface area, pore volume, and adsorbed moisture, which parallel one another (Anderson, 1992). Materials with a porous structure or build up of needle crystals show higher electrochemical utilization by weight (Ilchev, 1992).

Block density and Vickers hardness have been shown to be linearly related over a significant range. This relationship is given by

$$HV = 996 \times \text{Block Density} - 3478 \qquad (3.17)$$

where HV = Vickers Hardness and the block density is expressed in g/cm^3 (Swinkels, 1992).

The Ruetschi vacancy model for EMD allows us to calculate a real or true density. Assuming typical values for the vacancy fraction (0.06) and the Mn^{3+} fraction (0.08) and a structure intermediate between ramsdellite and ϵ-MnO_2, we find a true density of 4.55 g/cm^3. This value is similar to the true density of EMD as measured using a kerosene pycnometer (Swinkels, 1992).

Using this the porosity for any value of block density can be calculated as follows:

$$\text{Porosity} = 1 - \frac{\text{Block Density}}{\text{True Density}} \qquad (3.18)$$

and hence the Vickers hardness may be related to the porosity using the value of 4.55 g/cm^3 for the true density (Swinkels, 1992):

$$HV = 918 - 4395 \times \text{Porosity} \qquad (3.19)$$

Higher porosity is associated with lower block density and lower hardness (Swinkels, 1992).

3.9.3 Particle Size

A significant population of particles larger than an average of 35 to 40 microns in "diameter" detract from the achievement of the highest cell efficiency. If the particle size is very small, however, then more carbon (or acetylene black or graphite) is necessary in a cathode mixture to obtain the most efficient discharge and the energy density of the cell is effectively reduced (Schumm, 1990).

3.9.4 Specific Surface Area

Lower surface area reflects a change in the pore size distribution and possibly crystallite formation in γ-MnO_2 materials. In other words, the effect is seen of fewer smaller pores but certainly more larger pores. The larger pores associated with surface areas around 30 m^2/g allow bulk electrolyte to penetrate the pore structure and encourage better electrolyte ion movement into the interior of each particle. However, if the surface area were to approach that of a solid particle, expected electrochemical activity might all but cease (Schumm, 1990).

3.9.5 Gamma Content

The near absence of the peak at 3.11 Å for pyrolusite or cryptomelane is indicative of an improved γ-MnO_2 material. It is interpreted that the X-ray powder diffraction pattern without the 3.11 Å peak means more of the sample is gamma crystal (Schumm, 1990).

3.9.6 Pre-Treatment Temperature of MnO_2 for Lithium Battery Applications

MnO_2 shows a γ-phase between room temperature and 250°C, a γ/ß-phase between

250°C and 350°C, and a ß-phase at temperatures above 350°C. Heat-treatment in a vacuum gives the same results (Ikeda, 1983).

The higher the heat-treating temperature, the lower the open-circuit voltage and initial discharge voltages become. The maximum discharge capacity to a 2.0 V cut off vs Li is obtained when the material was heated at 350°C (Ikeda, 1983; Kozawa, 1989).

Up to 200°C the main product of the thermal decomposition of MnO_2 is water, above 200°C the rate of oxygen evolution increases, and over 300°C the weight losses due to oxygen evolution are dominant. Naturally the thermal stability of MnO_2 samples of different origin can differ. At 300°C the oxygen losses are due to the surface oxygen which has a different bond energy from the bulk oxygen. It was estimated that over 24 hours at 400°C the samples lost between 3 and 6 wt% oxygen. After 48 h of heating in an inert atmosphere at 400°C MnO_2 can be converted into $MnO_{1.5}$ (Manev, 1989). Different manganese dioxides show maximum utilization at different heat-treatment temperatures. The maximum utilization of most types of manganese dioxide was reached by treatment at 300°C, but if it is sustained for more than 8 h the utilization is degraded (Ilchev, 1989 and 1992).

3.9.7 Water Content

Although it is important that there be no water in the cathodic materials for non-aqueous lithium cells, the presence of a little water is unavoidable when MnO_2 is used as active material. However, it is considered that this water is bound in the crystal structure and has no effect on the storage characteristics (Ikeda, 1983).

The water content of EMD is over 5 wt%. Water contents of NMD and CMD are less than that of EMD (Ikeda, 1983). The battery-grade electrolytic MnO_2 commercially available contains 5 to 10 wt% water (Ohzuku, 1981).

There are three basic types of bonded water which are lost at different temperatures

(Manev, 1989):

(i) in the temperature range 100°C to 130°C, absorbed water;

(ii) in the temperature range 150°C to 200°C, water in the MnO_2 micropores; and

(iii) in the temperature range 150°C to 200°C, water release due to the chemical decomposition of MnOOH to Mn_2O_3.

The structural water content is inversely proportional to the specific capacity of the materials (Ilchev, 1992).

The synthesis procedure has a major influence on the water content of the materials. Materials produced via a solid-state reaction at elevated temperatures (400 to 800°C) contain less water than materials prepared from solution techniques, e.g. acid-leaching. Materials synthesized by acid-leaching should thus be dehydrated prior to utilization in lithium cells. Care needs to be taken, however, not to destroy the structure of the material during the dehydration process.

Chapter 4

Layered-MnO_2

ABSTRACT : In this chapter the attempts to synthesize novel layered Li_xMnO_2 compounds ($0 \leq x \leq 1$) from the layered rock salt phase Li_2MnO_3 ($Li_2O \bullet MnO_2$) are described. Particular attention has been given to the structural and electrochemical characterization of a novel lithium-manganese-oxide phase of composition $Li_{0.36}Mn_{0.91}O_2$.

4.1 Introduction

AMO_2 oxides (A = Li, Na; M = V, Cr, Co, Ni) crystallize in a layered rock salt structure in which alternate cation planes are occupied by M and A cations. This arrangement gives rise to sheets of edge-shared [MO_6] octahedra which are held together by interlayer A cations; the bonding within the M-O layers is quite strong compared to the weak interlayer A-O bonding. Although it is possible to remove alkali metals from AMO_2 either chemically or electrochemically to give $A_{1-x}MO_2$ oxides, complete removal of the alkali metal destroys the crystallinity of the structure (Gopalakrishnan, 1988). The ionic character of the A-O bonds leads to strong repulsions between adjacent oxygen layers, so that these materials cannot, in principle, be completely deintercalated (Delmas, 1989).

Investigation of the crystal chemistry of the sodium-manganese-oxide system by classical high temperature synthesis has shown the existence of several phases in the range $0 \leq x \leq 1$ for Na_xMnO_2 (Parant, 1971). In general, structures are three-dimensional for the lower x values and two-dimensional for higher values. For example, in $Na_{0.40}MnO_2$ and $Na_{0.44}MnO_2$ edge-sharing MnO_6 octahedra are linked to form three-dimensional channels

in which the sodium ions can be intercalated, whereas in $Na_{0.70}MnO_{2+y}$ and α-$NaMnO_2$ two-dimensional layered structures have been identified. These layered structures are composed of MnO_2 sheets, built up of edge-sharing [MnO_6] octahedra (Mendiboure, 1985). No lithium analogue of the layered Na_xMnO_2 phases has been reported.

The lithium-metal-oxides Li_2MO_3 (M = Ti, Mn, Mo and Sn), or alternatively $Li(Li_{0.33}M_{0.67})O_2$, crystallize in a related layered structure in which planes of lithium alternate with planes containing lithium and the other metal M in the ratio 1:2. The cation layers are separated from one another by the close-packed oxygen anions. The true symmetry of the ordered structure is monoclinic, C2/m or C2/c.

It is well-known that lithium can be extracted from layered $LiMO_2$ (M = V, Cr, Co, Ni) oxides. The Li^+ and M^{3+} cations reside in alternate layers of octahedral sites between cubic-close-packed oxygen anions. If the MO_2 subarray remained stable, removal of all the lithium would generate an MO_2 phase having the layered $CdCl_2$ structure (Goodenough, 1982; de Picciotto, 1984). Extraction of lithium from layered $LiMO_2$ compounds such as $LiVO_2$ (de Picciotto, 1984 and 1985), $LiCrO_2$, $LiCoO_2$ (Mizushima, 1981; Goodenough, 1982; Wizanski, 1989) and $LiNiO_2$ (Dahn, 1991) have been reported. These materials are of interest as insertion electrodes for rechargeable lithium cells because lithium can be extracted from, and inserted into the structure with a concomitant change in the oxidation state of the transition-metal cation.

For example, lithium was extracted chemically from $LiVO_2$ using stoichiometric quantities of bromine in chloroform according to the reaction:

$$LiVO_2 + {}^{x}/_{2}\, Br_2 \rightarrow Li_{1-x}VO_2 + x\, LiBr \qquad (4.1)$$

For $0 < x < 0.33$ a single phase product was obtained and the VO_2 sublattice remained intact. For $x \geq 0.33$ removal of lithium resulted in a rearrangement of the vanadium cations in the cubic-close-packed oxygen lattice. In $Li_{0.22}VO_2$ approximately one-third of the vanadium cations were located in octahedral sites left vacant in the lithium layer (de Picciotto, 1984).

In the case of $Li_{1-x}CoO_2$, it was possible to maintain an ordering of Li^+ and Co^{3+} ions and to extract reversibly nearly all the Li^+ ions. Open-circuit voltages exceeding 4.0 V were obtained in a $Li/Li_{1-x}CoO_2$ cell, but the high oxidizing power of a Co^{4+}/Co^{3+} couple limits the electrolytes that can be used with such a system (Goodenough, 1982).

Lubin (1991a and 1991b) delithiated a Li_2MnO_3 product that had been synthesized at 700°C from Li_2CO_3 and MnO_2. Delithiation took place at 80°C in a 1M HCl solution. Reaction times varied from 15 minutes to more than 90 minutes. The Li/Mn ratios in the various compounds investigated were determined to be 1.16, 1.049, 0.833, 0.807, 0.60, 0.42 and zero. Up to half the lithium ions could be extracted without destroying the Li_2MnO_3 framework. The 4+ oxidation state of the manganese ions was maintained during the reaction. When the amount of extracted lithium increased, two phases were obtained, firstly, a phase with an Li_2MnO_3-related structure and secondly, γ-MnO_2. Protons were eliminated from the structure by a further thermolysis at 300°C.

Two reaction routes were proposed by Lubin (1991b):

$$Li_2MnO_3 \rightarrow Li_{2-x}H_xMnO_3 \rightarrow {}^{x}/_{2}\, H_2O + Li_{2-x}MnO_{3-x/2} \qquad (4.2)$$

$$Li_2MnO_3 \rightarrow Li_xH_yMn_zO_3 \rightarrow {}^{y}/_{2}\, H_2O + Li_xMn_zO_{3-y/2} \qquad (4.3)$$

Both processes involved an ion-exchange between lithium and hydrogen ions. In reaction 4.2, no manganese is dissolved by the acid-treatment, whereas in reaction 4.3, some manganese is removed by acid leaching (i.e. $z < 1$).

The layered rock salt phase Li_2MnO_3 can be written alternatively as $Li(Li_{0.33}Mn_{0.67})O_2$ by analogy to the well-known layered compound $LiMO_2$ (M = Co, Ni). It is also a member of the $Li_2O \bullet yMnO_2$ system with $y = 1$. Because lithium has been extracted as Li_2O from $Li_2O \bullet yMnO_2$ compounds having a spinel-type structure ($2.5 \leq y \leq 4.0$) to leave the defect spinel, λ-MnO_2 (Thackeray, 1993b), attempts were made to leach Li_2O from Li_2MnO_3 ($Li_2O \bullet MnO_2$) to leave a novel layered MnO_2 compound with a cubic-closed-packed anion array (Rossouw, 1991 and 1993). This approach is similar to the synthesis

route reported by Lubin (1991a and 1991b), although the concept of leaching Li_2O from the Li_2MnO_3 structure was not considered by these investigators.

4.2 Experimental

4.2.1 Synthesis of Li_2MnO_3 Precursors

Li_2MnO_3 precursors were synthesized by using stoichiometric quantities of $LiOH \cdot H_2O$ or Li_2CO_3 and EMD or $MnCO_3$ at 700°C and 400°C. Li_2MnO_3 synthesized at 700°C is referred to as "high-temperature"-Li_2MnO_3 (HT-Li_2MnO_3 for convenience), and Li_2MnO_3 synthesized at 400°C as "low-temperature"-Li_2MnO_3 (LT-Li_2MnO_3 for convenience).

At 700°C, a highly crystalline bright red material forms within 24 hours, while at 400°C it takes at least three weeks for a reasonably crystalline Li_2MnO_3 phase to form.

4.2.2 Synthesis of $Li_{2-x}MnO_{3-x/2}$ Compounds by Acid Leaching

It proved to be more difficult to leach the Li_2O component from HT-Li_2MnO_3 by acid treatment than from LT-Li_2MnO_3. The layered-MnO_2 phases that were synthesized from the two types of Li_2MnO_3 were significantly different and will thus be discussed separately.

$Li_{2-x}MnO_{3-x/2}$ ($0 < x < 2$) products were prepared by reacting m g Li_2MnO_3 with $10m$ ml H_2SO_4. LT-Li_2MnO_3 was subjected to acid treatment at room temperature only. The reaction time of the LT-Li_2MnO_3 with the acid was typically 3 days and the concentration of the sulphuric acid 2.25M.

For the HT-Li_2MnO_3 precursors, reaction temperatures were varied between 25°C (room temperature) and 100°C (reflux conditions) and the reaction time from 24 hours to 4 days. The products were dried overnight at 100°C. Selected samples were dehydrated

further at 250°C or 300°C. The effects of varying the concentration of the H_2SO_4 solution on the final products were also investigated.

Unlike Lubin (1991a and 1991b) H_2SO_4 was used instead of HCl. An advantage of using H_2SO_4 was that reaction temperatures higher than 80°C could be employed, because Li_2MnO_3 tended to dissolve in HCl solutions thereby giving very low yields.

4.2.3 Synthesis of Chemically Lithiated Products

Chemical lithiation of the LT-$Li_{2-x}MnO_{3-x/2}$ ($0 < x < 2$) phases was achieved by reaction with either with *n*-butyllithium in hexane or with LiI in acetonitrile. The latter method has the advantage that lithiated products of well-controlled and defined composition can be prepared (Tarascon, 1991b).

The *n*-butyllithium reaction was carried out in an inert argon atmosphere; the resulting products were highly hygroscopic. An inherent problem of using *n*-butyllithium is that it is a very strong reducing agent and tends to destroy the structure of the intercalated compounds. An alternative approach is to use a milder reducing agent such as lithium iodide with this material. The resulting products have been found to be more stable in air than those synthesized with *n*-butyllithium.

A dehydrated LT-$Li_{2-x}MnO_{3-x/2}$ product, with $x = 1.6$, i.e. $Li_{0.36}Mn_{0.91}O_2$, was chemically lithiated with *n*-butyllithium in hexane under an argon atmosphere. 200 ml dry hexane (dried over sodium) was added initially to 1 g $Li_{0.36}Mn_{0.91}O_2$. The required amount of 15 % *n*-butyllithium in hexane was added. The reaction was stirred at 40°C for 2 days. $Li_{0.36}Mn_{0.91}O_2$ was also chemically lithiated with LiI in acetonitrile at 70°C for 5 h. A stoichiometric quantity of LiI dissolved in 25 ml acetonitrile was added to 1 g $Li_{0.36}Mn_{0.91}O_2$ to obtain $Li_{0.36+x}Mn_{0.91}O_2$ products. An excess of LiI was used to obtain a fully lithiated product, i.e. $Li_{1.09}Mn_{0.91}O_2$.

4.2.4 Chemical Analyses of the Reaction Products

Lithium and manganese concentrations of the HT-$Li_{2-x}MnO_{3-x/2}$, LT-$Li_{2-x}MnO_{3-x/2}$ and chemically lithiated products were determined by atomic absorption spectroscopy. Typically, a 0.1 g sample was dissolved in 10 ml 5M HCl. Approximately 5 drops H_2O_2 was added to enhance the solubility of the sample.

The hydrogen concentration was determined by thermogravimetric techniques. Thermogravimetric analysis (TGA) and differential scanning calorimetry (DSC) were undertaken on a Perkin Elmer System 7 Analyser at the University of Cape Town. For the TGA experiments the gas flow rate was 50 ml/min and the heating rate 20°C/min, while the DSC experiments were carried out under an air flow of 20 ml/min and at a heating rate of 20°C/min.

4.2.5 X-ray and Neutron Diffraction Patterns of the Reaction Products

Powder X-ray and neutron diffraction patterns were obtained at CSIR and at the Rutherford Appleton Laboratory, respectively.

X-ray diffraction patterns were obtained on an automated Rigaku diffractometer with CuKα radiation monochromated by a graphite single crystal. Lattice constants were determined against an internal Si standard. Lattice parameters and structures of the samples were determined from neutron diffraction data collected on the Polaris diffractometer at the Rutherford Appleton Laboratory (RAL) with time-of-flight methods. Data were collected over the range 0.48 Å to 2.90 Å. Structure analyses were undertaken by profile refinement of the neutron diffraction patterns utilizing software developed at the RAL by W I F David and R M Ibberson and the programs of the Cambridge Crystallographic Subroutine Library.

4.2.6 Electrochemical Evaluation of the Reaction Products

Electrode capacities and discharge profiles were obtained from two-electrode cells of the type:

$$\text{Li} \mid \text{1 M } LiClO_4 \text{ in 1:1 PC:DME} \mid \text{Li-Mn-O product} \qquad (4.4)$$

where PC = propylene carbonate, and
DME = 1,2-dimethoxyethane

Approximately 40 mg active material was pressed on stainless steel gauze current collectors; the surface area of the active cathode material was approximately 0.80 cm^2. Cells were cycled between voltage limits of 2.0 V and 4.0 V with a discharge current of 0.2 mA and a charge current of 0.1 mA. A more detailed description of the cell construction and electrode composition are given in Chapter 3 (§ 3.3).

Cyclic voltammetry experiments were carried out in a three-electrode cell that had been assembled under argon, using a Princeton Applied Research (PAR) Model 173 Potentiostat coupled to a PAR Model 175 Universal Programmer. The scan rate used was 1 mV/sec.

Part I - $Li_{2-x}MnO_{3-x/2}$ Compounds from HT-Li_2MnO_3

4.3 Results and Discussion

4.3.1 Synthesis of HT-$Li_{2-x}MnO_{3-x/2}$ Reaction Products

It is more difficult to leach Li_2O (or to ion-exchange Li^+ for H^+) from Li_2MnO_3 synthesized at 700°C, than from Li_2MnO_3 synthesized at 400°C. In Part I of this chapter, the influence of the reaction temperature, the reaction time and the concentration of the H_2SO_4 used with a HT-Li_2MnO_3 precursor is reported.

Fig. 4.1 (a-e) shows the powder X-ray diffraction patterns of the HT-Li_2MnO_3 precursor and products obtained after reaction with 0.5M H_2SO_4 for 24 hours at 25°C, 50°C, 70°C and 90°C, respectively. The patterns are characterized mainly by unreacted Li_2MnO_3, but contain, in addition, a well-resolved, shifted peak at 19°2θ and broad, more intense peaks at 38°2θ and 49°2θ. These peaks indicate the formation of a novel layered phase in the system $A_{2-x}MnO_{3-x/2}$ (A = Li, H; $0 \leq x \leq 2$) as a result of the leaching of an appreciable amount of Li_2O from the Li_2MnO_3 structure and by ion-exchange of H^+ for some of the residual Li^+. The novel layered phase is discussed in detail in Part II of this chapter. A single phase layered product could not be obtained by using HT-Li_2MnO_3 as precursor.

Apart from the reaction temperature, the concentration of the acid also influences the final product. HT-Li_2MnO_3 (Fig. 4.2a) was reacted with 4.5M H_2SO_4, as opposed to 0.5M, for 4 days at 25°C, 50°C, 70°C and 90°C; the powder X-ray diffraction patterns of the products are shown in Fig. 4.2 (b-e), respectively. At 25°C (Fig. 4.2b) the onset of the layered-MnO_2 phase can be seen by the small shoulder on the [0 0 2] peak at 18.7°2θ, while at 50°C (Fig. 4.2c) the layered-MnO_2 phase is present in a higher concentration.

At 70°C (Fig. 4.2d) three phases can be identified, viz. unreacted HT-Li_2MnO_3, a layered-MnO_2 phase and an α-MnO_2 phase (see Chapter 5). At 90°C (Fig. 4.2e) a pure α-MnO_2 phase was obtained.

4.3.2 Thermal Stability of HT-$Li_{2-x}MnO_{3-x/2}$ Phases

The powder X-ray diffraction patterns of HT-$A_{2-x}MnO_{3-x/2}$ with Li/Mn = 0.94 and [H^+] = 0.89 wt%, ($Li_{0.94}MnO_{2.47} \equiv Li_{1.14}Mn_{1.21}O_3$) after heat-treatment in air at 300°C ([H^+] = 0.07 wt%), 500°C and 800°C are shown in Fig. 4.3 c, d and e, respectively. Examination of the powder X-ray diffraction pattern of the material heated to 300°C (Fig. 4.3c) shows that the doublet at 19°2θ has reverted back to a singlet and that the intensities of the peaks at 38°2θ and 49°2θ have decreased significantly. Although the pattern in Fig. 4.3c is very similar to the original HT-Li_2MnO_3 precursor (Fig. 4.3a) the peaks have shifted, are also broader, and differ in their relative intensities.

After heat-treatment to 500°C (Fig. 4.3d) a second phase could be detected. After heat-treatment to 800°C, the $A_{2-x}MnO_{3-x/2}$ product which initially was assumed to contain tetravalent manganese, decomposes into the rock salt phase Li_2MnO_3 and the stoichiometric spinel $LiMn_2O_4$ (Fig. 4.3e), according to reaction 4.5:

$$Li_{1.14}Mn_{1.21}O_3 \rightarrow 0.355\ Li_2MnO_3 + 0.430\ LiMn_2O_4 + 0.108\ O_2 \qquad (4.5)$$

The [H^+] which is removed from the structure was excluded from the reaction, for simplicity.

The powder X-ray diffraction patterns of a HT-$A_{2-x}MnO_{3-x/2}$ product with a Li/Mn ratio of 0.55 ($Li_{0.55}MnO_{2.28} \equiv Li_{0.724}Mn_{1.316}O_3$) after heating at 100°C to 800°C are shown in Fig. 4.4(a-f). Fig. 4.4f shows that the spinel $LiMn_2O_4$ is the major phase present after heating in air at 800°C. A trace of Li_2MnO_3 can also be detected. This is consistent with the decomposition reaction 4.6:

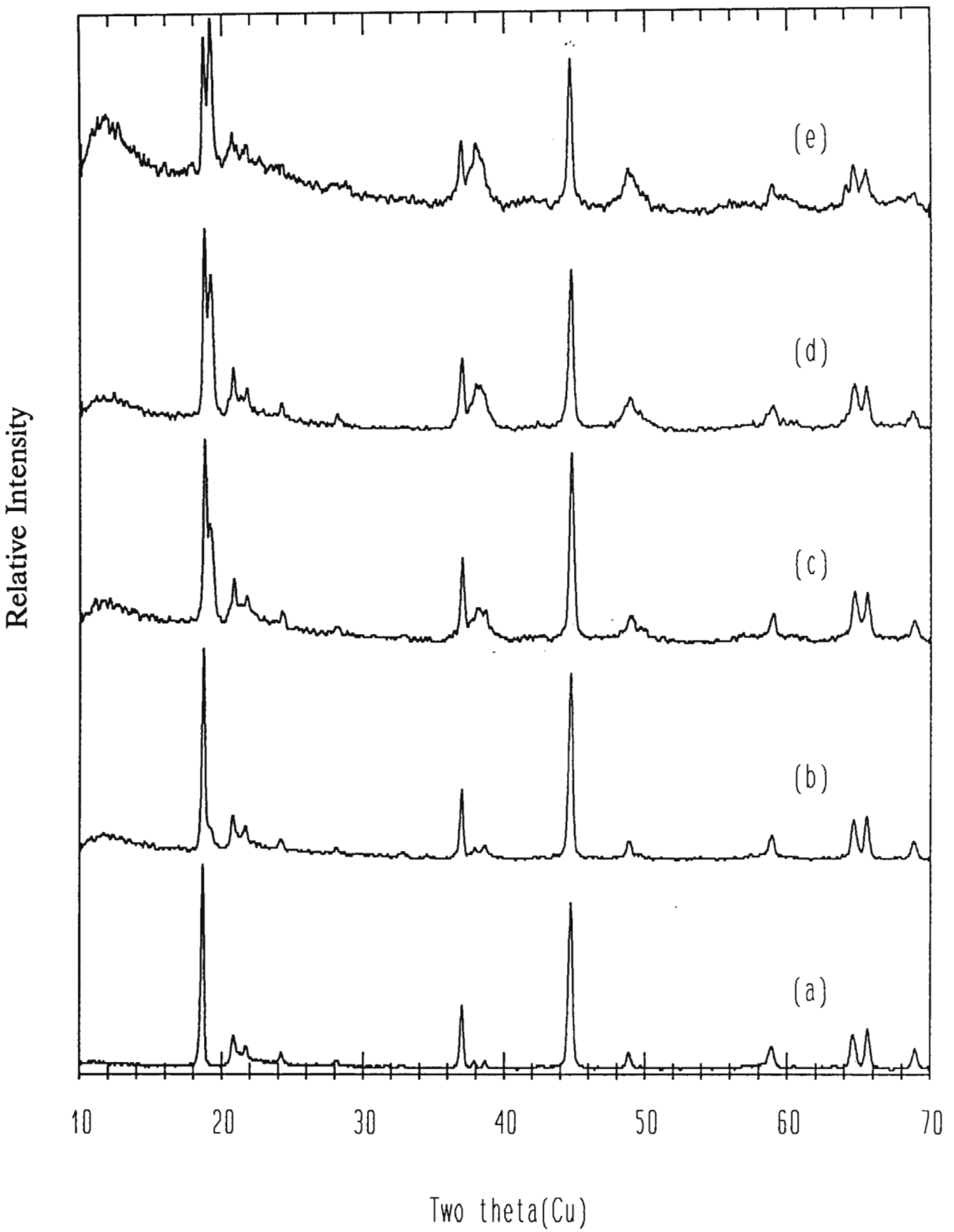

Fig. 4.1 Powder X-ray diffraction patterns of (a) HT-Li_2MnO_3, after being acid leached in 0.5M H_2SO_4 for 24 hours at (b) 25°C, (c) 50°C, (d) 70°C, and (e) 90°C.

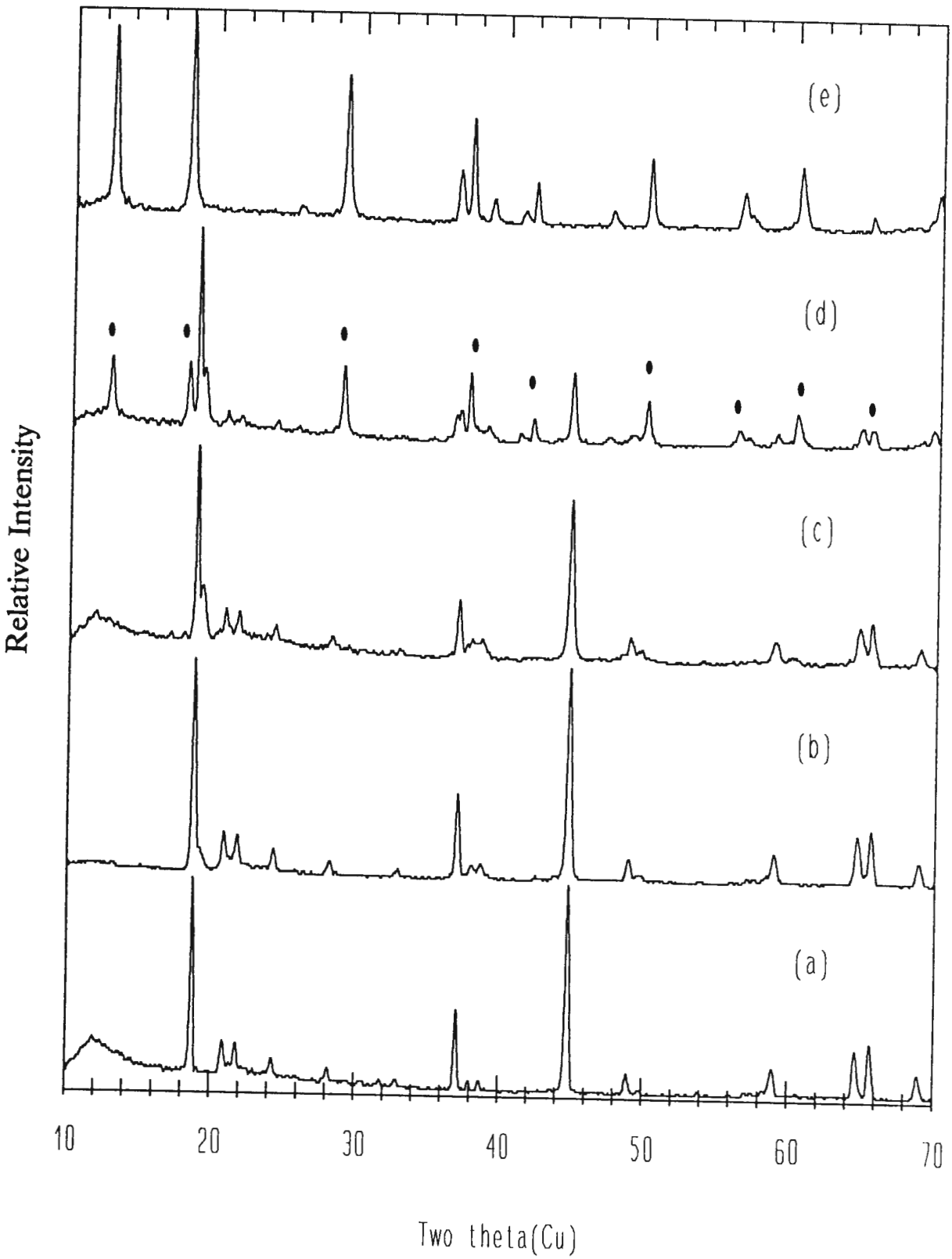

Fig. 4.2 Powder X-ray diffraction patterns of (a) HT-Li_2MnO_3, after being acid leached in 4.5M H_2SO_4 for 4 days at (b) 25°C, (c) 50°C, (d) 70°C, and at (e) 90°C. (• = α-MnO_2 phase).

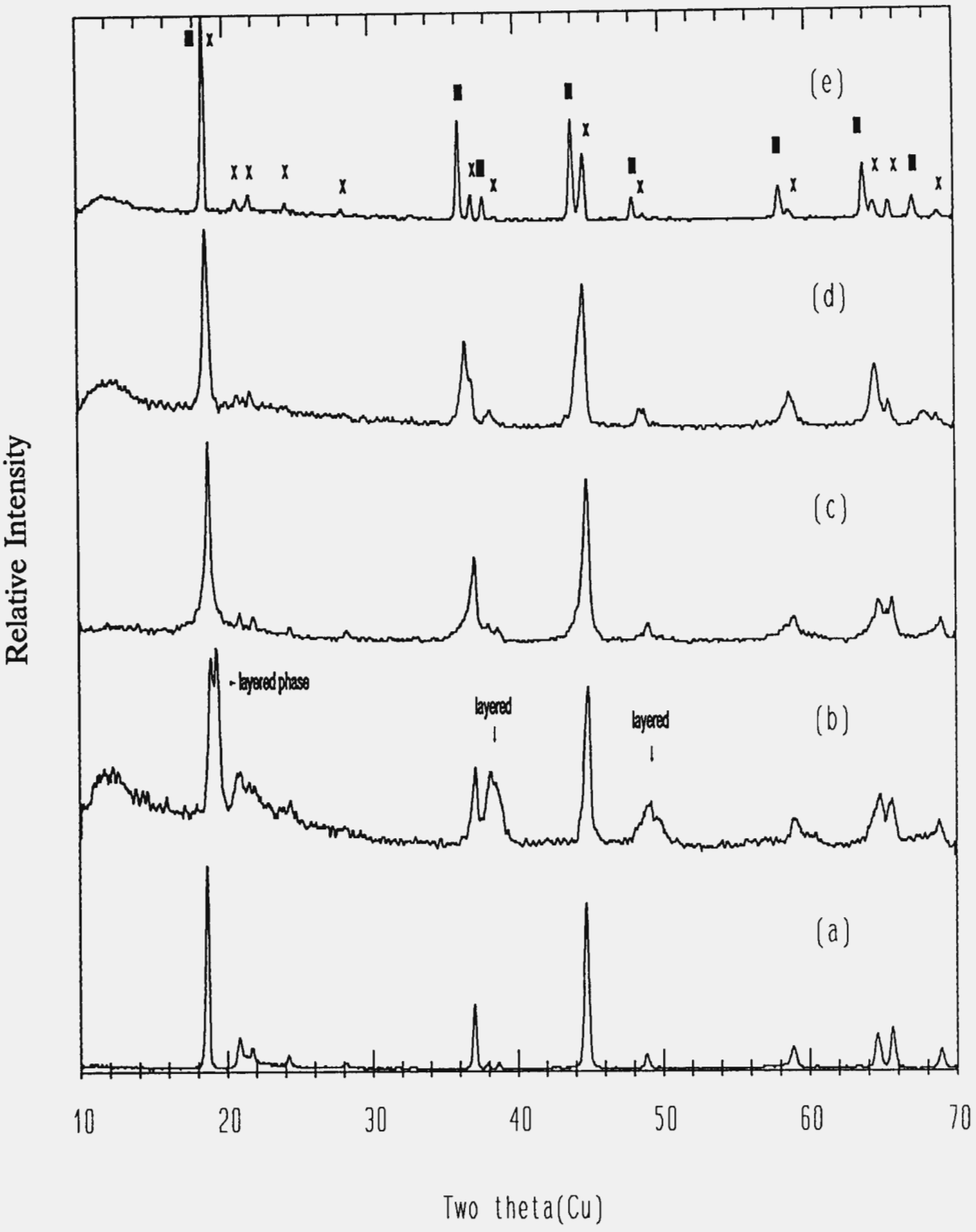

Fig. 4.3 Powder X-ray diffraction patterns of (a) HT-Li_2MnO_3, (b) HT-$A_{2-x}MnO_{3-x/2}$ (Li/Mn = 0.94) heat-treated to (c) 300°C, (d) 500°C, and to (e) 800°C. (x = Li_2MnO_3; ◙ = spinel phase).

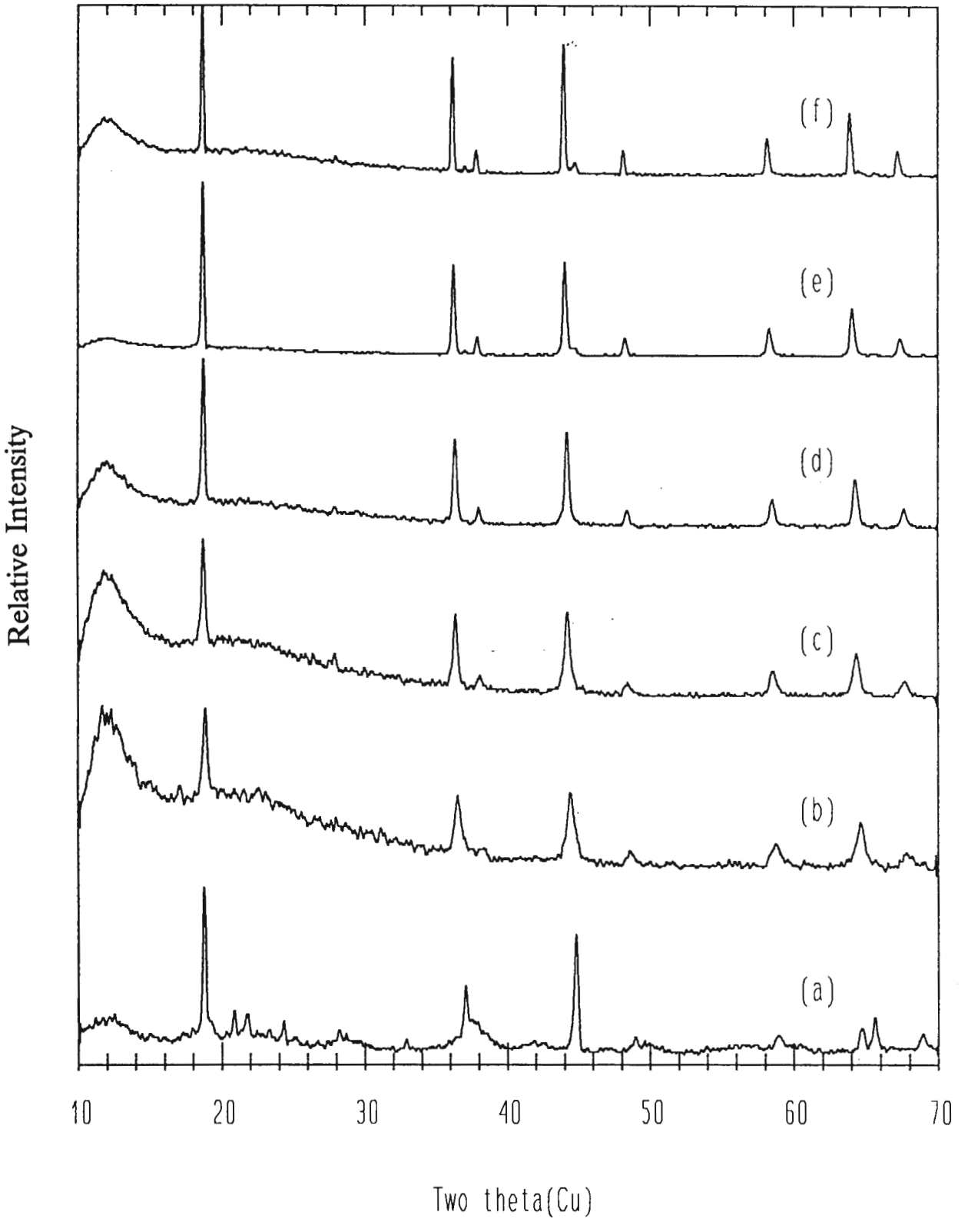

Fig. 4.4 Powder X-ray diffraction patterns of a HT-$A_{2-x}MnO_{3-x/2}$ product, with Li/Mn = 0.55, heated to (a) 100°C, (b) 400°C, (c) 500°C, (d) 600°C, (e) 700°C, and (f) 800°C.

$$Li_{0.724}Mn_{1.316}O_3 \rightarrow 0.044\ Li_2MnO_3 + 0.636\ LiMn_2O_4 + 0.162\ O_2 \qquad (4.6)$$

The powder X-ray diffraction patterns in Fig. 4.4 (b-f) show the development of the spinel phase $LiMn_2O_4$ as the temperature was increased from 400°C to 800°C at intervals of 100°C. At 400°C it is believed that a defect spinel $Li_2Mn_4O_9$, $(Li_{0.89}\square_{0.11})[Mn_{1.78}\square_{0.22}]O_4$, formed. Note that the defect spinel has a Li:Mn ratio of 0.5:1 which is the same as in $LiMn_2O_4$ and closely approximates that in the precursor $Li_{0.724}Mn_{1.316}O_3$. As the temperature was increased further, oxygen was lost until the stoichiometric spinel $Li[Mn_2]O_4$ formed. During this process the peaks became sharper (and the product more crystalline) and the peaks shifted to lower 2θ-values. This process is consistent with the following reaction:

$$Li_2Mn_4O_9 \rightarrow 2\ LiMn_2O_4 + \tfrac{1}{2}\ O_2 \qquad (4.7)$$

Thermogravimetric analysis (TGA) data and differential scanning calorimetric (DSC) data of a HT-$A_{2-x}MnO_{3-x/2}$ product with a Li/Mn ratio of 1.29 ("$Li_{1.46}Mn_{1.13}O_3$") are given in Fig. 4.5 and Fig. 4.6, respectively.

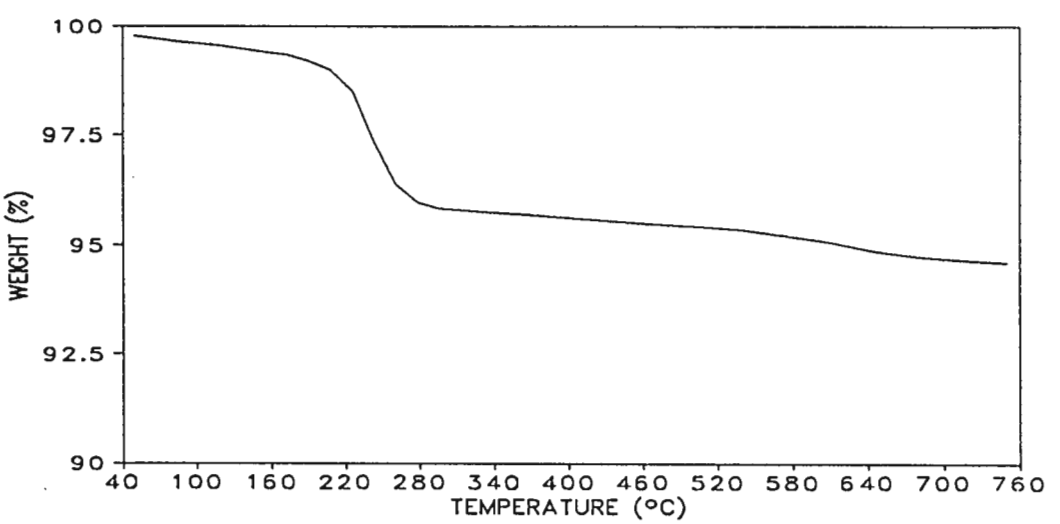

Fig. 4.5 Thermogravimetric analytical (TGA) curve of a HT-layered product (Li/Mn = 1.29). (Heat rate = 20°C/min).

Ignoring the water content, the decomposition of this phase at elevated temperatures can be written as:

$$\text{"}Li_{1.46}Mn_{1.13}O_3\text{"} \rightarrow 0.597\ Li_2MnO_3 + 0.267\ LiMn_2O_4 + 0.071\ O_2 \qquad (4.8)$$

The TGA curve (Fig. 4.5) shows an overall a weight loss of 3.7 % when "$Li_{1.46}Mn_{1.13}O_3$" is heated to 320°C, which is associated predominantly with the loss of water from the structure; it takes place in two stages. The initial weight loss of approximately 1 % to 200°C, is due to surface water loss. The second weight loss (2.7 %) is attributed predominantly to "chemically-bound" water which is removed as the structure transforms to one in which the cation distribution is intermediate between that in the rock salt phase Li_2MnO_3 and the spinel phase $LiMn_2O_4$. From approximately 320°C to 760°C the weight loss (1.2 %) is very slow as oxygen is lost from the structure in accordance with reaction 4.8. During reaction 4.8, the weight loss due to the removal of oxygen is 1.9 %.

The DSC curve in Fig. 4.6 shows an exothermic peak at 230°C which is associated with the structural rearrangement of HT-$A_{2-x}MnO_{3-x/2}$ (A = H, Li). Hydrogen is lost from the structure as H_2O during this process. The broad exothermic peak at 500°C to 700°C can be attributed to the formation of the reduced spinel phase $LiMn_2O_4$ and the rock salt phase Li_2MnO_3, and the associated loss of oxygen according to reaction 4.8.

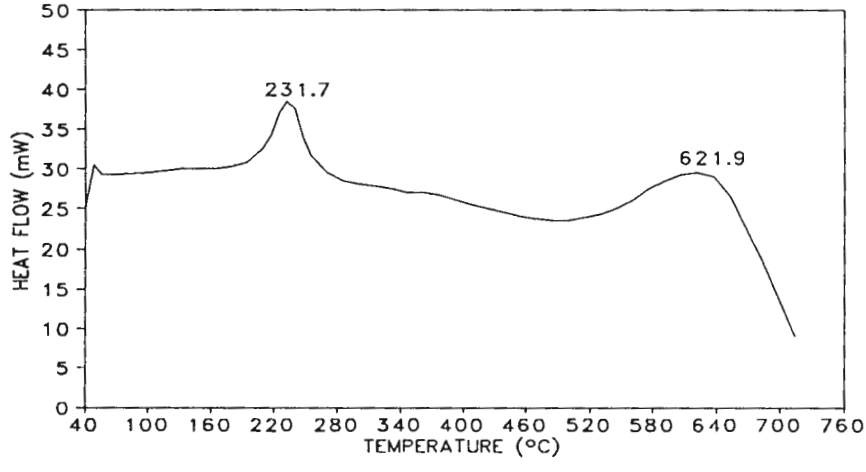

Fig. 4.6 Differential scanning calorimetric (DSC) curve of a HT-layered material (Li/Mn = 1.29). (Heat rate = 20°C/min).

4.3.3 Structural Characterization of HT-$Li_{2-x}MnO_{3-x/2}$ Phases

(a) Refinement of HT-Li_2MnO_3

The structure of HT-Li_2MnO_3 was refined with neutron powder diffraction data. The results were in good agreement with those obtained from previous studies. The cell parameters for Li_2MnO_3 as found in the various studies are summarized in Table 4.1.

Table 4.1
Unit Cell Parameters of Li_2MnO_3

	Jansen (1973)	Strobel (1988)	Riou (1992)	Neutron data (this work)
a (Å)	4.92(8)	4.937(1)	4.921(6)	4.9304(9)
b (Å)	8.53(3)	8.532(1)	8.526(3)	8.5303(4)
c (Å)	9.60(4)	5.030(2)	9.606(5)	5.0269(8)
ß (°)	99.5	109.46(3)	99.47(5)	109.37(5)
Z	8	4	8	4
V (Å^3)	398.32	199.78	397.5(8)	199.46
Space group	monoclinic C2/c	monoclinic C2/m	monoclinic C2/c	monoclinic C2/m

In Li_2MnO_3, lithium ions occupy three types of octahedral sites. Using monoclinic symmetry C2/c these sites, in Wyckoff notation, are 4d, 4e and 8f. The manganese ions are located in two independent octahedral 4e sites. The oxygen ions are distributed over 3 independent 8f sites. This setting gives the number of cations in the unit cell, $Z = 8$.

Strobel (1988) noticed the occurrence of a mirror plane parallel to the *ac* plane that results from the stacking of the (Mn_2Li) layers. In Strobel's refinement a C-cell of half volume was therefore used ($Z = 4$). This refinement showed that powders of Li_2MnO_3 are slightly disordered with 12 ± 3 % Mn on the Li sites. A partial substitutional disorder of the Li and the Mn atoms was also reported by Riou (1992); in this refinement the Li3

(4e) sites were occupied by both Li and Mn, while the Mn2 (4e) sites were partially occupied by Li. The substitution amounted to about 12.5 %.

The crystallographic parameters of Li_2MnO_3 with the space group C2/c (Riou, 1992) and space group C2/m (Strobel, 1988) are tabulated in Table 4.2 and Table 4.3, respectively.

Table 4.2

Crystallographic Parameters of Li_2MnO_3 from X-ray Data (Riou, 1992)

Space group: C2/c

Atom	Position	*x*	*y*	*z*	n	B (Å^2)
Li1	8f	0.241(9)	0.089(2)	0.010(7)	1	1.7(2)
Li2	4d	0.250	0.250	0.5	1	1.1(3)
Li3	4e	0	0.757(1)	0.250	1.80	1.1(2)
Mn1	4e	0	0.4101(3)	0.250	1	0.29(2)
Mn2	4e	0	0.0757(3)	0.250	0.88	0.26(2)
O1	8f	0.1079(9)	0.256(2)	0.1364(5)	1	0.65(6)
O2	8f	0.141(1)	0.5655(6)	0.1371(5)	1	0.22(7)
O3	8f	0.141(1)	0.9169(9)	0.1398)7)	1	1.30(9)

Table 4.3

Crystallographic Parameters of Li_2MnO_3 from X-Ray Data (Strobel, 1988)

Space group: C2/m

Atom	Position	*x*	*y*	*z*	n	B (Å^2)
Li1	2b	0	0.5	0	1	0.28(3)
Li2	2c	0	0	0.5	1	1.10(6)
Li3	4h	0	0.6606(3)	0.5	2	1.01(4)
Mn	4g	0	0.16708(3)	0	0.88	0.244(2)
O1	4i	0.2189(2)	0	0.2273(2)	1	0.41(1)
O2	8j	0.2540(1)	0.32119(7)	0.2233(1)	1	0.42(7)

The observed and calculated diffraction profile of a typical HT-Li_2MnO_3 sample is shown in Fig. 4.7. The crystallographic parameters obtained from this refinement are given in Table 4.4. Because it is not possible to determine the exact distribution of Mn and Li on

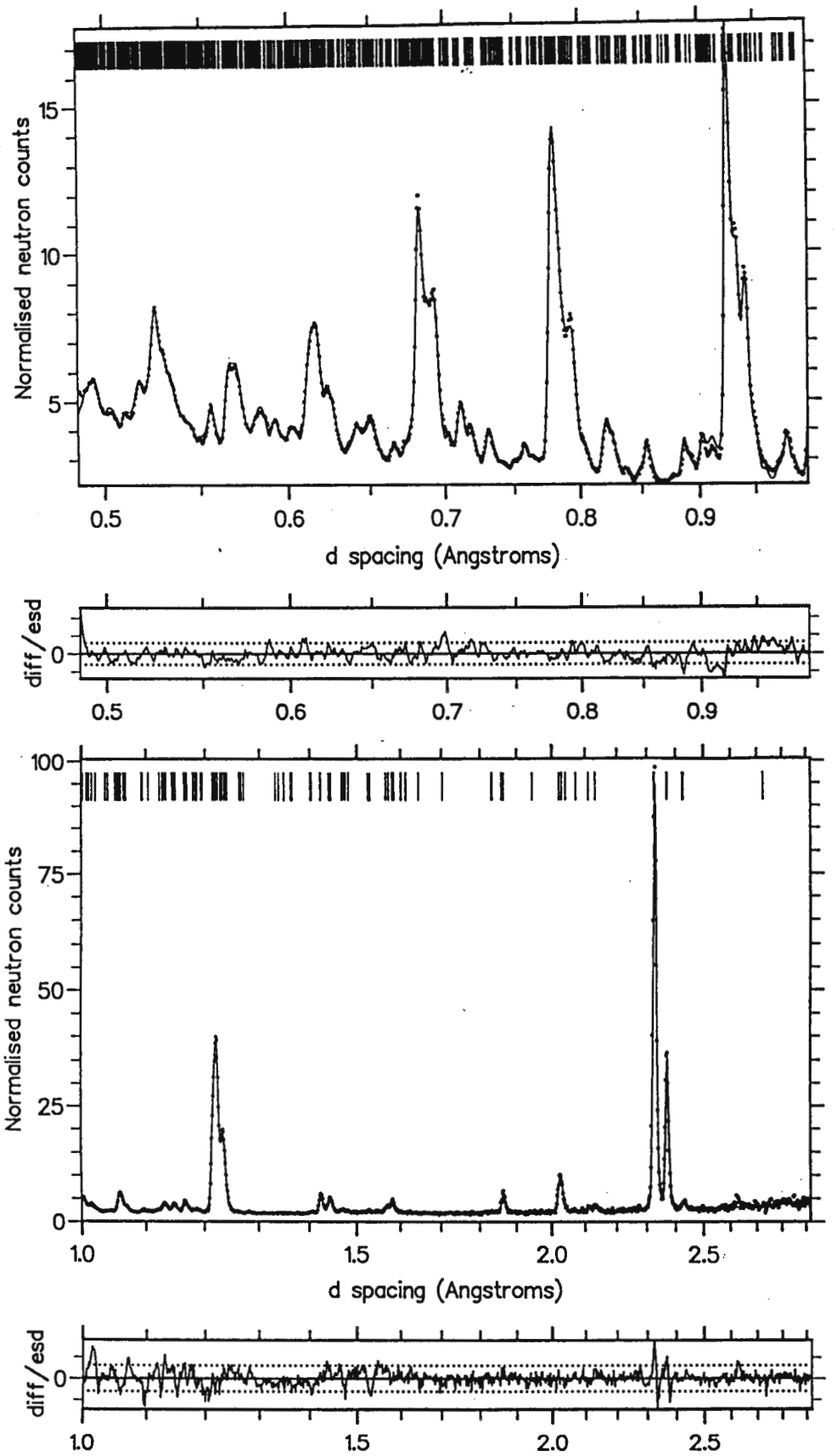

Fig. 4.7 Observed and calculated neutron diffraction patterns of HT-Li_2MnO_3.

each particular site, a best model was calculated from the site occupancy factors obtained from the refinement in accordance with the scattering length of Li and Mn and the stoichiometry closest to Li_2MnO_3 (Table 4.4). The stoichiometry of the HT-Li_2MnO_3 phase according to this refinement was calculated to be $Li_{1.8}Mn_{1.8}O_3$, which is in reasonable agreement with the expected stoichiometry. Note that the average valency of Mn is 4.08 which is slightly above the expected (allowed) value of 4.00.

Table 4.4
Crystallographic Parameters of Li_2MnO_3 from Neutron Data

Space group: C2/m

Atom	Position	*x*	*y*	*z*	n	B (Å^2)
Li1	2b	0	0.5	0	0.88(9)	0.74(2)
Mn1	2b	0	0.5	0	0.12(9)	
Li2	2c	0	0	0.5	0.88(1)	1.38(3)
Mn2	2c	0	0	0.5	0.12(1)	
Li4	4h	0	0.659(1)	0.5	0.83(6)	0.76(2)
Mn3	4g	0	0.1671(5)	0	0.91(3)	0.23(5)
Li3	4g	0	0.1671(5)	0	0.09(3)	
O1	4i	0.2173(7)	0.0000	0.2256(6)	1.0000	0.33(4)
O2	8j	0.2541(5)	0.3215(2)	0.2241(4)	1.0000	0.39(2)

R_p = 6.31 %; R_{wp} = 4.86 %; R_E = 2.47 %

Chi-squared = 3.8728 for 1792 observations and 35 basic variables (N - P + C = 1757)

Notes:

1. $$R_p = \frac{\Sigma| Y_{obs} - Y_{calc}|}{\Sigma Y_{obs}} \quad ; \quad R_{wp}^2 = \frac{\Sigma w | Y_{obs} - Y_{calc}|^2}{\Sigma w| Y_{obs}|^2} \quad ; \quad R_E^2 = \frac{N-P+C}{\Sigma w| Y_{obs}|^2}$$

2. Y_{obs} = number of observations at time of flight, t_{obs},
   w = weights, and
   N - P + C = number of observations - number of variables + number of constraints.

This model (Table 4.4) confirmed Strobel and Riou's data; it showed that Li_2MnO_3 samples do not have ideally ordered structures, and that in an "overall" structure, Li and Mn ions can substitute for one another at least to a minor extent.

The idealized structure of Li_2MnO_3 is shown in Fig. 4.8.

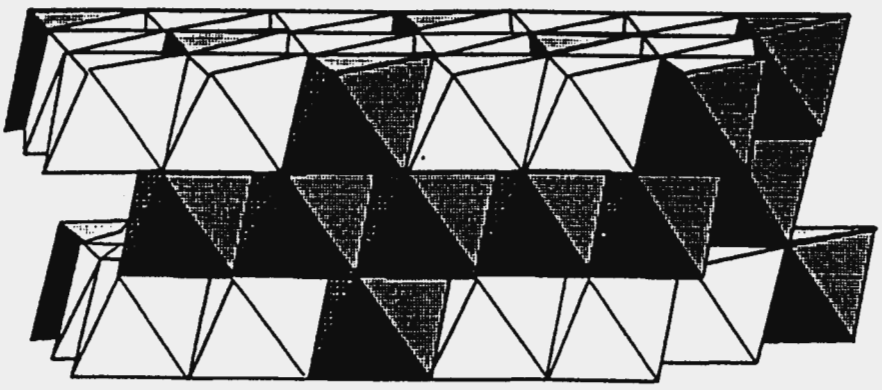

Fig. 4.8 Idealized structure of Li_2MnO_3.

(b) Comments on the Structures of Heat-Treated $Li_{1.28}Mn_{1.17}O_3$, $Li_{1.14}Mn_{1.21}O_3$ and $Li_{0.73}Mn_{1.32}O_3$

The powder X-ray diffraction pattern of Li_2MnO_3 is shown in Fig. 4.9a and the powder X-ray diffraction patterns of HT-$Li_{1.28}Mn_{1.17}O_3$, HT-$Li_{1.14}Mn_{1.21}O_3$ and HT-$Li_{0.73}Mn_{1.32}O_3$ after heat-treatment to 300°C are shown in Fig. 4.9 (b-d), respectively. These patterns could be indexed to the monoclinic space group C2/c; the unit cell dimensions are summarized in Table 4.5.

No satisfactory structural information could be determined by profile refinement of the powder X-ray diffraction data of the heat-treated samples because of the limited intensity data available and the poor quality of the data. However, certain features about the structures of these heat-treated samples could be deduced from the X-ray data.

Table 4.5
Unit Cell Parameters of Selected Heat-Treated HT-$Li_{2-x}MnO_{3-x/2}$ Materials

Li/Mn	2.00	1.10	0.94	0.55
Formula	Li_2MnO_3	$Li_{1.28}Mn_{1.17}O_3$	$Li_{1.14}Mn_{1.21}O_3$	$Li_{0.73}Mn_{1.32}O_3$
a (Å)	4.918(9)	4.943(6)	4.949(0)	4.196(3)
b (Å)	8.525(3)	8.536(0)	8.531(1)	8.528(1)
c (Å)	9.611(8)	9.576(3)	9.548(6)	9.594(2)
ß (°)	99.0	99.0	99.0	99.0

When lithium was extracted from HT-Li_2MnO_3, the powder X-ray diffraction patterns showed a well-resolved shifted [0 0 2] peak at 19.3°2θ which is indicative of the retention of the layering of the oxygen array in the HT-$A_{2-x}MnO_{3-x/2}$ product. The significant shift of the [0 0 2] peak to a higher 2θ-value is indicative of a contraction of the layers of the lattice, which is an expected consequence of the delithiation. However, the changes in intensity of certain peaks for example at 38°2θ and 49°2θ, indicate that an additional and significant modification to the parent structure occurs.

With heat-treatment to 300°C, the powder X-ray diffraction patterns are strikingly similar to the parent structure, despite large compositional differences. In this respect it should be noted that all the peaks in the powder X-ray diffraction pattern of a spinel such as $Li_2Mn_4O_9$ (which has cubic symmetry Fd3m) are coincident (or nearly coincident) with the peaks of the Li_2MnO_3 structure (Fig. 4.9 a and e, respectively).

In a spinel structure such as $Li_2Mn_4O_9$, the manganese cations occupy octahedral sites in alternate layers in a 3:1 ratio. The doublet at 64-66°2θ in the powder X-ray diffraction pattern of Li_2MnO_3 (Fig. 4.9a) is reflected by a single peak in the pattern of $Li_2Mn_4O_9$ (Fig. 4.9e). The X-ray diffraction patterns of the HT-$A_{2-x}MnO_{3-x/2}$ phases (Fig. 4.9(b-d)) show a broad peak at 65°2θ which implies that these compounds are probably characterized by an intergrowth structure comprised of a layered Li_2MnO_3-type structure with monoclinic structure and domains of spinel with cubic symmetry.

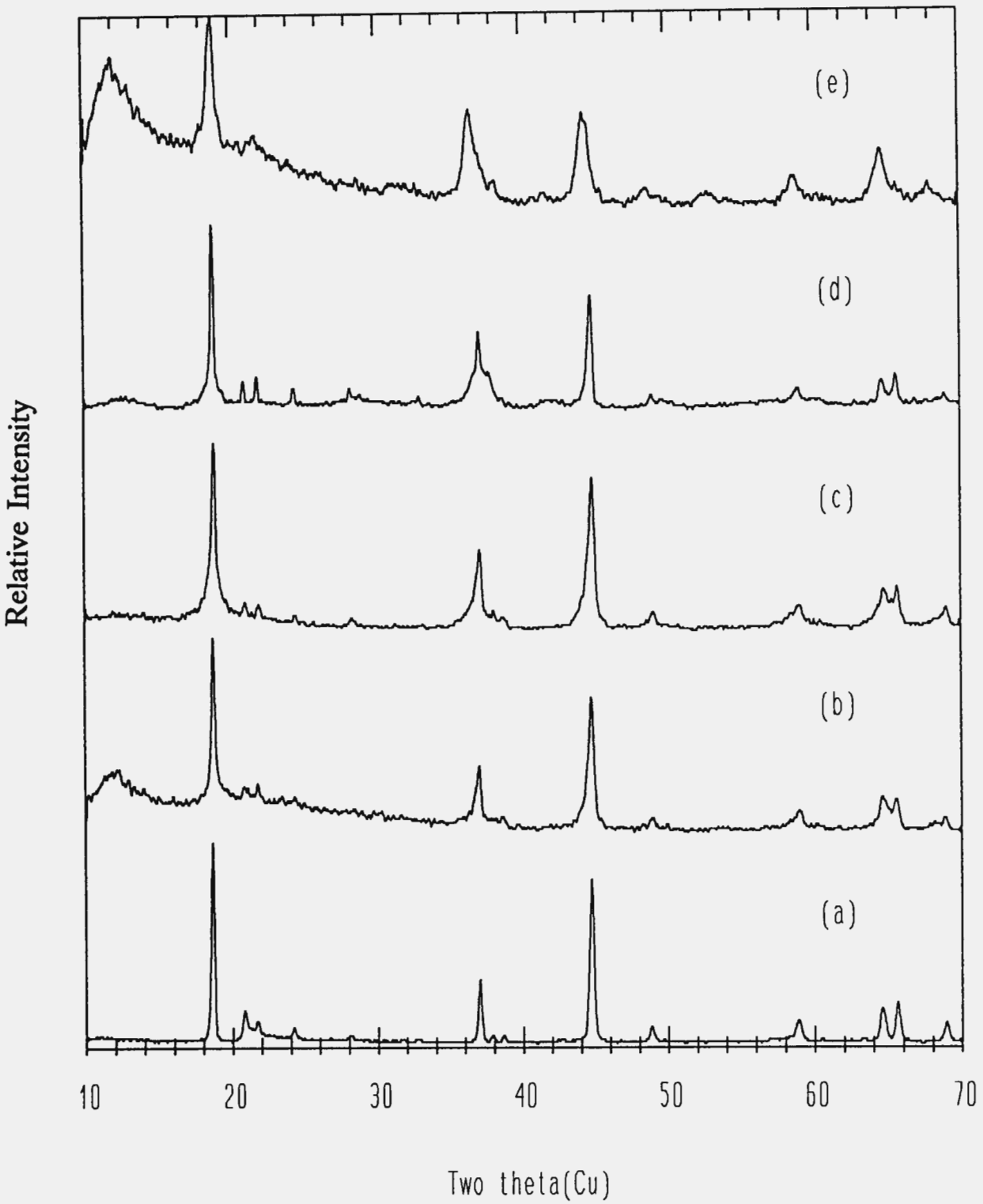

Fig. 4.9 Powder X-ray diffraction patterns of (a) HT-Li_2MnO_3, (b) HT-$Li_{1.28}Mn_{1.17}O_3$, (c) HT-$Li_{1.14}Mn_{1.21}O_3$, (d) HT-$Li_{0.73}Mn_{1.32}O_3$, and (e) $Li_2Mn_4O_9$. Note that (b-d) were obtained after heat-treatment to 300°C.

It is therefore believed that during heat-treatment of HT-$A_{2-x}MnO_{3-x/2}$ materials, the Mn cations migrate into the Li-depleted layers to leave a structure that is intermediate between the ideal layered structure of Li_2MnO_3 in which the manganese cations are restricted to alternate cation layers, and that of a spinel in which the manganese cations are distributed between alternate layers in a 3:1 ratio.

4.3.4 Electrochemical Evaluation of the HT-$Li_{2-x}MnO_{3-x/2}$ Phases

(a) Galvanostatic Discharge

The initial discharge curves of lithium cells containing a HT-$Li_{1.14}Mn_{1.21}O_3$ cathode dehydrated at 300°C and a dehydrated HT-$Li_{0.73}Mn_{1.32}O_3$ cathode ([H^+] typically 0.07 $^w/_o$) are shown in Fig. 4.10 a and b, respectively. Both samples show a predominant discharge plateau at 2.8 V during which Li^+ ions are inserted into the cathode structure with a concomitant reduction of the Mn^{4+} ions. If the samples are not dehydrated a significant reduction in capacity is observed (Fig. 4.10c).

On the initial discharge HT-$Li_{1.14}Mn_{1.21}O_3$ delivered 127.5 mAh/g at the end of the 2.8 V plateau which is 89.6 % of its theoretical capacity of 142 mAh/g, based on the insertion of lithium to the rock salt stoichiometry $Li_{1.79}Mn_{1.21}O_3$. HT-$Li_{0.73}Mn_{1.32}O_3$ delivered 128.8 mAh/g which is 60.9 % of its theoretical capacity of 211.3 mAh/g.

Lithium cells containing $Li_2O \cdot yMnO_2$ spinels, for example $Li_2Mn_4O_9$ (y = 4.0), typically discharge on a flat plateau at 2.8 V to 2.9 V. Therefore, the similarity between the discharge curves of Li/HT-$Li_{2-x}MnO_{3-x/2}$ cells in Fig. 4.10 and those of Li/spinel cells, supports the hypothesis that the structures of the heat-treated HT-$Li_{2-x}MnO_{3-x/2}$ phase have spinel-like character.

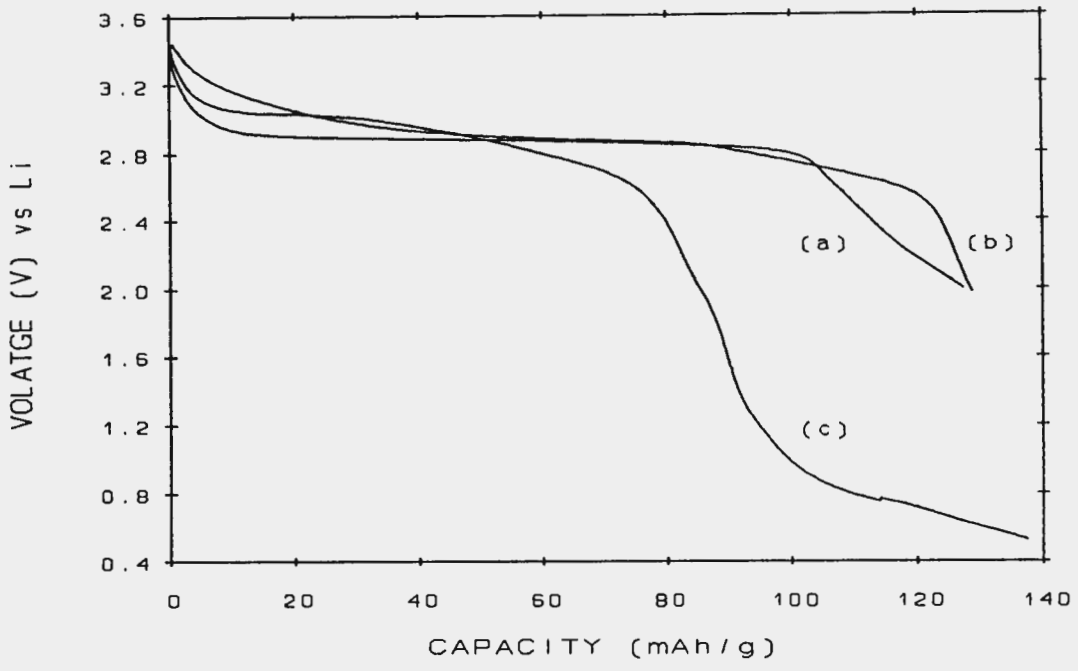

Fig. 4.10 Discharge curves of lithium cells containing (a) a HT-$Li_{1.14}Mn_{1.21}O_3$ cathode, and (b) a HT-$Li_{0.73}Mn_{1.32}O_3$ cathode. The HT-$Li_{2-x}MnO_{3-x/2}$ products were dehydrated at 300°C. (c) the discharge curve of HT-$Li_{1.14}Mn_{1.21}O_3$ without any heat-treatment.

(b) Rechargeability

Fig. 4.11 (a-d) shows the cyclic voltammograms of a typical HT-$A_{2-x}MnO_{3-x/2}$ product. Fig. 4.11 (a-c) shows the cyclic voltammograms of HT-$Li_{1.28}Mn_{1.17}O_3$ dried at 100°C, dehydrated at 250°C and dehydrated at 300°C, respectively, cycled between the voltage limits 1.1 V and 4.6 V. Fig. 4.11d shows the cyclic voltammogram of HT-$Li_{1.28}Mn_{1.17}O_3$ (dehydrated at 300°C) cycled between narrower voltage limits, i.e. 2.0 V and 4.6 V.

As the temperature of heat-treatment of HT-$Li_{1.28}Mn_{1.17}O_3$ products was increased, it was clear from the cyclic voltammograms that lithium insertion in the dehydrated products took place in two steps, as manifest by the two cathodic peaks at approximately 3.8 V and 2.5 V. This profile is typical of the discharge of spinel-type phases; the peak at 3.8 V is attributed to lithium insertion into tetrahedral sites, and the peak at 2.5 V to lithium insertion into octahedral sites. Although the lithium insertion processes are clearly

distinguishable on the cathodic scan, the lithium extraction (oxidation) processes from the octahedral and tetrahedral sites are not well-resolved on the anodic scan. The cyclic voltammograms of the samples heated at 250°C and 350°C therefore provide further evidence that these HT-$A_{2-x}MnO_{3-x/2}$ phases have structures with spinel-type character.

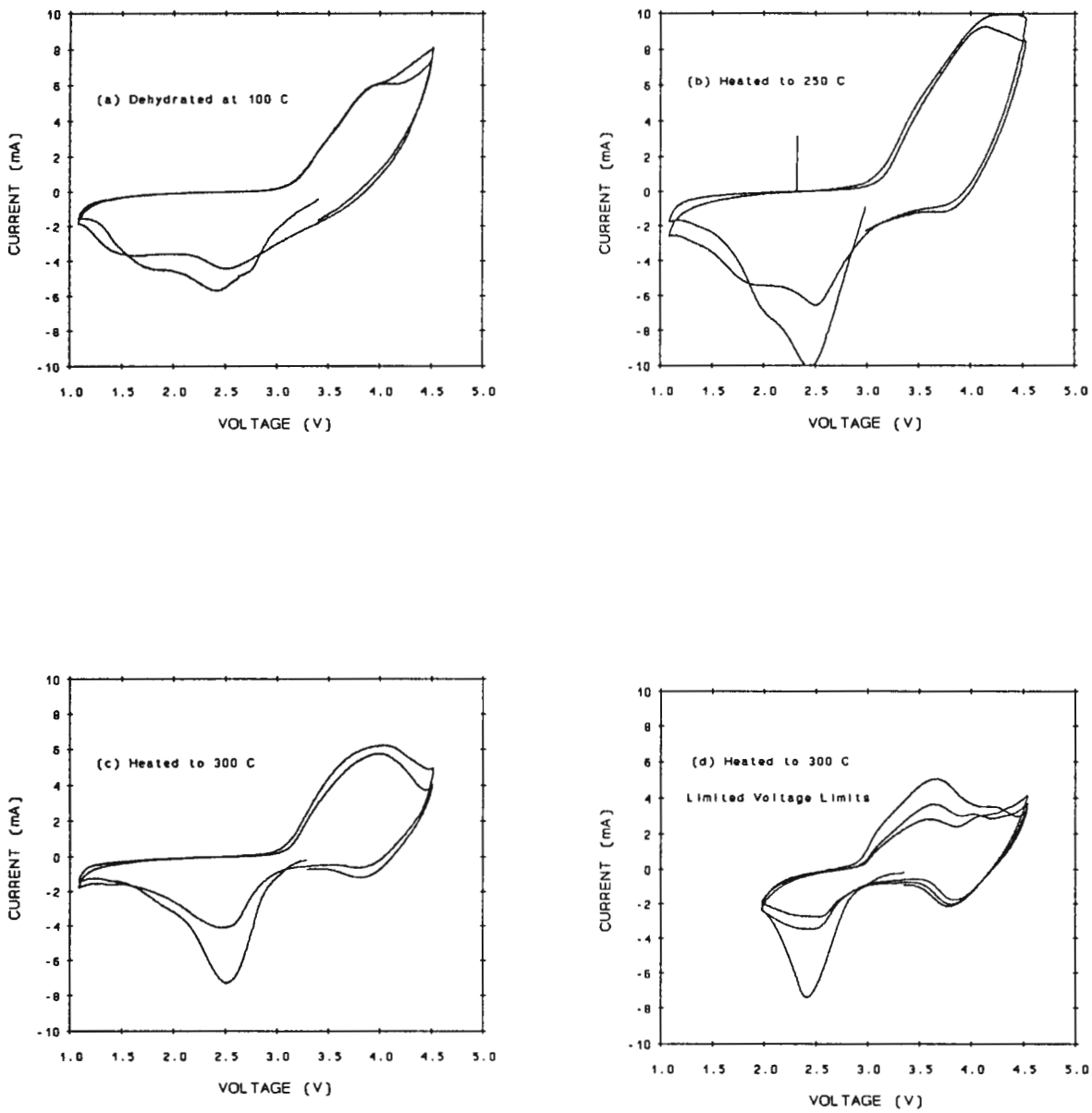

Fig. 4.11 Cyclic voltammetry curves of HT-$A_{2-x}MnO_{3-x/2}$ dehydrated at (a) 100°C, (b) 250°C and (c) 300°C (HT-$Li_{1.28}Mn_{1.17}O_3$). (d) HT-$Li_{1.28}Mn_{1.17}O_3$.

Of interest is that the cyclic voltammogram of HT-$Li_{1.28}Mn_{1.17}O_3$ that had been heat-treated to only 100°C showed no reduction peak at 3.8 V (Fig. 4.11a), analogous to the initial discharge curve of HT-$Li_{1.14}Mn_{1.21}O_3$ dehydrated at 100°C which showed no distinct plateau at 2.8 V (Fig. 4.10c). It is therefore concluded that this heat-treatment temperature is too low to displace the manganese ions to generate spinel-type domains, and that lithium insertion/extraction is restricted to the occupation/depletion of octahedral sites in a defect rock salt phase with a layered structure.

Limited success was obtained when HT-$Li_{2-x}MnO_{3-x/2}$ cathodes were cycled in room temperature lithium cells. These cells lose capacity slowly on consecutive cycles as shown in the capacity vs cycle number plots in Fig. 4.12.

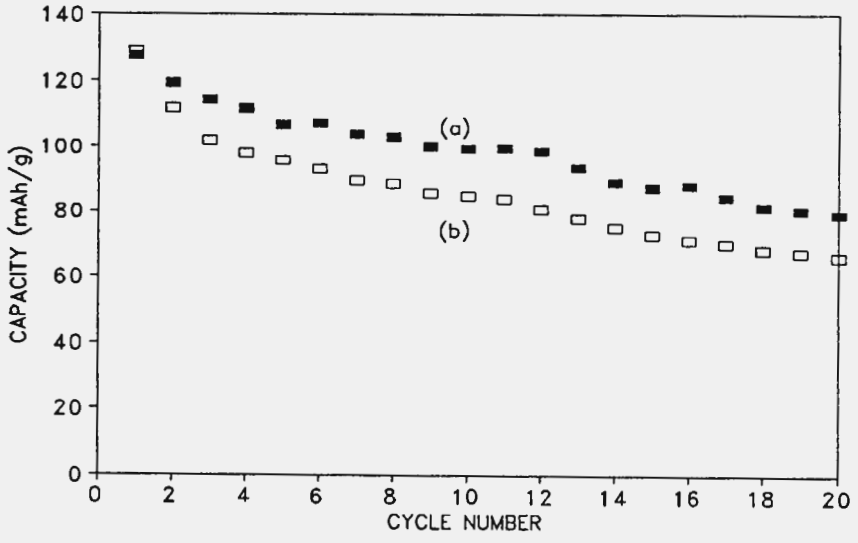

Fig. 4.12 Cycling behaviour of (a) HT-$Li_{1.14}Mn_{1.21}O_3$ and (b) HT-$Li_{0.73}Mn_{1.32}O_3$ in room-temperature lithium cells.

The powder X-ray diffraction patterns of the cycled cathodes (obtained in charged and discharged states) in Fig. 4.13 did not reveal any significant modification demonstrating that the HT-$Li_{2-x}MnO_{3-x/2}$ cathodes operate as insertion electrodes in which lithium can move in and out of the structure without destroying the structural integrity of the host framework.

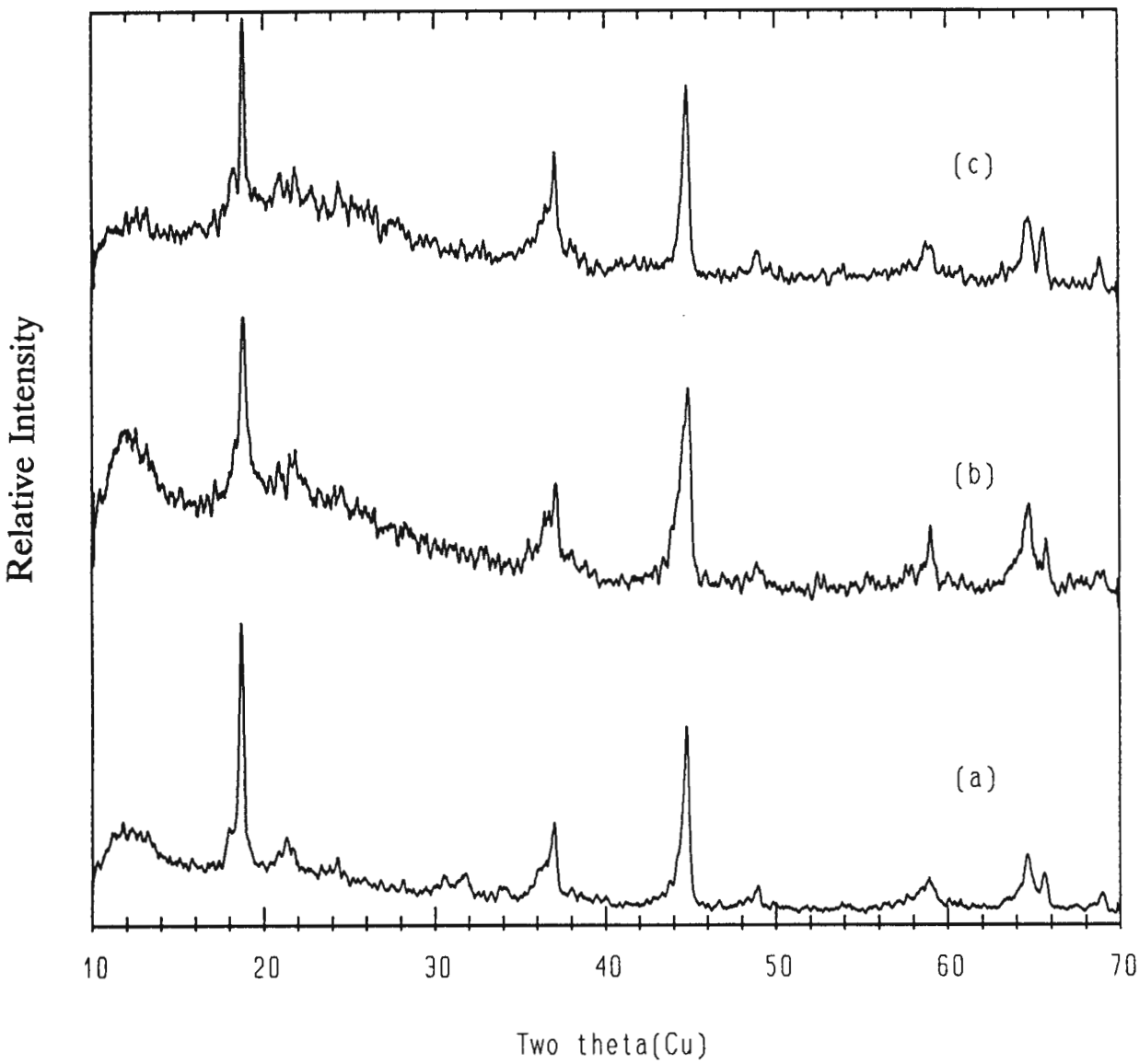

Fig. 4.13 Powder X-ray diffraction patterns of the cycled cathodes of (a) HT-$Li_{1.28}Mn_{1.17}O_3$ (discharged state), (b) HT-$Li_{1.14}Mn_{1.21}O_3$ (charged state), and (c) HT-$Li_{0.73}Mn_{1.32}O_3$ (charged state).

Part II - $Li_{2-x}MnO_{3-x/2}$ Compounds from LT-Li_2MnO_3

4.4 Results and Discussion

4.4.1 Synthesis of LT-$Li_{2-x}MnO_{3-x/2}$ Reaction Products

In contrast to HT-Li_2MnO_3, it is possible to remove almost all the lithium from the LT-Li_2MnO_3 precursor by acid-treatment with 2.25M H_2SO_4 at room temperature. Fig. 4.13 shows the powder X-ray diffraction patterns of the LT-Li_2MnO_3 precursor (Fig. 4.13a) and several products, Samples B - G, obtained by acid-leaching. The Li/Mn ratios varied considerably as indicated in Table 4.6.

Table 4.6
List of LT-$Li_{2-x}MnO_{3-x/2}$ Products

Sample	Li/Mn	$[H^+]$	Phases
A	2.00	-	LT-Li_2MnO_3 precursor
B	1.18	0.69	LT-$Li_{2-x}MnO_{3-x/2}$ + δ'-MnO_2
C	0.67	1.05	LT-$Li_{2-x}MnO_{3-x/2}$ + δ'-MnO_2
D	0.40	0.54	δ'-MnO_2
E	0.20	1.58	δ'-MnO_2 + trace α-MnO_2
F	< 0.05	1.98	δ-MnO_2 (crystalline product with uncharacteristically strong peak at 19°2θ)
G	< 0.05	-	γ-MnO_2 + trace α-MnO_2

In this table δ'-MnO_2 refers to a novel layered manganese dioxide phase that contains a minor concentration of Li^+ ions and ion-exchanged H^+ ions. By contrast, δ-MnO_2 refers to the pattern of the well-known family of hydrated, layered manganese dioxides.

A significant shift of the [0 0 2] peak at 18.8°2θ of the LT-Li_2MnO_3 precursor (Sample A; Fig. 4.13a) to a higher 2θ-value, and also a marked collapse of the remaining peaks to broad, diffuse peaks can be seen in the powder X-ray diffraction patterns of Samples B and C (Fig. 4.13 b and c); this trend is similar to that observed with HT-$A_{2-x}MnO_{3-x/2}$ products described in Part I.

The powder X-ray diffraction pattern of Sample D shows a completely new phase (Fig. 4.13d); it shows a total disappearance of the Li_2MnO_3 peaks and the development of strong peaks at 38°, 49°, 59° and 64°2θ. This novel phase, which contains some residual lithium and possibly some ion-exchanged H^+ ions, is named δ'-MnO_2 in this study; it will be shown to have a layered-type structure.

Sample E is mainly a δ'-MnO_2 phase but contains a trace impurity, believed to be an α-MnO_2 phase (Fig. 4.13e). The α-MnO_2 phase is identified by the characteristic peaks at 12.5°2θ, 18°2θ and 28.5°2θ.

Extensive leaching of the Li_2O component from the Li_2MnO_3 ($Li_2O \bullet MnO_2$) structure leads to the formation of a layered phase with a strong δ-MnO_2 character (Sample F; Fig. 4.13f) as opposed to the δ'-MnO_2 phase of Sample D. The distinction between δ-MnO_2 and δ'-MnO_2 lies in the crystallinity and lower water content of the latter phase and the small but significant differences in peak positions (d-spacings). δ-MnO_2 materials are basically characterized by 2 broad peaks near 2.4 Å (38°2θ) and 1.4 Å (66°2θ) (cf. Chapter 2, § 2.4.2). However, it should be noted that the strong peak at 19°2θ is uncharacteristically strong for a δ-MnO_2 product; it suggests that the δ-MnO_2 product synthesized in this study is significantly more crystalline than the better-known δ-MnO_2 compounds.

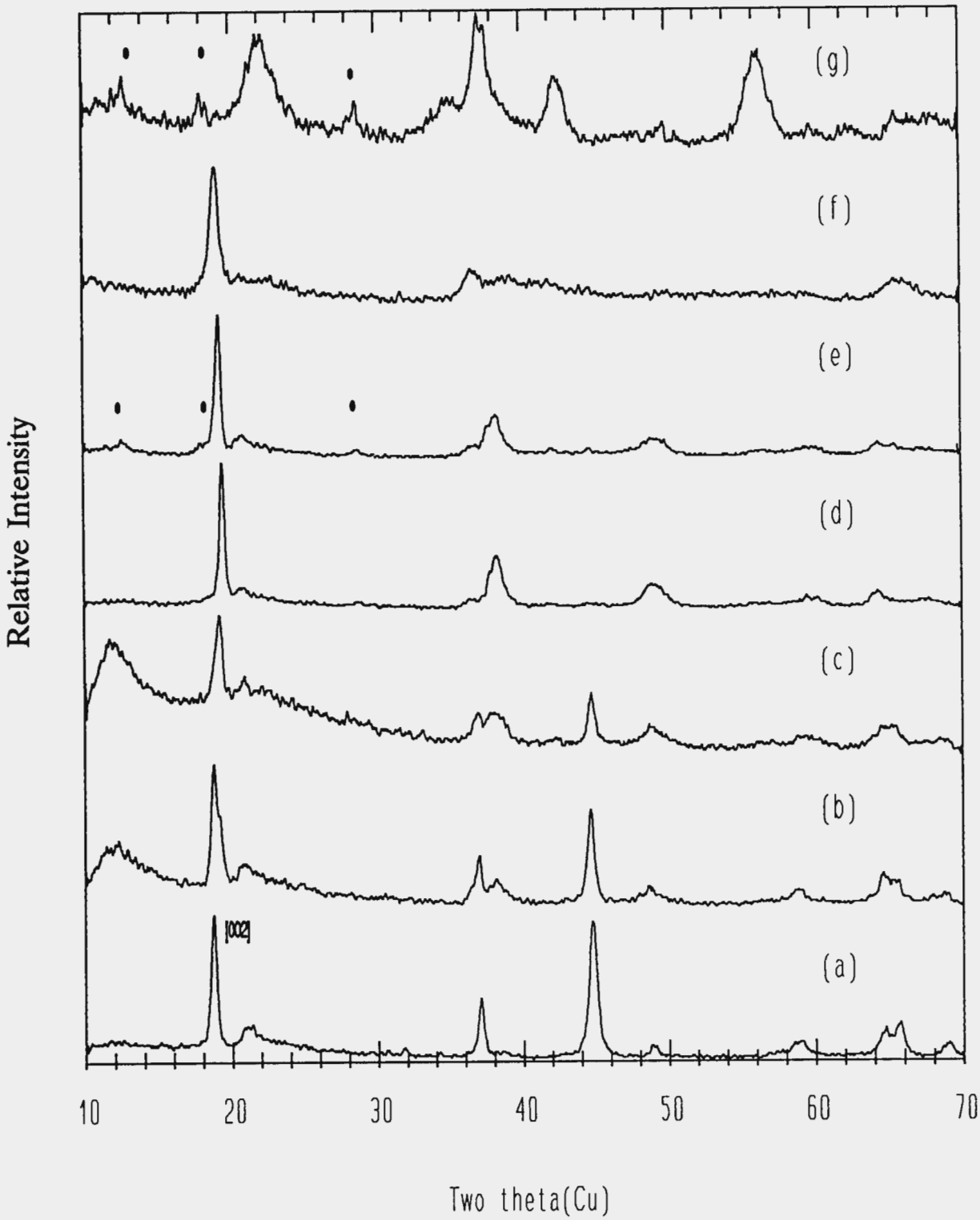

Fig. 4.13 Powder X-ray diffraction patterns of (a) a LT-Li_2MnO_3 precursor and (b) - (g) acid-leached LT-layered materials, Samples B - G, respectively. (• = α-MnO_2).

A γ-MnO_2 phase is ultimately formed upon extensive acid-leaching of the lithium component from LT-Li_2MnO_3 precursor (Fig. 4.13g). The powder X-ray diffraction pattern also shows a trace of an α-MnO_2 phase.

Because the powder X-ray diffraction pattern of Sample D (Fig. 4.13d) reveals a novel phase which was essentially single-phase in character, it is discussed and characterized further in this chapter. Atomic absorption spectroscopic analysis gave the Li/Mn ratio as 0.40, and hydrogen analysis gave the $[H^+]$ as 0.54 wt% after it was dried at 100°C overnight. If the $[H^+]$ content is ignored Sample D can be formulated as $Li_{0.4}MnO_{2.2}$ (i.e. $x = 1.6$ in $Li_{2-x}MnO_{3-x/2}$) or alternatively, $Li_{0.36}Mn_{0.91}O_2$. Because of the structural relationship between $Li_{0.4}MnO_{2.2}$ and the well-known layered structures Li_xMO_2 (M = Co, Ni), this product will be referred to as $Li_{0.36}Mn_{0.91}O_2$ in the discussion that follows.

4.5 Characterization of $Li_{0.36}Mn_{0.91}O_2$

4.5.1 Thermal Stability

The reaction products obtained from acid-leaching of LT-Li_2MnO_3, contain in addition to the hydrogen cations in the lithium layers, some surface water and some occluded water associated with grain boundaries in the particles. For use in lithium cells the material should be anhydrous as water is undesirable and can react with the lithium anode. Surface water and some occluded water can be partially removed by heating to about 100°C. Additional occluded water can be removed by heating to higher temperatures (200°C to 300°C). If the H^+ ions present are attributed only to surface and occluded water (i.e. no ion-exchanged H^+ in the structure), then the structures obtained by acid-leaching LT-Li_2MnO_3 and subsequent heat-treatment can be defined in terms of lithium-manganese-oxide phases.

The powder X-ray diffraction patterns of $Li_{0.36}Mn_{0.91}O_2$ (Fig. 4.14a) after being heat-treated to various temperatures are shown in Fig. 4.14. No visible change occurred at

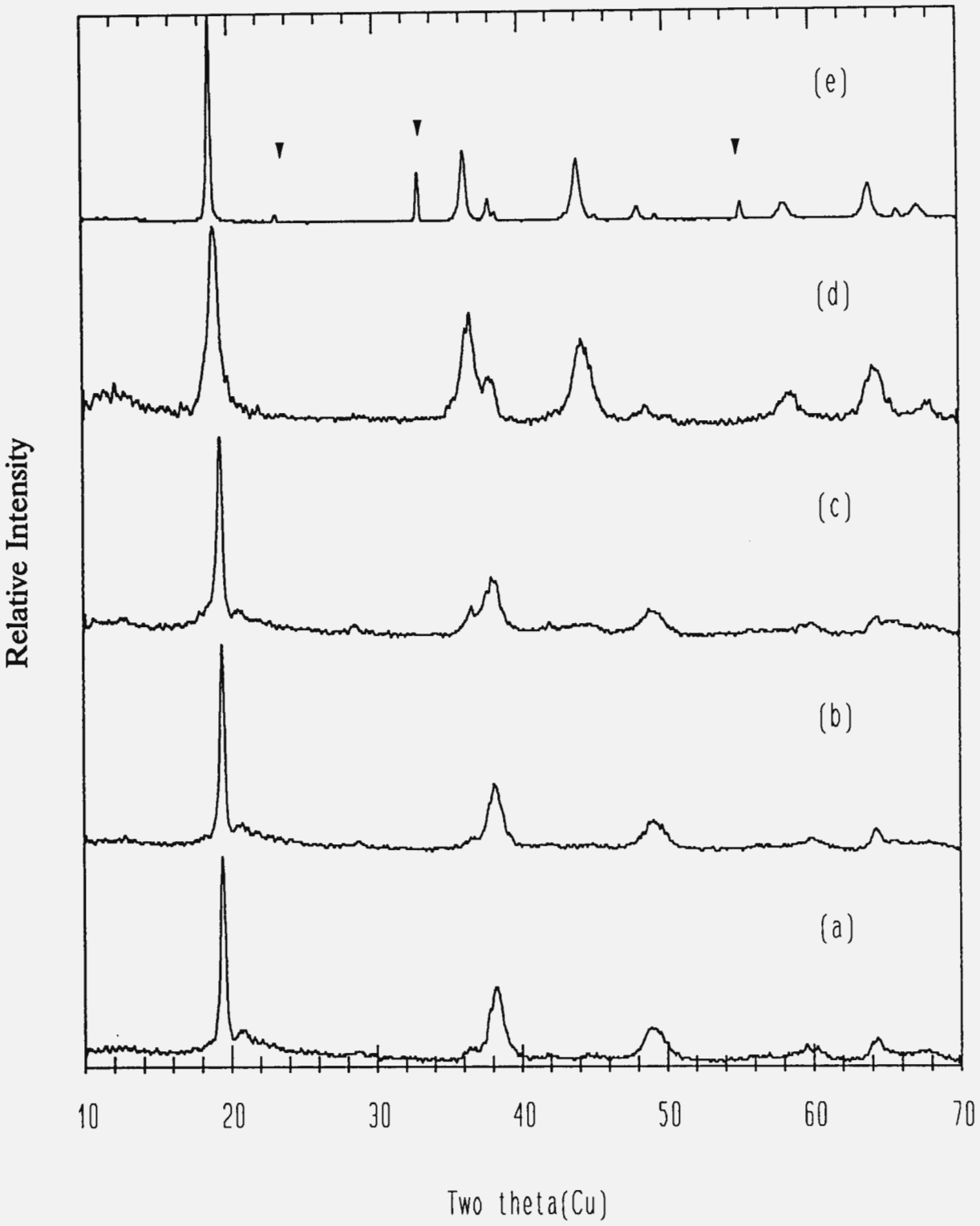

Fig. 4.14 Powder X-ray diffraction patterns of (a) $Li_{0.36}Mn_{0.91}O_2$ heat-treated at (b) 100°C, (c) 150°C, (d) 200°C, and (e) 700°C. (▾ = Mn_2O_3).

100°C as can be seen in Fig. 4.14b. At 150°C (Fig. 4.14c) a new sharp peak at 36°2θ and a broad peak at 44°2θ can be observed, which was attributed to the onset of spinel formation. At 700°C (Fig. 4.14e), it was evident that $Li_{0.36}Mn_{0.91}O_2$ ($Li_{0.4}MnO_{2.2}$) had disproportionated and decomposed according to the reaction:

$$20\ Li_{0.4}MnO_{2.2} \rightarrow 8\ LiMn_2O_4 + 2\ Mn_2O_3 + 3\ O_2 \qquad (4.9)$$

4.5.2 Chemical Lithiation

Because the thermal data given above showed that $Li_{0.36}Mn_{0.91}O_2$ was only stable below 150°C, $Li_{0.36}Mn_{0.91}O_2$ was dehydrated at 100°C overnight prior to being reacted with chemical lithiation agents.

(a) *n*-Butyllithium in Hexane

The powder X-ray diffraction pattern of the products obtained after $Li_{0.36}Mn_{0.91}O_2$ (Fig. 4.15a) had been reacted with an excess 15% *n*-butyllithium in hexane, is shown in Fig. 4.15b.

Atomic absorption spectroscopic analysis gave the Li/Mn ratio of the lithiated material as 2.28. If a single phase product was formed, the reaction can be formulated as follows:

$$Li_{0.36}Mn_{0.91}O_2 + 1.71\ BuLi \rightarrow Li_{2.07}Mn_{0.91}O_2 \qquad (4.10)$$

During this reaction the oxidation state of the manganese decreases from +4 to +2.12. Although it is known that a layered Li_2MnO_2 phase exists (David, 1983), the X-ray pattern of this phase is significantly different to that in Fig. 4.15b. Of significance, however, is that the X-ray pattern in Fig. 4.15b contains peaks that are coincident with those of the original LT-Li_2MnO_3 precursor (Fig. 4.15c). These peaks are therefore attributed to a lithiated $Li_{0.36+x}Mn_{0.91}O_2$ phase ($x \leq 0.73$) with a structure that closely resembles that of LT-Li_2MnO_3. The additional peaks in Fig. 4.15b, for example, the

multiplet peak between 30 and 34°2θ, are attributed to a lithium oxide, hydroxide or carbonate, by-product which have characteristically strong peaks in this 2θ-region; the presence of this phase would account for the surplus lithium detected by atomic absorption analysis.

Because of the strong reducing power of *n*-butyllithium, attempts were made to synthesize a single phase $Li_{0.36+x}Mn_{0.91}O_2$ by using a milder reducing agent such as LiI in acetonitrile.

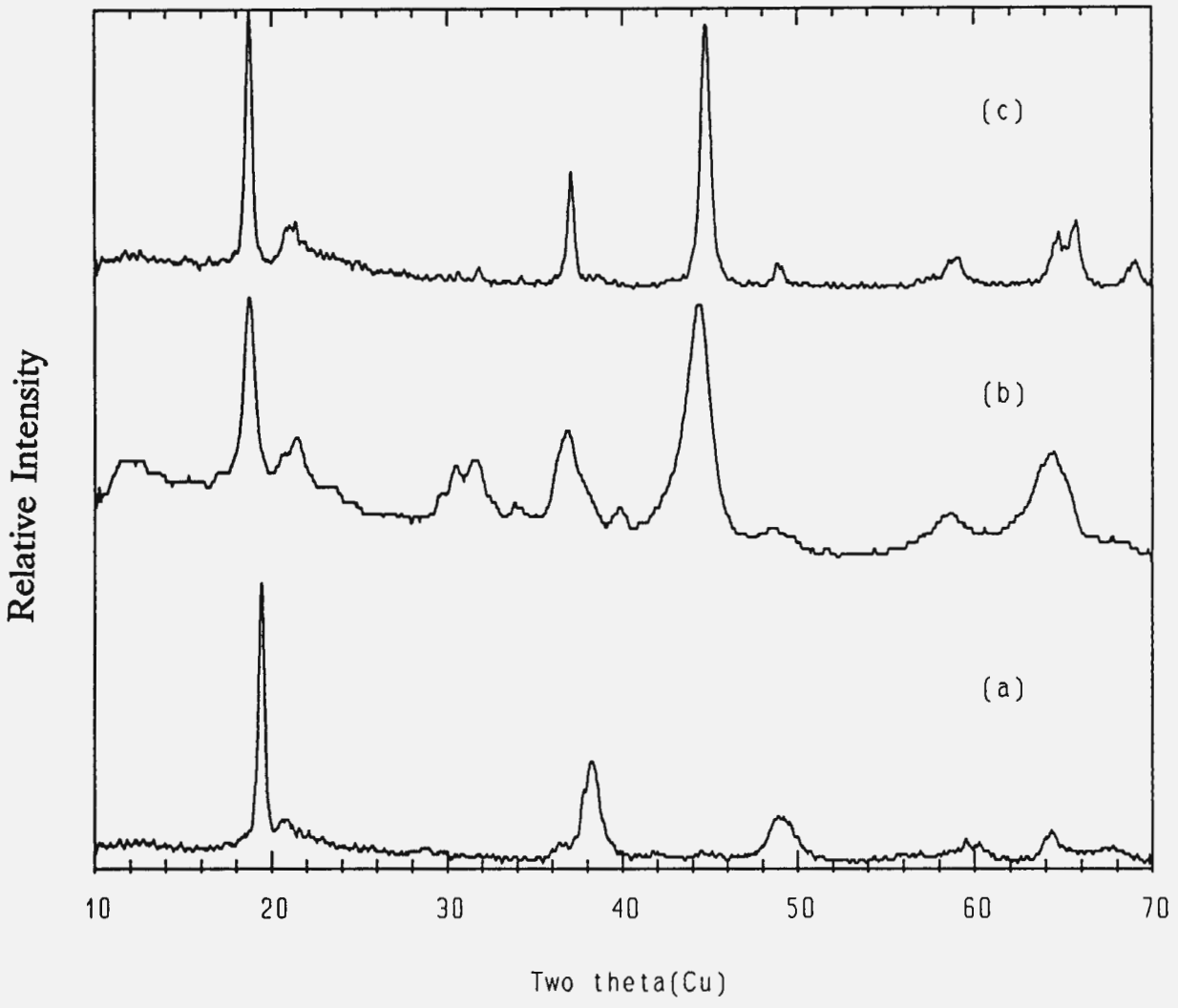

Fig. 4.15 Powder X-ray diffraction patterns of (a) $Li_{0.36}Mn_{0.91}O_2$ dehydrated at 100°C, (b) after reaction with *n*-butyllithium, and (c) LT-Li_2MnO_3.

(b) Lithium Iodide in Acetonitrile

$Li_{0.36}Mn_{0.91}O_2$ was reacted with LiI in acetonitrile at 80°C according to the reaction,

$$Li_{0.36}Mn_{0.91}O_2 + {}^{3x}/_{2}\ LiI \rightarrow Li_{0.36+x}Mn_{0.91}O_2 + {}^{x}/_{2}\ LiI_3 \qquad (4.11)$$

The transformation from $Li_{0.36}Mn_{0.91}O_2$ to $Li_{1.09}Mn_{0.91}O_2$ through a series of $Li_{0.36+x}Mn_{0.91}O_2$ phases as the LiI concentration was increased, and thus the Li/Mn ratio, can be followed in the powder X-ray diffraction patterns in Fig. 4.16. The experimental data is summarized in Table 4.7.

Table 4.7
List of $Li_{0.36+x}Mn_{0.91}O_2$ Chemically-Lithiated Products ($0 \leq x \leq 0.73$)

XRD Pattern	Li/Mn	Structural Notation	Structural Notation# (defect rock salt)
Fig. 4.16a	2.00	$[Li_{1.00}](Mn_{0.67}Li_{0.33})O_2$	$M_{1.00}O$
Fig. 4.16b	0.40	$[Li_{0.27}](Mn_{0.91}Li_{0.09})O_2$	$M_{0.635}O$
Fig. 4.16c	0.55	$[Li_{0.41}](Mn_{0.91}Li_{0.09})O_2$	$M_{0.705}O$
Fig. 4.16d	0.65	$[Li_{0.50}](Mn_{0.91}Li_{0.09})O_2$*	$M_{0.75}O$
Fig. 4.16e	0.92	$[Li_{0.75}](Mn_{0.91}Li_{0.09})O_2$	$M_{0.875}O$
Fig. 4.16f	1.05	$[Li_{0.87}](Mn_{0.91}Li_{0.09})O_2$	$M_{0.935}O$
Fig. 4.16g	1.16	$[Li_{0.97}](Mn_{0.91}Li_{0.09})O_2$	$M_{0.985}O$
Fig. 4.16h	1.20	$[Li_{1.00}](Mn_{0.91}Li_{0.09})O_2$	$M_{1.00}O$

* Two-phase material.
\# M = total Mn + Li content

The powder X-ray diffraction pattern of $Li_{0.36}Mn_{0.91}O_2$ changes dramatically on lithiation to $Li_{1.09}Mn_{0.91}O_2$ (Fig. 4.16). A profile that strongly resembles that of the original precursor material LT-Li_2MnO_3 (Fig. 4.16a) can be distinguished (Fig. 4.16h). The peak at 19.4°2θ and the peak at 38.1°2θ move to lower 2θ-values, 18.5°2θ and 36.8°2θ,

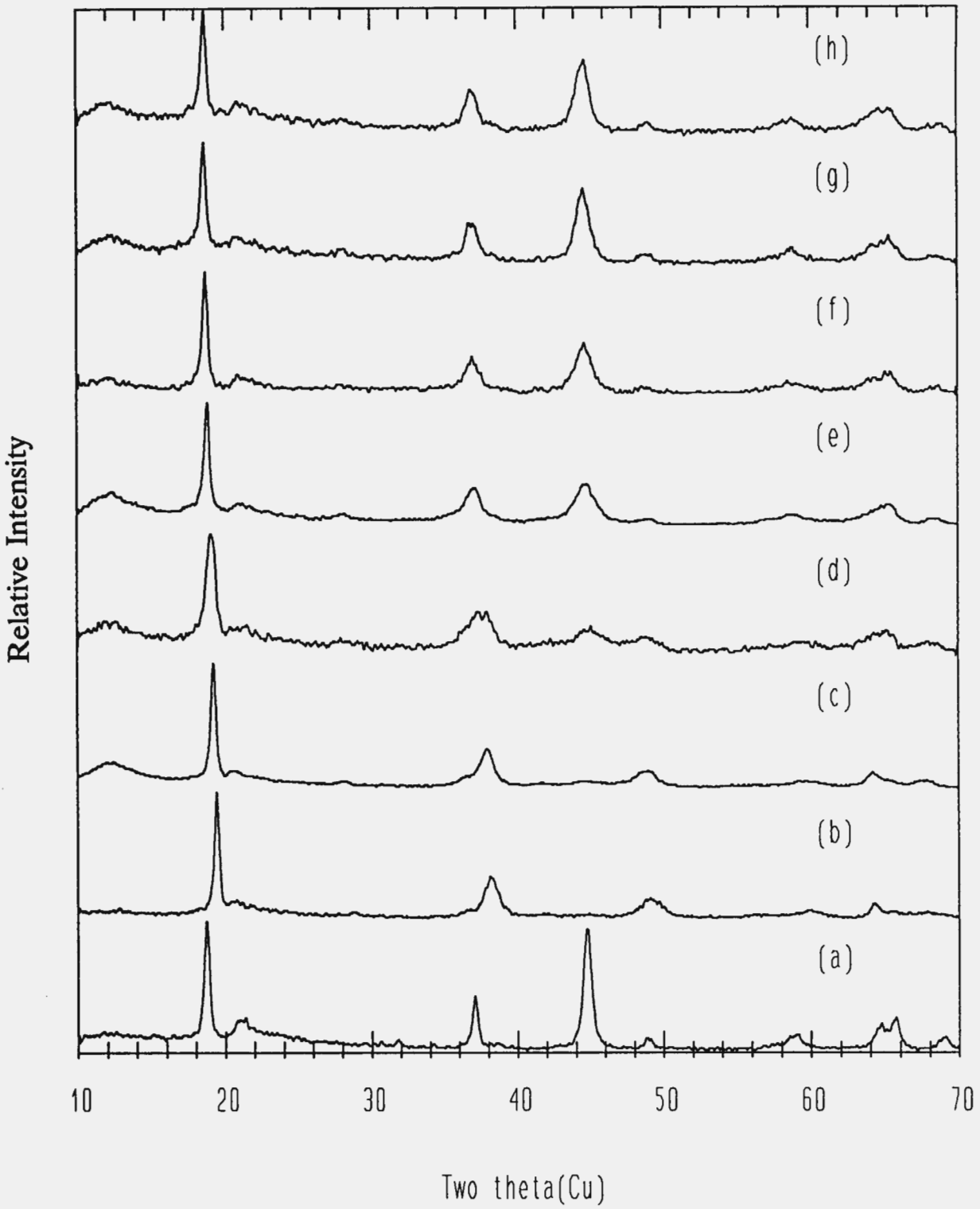

Fig. 4.16 Powder X-ray diffraction patterns of (a) LT-Li_2MnO_3, (b) $Li_{0.36}Mn_{0.91}O_2$ (c-h) reacted with various amounts of LiI. See Table 4.7 for compositions of the various phases.

respectively. The shift of the latter peak results in a doublet peak when the Li/Mn ratio is 0.65 (Fig. 4.16d). At this ratio the onset of the peak at 44.6°2θ and the disappearance of the peak at 38.9°2θ can also be observed. The peak at 49.1°2θ loses relative intensity, while the peak at 60.0°2θ gains relative intensity and moves to a lower 2θ-value, i.e. 59.1°2θ. The peak at 64.4°2θ splits into a doublet peak in the 63.2 to 66.2°2θ-range.

From a cursory examination of the powder X-ray diffraction patterns of $Li_{1.09}Mn_{0.91}O_2$ (Fig. 4.16h) and LT-Li_2MnO_3 (Fig. 4.16a), it can be concluded that the structures of $Li_{1.09}Mn_{0.91}O_2$ and LT-Li_2MnO_3 bear a strong relationship to one another, despite a significant change in the Li:Mn ratio. This is consistent with the results obtained with *n*-butyllithium (Section 4.5.2(a)).

4.5.3 Structural Characterization

(a) $Li_{0.36}Mn_{0.91}O_2$

The powder X-ray diffraction pattern of $Li_{0.36}Mn_{0.91}O_2$ (Fig. 4.16b) differs significantly from that of the precursor LT-Li_2MnO_3 (Fig. 4.16a) both in peak positions and relative peak intensities. As mentioned before, Li_2MnO_3 has a rock salt structure in which the oxygen-ion array is slightly distorted from cubic-close-packing and in which layers of Li^+ ions alternate with layers containing Mn^{4+} ions and Li^+ ions in a 2:1 ratio (Fig 4.8).

Although the lack of high quality X-ray data and the small number of strong reflections prevented satisfactory structural refinements using the monoclinic symmetry (C2/c) of the precursor material Li_2MnO_3, the gross structural features of $Li_{0.36}Mn_{0.91}O_2$ and $Li_{1.09}Mn_{0.91}O_2$ were obtained by profile refinement of their powder X-ray diffraction patterns (Fig. 4.16 b and h, respectively) using the higher symmetry space group $R\bar{3}m$ that characterizes the layered $LiCoO_2$ and $LiNiO_2$ structures. The structure refinements demonstrated that:

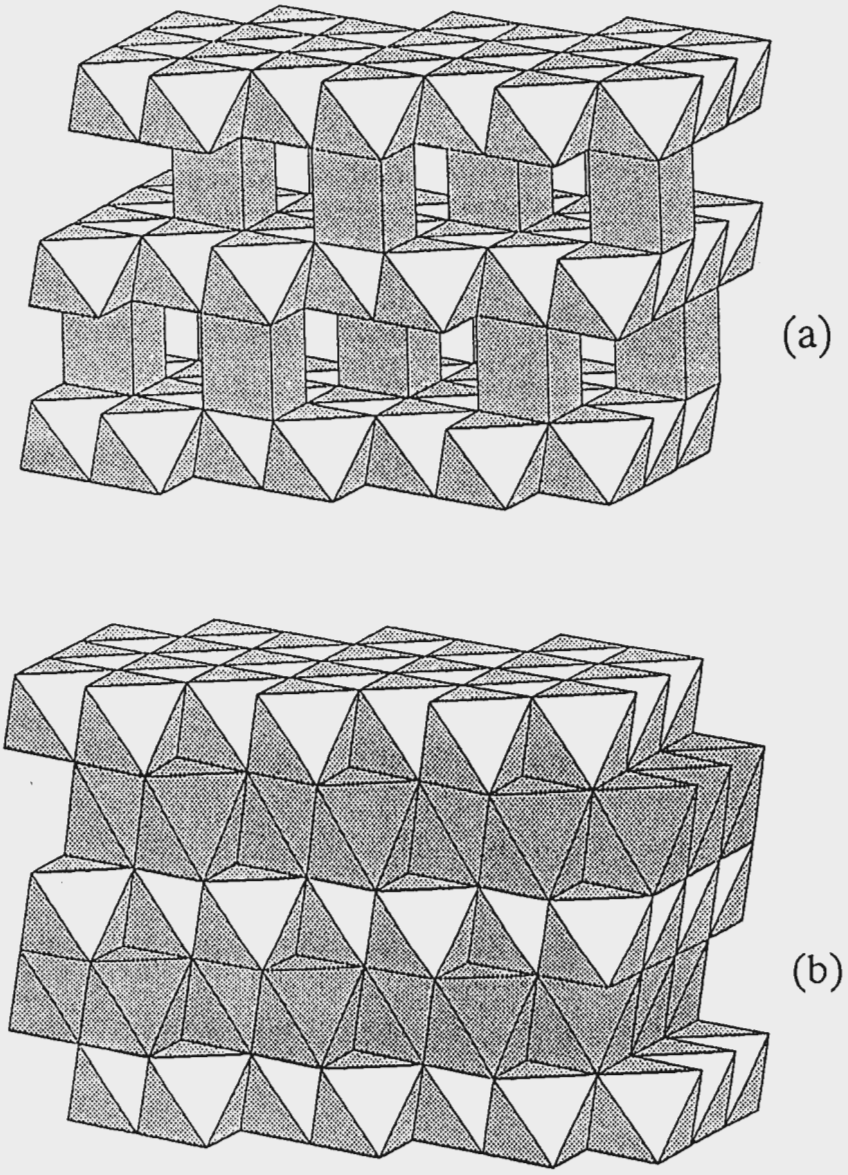

Fig. 4.17 The layered structures of (a) $Li_{0.36}Mn_{0.91}O_2$ ($R\bar{3}m$, a = 2.9029(5) Å, c = 13.803(5) Å) and (b) $Li_{1.09}Mn_{0.91}O_2$ ($R\bar{3}m$, a = 2.850(6) Å, c = 14.259(6) Å) as determined from X-ray data.

1. Removal of Li_2O from Li_2MnO_3 causes a shearing of the close-packed oxygen planes to yield an oxygen array in $Li_{0.36}Mn_{0.91}O_2$ which was comprised of alternate layers of trigonal prisms and sheets of edge-shared octahedra (Fig. 4.17a).

2. The manganese ions remain in alternate layers and do not migrate to the lithium layers during the leaching process. The Li^+-ion positions could not be located because of the weak scattering power of lithium; it was presumed that they resided in the small fraction of octahedral sites that were not occupied by manganese, and partially occupied the trigonal prismatic sites. With this arrangement the structural notation would be $[Li_{0.27}]_{tr.pr}(Mn_{0.91}Li_{0.09})_{oct}O_2$.

(b) **$Li_{1.09}Mn_{0.91}O_2$**

The powder X-ray diffraction pattern of $Li_{1.09}Mn_{0.91}O_2$ (Fig. 4.16h) shows that the lithiation of $Li_{0.36}Mn_{0.91}O_2$ with LiI regenerates the close-packed oxygen array of the parent Li_2MnO_3 structure. Note that $Li_{1.09}Mn_{0.91}O_2$ (Fig. 4.17b), like $Li_2MnO_3 \equiv Li_{1.33}Mn_{0.67}O_2$, has the ideal rock salt stoichiometry; the structure only differs in the Li/Mn ratio in the manganese rich layer and the oxidation state of the manganese cations. $Li_{1.09}Mn_{0.91}O_2$ therefore has a structure that closely approximates the ideal structure of $LiCoO_2$ and $LiNiO_2$. This is the first time that such a layered "$LiMnO_2$" phase has been synthesized.

4.5.4 Electrochemical Evaluation

(a) Galvanostatic Discharge

As can be seen from the electrochemical data in Fig. 4.18 an attractive gravimetric capacity can be obtained from an $Li_{0.36}Mn_{0.91}O_2$ cathode. The $Li/Li_{0.36}Mn_{0.91}O_2$ cell delivers 215 mAh/g, which is 93 % of its theoretical capacity of 232 mAh/g (with respect to the mass of the cathode when discharged to the rock salt composition, $Li_{1.09}Mn_{0.91}O_2$). The additional capacity which is obtained at lower voltages is attributed to a displacement reaction which destroys the structural integrity of the oxygen framework structure.

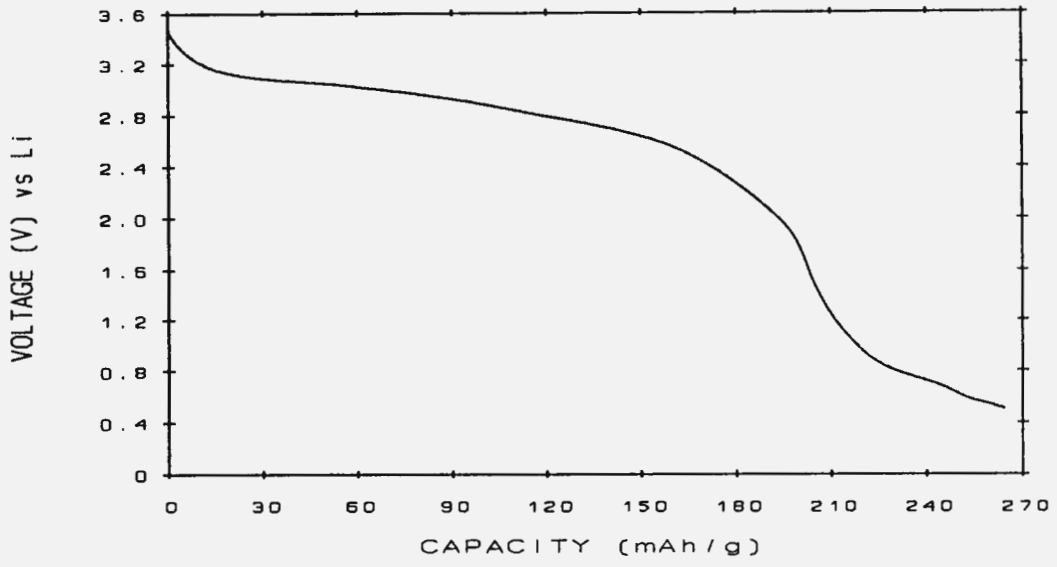

Fig. 4.18 Discharge curve of $Li_{0.36}Mn_{0.91}O_2$ in a room temperature lithium cell.

(b) Rechargeability

The cyclic voltammograms of $Li_{0.36}Mn_{0.91}O_2$ scanned initially cathodically and initially anodically are shown in Fig. 4.19 a and b, respectively. The major reduction peak which is observed at approximately 2.8 V is associated with the lithium insertion into octahedral sites of the defect rock salt structure.

Although the cyclic voltammograms illustrate that $Li_{0.36}Mn_{0.91}O_2$ can incorporate lithium reversibly, the decrease in intensity of the 2.8 V peak on the second and third cycles indicates that a significant capacity loss can be anticipated when cycling Li/$Li_{0.36}Mn_{0.91}O_2$ cells.

The small activity that can be observed on the initial anodic scan is most probably due to a small portion of Mn^{3+} in the starting cathode. The sharp increase in current at 4.2 V is due to electrolyte decomposition.

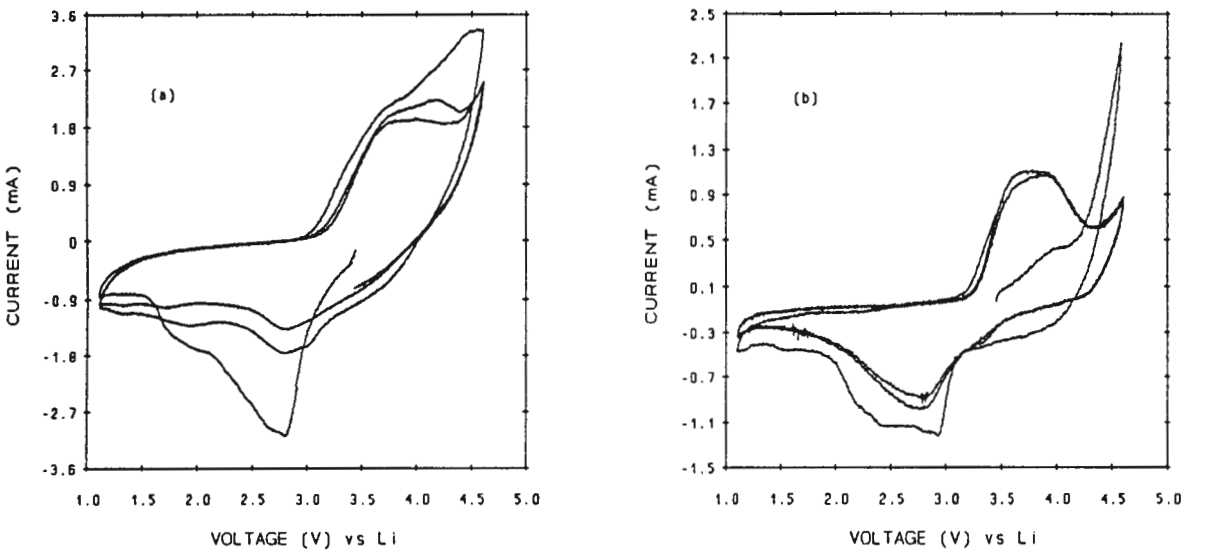

Fig. 4.19 Cyclic voltammograms of $Li_{0.36}Mn_{0.91}O_2$ scanned initially (a) cathodically and (b) anodically.

The shape of the cyclic voltammogram of $Li_{0.36}Mn_{0.91}O_2$ (Fig. 4.19a) is typically that of a γ-MnO_2 electrode, for example EMD or CMD. Lithium insertion and extraction reactions proceed essentially in a one-stage process, during which lithium ions are inserted and extracted from the octahedral sites of a defect rock salt structure.

$Li_{0.36}Mn_{0.91}O_2$ and its chemically lithiated derivative $Li_{1.09}Mn_{0.91}O_2$ were cycled in room temperature lithium cells. The $Li/Li_{0.36}Mn_{0.91}O_2$ cell was discharged at 200 μA and charged at 100 μA between the voltage limits 2.0 V and 4.0 V. The capacity dropped steadily from the initial 196 mAh/g to 120 mAh/g after 6 cycles (Fig. 4.20a). The capacity retention was improved by increasing the current rates 10 fold; however, this cell yielded a much lower capacity, as expected, as can be seen in Fig. 4.20b. After 10 cycles at a discharge of 2 mA and a charge of 1 mA, the cell lost capacity very slowly. The capacity loss is believed to be due to problems associated with the lithium anode, for example, passivation and dendrites, rather than to the degradation of the cathode.

After being subjected to an initial discharge at 2 mA to 2 V, the chemically lithiated product, $Li_{1.09}Mn_{0.91}O_2$, was continuously charged at 1 mA and discharged at 2 mA. The

capacity of this cell levelled out at about 90 mAh/g (Fig. 4.20c), which was slightly superior (12 %) to the capacity achieved on cycling Li/$Li_{0.36}Mn_{0.91}O_2$ cells under identical conditions.

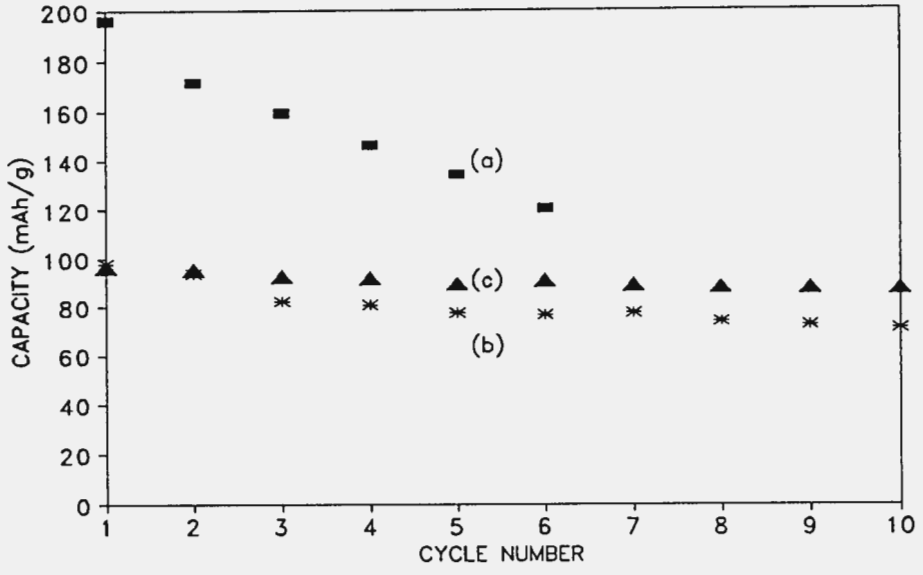

Fig. 4.20 Cycling behaviour of (a) $Li_{0.36}Mn_{0.91}O_2$ discharged at 0.2 mA and charged at 0.1 mA, (b) $Li_{0.36}Mn_{0.91}O_2$ discharged at 2 mA and charged at 1 mA, and (c) $Li_{1.09}Mn_{0.91}O_2$ discharged at 2 mA and charged at 1 mA.

The profiles of the first 6 discharge curves of Li/$Li_{0.36}Mn_{0.91}O_2$ and Li/$Li_{1.09}Mn_{0.91}O_2$ cells are shown in Fig. 4.21 a and b, respectively. The discharge current was 2 mA and the charge current 1 mA, between the voltage limits 2.0 V and 4.0 V. The sloping shape of the discharge profiles confirm that lithium insertion proceeds essentially in a one-stage process, confirming observations made from the cyclic voltammograms in Fig. 4.19.

$Li_{0.36}Mn_{0.91}O_2$ cathodes that had been heat-treated to 100°C, 150°C and 200°C were cycled between 2.0 V and 4.0 V with a discharge current of 2 mA and a charge current of 1 mA, to observe the effect of heat-treatment on the performance of the cells.

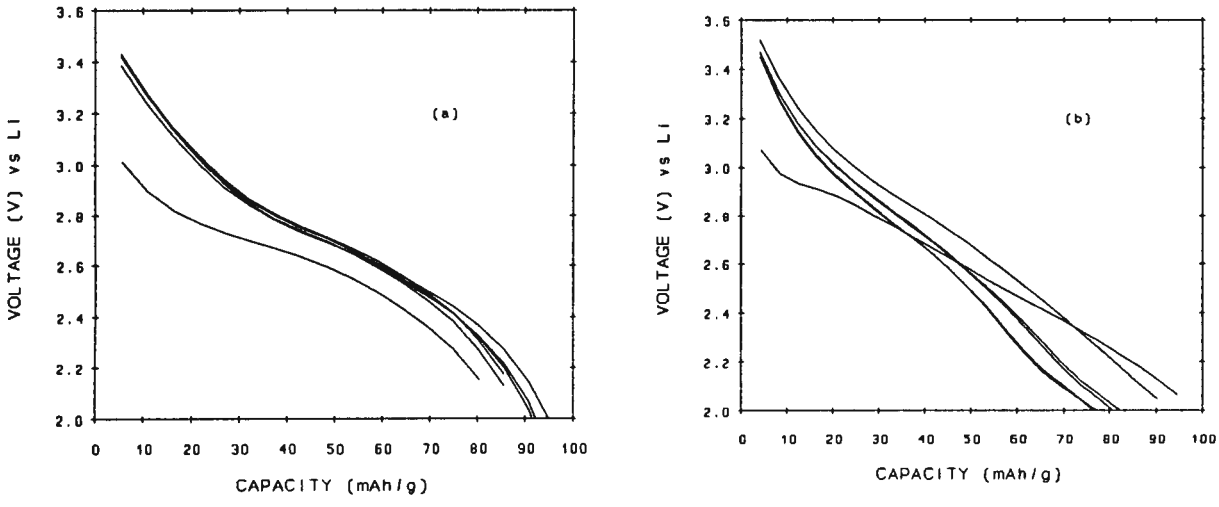

Fig. 4.21 Profiles of the discharge curves of (a) $Li/Li_{0.36}Mn_{0.91}O_2$ and (b) $Li/Li_{1.09}Mn_{0.91}O_2$ cells.

In Section 4.5.1 it was shown that after heating $Li_{0.36}Mn_{0.91}O_2$ to 150°C, a two-phase product consisting of layered and spinel domains formed, while heating $Li_{0.36}Mn_{0.91}O_2$ at higher temperatures (≥ 200°C) a single-phase product with definite spinel character was formed. The cycling behaviour of $Li_{0.36}Mn_{0.91}O_2$ and its heat-treated derivatives are shown in Fig. 4.22. Although all the products show a relative slow drop in capacity over 20 cycles, this is believed to be due predominately to problems associated with the lithium anode, as stated earlier.

The material heated to 200°C (Fig. 4.22c) provided the highest capacity which was in excess of 140 mAh/g for the first 10 cycles. The significantly superior capacity of this electrode compound to electrodes that had been dried at lower temperatures is not unexpected; it can be attributed to the low water content in the cathode and the presence of stable spinel domains within the cathode structure.

The profiles of the first 10 discharge curves of $Li/Li_{0.36}Mn_{0.91}O_2$ cells with the cathodes heated to 100°C and 200°C are shown in Fig. 4.23 (a-b). A slight plateau at 2.9 V in the first discharge curve of the cathode heated to 100°C can be observed (Fig. 4.23a). On consecutive discharge curves this plateau can be observed at approximately 2.7 V, while a second slight plateau can be seen at approximately 2.3 V.

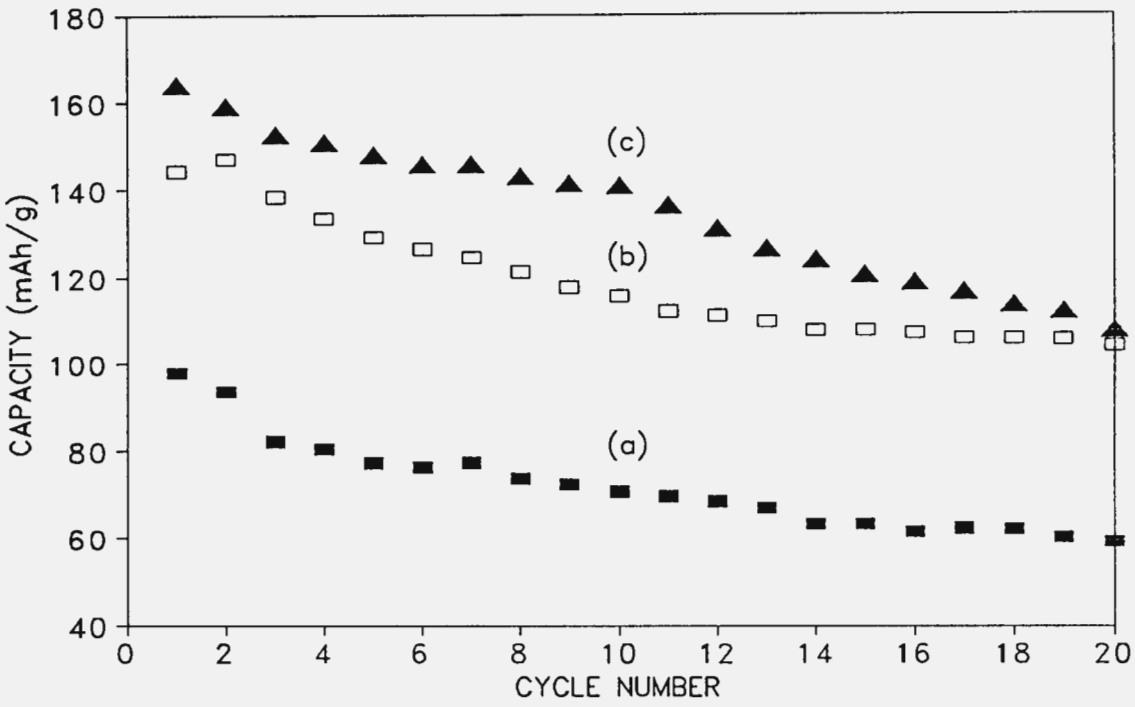

Fig. 4.22 Cycling behaviour of $Li_{0.36}Mn_{0.91}O_2$ discharged at 2 mA and charged at 1 mA after (a) no heat-treatment, and heat-treatment to (b) 100°C, and (c) 200°C.

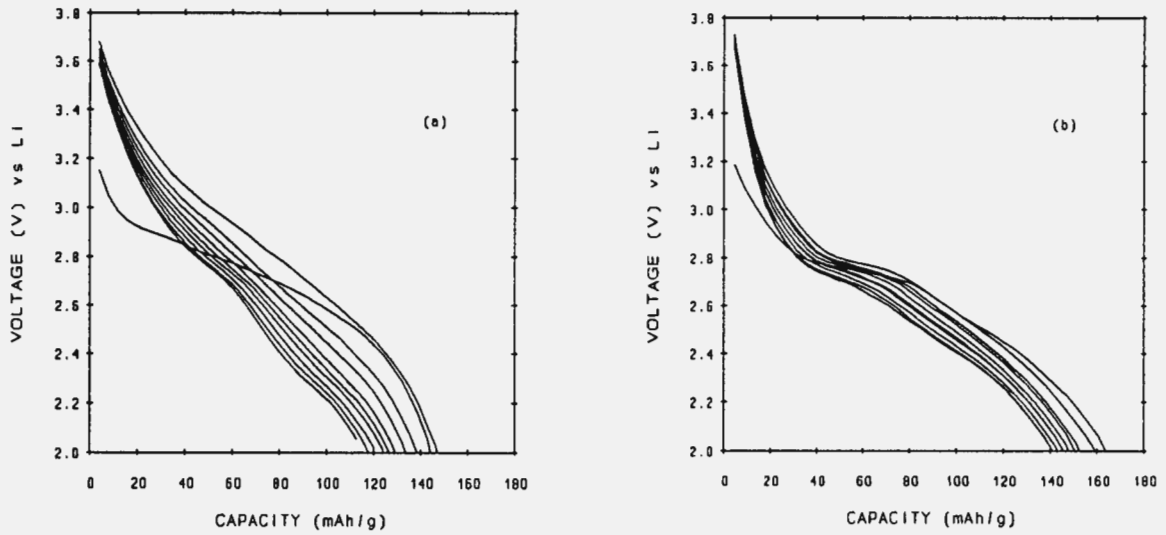

Fig. 4.23 Profiles of the discharges curves of $Li/Li_{0.36}Mn_{0.91}O_2$ cells with the cathodes heated to (a) 100°C and (b) 200°C.

The cathode heated at 200°C (Fig. 4.23b) displayed a more definite plateau at 2.8 V. Spinel electrodes usually discharge on a plateau at 2.8 to 2.9 V. The plateau indicates a two-phase process as lithium ions are inserted into the octahedral 16c sites, and the lithium ions on the tetrahedral 8a sites are displaced to the octahedral 16c sites.

The presence of the plateaux in the discharge curves of the heated cathodes indicates the existence of spinel-type domains in the electrode material.

Chapter 5

Alpha-MnO_2

ABSTRACT: This chapter discusses the synthesis and characterization of a highly crystalline α-MnO_2 phase that contains no foreign "stabilizing" cations such as NH_4^+, K^+, Na^+ or Rb^+. Preliminary electrochemical results of Li/α-MnO_2 room temperature lithium cells are reported.

5.1 Introduction

The name α-MnO_2 is a general term given to isostructural minerals and synthetic manganese oxides which are part of the hollandite group (Burns, 1980). In α-MnO_2 each manganese cation is surrounded by six oxygen ions forming an octahedron. The [MnO_6] octahedra are linked together, sharing edges to form double chains along the *c*-axis of a tetragonal unit cell. The double chains of octahedra share corners with one another, thereby creating [2x2] tunnels in the structure. The α-MnO_2 structure is usually "stabilized" by large alkali or alkaline earth ions that reside in the centre of the tunnels; Fig. 5.1 (Bayer, 1966; Buser, 1954; Giovanoli, 1980).

Several synthetic α-MnO_2 materials, such as KMn_8O_{16} and $NH_4Mn_8O_{16}$, containing "stabilizing" cations have been investigated as cathode materials in lithium cells. These materials are prepared typically by the oxidation of $MnSO_4 \cdot H_2O$ with $KMnO_4$ and $(NH_4)_2S_2O_8$, respectively, at 80°C (Lecerf, 1990; Lubin, 1991a). A significant improvement in the electrochemical rechargeability of these α-MnO_2 materials was achieved if the electrodes were reacted with $LiOH \cdot H_2O$ at 300°C in air with a Li/Mn ratio ranging from 0.3 to 0.5 prior to cell assembly. At this temperature the lithiated compound retains the

crystal structure of the initial α-MnO_2 compound (Lecerf, 1990; Humbert, 1992; Botkovitz, 1992).

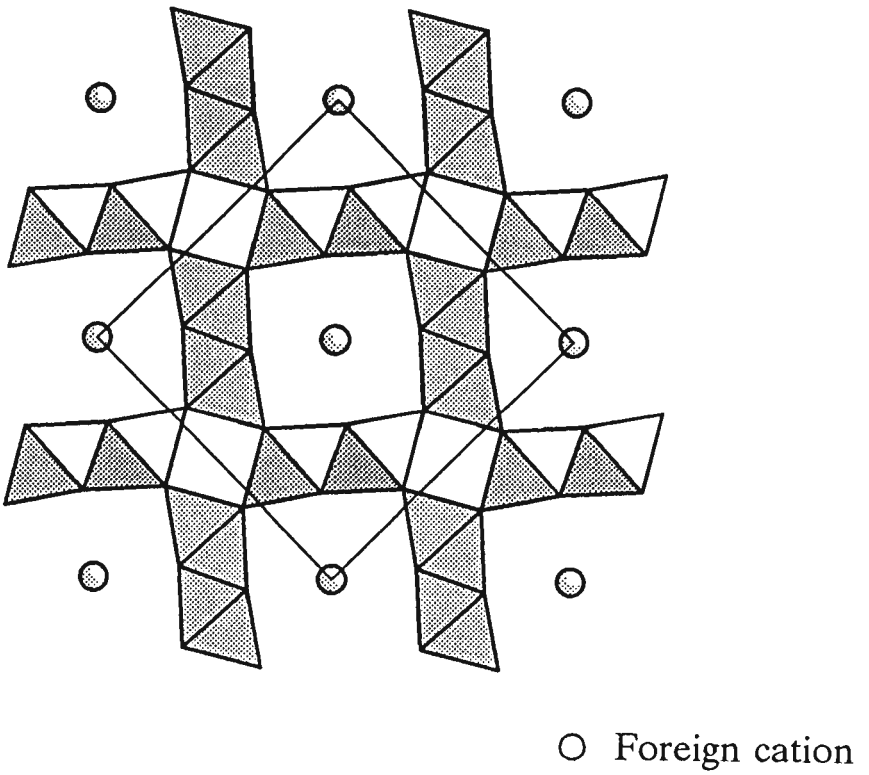

Fig. 5.1 Structure of α-MnO_2 "stabilized" by a large cation.

α-MnO_2 materials can also be prepared by reacting Mn_2O_3 with a 0.5M H_2SO_4 solution containing 0.5M R_2SO_4 (R = NH_4^+, K^+, and Rb^+) at 95°C to 100°C (Ohzuku, 1991). A disadvantage of α-MnO_2 electrodes that contain "stabilizing" R cations is that these large cations in the centre of the [2x2] tunnels will impede Li^+-ion transport during lithium insertion/extraction reactions.

This chapter describes a novel synthesis method for the preparation of an essentially pure α-MnO_2 material by using the rock salt phase Li_2MnO_3 as precursor. Powder X-ray diffraction and neutron diffraction data were used for the structural characterization of the α-MnO_2 materials. Selected materials were evaluated electrochemically as cathode materials in room temperature lithium cells. α-MnO_2 materials were lithiated chemically using *n*-butyllithium in hexane.

5.2 Experimental

5.2.1 Synthesis of α-MnO_2

A Li_2MnO_3 precursor was synthesized by reacting stoichiometric quantities of $MnCO_3$ or γ-MnO_2 (EMD) with either Li_2CO_3 or $LiOH \cdot H_2O$ at 700°C for 24 hours. The resulting Li_2MnO_3 product had a characteristic bright red colour.

α-$MnO_2 \cdot xA_2O$ (A = Li, H; $x \leq 0.3$) products were prepared by reacting m g Li_2MnO_3 with $10m$ ml 2.25M H_2SO_4. Reaction temperatures were varied between 25°C (room temperature) and 100°C (reflux conditions) and the reaction time from 24 hours to 1 week. The products were dried overnight at 100°C. Selected samples were dehydrated further at 250°C or 300°C. The effects of varying the molarity of the H_2SO_4 solution were also investigated. Reactions of Li_2MnO_3 with 5M HCl and 5M HNO_3 were undertaken to compare the nature of the reaction products when different acids were used.

A standard K-stabilized α-MnO_2 phase which was prepared by the reduction of $KMnO_4$ with HCl was used as a reference material; it is denoted α-$MnO_2(K^+)$. In this preparation 250 ml 5M HCl was added to 500 ml of a boiling 0.5M $KMnO_4$ solution. The solution was boiled for 1 hour, allowed to cool, filtered, washed and dried at 100°C. A further 250 ml 5M HCl was added to the dry material and the solution was heated to boiling point before it was allowed to cool and was filtered.

5.2.2 Synthesis of Chemically Lithiated α-MnO_2 Products

Chemical lithiation of α-MnO_2 was achieved by reacting α-MnO_2 either with *n*-butyllithium in hexane or with lithium iodide in acetonitrile as described in § 4.2.3.

5.2.3 Chemical Analyses of the Reaction Products

Lithium and manganese concentrations in α-MnO_2 and Li_xMnO_2 products were

determined by atomic absorption spectroscopy as described in § 4.2.4.

The determination of the hydrogen concentration and the thermal analyses (TGA and DSC) were discussed in § 4.2.4.

5.2.4 Diffraction Patterns of the Reaction Products

Powder X-ray and neutron diffraction patterns were obtained at CSIR and at the Rutherford Appleton Laboratory (RAL) as discussed previously in § 4.2.5.

5.2.5 Electrochemical Evaluation of the Reaction Products

Electrochemical experiments were carried out as described in § 3.3 and § 4.2.6. The conditions under which the experiments were undertaken, for example charge/discharge current rates, scan rates, voltage limits, etc. are provided with the electrochemical data in the Results and Discussion section 5.3. Open-circuit voltage readings were recorded at regular intervals allowing a 72 h equilibration time at each point.

5.3 Results and Discussion

5.3.1 Synthesis of the Reaction Products

The α-MnO_2 products prepared from Li_2MnO_3 have highly crystalline structures as is evident from the sharp peaks of the powder X-ray diffraction patterns of a hydrated phase (Fig. 5.2a) and of a dehydrated phase (Fig. 5.2b). The peaks were indexed to a tetragonal unit cell. The prototypic space group for hollandite-MnO_2 is I4/m.

The powder X-ray diffraction pattern of α-$MnO_2(K^+)$ (Fig. 5.2c) has broader peaks than those of the products obtained from Li_2MnO_3 indicating a less crystalline material; the relative intensities of the peaks are also significantly different, which can be attributed to the presence of K^+ ions in the centre of the [2x2] channels.

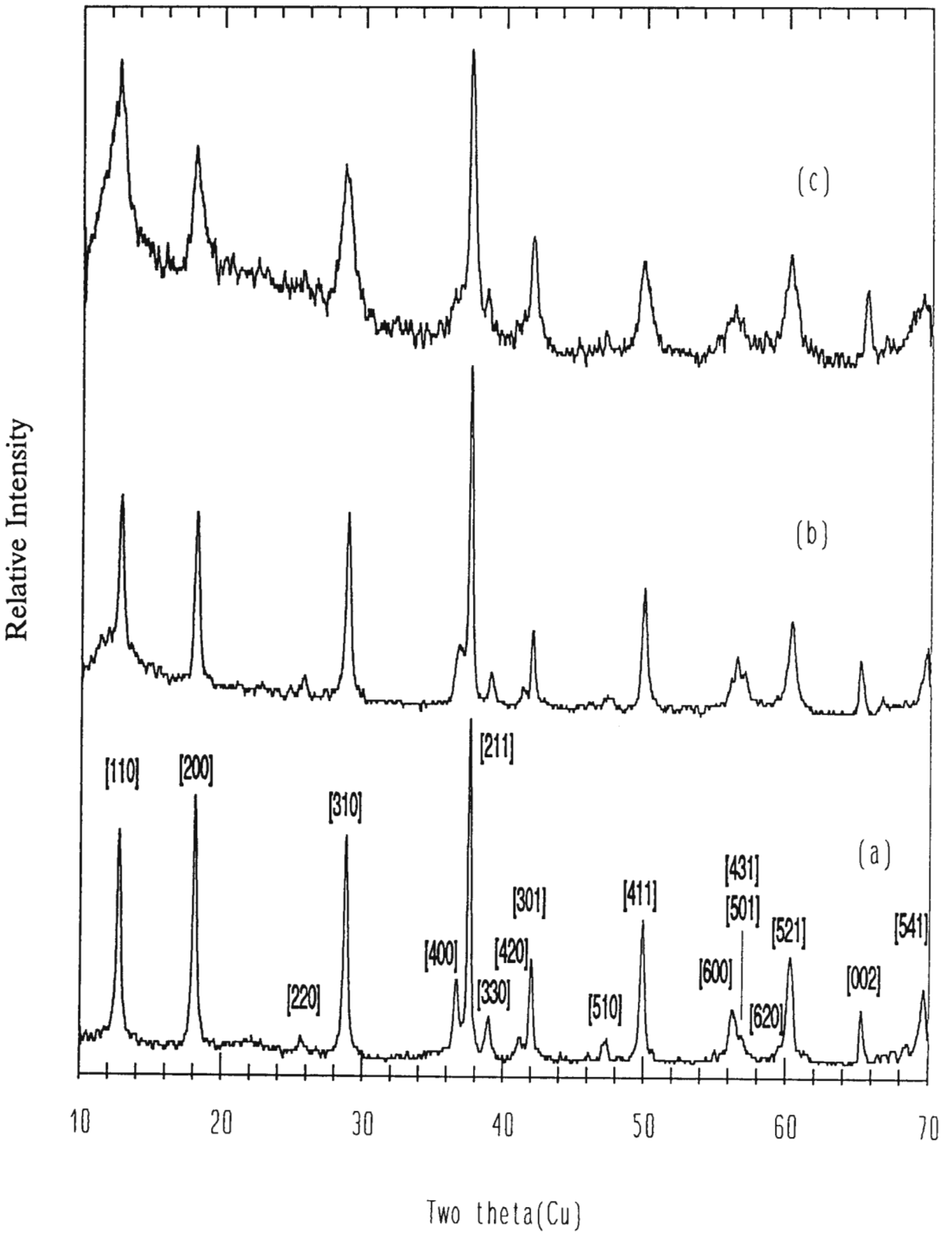

Fig. 5.2 Powder X-ray diffraction patterns of (a) α-$MnO_2 \cdot 0.3H_2O$, (b) the dehydrated α-MnO_2 product, and (c) α-$MnO_2(K^+)$.

The powder X-ray diffraction patterns in Figs. 5.3 to 5.6 show the effect of changing the reaction temperature, reaction time, the concentration of the H_2SO_4 and the nature of the acid on products synthesized from Li_2MnO_3.

The powder X-ray diffraction patterns of the products formed using 2.25M H_2SO_4 and a reaction time of 2 days as a function of reaction temperature are shown in Fig. 5.3 (a-e). At room temperature (Fig. 5.3a) the onset of a layered-MnO_2 phase (See Chapter 4) as evident from the shoulder on the right of the peak at 19°2θ, can be seen. At 50°C (Fig. 5.3b) the layered-MnO_2 phase is even more pronounced, while at 90°C (Fig. 5.3c) a pure α-MnO_2 material was formed. At 100°C (Fig. 5.3d) the product contains a trace of γ-MnO_2 as evident from the broad peak at 22°2θ.

The powder X-ray diffraction patterns of the products formed using 2.25M H_2SO_4 at 100°C (under reflux) as a function of reaction time are shown in Fig. 5.4 (a-e). After a reaction period of 24 hours a three phase material consisting of the Li_2MnO_3 precursor, a layered-MnO_2 phase and an α-MnO_2 phase was formed (Fig. 5.4a). After 48 hours (Fig. 5.4b) a pure α-MnO_2 phase was produced. After 72 hours (Fig. 5.4c) and even a week (Fig. 5.4d) of refluxing the α-MnO_2 phase still proved to be stable and was the only phase present in the product. The major changes in the X-ray diffraction patterns as a function of reaction time are the increase in intensity of the [3 1 0] peak at 29°2θ and the improved resolution of the [4 0 0] and [2 1 1] peaks at 37-39°2θ.

The concentration of the sulphuric acid also has an influence on the final product as can be seen from the powder X-ray diffraction patterns in Fig. 5.5 (a-e). With a 0.5M H_2SO_4 solution (Fig. 5.5a) a layered-MnO_2 phase formed; with a 1.125M H_2SO_4 solution (Fig. 5.5b) the onset of α-MnO_2 is clearly visible in addition to traces of the Li_2MnO_3 precursor and layered-MnO_2 phase. A pure α-MnO_2 phase formed with the 2.25M H_2SO_4 solution (Fig. 5.5c), whereas with a 4.5M H_2SO_4 solution both α-MnO_2 and a trace of γ-MnO_2 can be observed in the X-ray pattern from the broad peak at 22°2θ (Fig. 5.5d).

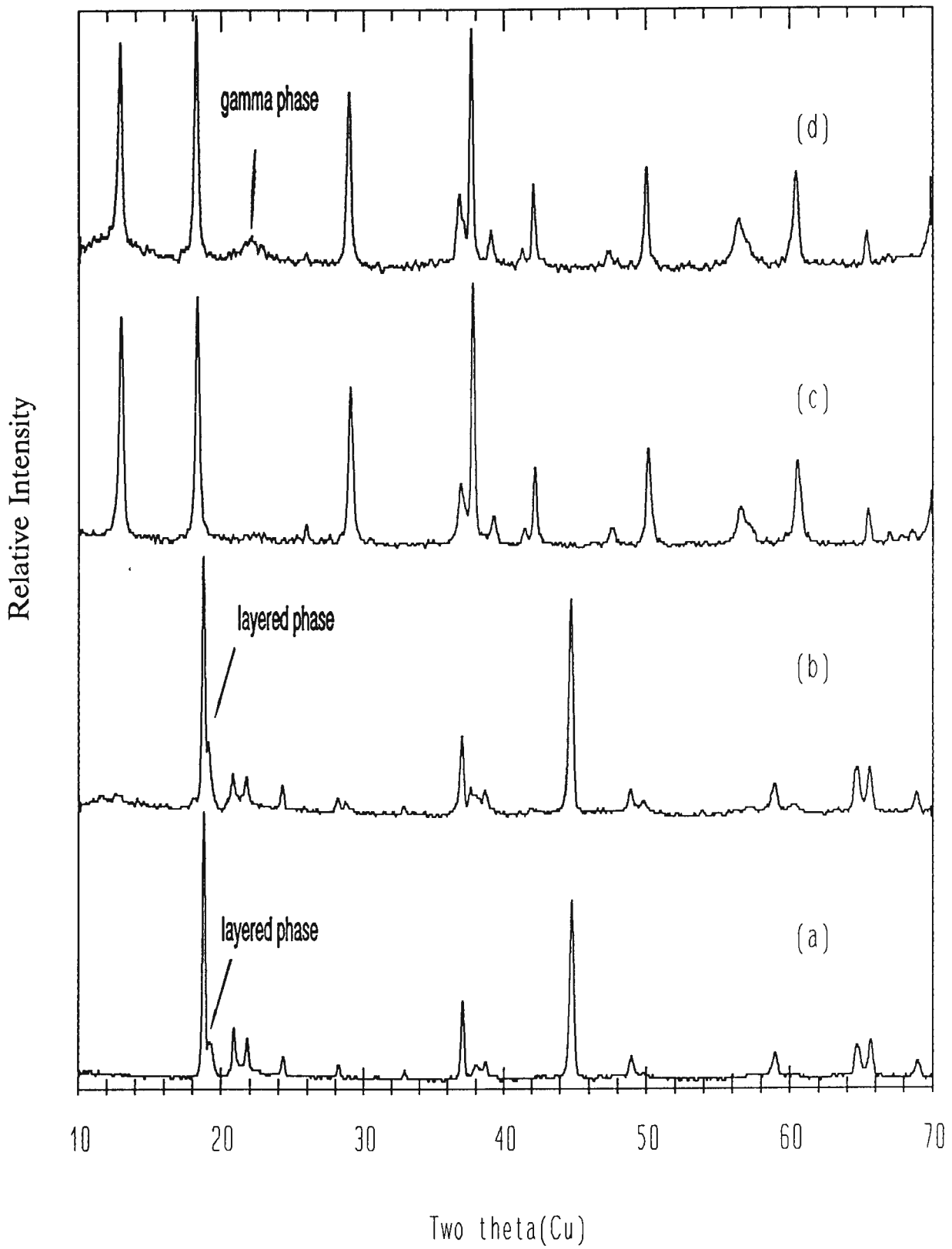

Fig. 5.3 Powder X-ray diffraction patterns illustrating the effect of varying the reaction temperature. Li_2MnO_3 was reacted with 2.25M H_2SO_4 for 2 days at (a) 25°C, (b) 50°C, (c) 90°, and (d) 100°C.

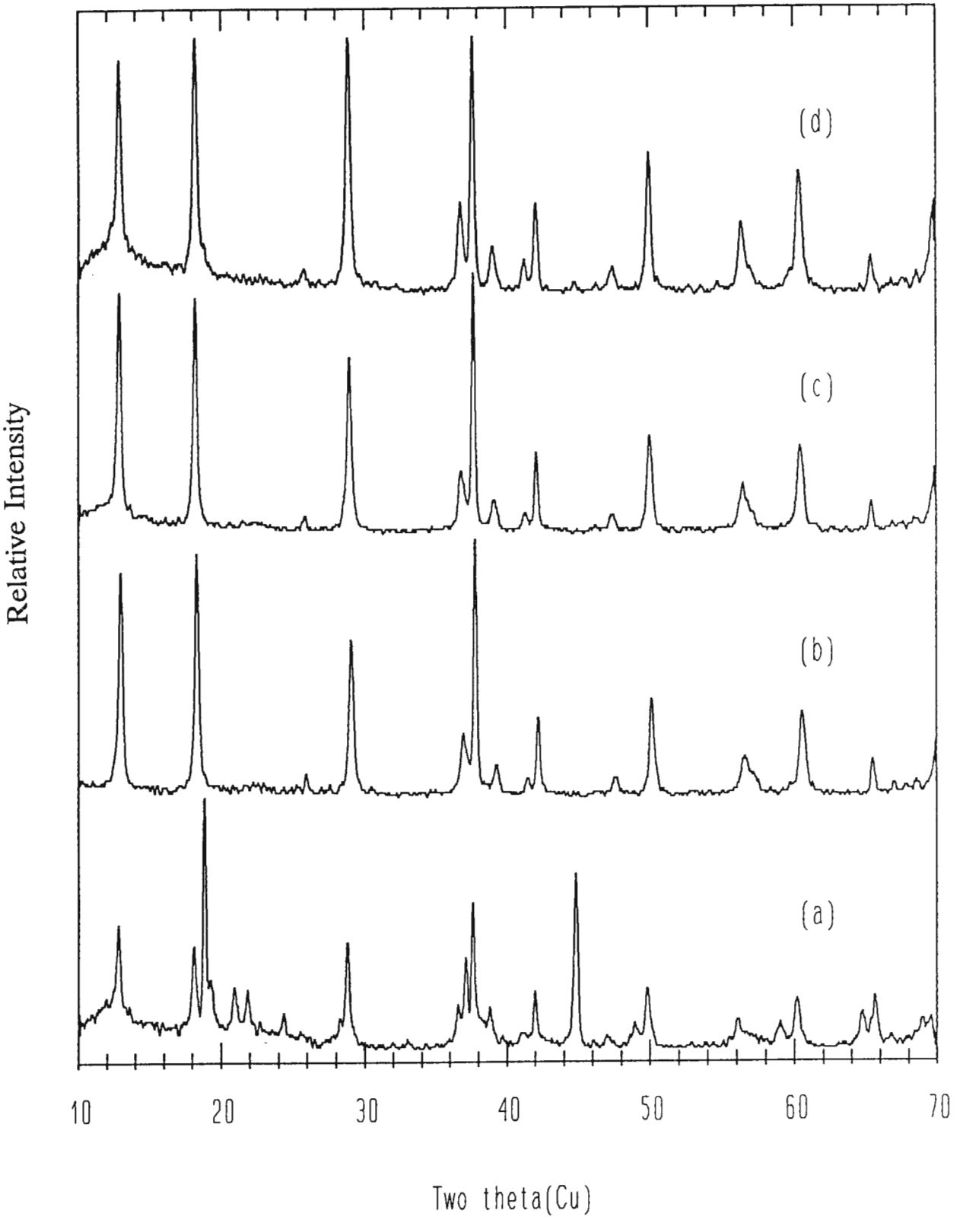

Fig. 5.4 Powder X-ray diffraction patterns illustrating the effect of varying the reaction time. Li_2MnO_3 was refluxed at 100°C in 2.25M H_2SO_4 for (a) 24 hours, (b) 48 hours, (c) 72 hours, and (d) 1 week.

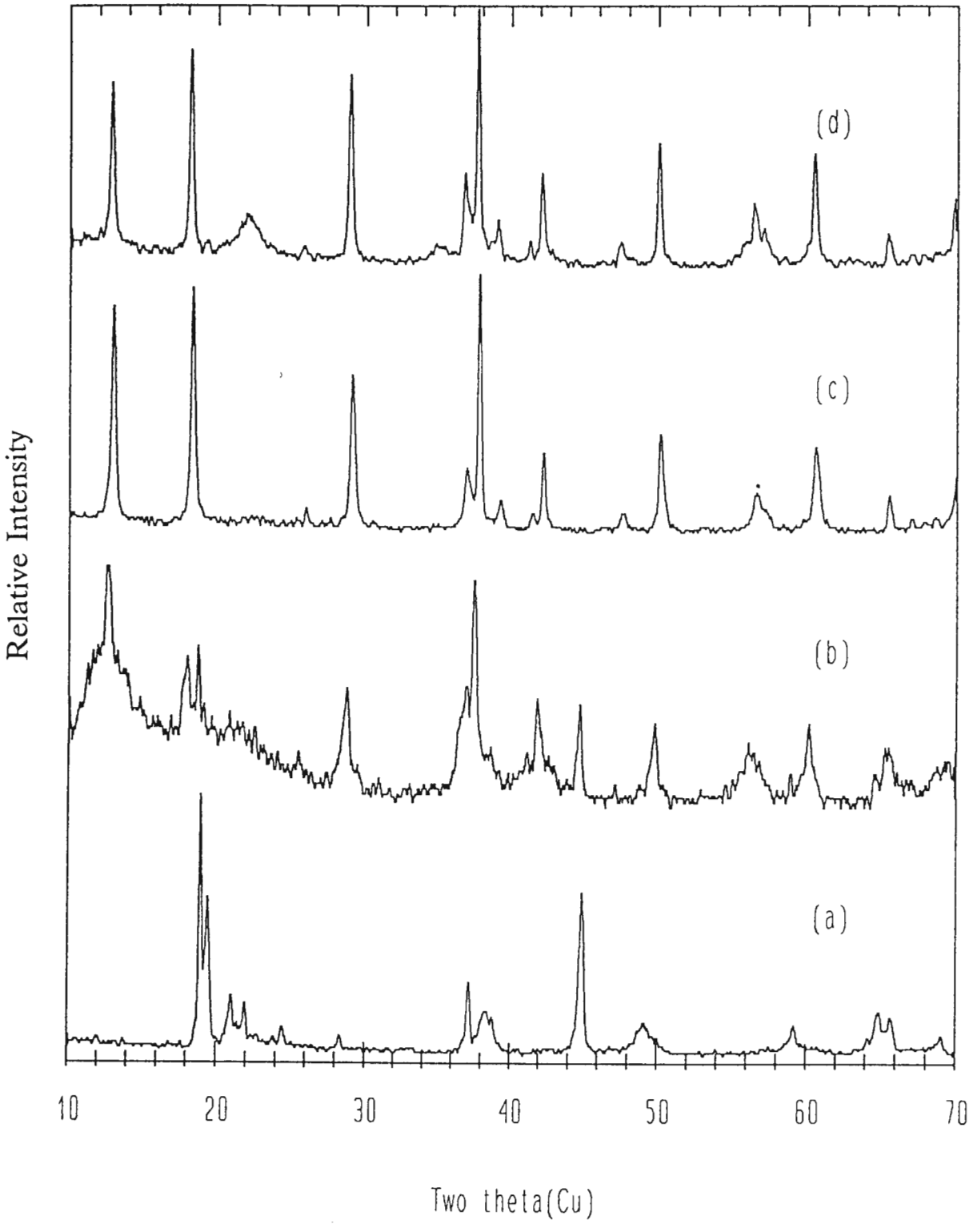

Fig. 5.5 Powder X-ray diffraction patterns illustrating the effect of varying the H_2SO_4 concentration. Li_2MnO_3 was refluxed at 100°C for 2 days in (a) 0.5M H_2SO_4, (b) 1.125M H_2SO_4, (c) 2.25M H_2SO_4, and (d) 4.5M H_2SO_4.

The powder X-ray diffraction patterns of Li_2MnO_3 refluxed in 5M HCl and 5M HNO_3 for 2 days are shown in Fig. 5.6 a and b, respectively. The yield obtained from the HCl reaction was very low (less than 1 g from 20 g Li_2MnO_3). The product shows a γ-MnO_2 type phase (orthorhombic symmetry, space group Pnma,) with a very strong [1 1 0] peak at 22°2θ and relatively strong overlapping [2 2 1] and [4 2 0] peaks at 56°2θ, while the intensity of the normally strong peak at 38°2θ is uncharacteristically low (Fig. 5.6a). The powder X-ray pattern of chemical MnO_2 (CMD), a typical γ-MnO_2 material, is shown in Fig. 5.6c, for comparison.

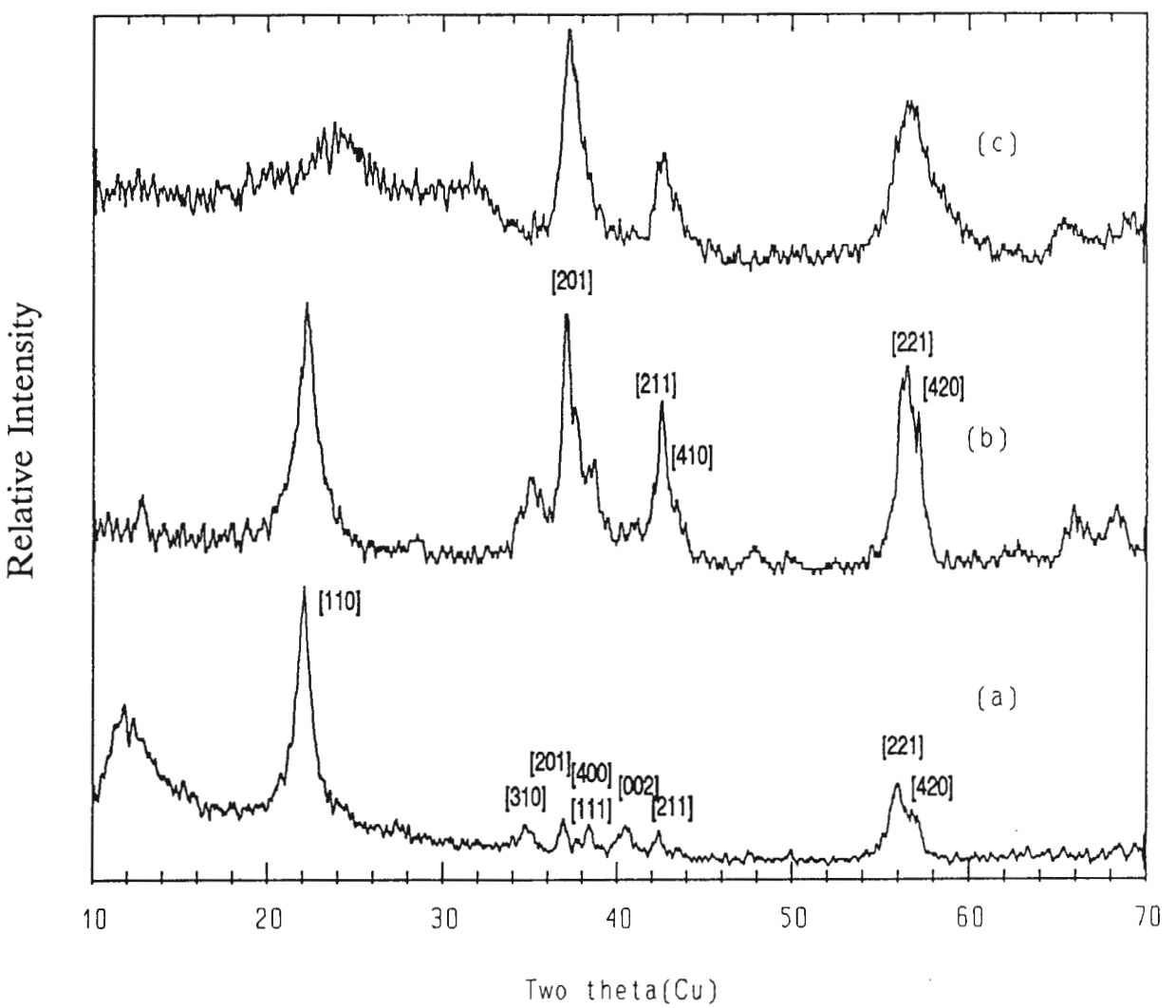

Fig. 5.6 Powder X-ray diffraction patterns illustrating the effect on the product by changing the nature of the acid. Li_2MnO_3 was refluxed for 2 days in (a) 5M HCl, and (b) 5M HNO_3. (c) A typical γ-MnO_2 pattern of CMD.

The product obtained from the HNO_3 reaction (Fig. 5.6b) shows a relatively crystalline γ-MnO_2 phase with severe overlapping of the [2 1 1] and [4 1 0] peaks at 42-44°2θ, and the [2 2 1] and [4 2 0] peaks at 56-58°2θ.

It is evident that acid treatment of Li_2MnO_3 at 100°C leaches out effectively all the lithium from the rock salt phase during the transformation to the α-MnO_2 structure. The optimum reaction conditions for producing a pure crystalline α-MnO_2 material from a Li_2MnO_3 precursor prepared at 700°C therefore appear to be 48 hours in a 2.25M H_2SO_4 solution while refluxing at 100°C. Although a γ-MnO_2 phase in the final product cannot always be predicted, this phase is not necessarily undesirable as it is electrochemically active.

The lithium concentrations of the α-MnO_2 materials ranged from 0.32 wt% down to 0.01 wt% (a pure phase). Hydrogen concentrations in the hydrated materials varied between 0.60 wt% and 0.41 wt%, whereas in the dehydrated materials that had been heat-treated at 250 to 400°C, the values ranged from 0.15 wt% to 0.03 wt%.

Table 5.1 gives the results of the chemical analyses of one typical α-MnO_2 product that was selected for structural characterization. The relatively high $[H^+]$ content in α-MnO_2 after drying the product at 100°C overnight (0.65 wt%) was attributed to residual water associated with the particle surface or grain boundaries and to protons that had been ion-exchanged for some of the lithium ions. Assuming that the tetravalent manganese ions maintain their oxidation state during the acid treatment of Li_2MnO_3 and ignoring the negligibly small Li^+-ion content in the product (0.027 wt%), the composition of the hydrated phase from the chemical analysis was determined to be $H_{0.6}MnO_{2.3}$ or $MnO_2 \cdot 0.3H_2O$. This compound could be almost entirely dehydrated by heat-treatment at 300°C ($[H^+]$ = 0.03 wt%). The powder X-ray diffraction pattern in Fig. 5.2b indicates that dehydration occurs without any apparent damage to the α-MnO_2 structure.

Table 5.1
Chemical Analyses of an α-MnO_2 Product

Compound	$[Li^+]$ wt%	$[H^+]$ wt%
Hydrated α-MnO_2	0.027	0.65
Dehydrated α-MnO_2	0.029	0.03

5.3.2 Thermal Stability of α-MnO_2

The powder X-ray diffraction patterns of α-MnO_2 products that contained minor impurities of a γ-MnO_2 phase or a layered-MnO_2 phase and their heat-treated products are shown in Fig. 5.7 (a-d). It was evident that the γ-MnO_2 (Fig. 5.7a) disappeared on heating the sample to 250°C (Fig. 5.7b) and that the layered-MnO_2 phase (Fig. 5.7c) disappeared when the sample was heated to 400°C (Fig. 5.7d). These patterns indicate that the framework structure of α-MnO_2 remains intact during the dehydration process, to at least 400°C, and that the MnO_2-impurity phases are probably incorporated into the α-MnO_2 framework on heat-treatment.

Plots of the thermogravimetric analyses (TGA) of α-$MnO_2 \cdot 0.3H_2O$ that were obtained under a nitrogen stream and under an air stream are shown in Fig. 5.8 a and b, respectively.

The decomposition of α-$MnO_2 \cdot 0.3H_2O$ occurs sooner in the inert nitrogen atmosphere (Fig. 5.8a) than in the oxidizing air atmosphere (Fig. 5.8b). Under the air atmosphere a sharp drop in weight was observed at 550°C, whereas under nitrogen, the weight loss was more gradual beyond 400°C. The average weight loss in the α-MnO_2 samples was approximately 13.7 %. In these samples, the $[H^+]$ content was determined to range between 0.41 and 0.60 wt%. The weight loss can be accounted for by the loss of water and also by the loss of oxygen as a result of the reduction of MnO_2 to Mn_2O_3 at 550°C. The reaction can thus be written in two steps as:

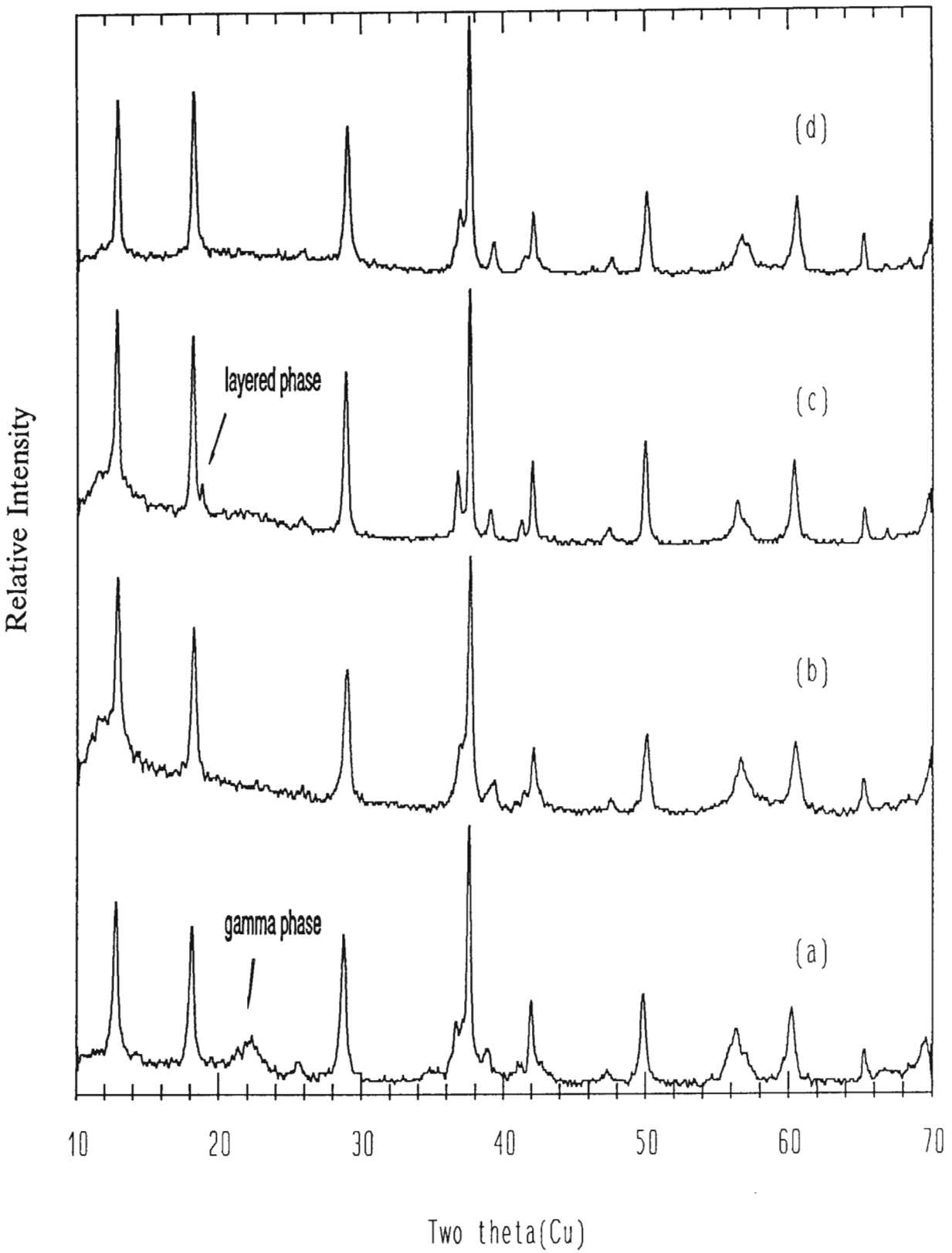

Fig. 5.7 Powder X-ray diffraction patterns of (a) an α-MnO_2 with an γ-impurity after being heated to (b) 250°C, and (c) an α-MnO_2 with a trace of the layered-MnO_2 phase after being heated to (d) 400°C.

$$\alpha\text{-}MnO_2 \cdot 0.3H_2O \rightarrow \alpha\text{-}MnO_2 + 0.3\ H_2O \quad (5.1)$$

$$2\ \alpha\text{-}MnO_2 \rightarrow Mn_2O_3 + \tfrac{1}{2}\ O_2 \quad (5.2)$$

The overall reaction is:

$$2\ \alpha\text{-}MnO_2 \cdot 0.3H_2O \rightarrow Mn_2O_3 + 0.6\ H_2O + \tfrac{1}{2}\ O_2 \quad (5.3)$$

Reaction 5.1 accounts for a weight loss of 5.85 %, and reaction 5.2 for a loss of 9.20 %. The overall weight loss of 15.05 % to 600°C correlates reasonably well with the 13.5 % determined experimentally by the TGA plot in Fig. 5.8.

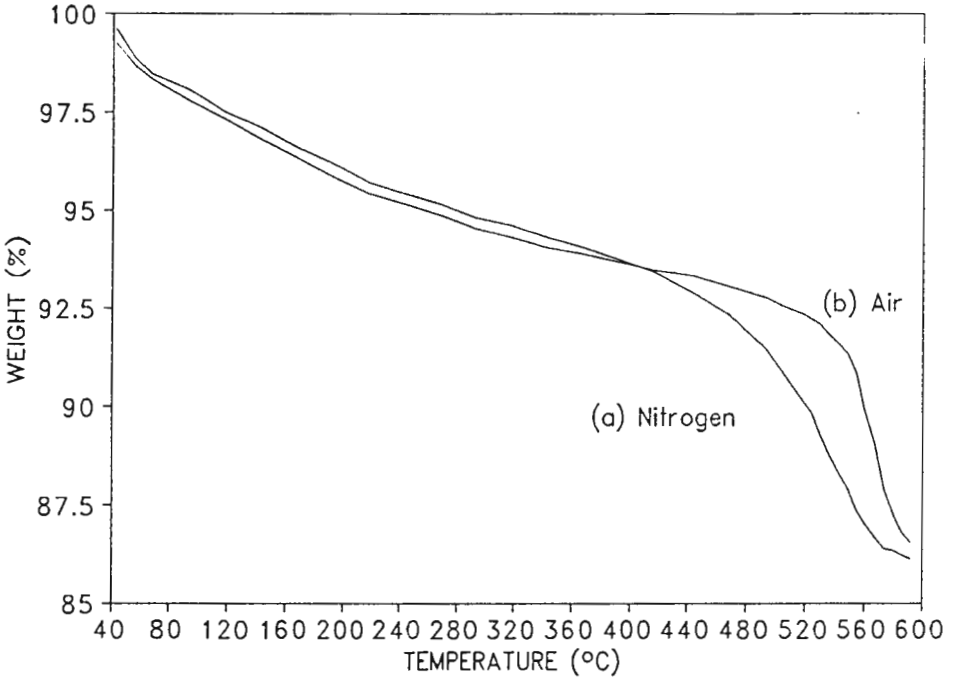

Fig. 5.8 Thermogravimetric analytical plots of $\alpha\text{-}MnO_2 \cdot 0.3H_2O$ undertaken in (a) a nitrogen stream and (b) an air stream. (Heat rate = 20°C/min).

The differential scanning calorimetric (DSC) plot of $\alpha\text{-}MnO_2 \cdot 0.3H_2O$ is shown in Fig. 5.9. It shows two processes. The first process, which occurs between 50°C and 70°C, consists

of an endothermic peak followed by an exothermic peak; this process is related to the loss of water. The onset of the second process occurs at approximately 350°C and reaches a maximum at 573°C. This exothermic process involves the slow decomposition of α-MnO_2 to Mn_2O_3, with the release of oxygen, in accordance with reaction 5.2.

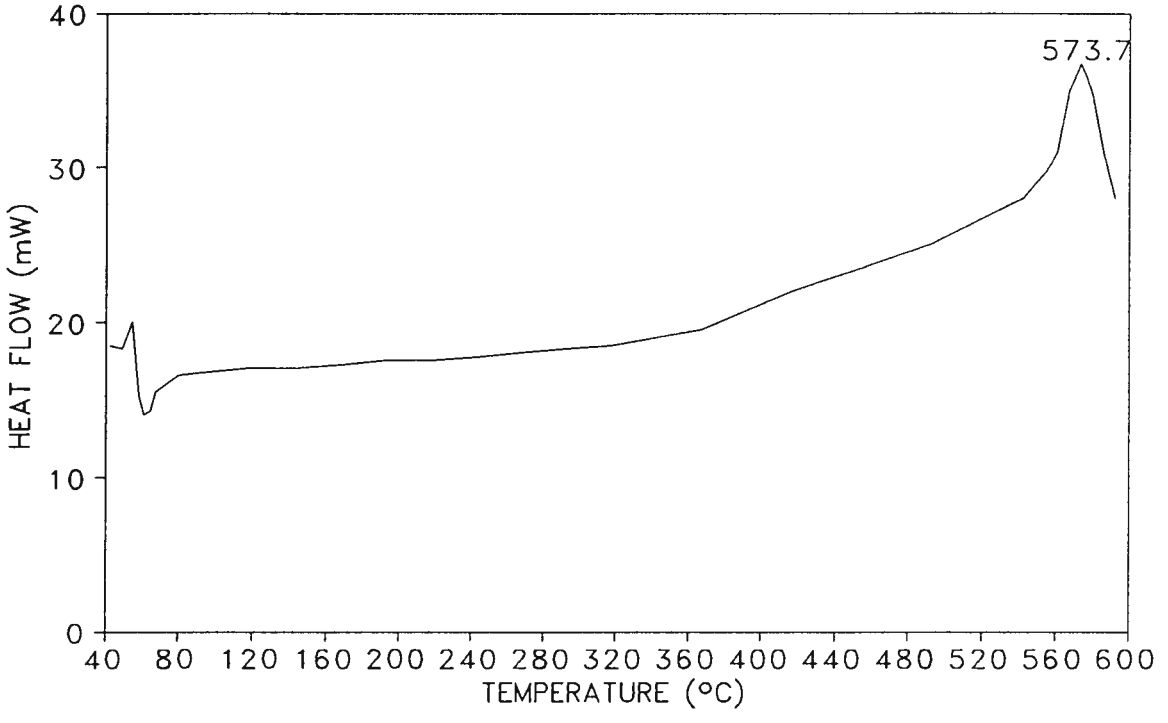

Fig. 5.9 Differential scanning calorimetric plot of α-$MnO_2 \cdot 0.3H_2O$. (Heat rate = 20°C/min).

5.3.3 Electrochemical Evaluation of α-MnO_2

(a) Galvanostatic Discharge

Capacities in excess of 200 mAh/g can be achieved from α-MnO_2 electrodes when discharged in room temperature lithium cells to a cut-off voltage of 2 V. Fig. 5.10 (a-e) shows typical discharge curves for lithium cells containing (a) α-MnO_2, 211 mAh/g, (b) α-MnO_2 with a trace of γ-MnO_2, 192 mAh/g, (c) α-MnO_2 with a trace of layered-MnO_2, 192 mAh/g, (d) an α-MnO_2 material heat-treated to 250°C, 227 mAh/g, and (e) α-

$MnO_2(K^+)$, 214 mAh/g, respectively. The sloping discharge curve indicates a single phase reaction process. No difference in the shape of the curves of the dehydrated compound compared to the hydrated materials could be observed. Although dehydration of the α-MnO_2 materials at 250°C improved the electrode capacity, no further improvement was achieved by dehydration at 300°C; at 400°C a decrease in capacity was observed. The data also show that α-MnO_2 electrodes perform slightly better than α-MnO_2 products that contained either a layered-MnO_2 or a γ-MnO_2 impurity phase.

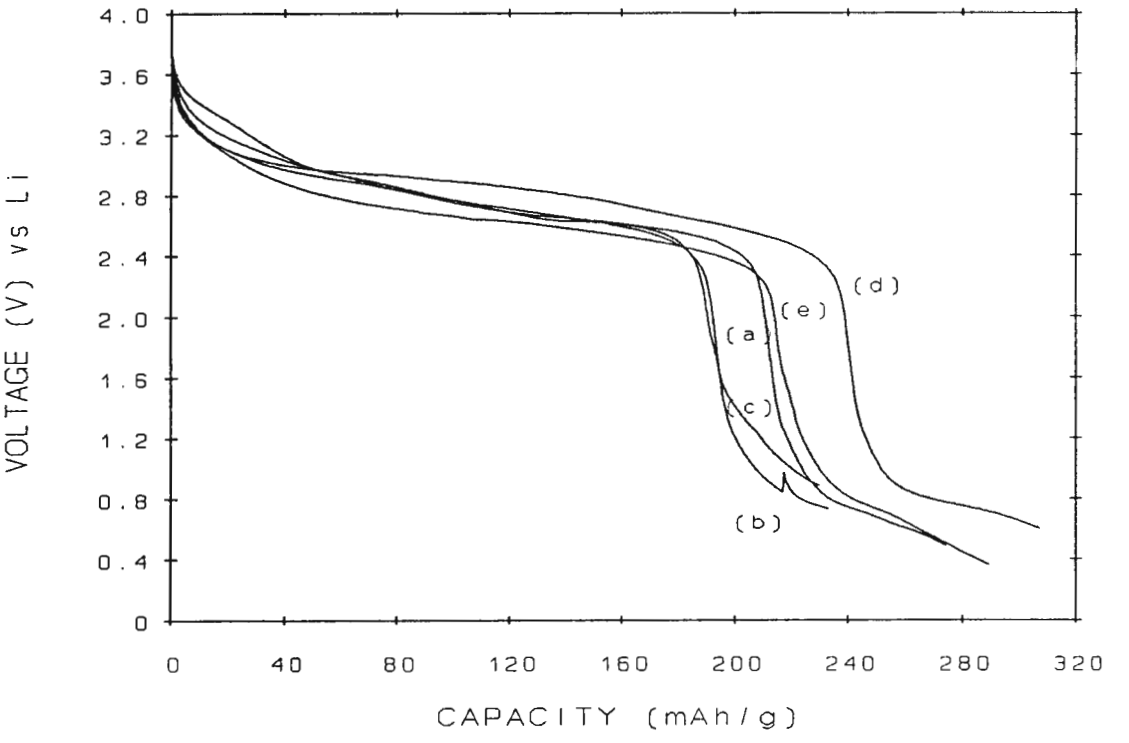

Fig. 5.10 Discharge curves of α-MnO_2, (a) a pure phase, (b) with a γ-MnO_2 phase, (c) with a layered-MnO_2 phase, (d) dehydrated at 250°C, and (e) α-$MnO_2(K^+)$, in lithium cells.

(b) Rechargeability

The rechargeability of the α-MnO_2 electrodes was evaluated by cyclic voltammetry. The cyclic voltammogram of an α-$MnO_2 \cdot 0.3H_2O$ product, when cycled between 1.1 V and 4.6V, demonstrates that lithium is inserted into the structure in a two-step process during discharge and that this process is reversible (Fig. 5.11a). The second cycle shows a large

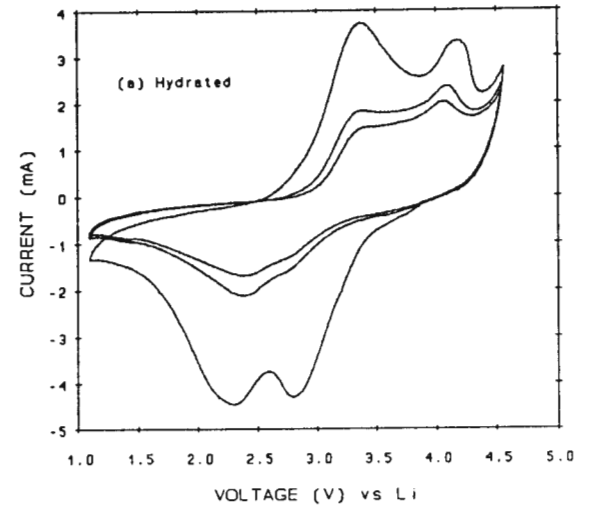

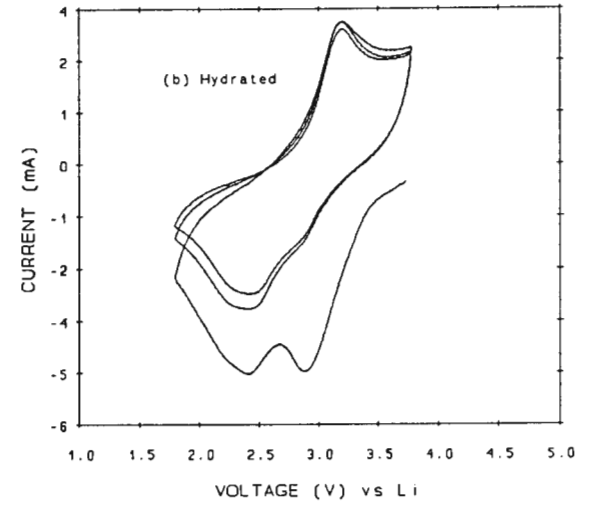

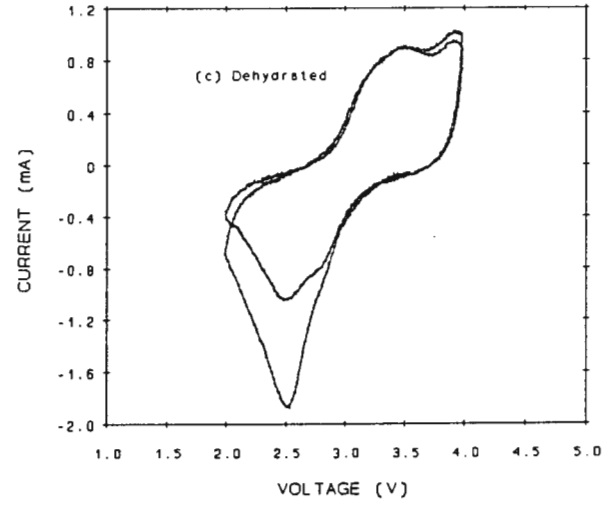

Fig. 5.11 Cyclic voltammograms of (a) and (b) hydrated α-$MnO_2 \cdot 0.3H_2O$ and (c) dehydrated α-MnO_2.

decrease in the current output, which indicates that capacity is lost on cycling the electrode. However, a significant improvement in the rechargeability can be obtained if the cells are cycled between 2.0 V and 4.0 V (Fig. 5.11b).

The two-step process on the initial cathodic sweep of a dehydrated (300°C) α-MnO_2 electrode (Fig. 5.11c) is not as strong nor as well resolved as it is in Fig. 5.11 a or b for the hydrated α-$MnO_2 \cdot 0.3H_2O$ electrodes. The two-step process is attributed to lithium insertion into two crystallographically non-equivalent sites in the [2x2] channels of the α-MnO_2 structure. Further work is required to test this hypothesis. However, it is believed that the first reduction process may be attributed to a lithium insertion reaction in which most of the lithium becomes "trapped" in the structure. These lithium ions seem to stabilize the structure on further cycling, as is apparent particularly in Fig. 5.11b.

Fig. 5.12 a and b show typical cycling behaviour of a hydrated α-$MnO_2 \cdot 0.3H_2O$ electrode and a dehydrated α-MnO_2 electrode, respectively. In general, an initial discharge capacity of more than 200 mAh/g can be obtained; this is followed by a sharp drop in capacity output which stabilizes at approximately 100 mAh/g in the case of the dehydrated α-MnO_2 electrode and at about 80 mAh/g in the case of α-$MnO_2 \cdot 0.3H_2O$, after 10 cycles.

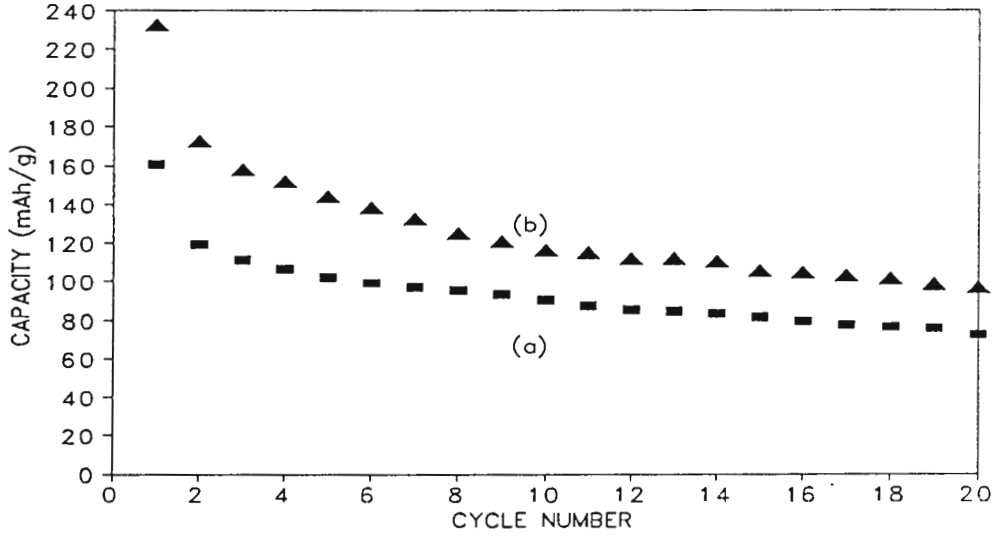

Fig. 5.12 Cycling behaviour of (a) α-$MnO_2 \cdot 0.3H_2O$, and (b) α-MnO_2 in lithium cells.

5.3.4 Lithiation of α-MnO_2

The powder X-ray diffraction patterns of α-$MnO_2 \cdot 0.3H_2O$ and two lithiated α-MnO_2 products are shown in Fig. 5.13 (a-c). Chemical lithiation of α-$MnO_2 \cdot 0.3H_2O$ with *n*-butyllithium at 40°C appears to damage the α-MnO_2 framework as is evident by the collapse and broadening of the individual peaks in the X-ray diffraction pattern (Fig. 5.13b). However, after 50 cycles in an electrochemical cell, it is evident from Fig. 5.13c that during "soft" electrochemical insertion and extraction of lithium at room

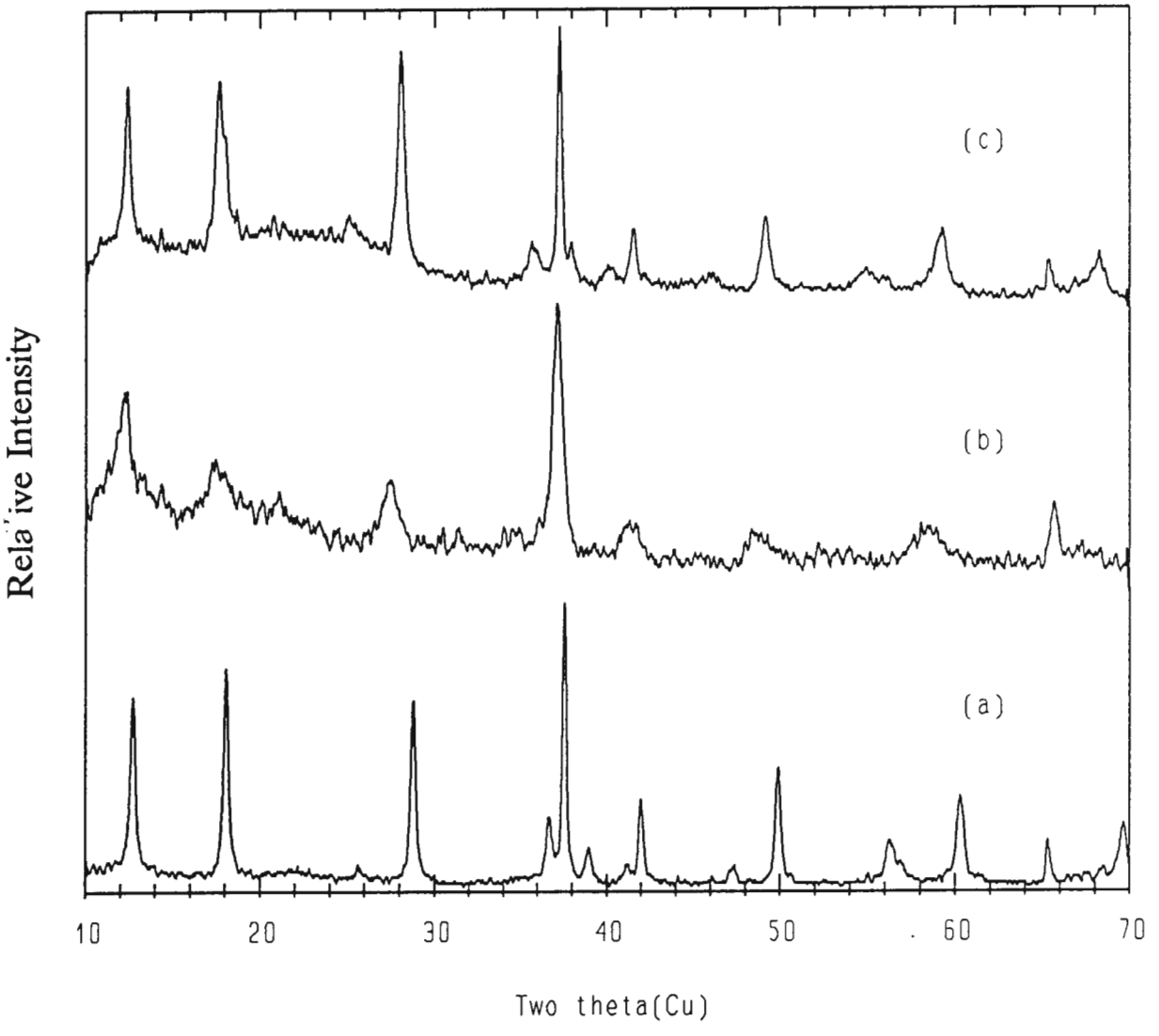

Fig. 5.13 Powder X-ray diffraction patterns of (a) α-$MnO_2 \cdot 0.3H_2O$ lithiated (b) chemically, and (c) electrochemically.

temperature, the crystallinity of the α-MnO_2 structure remains very much intact.

Electrochemical lithiation of α-MnO_2 to an approximate composition of $LiMnO_2$ increases the lattice parameters from a = 9.78 Å and c = 2.85 Å to a = 10.03 Å and c = 2.85 Å, which reflects a volume increase of 5.39 % of the unit cell (Table 5.3). The volume increase is attributed more to the increased concentration of Mn^{3+} ions rather than to the physical insertion of Li^+ ions into the α-MnO_2 framework structure.

5.3.5 Structural Characterization

The neutron diffraction profiles of a hydrated and a dehydrated α-MnO_2 phase, from which their structures were determined, are shown in Fig. 5.14 a and b, respectively. The crystallographic parameters of these compounds are listed in Table 5.2. The negative B_{33} (and B_{12}) values were the "best" fit that could be obtained with the data collected.

(a) Hydrated α-MnO_2

In the refined structure of hydrated α-MnO_2, the site occupancy of the octahedrally-coordinated manganese cations was determined to be 0.91. This refinement therefore shows that if the manganese ions are tetravalent, 0.36 H^+ ions are required to compensate for the imbalance in charge. In the resulting stoichiometry, $H_{0.36}Mn_{0.91}O_2$ or $MnO_2 \cdot 0.2H_2O$, the $[H^+]$ concentration is 0.40 wt% in contrast to the 0.65 wt% in the chemically determined composition $MnO_2 \cdot 0.3H_2O$. The difference in $[H^+]$ content (0.1 H_2O) was attributed to additional water associated either with the surface or the grain boundaries of the particles, or to occluded water within the [2x2] channels of the structure.

A Fourier map based on calculated structure factors (F_{calc}) in Fig. 5.15a, which shows a projection of the unit cell as viewed down the c-axis, clearly indicates the positions of the manganese and the oxygen atoms in the structure. Attempts to locate the H^+ (or Li^+) ions within the structure were unsuccessful.

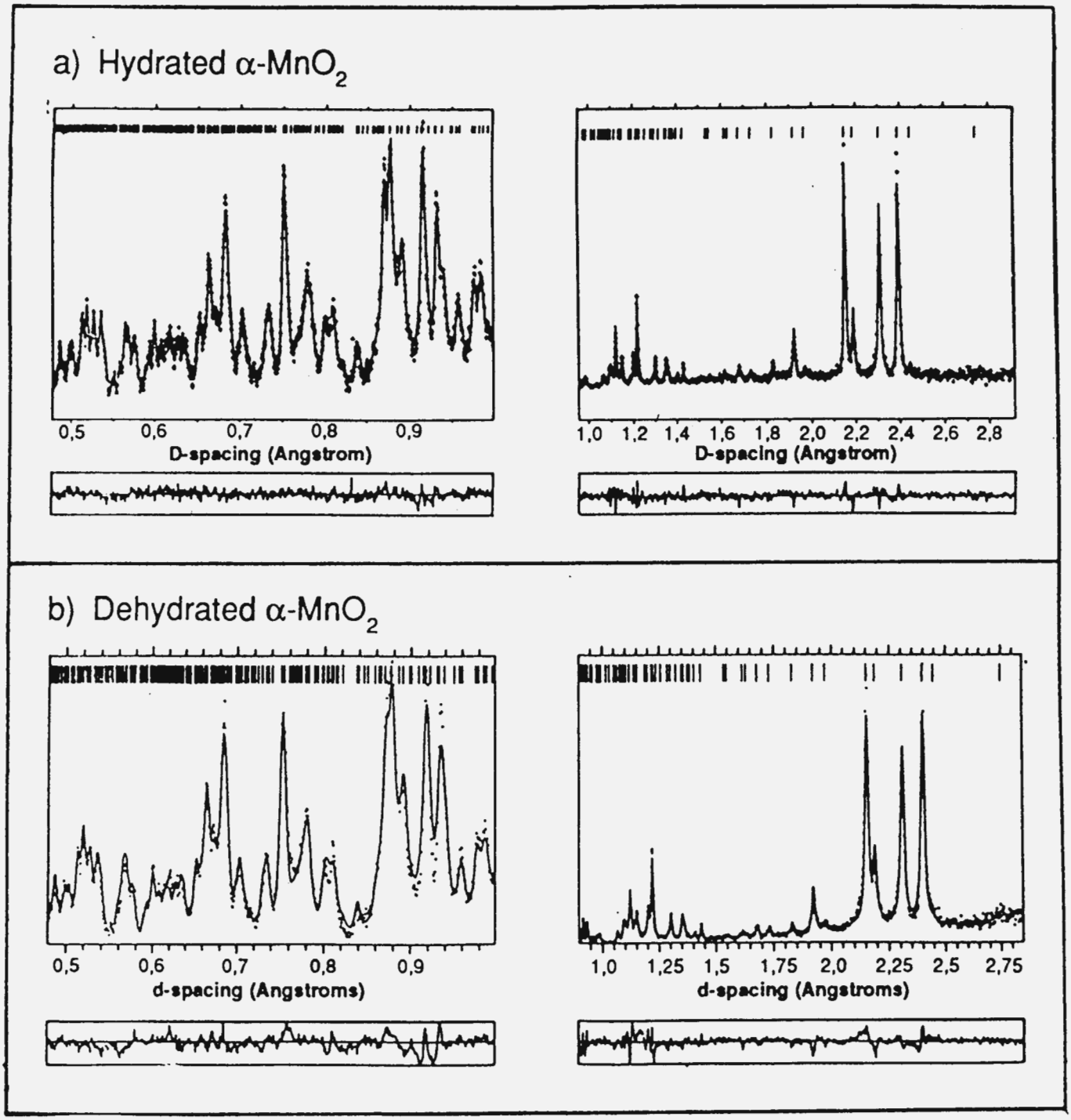

Fig. 5.14 Neutron diffraction patterns of (a) hydrated α-MnO_2, and (b) dehydrated α-MnO_2. The difference between the observed and the calculated patterns is given below each profile.

Table 5.2

Crystallographic parameters of (a) Hydrated α-MnO_2 and (b) Dehydrated α-MnO_2 as Determined from Neutron Diffraction Data

(a) Hydrated α-MnO_2

Space Group : I4/m $a = b = 9.7826(2)$ Å, $c = 2.8573(1)$ Å

Atom	x	y	z	n	B_{11}	B_{22}	B_{33}	B_{12}
Mn	.3471(4)	.1655(4)	0	0.91(1)	.6(1)	.3(1)	- .3(1)	- .2(1)
O(1)	.1542(3)	.2026(2)	0	1.0	.9(1)	1.1(1)	.1(1)	.7(1)
O(2)	.5408(2)	.1642(4)	0	1.0	.7(1)	1.4(1)	.1(1)	- .3(1)

$R_p = 3.88$ %, $R_{wp} = 3.00$ %, $R_E = 1.92$ %

Chi-squared = 2.44 for 3625 observations and 35 basic variables (N - P + C = 3590)

(b) Dehydrated α-MnO_2

Space Group : I4/m $a = b = 9.7876(3)$ Å, $c = 2.8650(1)$ Å

Atom	x	y	z	n	B_{11}	B_{22}	B_{33}	B_{12}
Mn	.3477(6)	.1653(8)	0	0.98(3)	1.1(2)	.9(2)	- .4(1)	.7(2)
O(1)	.1551(6)	.2031(4)	0	1.0	1.2(2)	.9(1)	- .3(1)	1.2(1)
O(2)	.5412(4)	.1651(8)	0	1.0	0.5(1)	1.4(2)	0.0(1)	.2(1)

$R_p = 4.99$ %, $R_{wp} = 4.08$ %, $R_E = 1.83$ %

Chi-squared = 4.96 for 1812 observations and 34 basic variables (N - P + C = 1778)

NOTES:

1. $B_{13} = B_{23} = 0.0$ for all atoms. All B factors are in Å^2.

2. $$R_p = \frac{\Sigma | Y_{obs} - Y_{calc} |}{\Sigma Y_{obs}} \qquad R_{wp}^2 = \frac{\Sigma | Y_{obs} - Y_{calc} |^2}{\Sigma w | Y_{obs} |^2} \qquad R_E^2 = \frac{N - P + C}{\Sigma w | Y_{obs} |^2}$$

3. Y_{obs} = number of observations at time of flight, t_{obs}, w = weights and N - P + C = number of observations - number of variables + number of constraints.

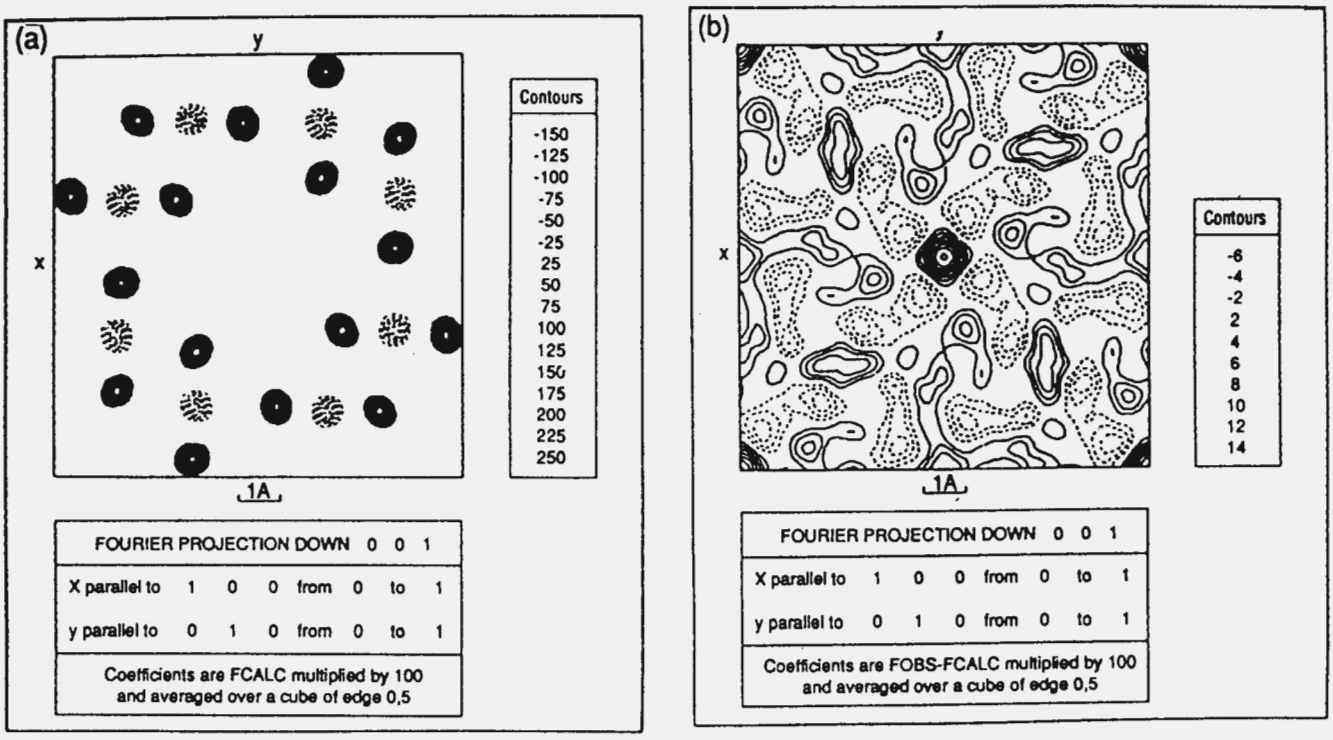

Fig. 5.15 (a) A Fourier map ([0 0 1] projection) of the hydrated α-MnO_2, showing the positions of the Mn atoms (dotted) and the O atoms (bold). (b) A difference Fourier map ([0 0 1] projection) of hydrated α-MnO_2, showing residual positive scattering at the centre of the [2x2] channels.

A difference Fourier map (Fig. 5.15b) could not detect any significant scattering from either H or Li atoms (both have negative scattering lengths, b(H) = -0.374×10^{-12} cm and b(Li) = -0.203×10^{-12} cm), at any particular site in the structure. However, the difference Fourier map did indicate a small amount of positive scattering at the crystallographic equivalent (0,0,0) and (½,½,½) sites at the centre of the [2x2] channels, which are normally occupied by large cations such as K^+, Na^+ and NH_4^+ in "stabilized" α-MnO_2 structures. This peak was attributed to a very minor concentration of oxygen (b(O) = 0.5805×10^{-12} cm) associated with some of the water molecules or hydronium ions. The site occupancy of the oxygen at these positions was calculated from the difference Fourier map to be approximately 0.06.

An illustration of the α-MnO_2 framework structure as determined from the neutron diffraction data is given in Fig. 5.16.

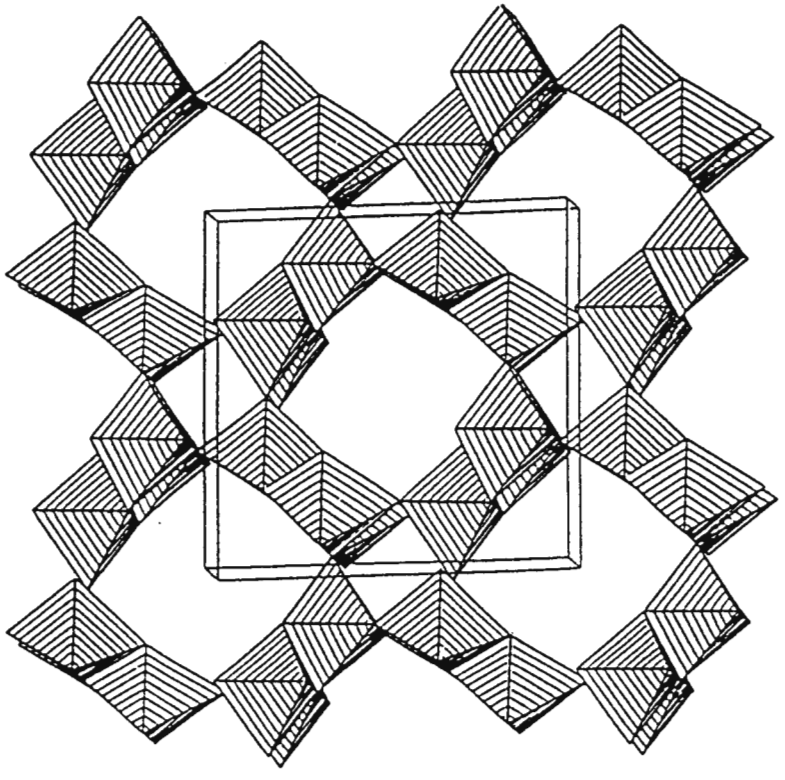

Fig. 5.16 The structure of α-MnO_2 as determined by neutron diffraction data.

(b) Dehydrated α-MnO_2

The structure analysis of the dehydrated α-MnO_2 showed that the Mn site occupancy increases on dehydration from 0.91(1) in the hydrated compound to 0.98(3), to yield, within experimental error, the ideal α-MnO_2 structure in which the [2x2] channels are empty. The *a* and *c* lattice parameters of α-MnO_2 increase marginally on dehydration and the unit cell expands by 0.4 % (Table 5.3). Table 5.3 also shows that the unit cell volumes of these α-MnO_2 structures (273 $Å^3$ - 274 $Å^3$) are slightly smaller than those hollandite-type structures that are not fully oxidized and contain relatively large cations such as K^+, Rb^+ and NH_4^+ in the [2x2] channels (275 $Å^3$ - 280 $Å^3$).

The crystallographic density of the dehydrated α-MnO_2 structure (4.21 g/cm^3) is significantly lower than those of the hexagonally-close-packed MnO_2 structures, ß-MnO_2 (5.12 g/cm^3) and dehydrated γ-MnO_2 (~5.19 g/cm^3), which have narrower unidimensional channels than α-MnO_2. The cubic-close-packed defect-spinel structure λ-MnO_2, which has a three-dimensional network of narrow [1x1] channels, has a crystallographic density of 4.46 g/cm^3.

Table 5.3
Unit Cell Parameters for α-MnO_2 and Some Derivatives
Space Group : I4/m

Compound	Radiation	Reference	*a* (Å)	*c* (Å)	Vol (Å^3)
α-$MnO_2 \cdot 0.3H_2O$	X-ray	a	9.7799	2.8534	272.9
α-$MnO_2 \cdot 0.3H_2O$	Neutron	a	9.7826	2.8573	273.4
MnO_2	X-ray	a	9.7851	2.8627	274.1
MnO_2	Neutron	a	9.7876	2.8650	274.5
$K_{1.3}Mn_8O_{16}$	X-ray	Ohzuku, 1991	9.831	2.848	275.3
$Rb_{1.3}Mn_8O_{16}$	X-ray	Ohzuku, 1991	9.882	2.858	279.1
$(NH_4)_{1.4}Mn_8O_{16}$	X-ray	Ohzuku, 1991	9.899	2.859	280.2
Li_xMnO_2 (Cycled electrode)	X-ray	a	10.0389	2.8539	287.6

a Thackeray, 1993a

Chapter 6

Ramsdellite-MnO_2

ABSTRACT: A highly crystalline ramsdellite-MnO_2 was synthesized by refluxing stable lithium-manganese-oxide compounds with spinel-type structures in acid solution. The synthesis and structural characterization of ramsdellite-MnO_2 and lithiated products are discussed. The application of ramsdellite-MnO_2 electrodes in lithium batteries is investigated.

6.1 Introduction

γ-MnO_2 materials, whether CMD or EMD, contain domains of intergrown ß-MnO_2 and ramsdellite-MnO_2; they are in general poorly crystalline. A high concentration of ß-MnO_2 in the structure impairs the performance of γ-MnO_2 electrodes because the narrow [1x1] channels in the rutile-type structure can accommodate only 0.2 Li^+ ions per formula unit (Thackeray, 1989). It would therefore seem advantageous to prepare an anhydrous γ-MnO_2 electrode with a very high concentration of ramsdellite domains in the structure, because the [2x1] channels in ramsdellite-MnO_2 can accommodate significantly more lithium than ß-MO_2.

It is well-known that at room temperature lithium can be extracted from $LiMn_2O_4$ by acid leaching and that an anhydrous, highly crystalline λ-MnO_2 phase which retains the Mn_2O_4 framework is obtained (Hunter, 1981a, 1981b and 1985; Goodenough, 1984). Thackeray (1988) found that by raising the reaction temperature to 30°C, using a 1M H_2SO_4 solution, a second additional phase, identified as γ-MnO_2, could be detected in the powder X-ray diffraction pattern. With the reaction temperature raised to 40°C and the

reaction time extended, a single phase γ-MnO_2 product was obtained; this product was significantly more crystalline than typical EMD products and contained only about one-quarter of the water content of EMD. In this study it was also found that a more rapid conversion from $LiMn_2O_4$ to γ-MnO_2 can be achieved by raising the reaction temperature above 40°C, these products contained a higher water content. Materials with a relatively high water content were generally less crystalline than those with a low water content. A crystalline γ-MnO_2 with predominant ramsdellite character, obtained electrolytically, has been reported by Yoshio (1991).

This chapter reports on the chemical, as opposed to the electrolytic, synthesis, structural characterization and electrochemical evaluation of a crystalline ramsdellite-type MnO_2. The ramsdellite-MnO_2 is denoted R-MnO_2 for convenience.

6.2 Experimental

6.2.1 Synthesis of Spinel Precursors

R-MnO_2 products were synthesized from various spinel precursors.

A $LiMn_2O_4$ precursor was synthesized by reacting stoichiometric quantities of $MnCO_3$ or γ-MnO_2 (EMD) with either Li_2CO_3 or $LiOH \cdot H_2O$ at 800°C to 850 °C for 24 hours. A blueish black powder was obtained. A λ-MnO_2 precursor was prepared by acid-treating $LiMn_2O_4$ with 2.25M H_2SO_4 at room temperature for 1 day, before it was washed with distilled water and dried at 100°C.

$Li_4Mn_5O_{12}$ and $Li_2Mn_4O_9$ precursors, which are spinels in the system $Li_2O \cdot yMnO_2$ ($2.5 \leq y \leq 4.0$), with $y = 2.5$ and $y = 4.0$, respectively, were synthesized by ball-milling a stoichiometric quantity of $MnCO_3$ and Li_2CO_3 in hexane for 2 days. The powders were air-dried, sieved and thereafter slowly heated to 400°C and reacted at this temperature for 24 hours.

6.2.2 Synthesis of R-MnO_2 Products

R-MnO_2 products were prepared by reacting *m* g precursor material ($LiMn_2O_4$, λ-MnO_2, $Li_4Mn_5O_{12}$ or $Li_2Mn_4O_9$) with 10*m* ml H_2SO_4. Reaction temperatures were varied between 25°C (room temperature) and 100°C (reflux conditions); reaction times from 24 hours to 1 week. The products were dried overnight at 100°C. Selected samples were dehydrated further at 250°C or 300°C. The effects of varying the molarity of the H_2SO_4 solution with respect to the nature of the final product were also investigated. Reactions of $LiMn_2O_4$ with 5M HCl and 5M HNO_3 were also investigated.

6.2.3 Synthesis of Chemically Lithiated R-MnO_2 Products

Chemical lithiation of R-MnO_2 was achieved by reacting R-MnO_2 either with *n*-butyllithium in hexane or with lithium iodide in acetonitrile as described in § 4.2.3.

6.2.4 Chemical Analyses of the Reaction Products

Lithium and manganese concentrations in R-MnO_2 and Li_xMnO_2 products were determined by atomic absorption spectroscopy as described in § 4.2.4.

The determination of the hydrogen concentration and the thermal analyses (TGA and DSC) were discussed in § 4.2.4.

Differential thermal analytic (DTA) experiments were undertaken at the Division of Energy Technology (Enertek) at CSIR on a Du Pont Instruments 1090 Thermal Analyser. The experiments were carried out in air. The heating rate was 20°C/min.

6.2.5 Diffraction Patterns of the Reaction Products

Powder X-ray and neutron diffraction patterns were obtained at CSIR and at the Rutherford Appleton Laboratory (RAL) as discussed previously in § 4.2.5.

6.2.6 Electrochemical Evaluation of the Reaction Products

Electrochemical experiments were carried out as described in § 3.3 and § 4.2.6. The conditions under which the experiments were undertaken, for example charge/discharge current rates, scan rates, voltage limits, etc. are provided with the electrochemical data in Section 6.3.4. Open-circuit voltage readings were recorded at regular intervals allowing a 72 h equilibration time at each point.

6.3 Results and Discussion

6.3.1 Synthesis of the Reaction Products

Most of the R-MnO_2 products described in this chapter were derived from $LiMn_2O_4$. In general, however, it can be stated that no significant quantity of lithium could be detected by analytical techniques in the crystalline R-MnO_2 phases. Typical manganese concentrations were approximately 62 wt%, compared to 63.2 wt% in stoichiometric MnO_2. Hydrogen concentrations as low as 0.16 wt% were obtained.

Fig. 6.1a shows the powder X-ray diffraction pattern of the $LiMn_2O_4$ spinel precursor and Fig. 6.1b the X-ray diffraction pattern of the highly crystalline R-MnO_2 product. The X-ray diffraction pattern of a typical γ-MnO_2 (electrolytic manganese dioxide, EMD, for example) is shown in Fig. 6.1c for comparison.

Certain similarities can be observed in the powder X-ray diffraction patterns of R-MnO_2 (Fig. 6.1b) and EMD (Fig. 6.1c). Peaks at 22.5°, 37.5° and 43°2θ are common to both materials, although the EMD peaks are broader. The two peaks of R-MnO_2 in the 56 to 58°2θ-range, overlap as one broad peak in the EMD pattern, as do the two distinct peaks at 65.5° and 68.5°2θ. The improved resolution of the peaks in R-MnO_2 is indicative of a significantly more crystalline structure than that which characterizes EMD.

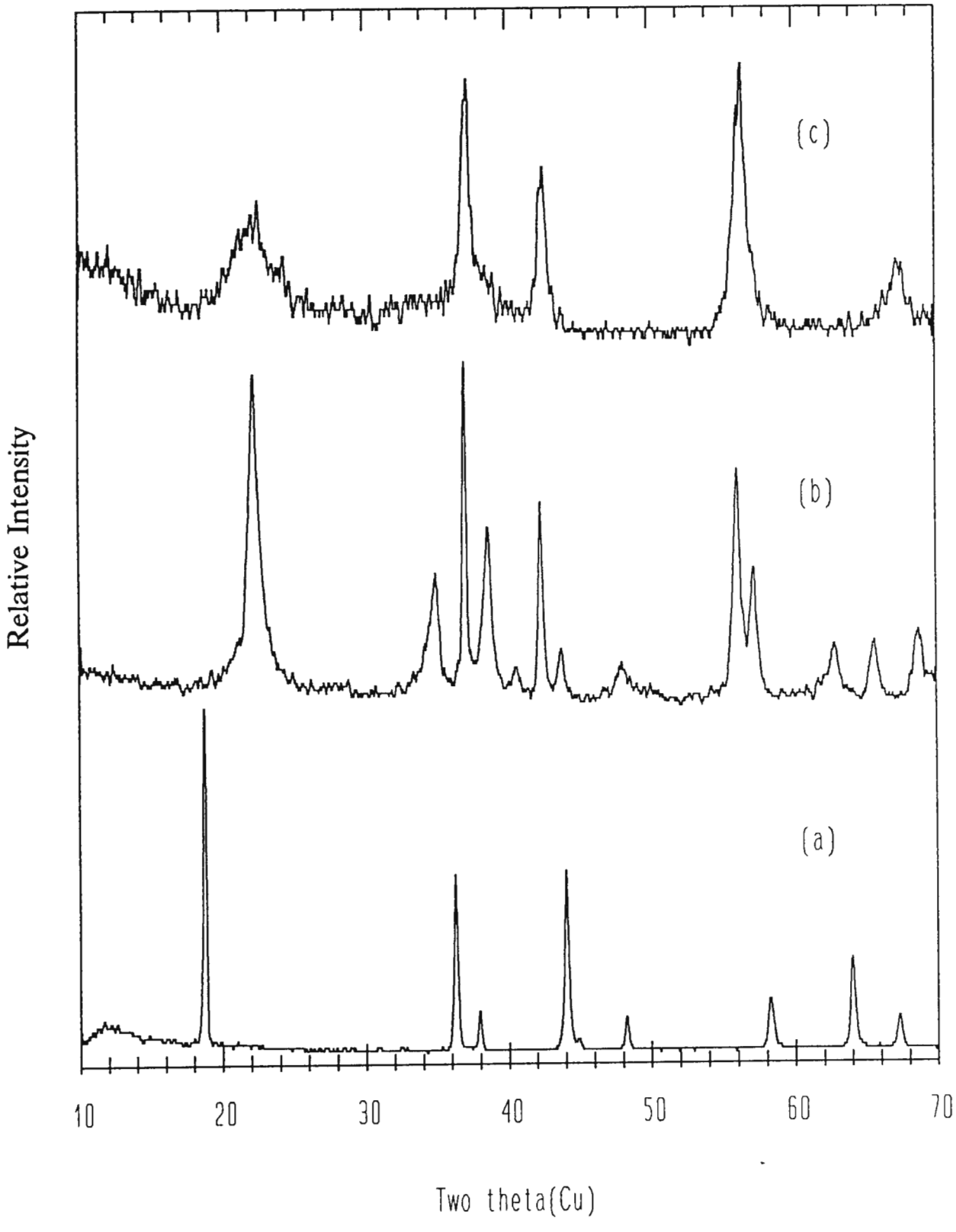

Fig. 6.1 Powder X-ray diffraction patterns of (a) $LiMn_2O_4$, (b) R-MnO_2, and (c) γ-MnO_2 (EMD).

The powder X-ray diffraction patterns in Figs. 6.2 - 6.4 show the effect of changing the reaction temperature, reaction time and the concentration of the H_2SO_4 when $LiMn_2O_4$ is used as precursor.

The powder X-ray diffraction patterns of the materials obtained when $LiMn_2O_4$ was reacted for 2 days with 2.25M H_2SO_4 as a function of reaction temperature are given in Fig. 6.2 (a-d).

At room temperature (25°C) the defect spinel λ-MnO_2 formed, while at the higher temperatures (66°C, 80°C and 100°C) a highly crystalline R-MnO_2 was produced. These R-MnO_2 products were significantly more crystalline than the γ-MnO_2 products obtained in the earlier study by Thackeray (1988).

The powder X-ray diffraction patterns of the products obtained when $LiMn_2O_4$ was refluxed at 100°C in 2.25M H_2SO_4 as a function of time is shown in Fig. 6.3 (a-d). After only 24 h a highly crystalline R-MnO_2 material formed (Fig. 6.3a). After 1 week a second phase, ß-MnO_2, as evident by the appearance of a peak at approximately 28°2θ, (Fig. 6.3d) was present.

The concentration of the H_2SO_4 also has an influence on the final product as can be seen from the powder X-ray diffraction patterns in Fig. 6.4 (a-c). Using a concentration of 0.5M H_2SO_4 a R-MnO_2 product with broad peaks was formed (Fig. 6.4a); these broad peaks can be attributed to strain within the individual crystallites, stacking fault disorder and micro-twinning. A concentration of 2.25M H_2SO_4 gave a significantly more crystalline R-MnO_2 product as can be seen in Fig. 6.4b. With a 4.5M H_2SO_4 solution a second phase was detected (Fig. 6.4c). This was identified as α-MnO_2, a hollandite-type material, as evident by the characteristic peaks at 12.5°2θ, 18°2θ, 29°2θ and 38°2θ (See Chapter 5).

The effect of using other acids was investigated by refluxing $LiMn_2O_4$ at 100°C in 5M HNO_3 and 5M HCl, respectively, for 48 hours. The product from the HNO_3 reaction gave a crystalline R-MnO_2 product, similar to those derived from the H_2SO_4 reactions. By contrast it was found that $LiMn_2O_4$ dissolved in the HCl solution, particularly at the

higher temperatures (80°C to 100°C).

The powder X-ray diffraction patterns of the products that were formed by the reaction of H_2SO_4 with spinels in the system $Li_2O \cdot yMnO_2$ ($y \geq 2.5$), i.e. $Li_4Mn_5O_{12}$ ($y = 2.5$), $Li_2Mn_4O_9$ ($y = 4.0$) and λ-MnO_2 ($y = \infty$) are shown in Fig. 6.5 (a-d).

Acid-treatment of the $Li_2O \cdot yMnO_2$ spinel phases at room temperature resulted in defect spinel phases with a higher MnO_2 content (e.g. Fig. 6.5a), while under reflux conditions, at approximately 95°C in 2.25M H_2SO_4, a R-MnO_2 phase was formed. With λ-MnO_2 and $Li_2Mn_4O_9$ a single phase R-MnO_2 product formed, as can be seen in Fig. 6.5 b and c, respectively, whereas with $Li_4Mn_5O_{12}$ a two-phase product consisting of R-MnO_2 and α-MnO_2 was synthesized (Fig. 6.5d). It is significant to note that $Li_4Mn_5O_{12}$ converts at high temperatures (≥600°C) into the rock salt phase Li_2MnO_3 and the stoichiometric spinel phase $LiMn_2O_4$, according to the reaction:

$$Li_4Mn_5O_{12} \rightarrow Li_2MnO_3 + 2\ LiMn_2O_4 + \tfrac{1}{2}\ O_2 \qquad (6.1)$$

and, as was shown in Chapter 5, that a crystalline α-MnO_2 forms when Li_2MnO_3 is refluxed in 2.25M H_2SO_4. The presence of the α-MnO_2 phase in the product derived from $Li_4Mn_5O_{12}$ is thus not totally unpredictable because it is possible that $Li_4Mn_5O_{12}$ may "decompose" into Li_2MnO_3 and $LiMn_2O_4$ when refluxed at 100°C in 2.25M H_2SO_4 for 2 days.

The fact that a highly crystalline single phase R-MnO_2 product can be obtained from numerous spinel precursors therefore strongly suggests that the $[Mn_2]O_4$ spinel framework plays a key role in the formation of the ramsdellite-MnO_2 structure. The observation that α-MnO_2 also forms as an additional phase when $LiMn_2O_4$ is refluxed in 4.5M H_2SO_4, is due to the oxidizing power of the acid causing $LiMn_2O_4$ to "decompose" into λ-MnO_2 and Mn_2O_3 instead of MnO.

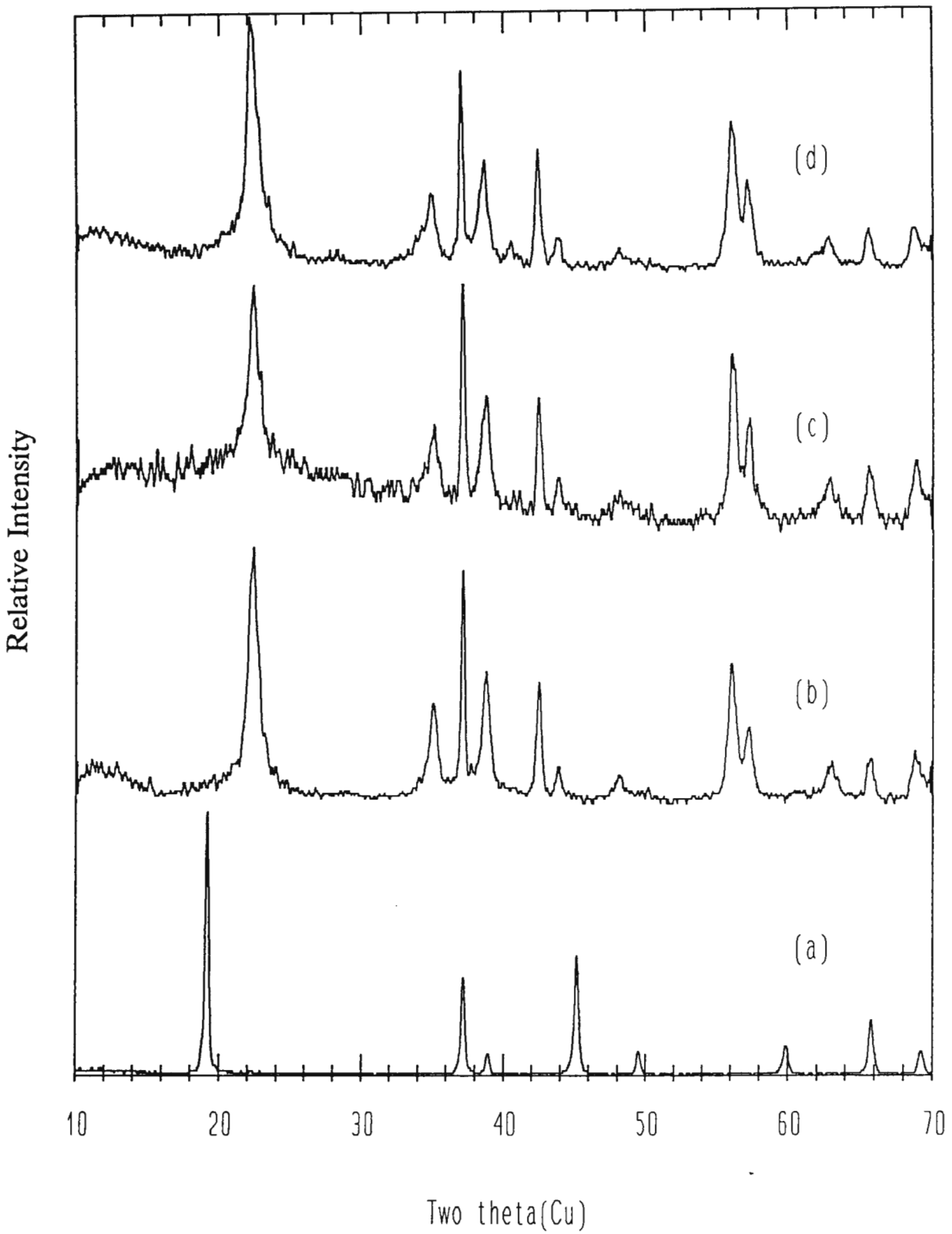

Fig. 6.2 Powder X-ray diffraction patterns of $LiMn_2O_4$ acid treated with 2.25M H_2SO_4 for 2 days at (a) 25°C, (b) 66°C, (c) 80°C, and (d) under reflux at 100°C.

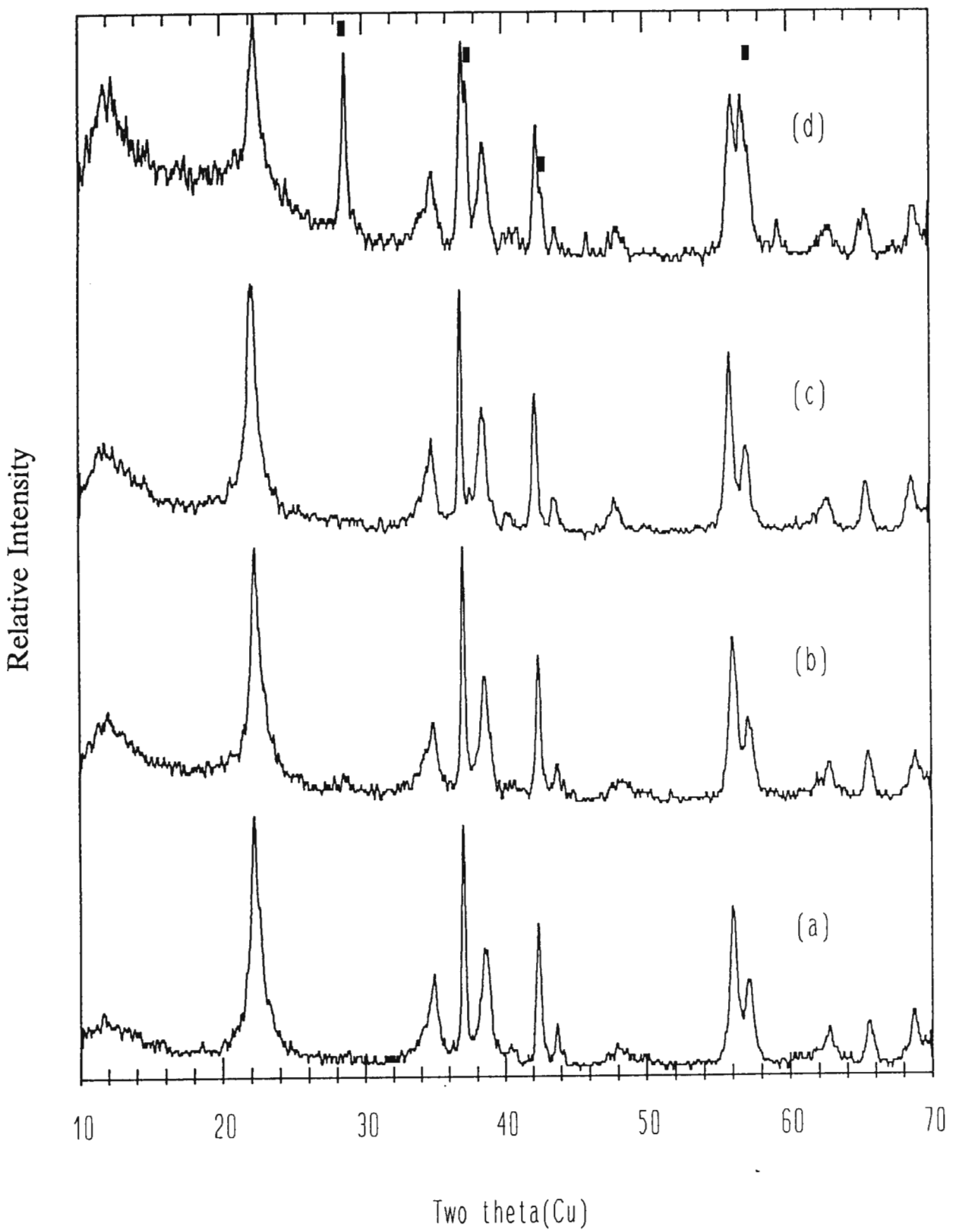

Fig. 6.3 Powder X-ray diffraction patterns of $LiMn_2O_4$ refluxed at 100°C in 2.25M H_2SO_4 for (a) 24 h, (b) 48 h, (c) 72 h, and (d) 1 week. (■ = ß-MnO_2).

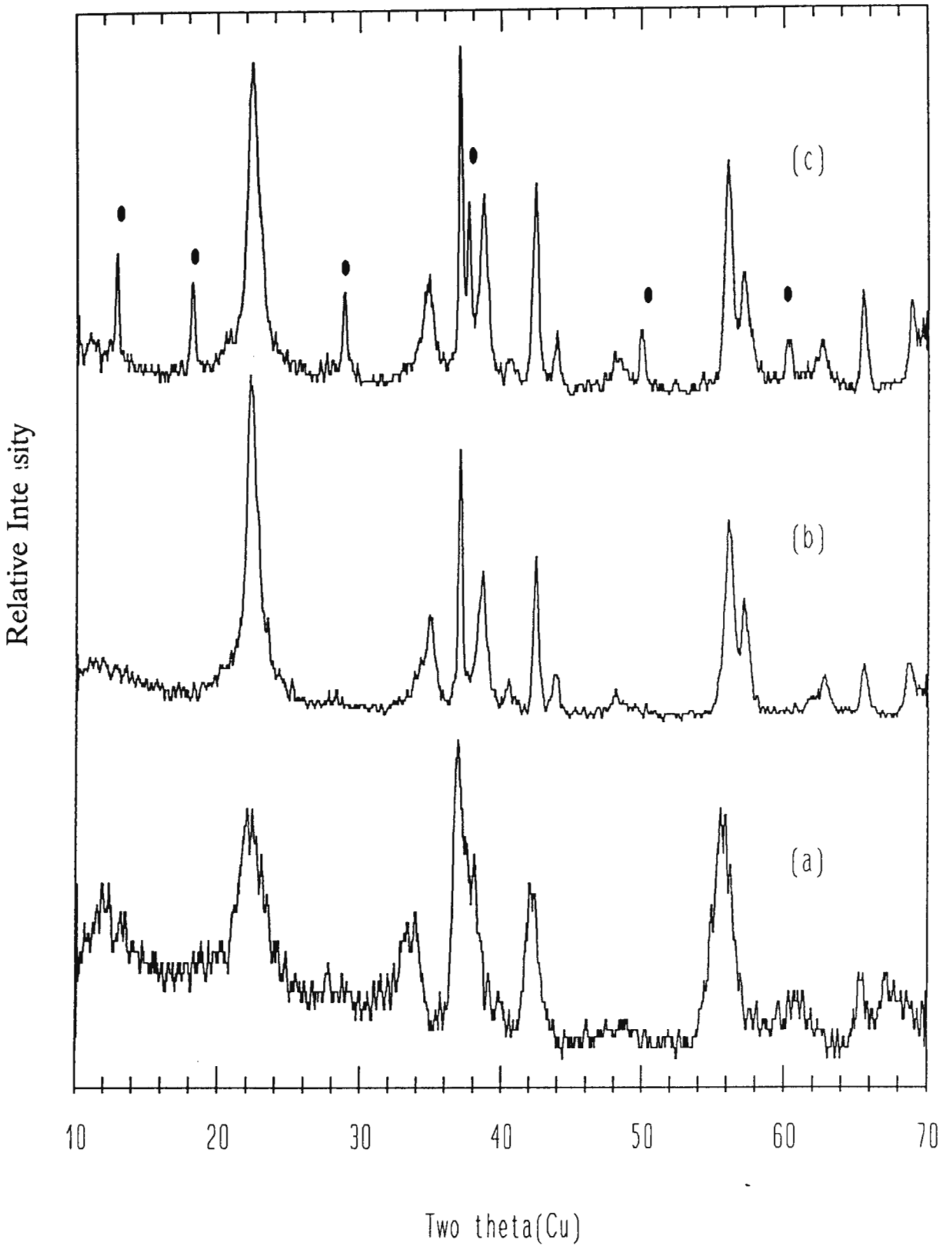

Fig. 6.4 Powder X-ray diffraction patterns of $LiMn_2O_4$ refluxed at 100°C for 48 h in (a) 0.5M, (b) 2.25M, and (c) 4.5M H_2SO_4. (• = α-MnO_2).

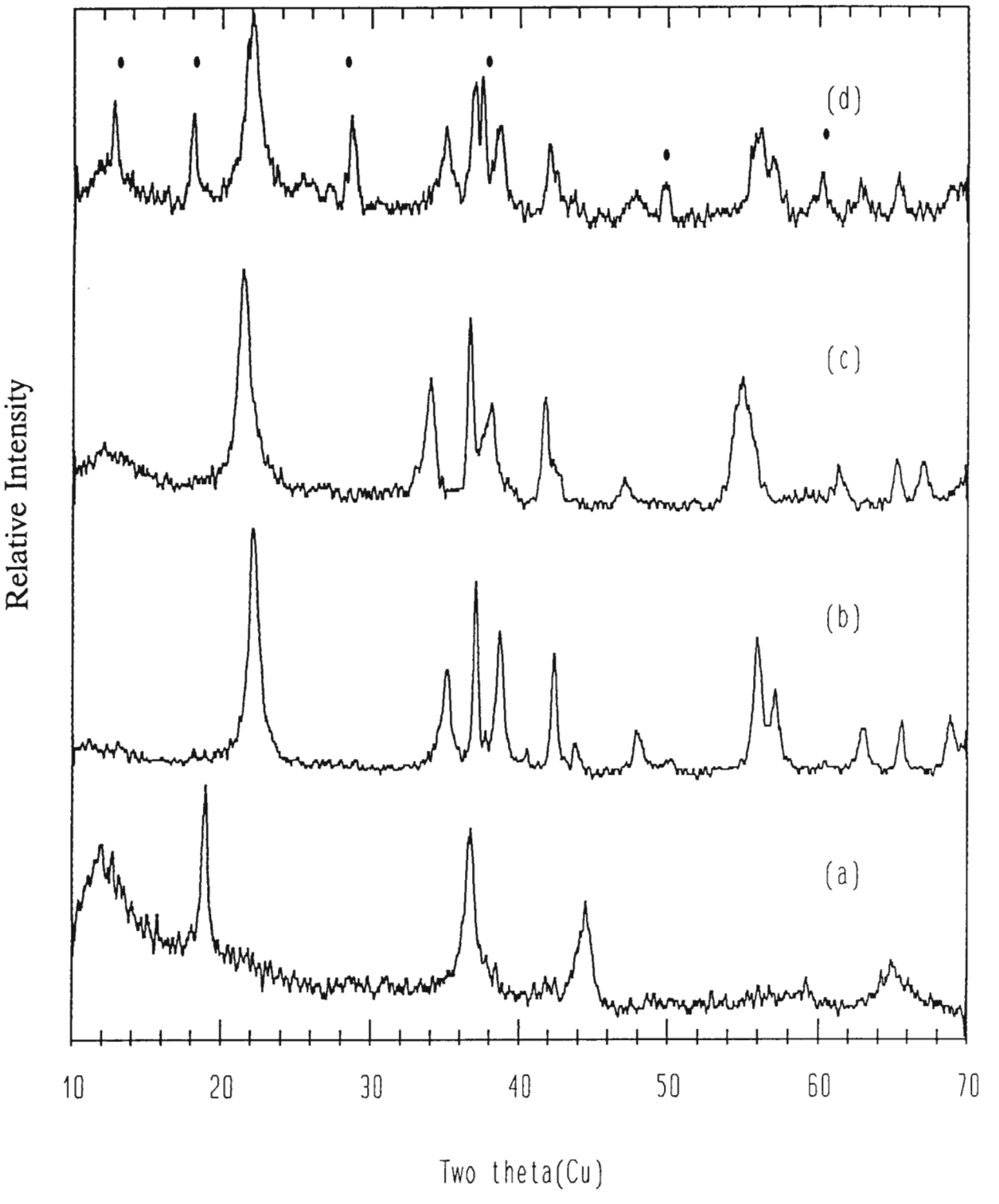

Fig. 6.5 Powder X-ray diffraction patterns of the products after (a) $Li_4Mn_5O_{12}$ was stirred in 2.25M H_2SO_4 at room temperature, (b) λ-MnO_2 refluxed at 100°C in 2.25M H_2SO_4, (c) $Li_2Mn_4O_9$ refluxed in 2.25M H_2SO_4, and (d) $Li_4Mn_5O_{12}$ refluxed in 2.25M H_2SO_4. (• = α-MnO_2).

6.3.2 Thermal Stability of R-MnO_2

The R-MnO_2 structure remains relatively intact when heat-treated to at least 250°C. Some products showed a strong retention of the R-MnO_2 framework even at 300°C, but for most products the onset of a ß-MnO_2 phase could be observed at 300°C. The powder X-ray diffraction patterns in Fig. 6.6 (a-h) show clearly the transformation of the R-MnO_2 structure (Fig. 6.6a) through a ß-MnO_2 phase to Mn_2O_3 (Fig. 6.6h) on heating from 200°C to 600°C.

At 200°C (Fig. 6.6b) R-MnO_2 is still very crystalline, but by heating it to 300°C (Fig. 6.6c) crystallinity was lost. At 350°C (Fig. 6.6d) the onset of ß-MnO_2 formation can be observed; at 400°C (Fig. 6.6e) R-MnO_2 has completely transformed into ß-MnO_2.

As the temperature was increased further, the ß-MnO_2 phase gained crystallinity as can be seen by the relative increase in intensity and sharpening of the peak at approximately 29°2θ. At 500°C (Fig. 6.6g), Mn_2O_3 starts to form as a secondary phase; at 600°C, only a single phase Mn_2O_3 product is present (Fig. 6.6h).

The thermogravimetric analytical (TGA) curves in Fig. 6.7 a and b, show the difference in the rate of decomposition when R-MnO_2 was heated under a nitrogen flow compared to under a flowing air stream, respectively. The sample heated under flowing nitrogen showed a slightly larger weight loss (11.8 %) to 650°C, than the sample heated under flowing air (11.1 %).

At approximately 250°C a change in the slope can be observed. Instead of only water being lost during the heating process, oxygen is also slowly lost. The conversion of the crystalline R-MnO_2 into ß-MnO_2 starts at about this point, as was shown in the powder X-ray diffraction patterns in Fig. 6.6.

Under an air flow (Fig. 6.7b), the weight loss took longer to reach completion with the onset of a sharp decrease at approximately 570°C. The sample heated under the flowing

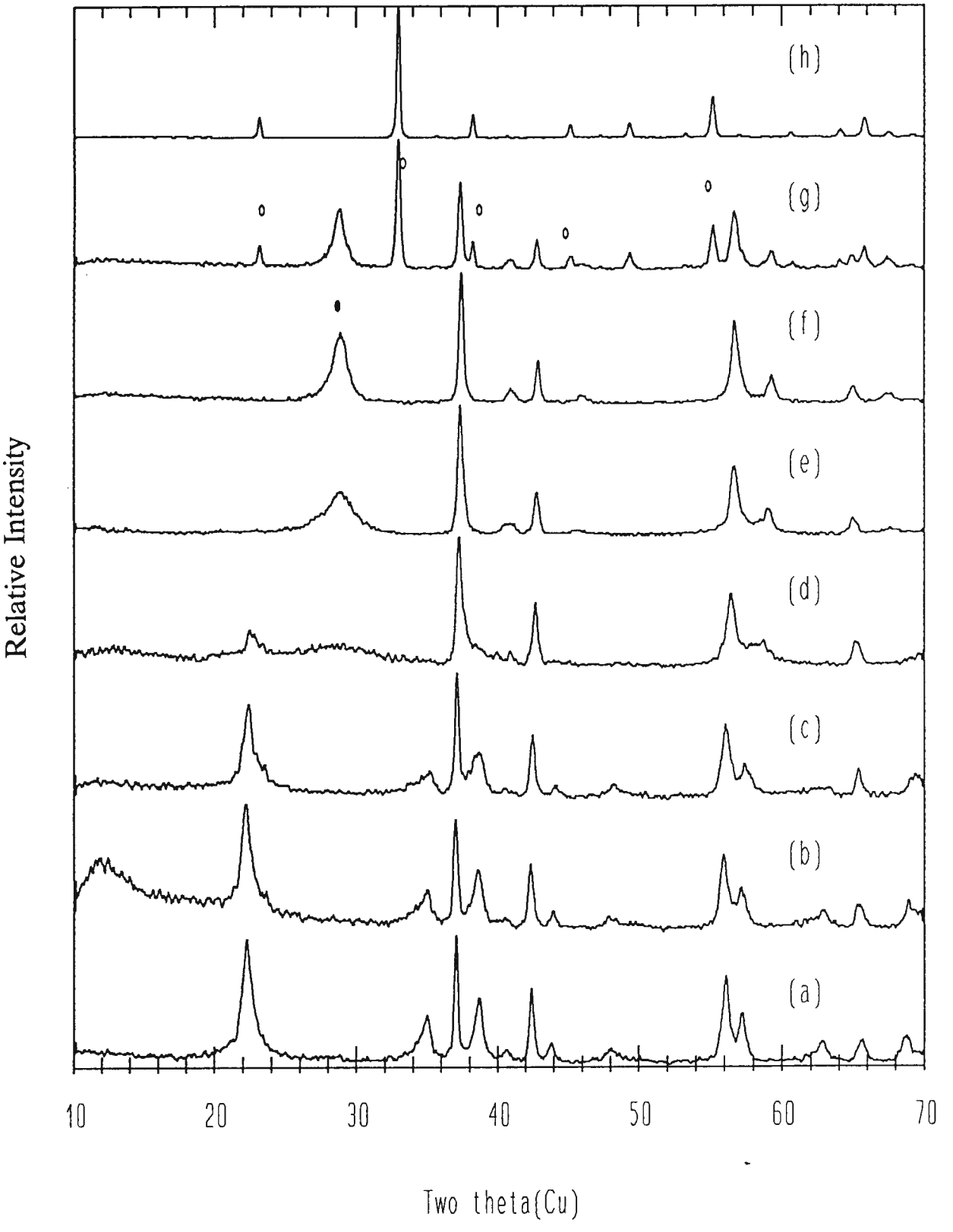

Fig. 6.6 Powder X-ray diffraction patterns of (a) R-MnO_2 heated to (b) 200°C, (c) 300°C, (d) 350°C, (e) 400°C, (f) 450°C, (g) 500°C, and (h) 600°C. (• = ß-MnO_2 and o = Mn_2O_3).

nitrogen stream lost weight more gradually but sooner; in this case the onset of a sharp decrease in mass occurred at approximately 510°C.

The complete reduction of MnO_2 into Mn_2O_3 would result in a theoretical weight change of 9.20 %. The additional weight loss of about 2 % is due to water associated with the initial R-MnO_2 product. Analytical techniques showed that R-MnO_2 contains about 0.17 wt% [H^+], which corresponds in good agreement with the weight loss due to a water content of 1.7 wt%.

The decomposition reactions at 250°C and 550°C can be written, respectively, as:

$$\text{R-}MnO_2 \rightarrow \text{ß-}MnO_2 \tag{6.2}$$

$$2\ \text{ß-}MnO_2 \rightarrow Mn_2O_3 + \tfrac{1}{2}\ O_2 \tag{6.3}$$

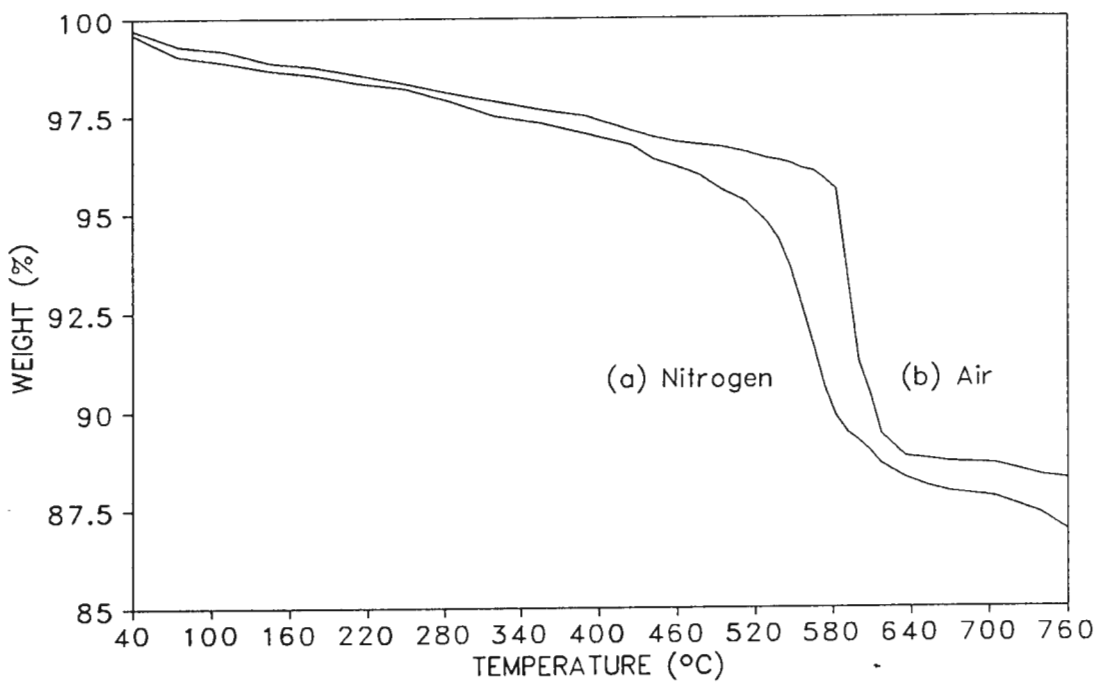

Fig. 6.7 Thermogravimetric analytical (TGA) curves of R-MnO_2 under a flowing (a) nitrogen stream and (b) air stream. (Heat rate = 20°C/min).

A differential scanning calorimetric (DSC) curve in Fig. 6.8 shows the two major transition processes in the decomposition of a typical R-MnO_2 sample. The R-MnO_2 to ß-MnO_2 phase transition is manifest by a small endothermic peak at approximately 410°C which is in good agreement with the DTA data in Fig. 6.9.

The onset of the MnO_2 to Mn_2O_3 transition (exothermic reaction) occurs at approximately 400°C, reaching a peak maximum at approximately 570°C. The reason for the additional peak at approximately 613°C is not understood.

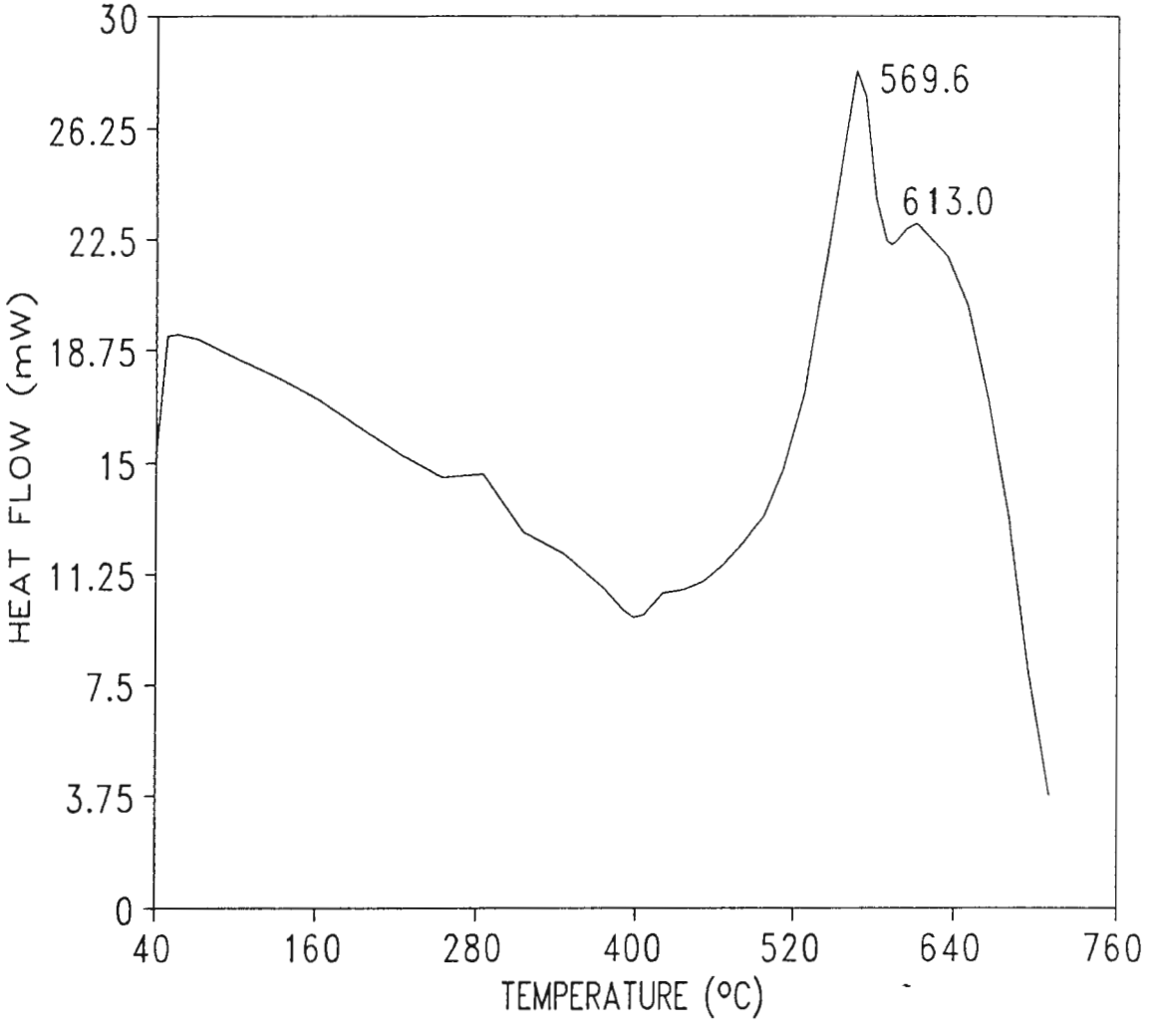

Fig. 6.8 A differential scanning calorimetric (DSC) curve of R-MnO_2 under a flowing nitrogen stream. (Heat rate = 20°/min).

The differential thermal analytic (DTA) curve of R-MnO_2 is compared with the curves of two commercial γ-MnO_2 samples (CMD and EMD), in Fig. 6.9 (a-c).

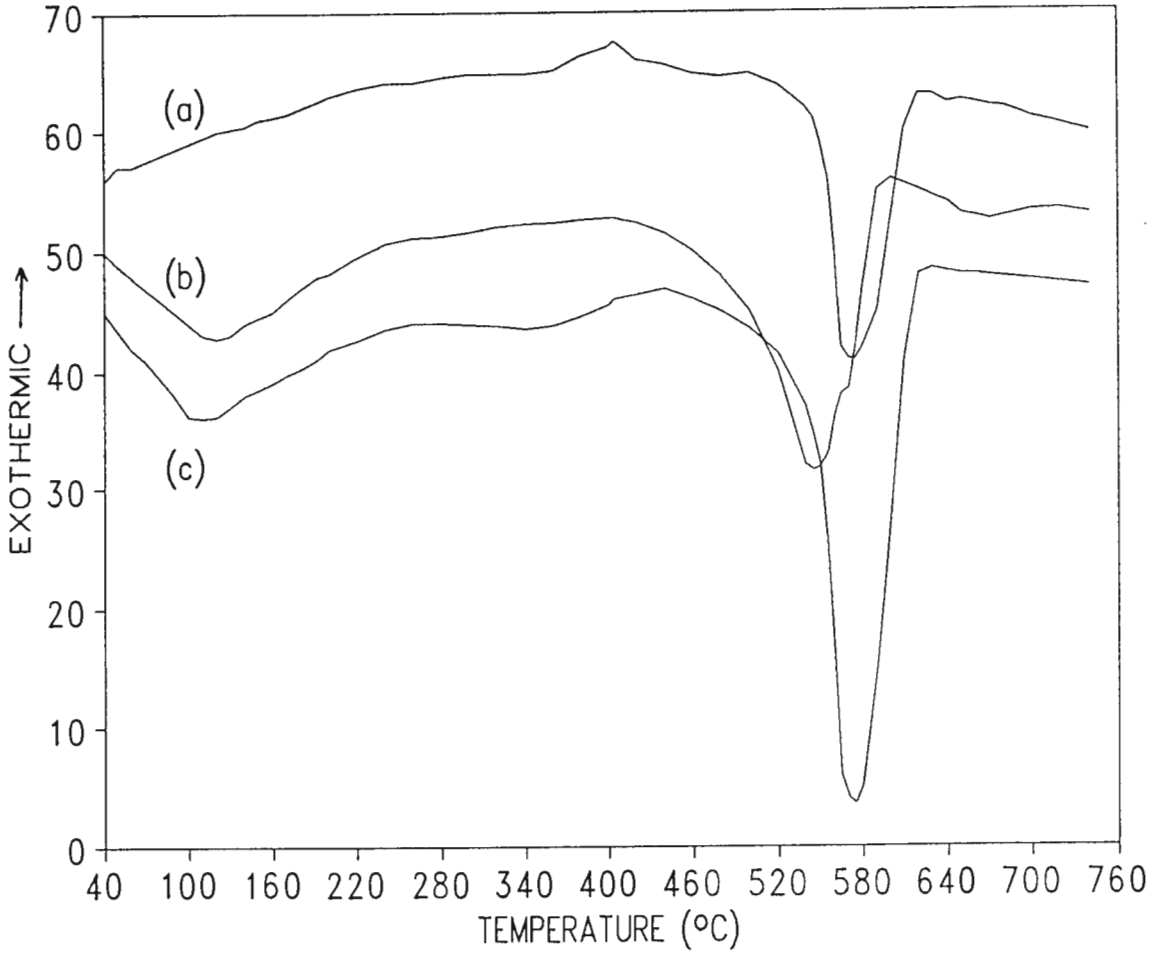

Fig. 6.9 Differential thermal analytical (DTA) curves of (a) R-MnO_2, (b) CMD, and (c) EMD in a static air medium. (Heat rate = 20°C/min).

CMD and EMD contain significantly more water than R-MnO_2 as can be seen by the major endothermic peaks at 110°C. R-MnO_2 contains typically 1.7 % H_2O, compared to CMD and EMD which typically contain 3.5 % and 3.0 % H_2O, respectively.

In CMD and EMD, the transition to the so-called γ/ß-MnO_2 phase appears in the temperature range 300°C to 400°C. This transition is evident in the powder X-ray

diffraction patterns of CMD and EMD, by the appearance of a more dominant ß-MnO_2 peak at 28.3°2θ. This transition is more noticeable in the DTA curve of EMD (Fig. 6.9c).

The R-MnO_2 to ß-MnO_2 transition occurs as an exothermic reaction at 405°C (Fig. 6.9c). This temperature of transition is in good agreement with the DSC data (Fig. 6.8) and is consistent with the powder X-ray diffraction data of R-MnO_2 which showed the development of ß-MnO_2 at 400°C. The DTA curves show also that the transition from CMD to Mn_2O_3 occurs at a significantly lower temperature than it does for EMD and R-MnO_2.

6.3.3 Structural Characterization

The powder X-ray diffraction patterns of R-MnO_2 and various chemically lithiated products Li_xMnO_2 ($0 < x < 1$) are shown in Fig. 6.10 (a-e).

(a) R-MnO_2

The symmetry of the mineral ramsdellite is orthorhombic (Pnam) with cell dimensions are a = 9.27 Å, b = 4.533 Å and c = 2.866 Å. Each manganese atom is surrounded by six oxygen atoms distributed at the corners of an octahedron with an average Mn-O distance of 1.89 Å. The oxygen octahedra are linked together by sharing edges to produce double strings of MnO_6 octahedra in the c direction (Fig. 2.1b) (Byström, 1949). The interstitial space of ramsdellite-MnO_2 consists of empty channels. The dimensions of the cross section of each channel is approximately [2x1]. The density of ramsdellite is calculated to be 4.8 g/cm^3, which is 0.4 g/cm^3 smaller than that of ß-MnO_2 (Ohzuku, 1988).

The structure of R-MnO_2 derived from $LiMn_2O_4$ was determined by profile refinement of both neutron data (Fig. 6.11) and X-ray data (Fig. 6.12). Two different samples were used for the refinements.

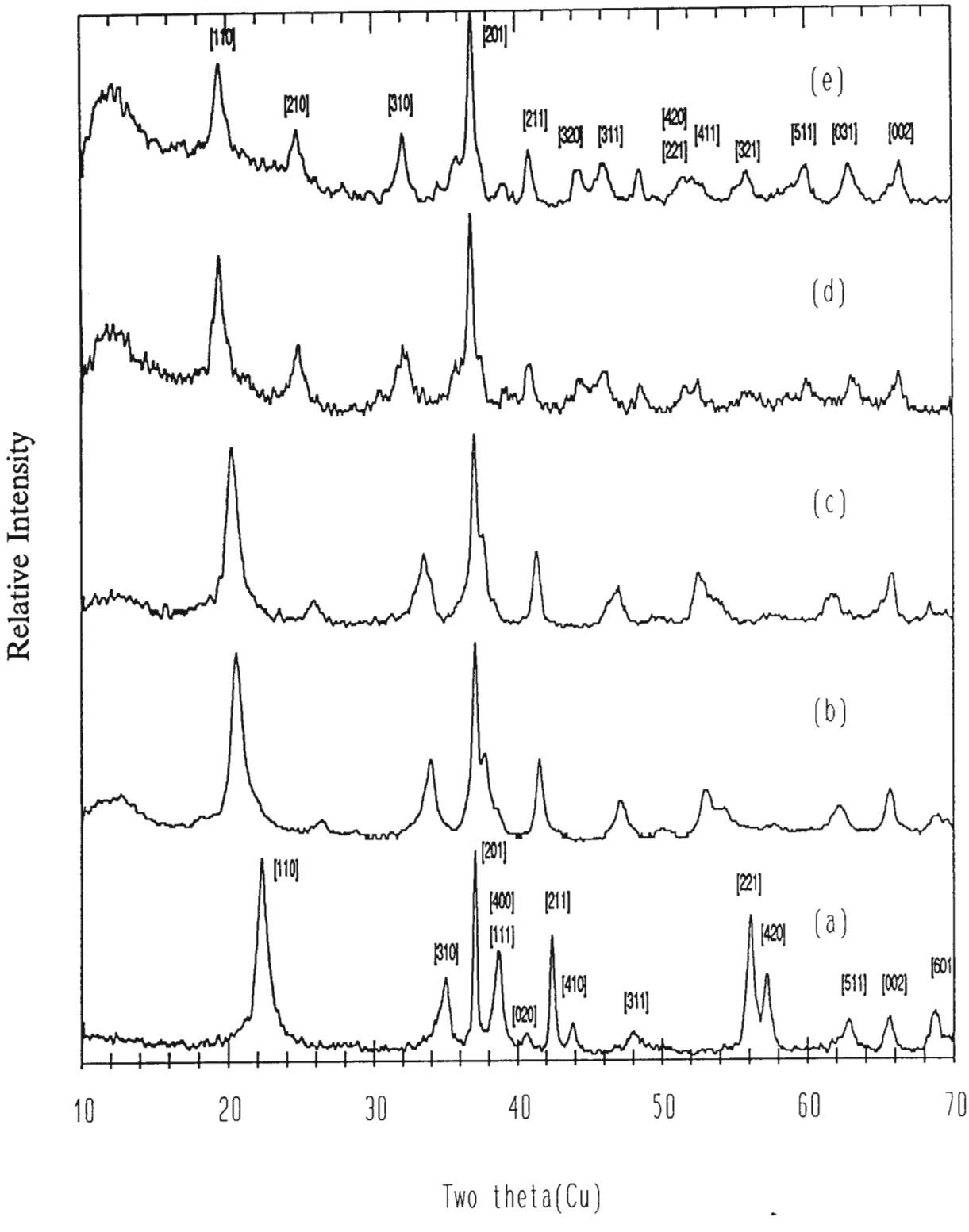

Fig. 6.10 Powder X-ray diffraction patterns of (a) R-MnO_2, (b) $Li_{0.3}MnO_2$, (c) $Li_{0.5}MnO_2$, (d) $Li_{0.5}MnO_2$, and (e) $Li_{0.9}MnO_2$. (b), (c) and (e) were synthesized with lithium iodide, whereas (d) was made with *n*-butyllithium.

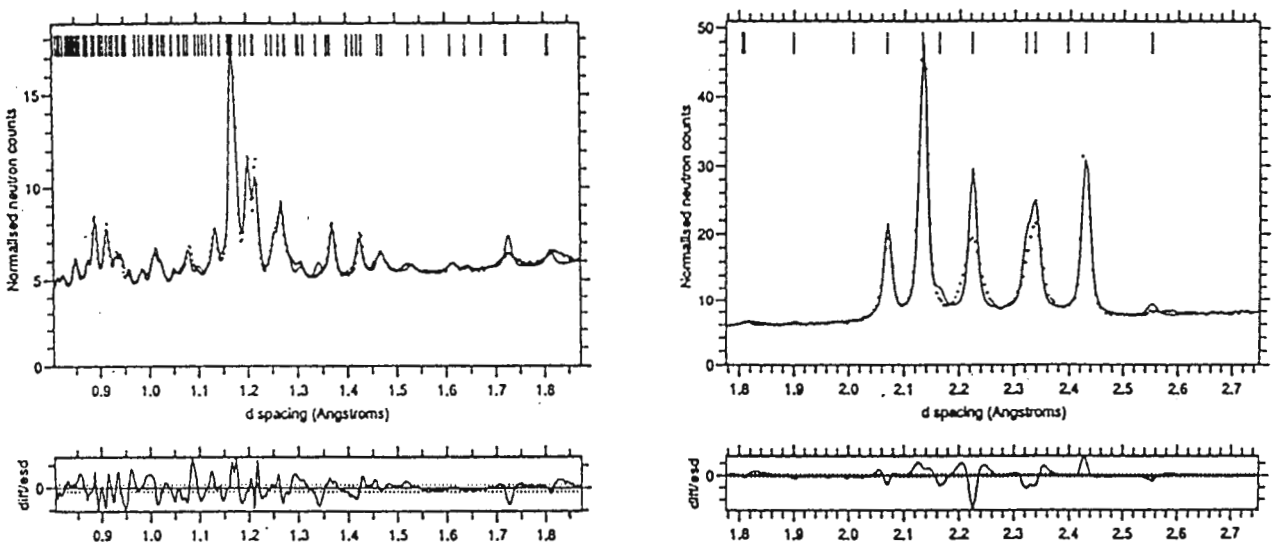

Fig. 6.11 The observed and calculated neutron diffraction patterns of R-MnO_2.

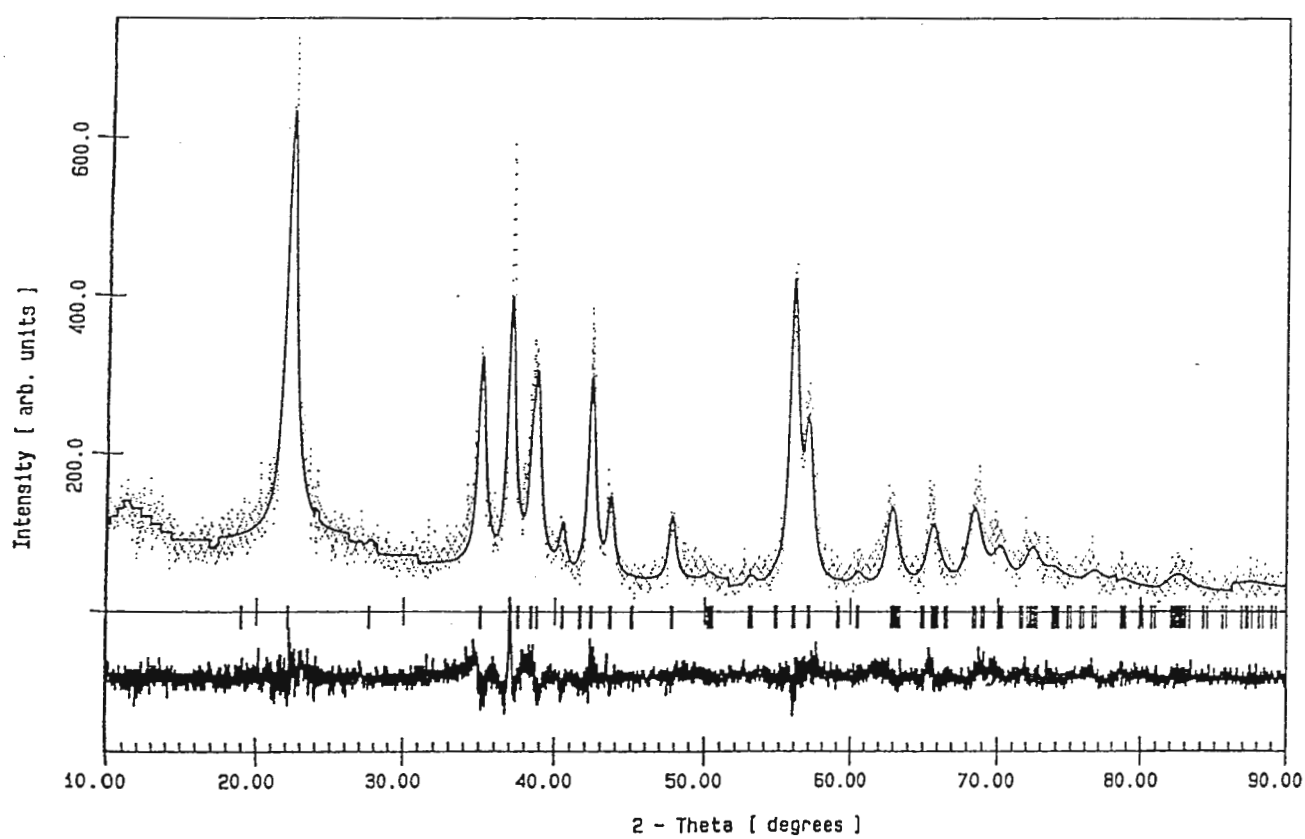

Fig. 6.12 The observed and calculated X-ray diffraction patterns of R-MnO_2.

The lattice parameters derived from these refinements (a = 9.372 Å, b = 4.471 Å, c = 2.851 Å) are in agreement with those reported for the mineral ramsdellite (JCPDS Powder Diffraction File 7-222). The structure of R-MnO_2 as determined by profile refinement of the X-ray data is shown in Fig. 6.13a.

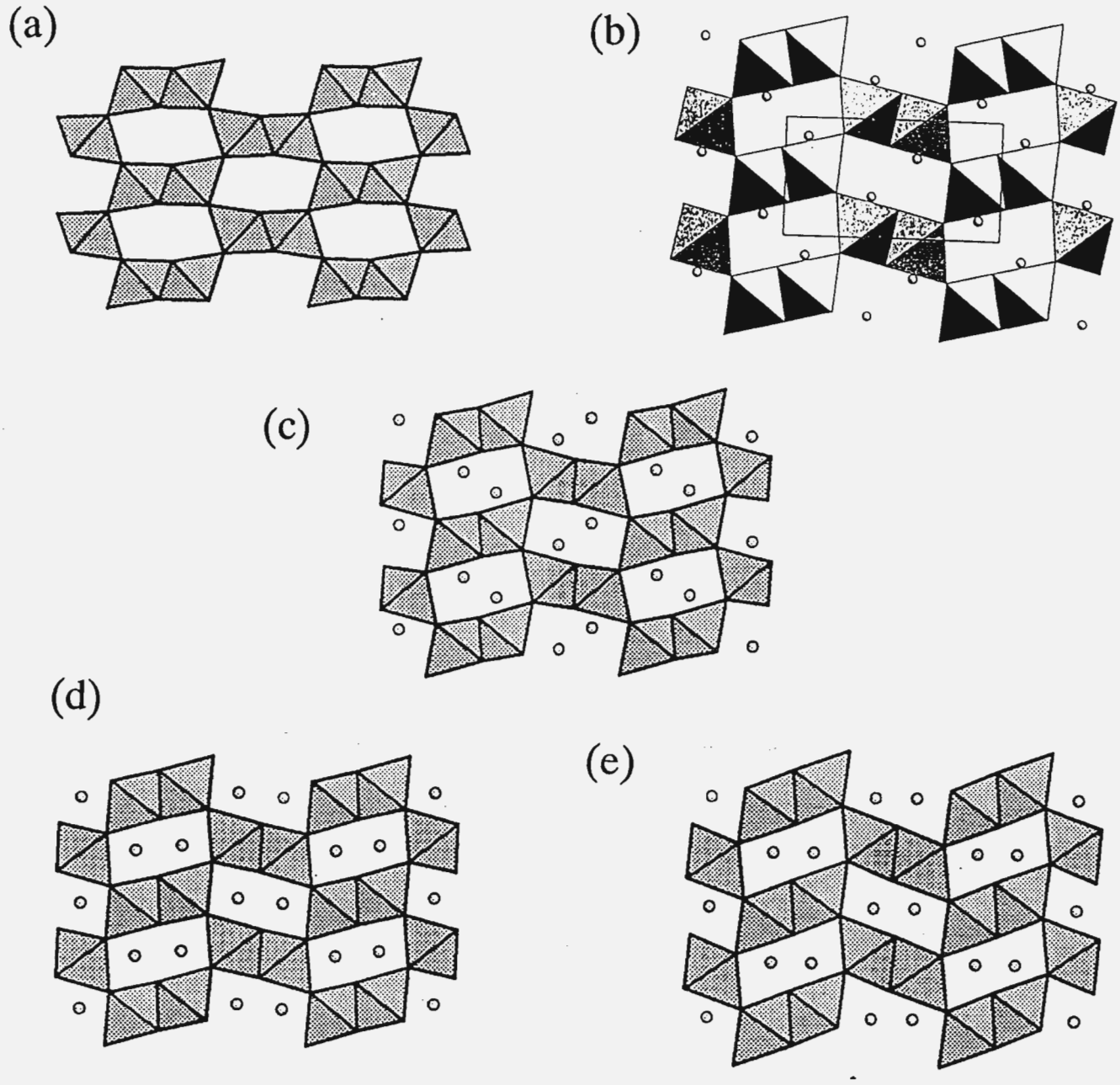

Fig. 6.13 The structures of (a) R-MnO_2, (b) $Li_{0.5}MnO_2$ (chemically lithiated with *n*-butyllithium), and the products lithiated with lithium iodide (c) $Li_{0.3}MnO_2$, (d) $Li_{0.5}MnO_2$ and (e) $Li_{0.9}MnO_2$ as determined from powder X-ray diffraction data.

Refinement of the R-MnO_2 structure in the sample indicated that there was a small amount (~10 %) of manganese in the [2x1] channels. A minor concentration of intergrown ß-MnO_2 in the R-MnO_2 structure could therefore not be discounted.

The lattice parameters of a R-MnO_2 sample determined from the refinement of neutron data are a = 9.351(1) Å, b = 4.449(1) Å and c = 2.845(1) Å.

A [001] Fourier projection of the neutron data, clearly shows the positions of the Mn and O atoms (Fig. 6.14a). Although the difference Fourier projection (Fig. 6.14b) of these data indicates some residual scattering at the Mn and O positions, there is no evidence of scattering from the interstitial octahedral sites in the [2x1] channels of the R-MnO_2 structure. It was therefore concluded that in this particular sample there was an insignificant concentration of ß-MnO_2 (rutile) domains in the R-MnO_2 structure.

(b) Chemically Lithiated R-MnO_2

The powder X-ray diffraction patterns of the sample chemically lithiated with *n*-butyllithium and with lithium iodide are shown in Fig. 6.10 (b-e). Lithiation results in single-phase Li_xMnO_2 products, the X-ray diffraction patterns of which could be indexed to an orthorhombic unit cell with the same symmetry as the parent R-MnO_2 (Pnam). The unit cell expands significantly on lithiation from 11.1 % in $Li_{0.3}MnO_2$ to 15.4 % in $Li_{0.5}MnO_2$ and to a massive 21.5 % in $Li_{0.9}MnO_2$. The increase in cell volume is a result of large increases in the a and b lattice parameters; the c parameter is effectively unchanged by lithiation (Table 6.1). Atomic parameters of the various products are listed in Table 6.2.

The structures of the chemically lithiated products show that lithium insertion into R-MnO_2 causes a buckling of the hexagonally-close-packed structure and a transformation towards a cubic-close-packed structure in response to an increase of electrostatic interactions between the inserted lithium ions and manganese ions in neighbouring face-shared octahedra.

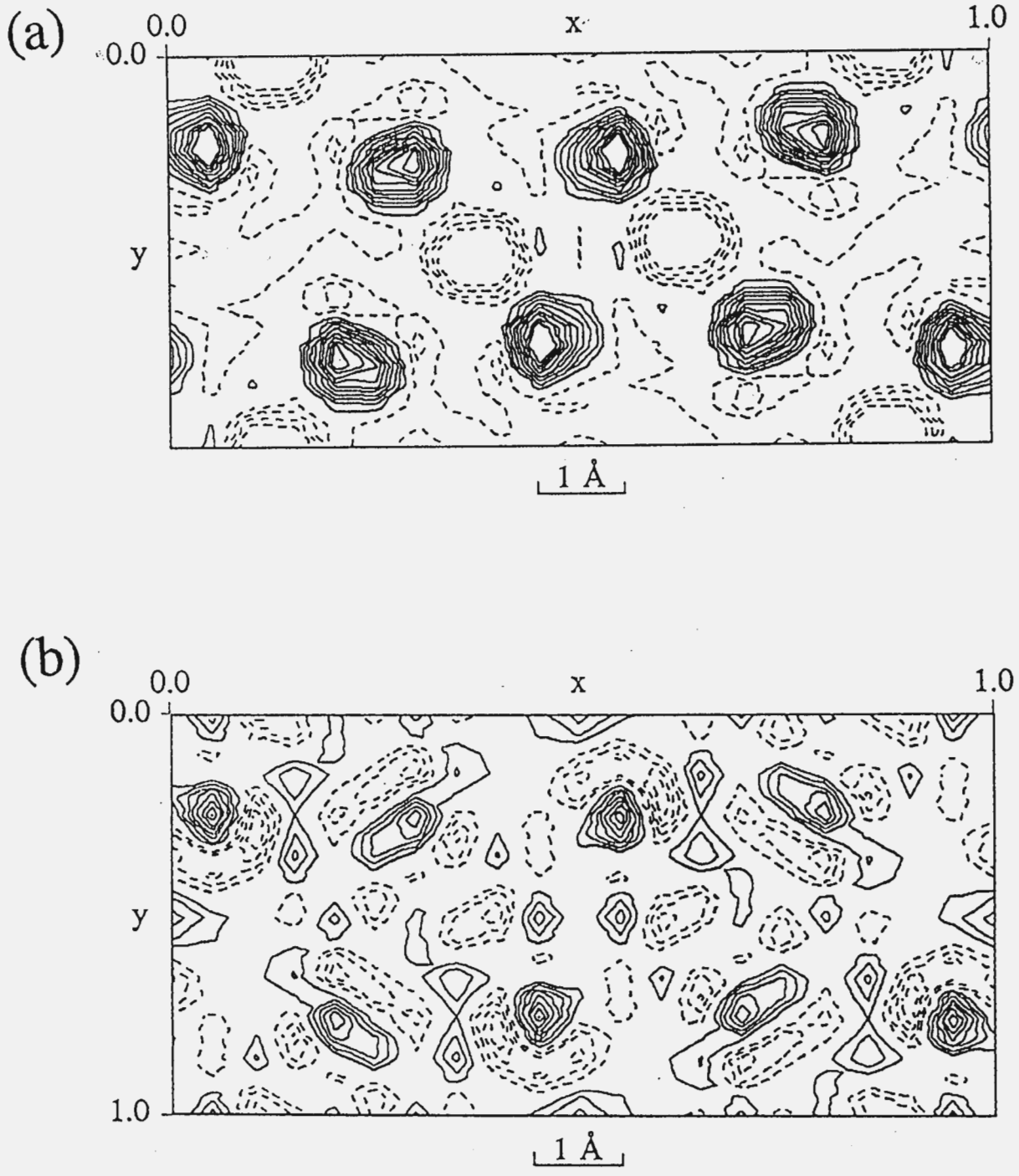

Fig. 6.14 (a) A Fourier projection of the R-MnO_2 unit cell onto the [001] plane from neutron-diffraction data showing the positions of the Mn atoms (dashed, negative contours) and O atoms (solid, positive contours). (b) A difference Fourier projection of R-MnO_2 showing residual scattering from the Mn and O sites but negligible scattering from the interstitial octahedral sites.

Table 6.1
Lattice Parameters of Ramsdellite-Related Li_xMnO_2 Compounds (Space Group Pnam)

	R-MnO_2 (neutron)	R-MnO_2 (X-ray)	$Li_{0.3}MnO_2$ (LiI)	$Li_{0.5}MnO_2$ (LiI)	$Li_{0.5}MnO_2$ (*n*-BuLi)	$Li_{0.9}MnO_2$ (LiI)
a (Å)	9.351(1)	9.372(2)	9.446(5)	9.501(4)	9.55	9.910(5)
b (Å)	4.449(1)	4.471(1)	4.932(4)	4.985(3)	5.06	5.208(3)
c (Å)	2.845(1)	2.851(1)	2.850(1)	2.841(1)	2.85	2.812(1)
Unit Cell Volume ($Å^3$)	118.4(1)	119.5(1)	132.8(2)	134.6(2)	137.7(2)	145.1(2)
Volume Expansion	-	-	11.1%	13.7%	15.4%	21.5%

The structures of R-MnO_2 and its chemically lithiated products $Li_{0.3}MnO_2$, $Li_{0.5}MnO_2$ and $Li_{0.9}MnO_2$, as determined by profile refinements of X-ray data are shown in Fig. 6.13 (a-e). The refinements of the Li_xMnO_2 structures demonstrate that at 70°C the R-MnO_2 framework remains intact over the whole compositional range of Li_xMnO_2 ($0 \leq x \leq 0.9$). Although it was not possible to determine accurately the positions of the Li^+ ions in the structures from the X-ray data, a small amount of scattering was detected from the interstitial octahedral sites of the R-MnO_2 framework. Lithium insertion into the hexagonally-close-packed oxygen array of R-MnO_2 causes a shear of the [2x1] ramsdellite blocks and a buckling of the structure towards cubic-close-packing in response to an increase in electrostatic interactions between lithium- and manganese ions in face-shared octahedra. The shear transforms the R-MnO_2 structure, in which the close-packed oxygen layers are initially parallel to the *ac* plane, to a lithiated structure in which the close-packing of the oxygens develops parallel to the *bc* plane. In $Li_{0.9}MnO_2$ the layering adopts a sequence ABACABAC which is a combination of hexagonal-close-packing (ABA) and cubic-close-packing (BAC) (Fig. 6.13e).

Table 6.2

Atomic Parameters of R-MnO_2 and Lithiated Derivatives (Space Group Pnam)

	x	*y*	*z*	B_{11}	B_{22}	B_{33}	B_{12}
R-MnO_2 (neutron data)							
Mn	.1265(16)	.0160(29)	0.25	1.44	1.13	1.83	0.18
O(1)	.2841(11)	.2941(18)	0.25	2.41	1.58	2.02	-1.78
O(2)	-.0380(15)	-.2340(6)	0.25	0.67	2.49	0.09	0.28
R-MnO_2 (X-ray data)							
Mn	.1333(6)	.0160(15)	.25				
O(1)	.2866(15)	.2838(22)	.25	Overall B = 0.45(7) Å^2			
O(2)	-.0339(15)	-.1992(24)	.25				
$Li_{0.3}MnO_2$ (X-ray data)							
Mn	.1326(7)	.0453(14)	.25				
O(1)	.2755(17)	.3545(25)	.25	Overall B = 2.46(14) Å^2			
O(2)	.0089(15)	-.2072(26)	.25				
$Li_{0.5}MnO_2$ (X-ray data)							
Mn	.1395(5)	.0498(10)	.25				
O(1)	.2607(16)	.3714(26)	.25	Overall B = 1.16(13) Å^2			
O(2)	.0051(13)	-.2276(27)	.25				
$Li_{0.9}MnO_2$ (X-ray data)							
Mn	.1280(7)	.0958(8)	.25				
O(1)	.2649(13)	.4271(24)	.25	Overall B = 2.05(20) Å^2			
O(2)	.0107(13)	-.2437(22)	.25				

NOTE: B in Å^2.

It is important to note that in R-MnO_2, as in all the chemically-lithiated products Li_xMnO_2 synthesized at 70°C (Fig. 6.13 (c-e)), the manganese ions are distributed equally in adjacent layers between the oxygen planes that lie parallel to the *bc* plane. At 300°C to 400°C lithiation induces a shear of the [2x1] ramsdellite blocks and a migration of the

manganese ions that changes the manganese distribution from the 2:2 ratio in adjacent layers towards the 3:1 ratio as required by the $[Mn_2]O_4$ framework of the $Li[Mn_2]O_4$ spinel structure.

Table 6.3
Mn-O Bond Distances in R-MnO_2 and Lithiated Derivatives in Å

	R-MnO_2 (neutron)	R-MnO_2 (X-ray)	$Li_{0.3}MnO_2$ (X-ray)	$Li_{0.5}MnO_2$ (X-ray)	$Li_{0.9}MnO_2$ (X-ray)
Mn-O(1)	1.924	1.87	2.04	1.97	2.19
Mn-O(1)	1.923	1.92	1.92	1.93	1.97
Mn-O(1)	1.923	1.92	1.92	1.93	1.97
Mn-O(2)	1.899	1.84	1.70	1.88	2.12
Mn-O(2)	1.910	1.89	2.11	2.17	2.11
Mn-O(2)	1.910	1.89	2.11	2.17	2.11
Mn-O (average)	1.913	1.88	1.97	2.01	2.08

6.3.4 Electrochemical Evaluation

(a) Galvanostatic Discharge

Capacities in excess of 210 mAh/g were obtained in lithium cells with the R-MnO_2 electrodes when discharged to a cut-off voltage of 2.0 V vs Li. When R-MnO_2 was dried at 100°C, a capacity of 218 mAh/g at a cut-off voltage of 2.0 V vs Li was obtained, whereas R-MnO_2 dehydrated at 250°C gave a capacity of 236 mAh/g under similar conditions. In general a sloping discharge curve is observed, but the dehydrated material shows a slightly flatter curve. Typical discharge curves of a hydrated and a dehydrated R-MnO_2 material are displayed in Fig. 6.15 a and b, respectively. The powder X-ray diffraction patterns of the starting electrode and the discharged electrode are given in Fig. 6.16 a and b, respectively; the pattern of the discharged electrode resembles quite strongly the X-ray pattern of the chemically lithiated sample $Li_{0.5}MnO_2$ (Fig. 6.10c).

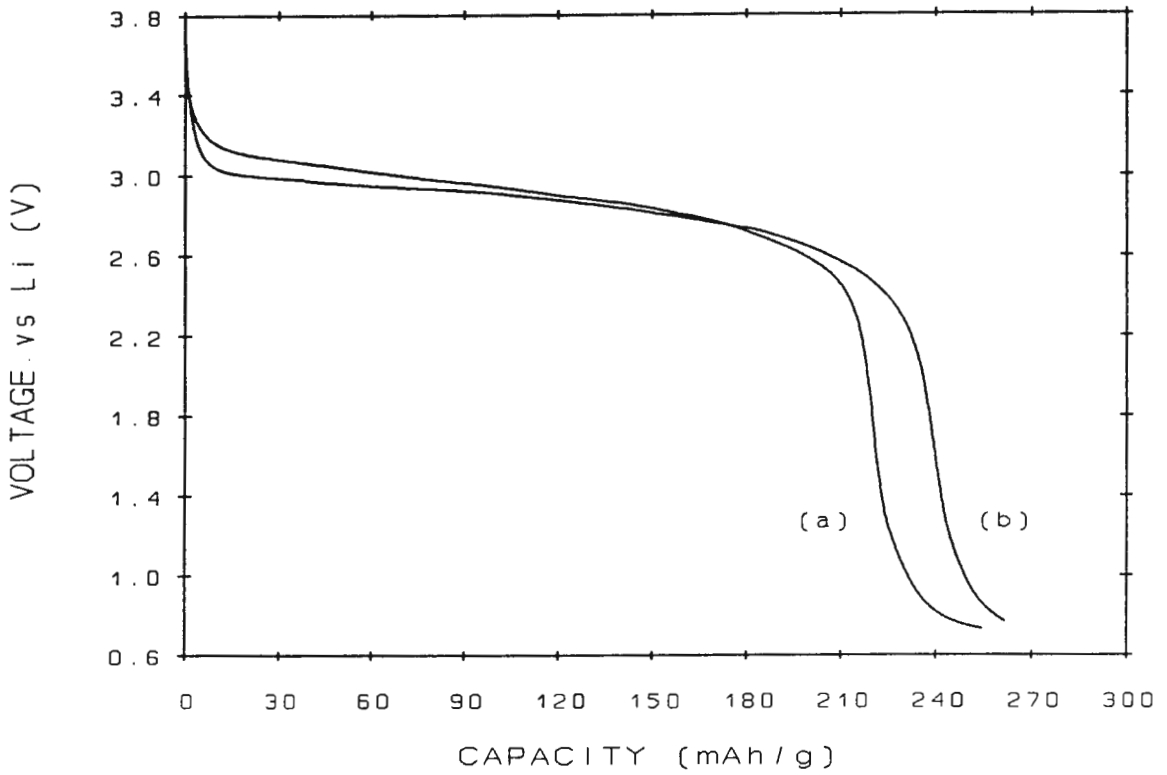

Fig. 6.15 Discharge curves of R-MnO_2 (a) dried at 100°C, and (b) dehydrated at 250°C, in a lithium cell.

(b) Open-Circuit Voltage

The open-circuit voltage (OCV) vs composition x in Li_xMnO_2 plot (Fig. 6.17) indicates that one lithium is inserted into the structure over the voltage range 3.72 to 2.81 V. The single-phase process that occurs for the range $0 \leq x \leq 0.25$, suggests that the R-MnO_2 structure incorporates 0.25 Li^+ ions before Li^+-$Mn^{4+/3+}$ electrostatic interactions induce the buckling of oxygen planes. This distortion is responsible for significant changes to the powder X-ray diffraction pattern of lithiated γ-MnO_2 products, for example, a major shift of the [1 1 0] peak at 22.2°2θ to a lower value of 19.8°2θ, and the shift of the doublet (the [2 2 1] and [4 2 0] peaks) between 56° and 57°2θ to 52°-53°2θ as can be evidenced in the powder X-ray diffraction patterns of starting and the discharged electrodes in Fig. 6.16 a and b, respectively.

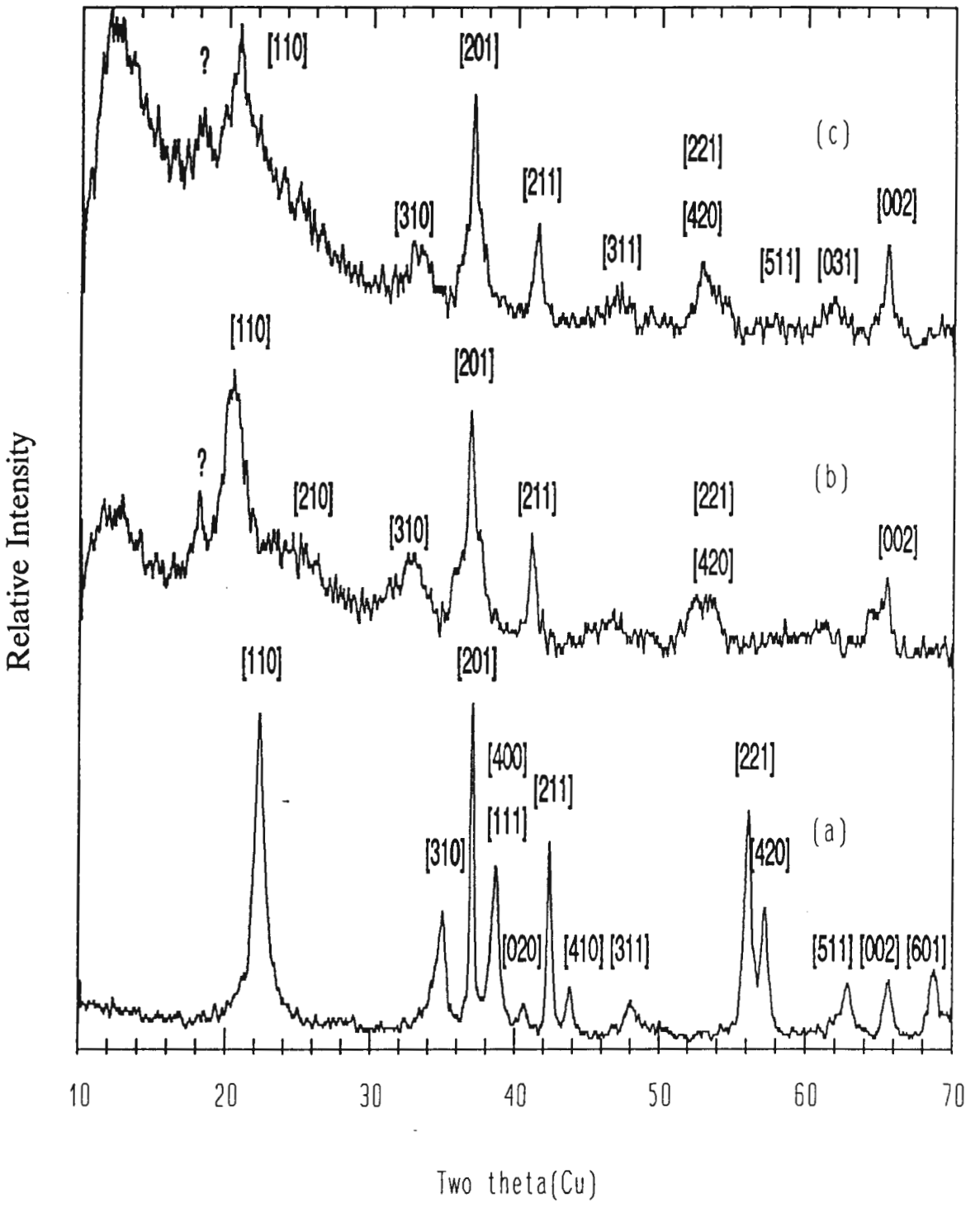

Fig. 6.16 Powder X-ray diffraction patterns of the (a) starting electrode, (b) the discharged electrode, and (c) the cycled electrode of R-MnO_2 in a lithium cell. The peaks at 18°2θ (?) are believed to be attributed to a minor concentration of a spinel phase that is formed during the lithium insertion reactions as a result of the displacement of some manganese ions.

The OCV profile shows that discharge occurs in three distinct stages to a composition Li_xMnO_2 with interruptions in the profile at $x \approx 0.3$ and $x \approx 0.9$. In view of the structural information given above, the first two stages can be attributed to the following processes:

(i) $0 \leq x \leq 0.3$: Insertion of lithium into an essentially hexagonally-close-packed R-MnO_2 structure.

(ii) $0.3 \leq x \leq 0.9$: Insertion of lithium into an R-MnO_2 framework structure in which the packing of the oxygens is essentially ABACABAC.

The process at the end of discharge ($0.9 \leq x \leq 1.0$) is not yet clearly understood; it can possibly be attributed to lithium insertion into an R-MnO_2 framework structure in which the oxygen packing is cubic-close-packed, ABCABC. In this event the end product is a rock salt phase $LiMnO_2$ in which the close-packed oxygen array is distorted from ideal cubic-close-packing by the Jahn-Teller Mn^{3+} (d^4) ions. Alternatively, the last process may be due to lithium insertion into some ß-MnO_2 domains that are intergrown with the R-MnO_2 structure.

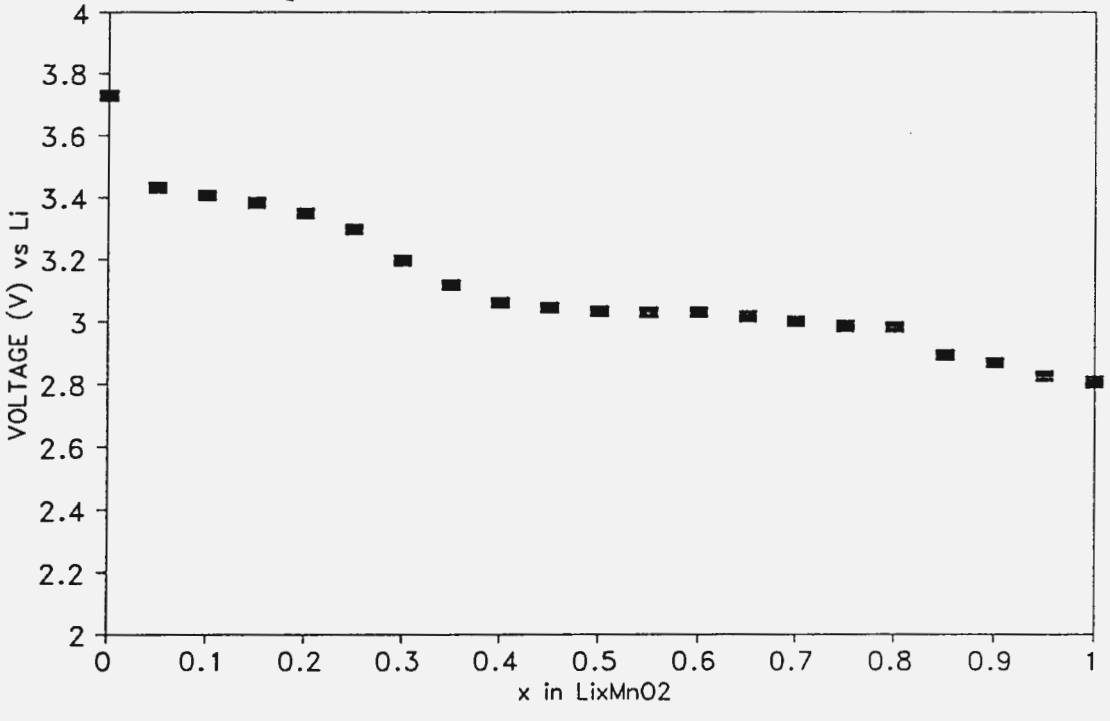

Fig. 6.17 Open-circuit-voltage data for a Li/R-MnO_2 cell.

(c) Rechargeability

Rechargeability was evaluated by employing cyclic voltammetry. The cyclic voltammograms of three different R-MnO_2 products are shown in Fig. 6.18 (a-c).

The three samples show different degrees of resolution of the oxidation and the reduction processes. Reduction appears to occur in two steps. The oxidation process are better resolved than the reduction process. A significant decrease in the reduction peak on the second cycle of the cyclic voltammograms can be observed; this indicates that a capacity loss can be anticipated on cycling a Li/R-MnO_2 cell. On the anodic scan, the voltammogram shows a two-stage process for lithium extraction, that corresponds to the first two reduction processes observed on the OCV vs composition plot in Fig. 6.17. The first oxidation peak at 3.6 V is therefore attributed to the removal of lithium from the intergrown hexagonal/cubic-close-packed anion array (ABACABAC); the second oxidation peak at 4.1 V is attributed to the further removal of Li^+ ions from the structure and a concomitant shear to regenerate the original hexagonally-close-packed structure.

Preliminary investigations of the rechargeability of room temperature Li/R-MnO_2 cells indicate that the R-MnO_2 electrode does not cycle well on deep discharge (Fig. 6.19 (a-c)). The capacity drops from an attractive initial 230 mAh/g to 160 mAh/g on the second discharge; thereafter the capacity declines steadily to reach a value of 115 mAh/g after 10 cycles (Fig. 6.19a). The capacity loss can be attributed to the large expansion and contraction of the unit cell on deep discharge and recharge, and to concomitant structural modifications that occur on cycling lithium between an essentially hexagonally-close-packed structure and one which has cubic-close-packed character. If the cycling regime is controlled to allow the electrode to operate only on the second plateau ($0.3 \leq x \leq 0.9$) an improved capacity retention can be expected; such an electrode has a theoretical capacity of 181 mAh/g.

After the first discharge not all the inserted lithium can be removed from the structure on charging the electrode, indicating that a minor concentration of Li^+ ions remain in the channels of the modified ramsdellite phase to stabilize the structure.

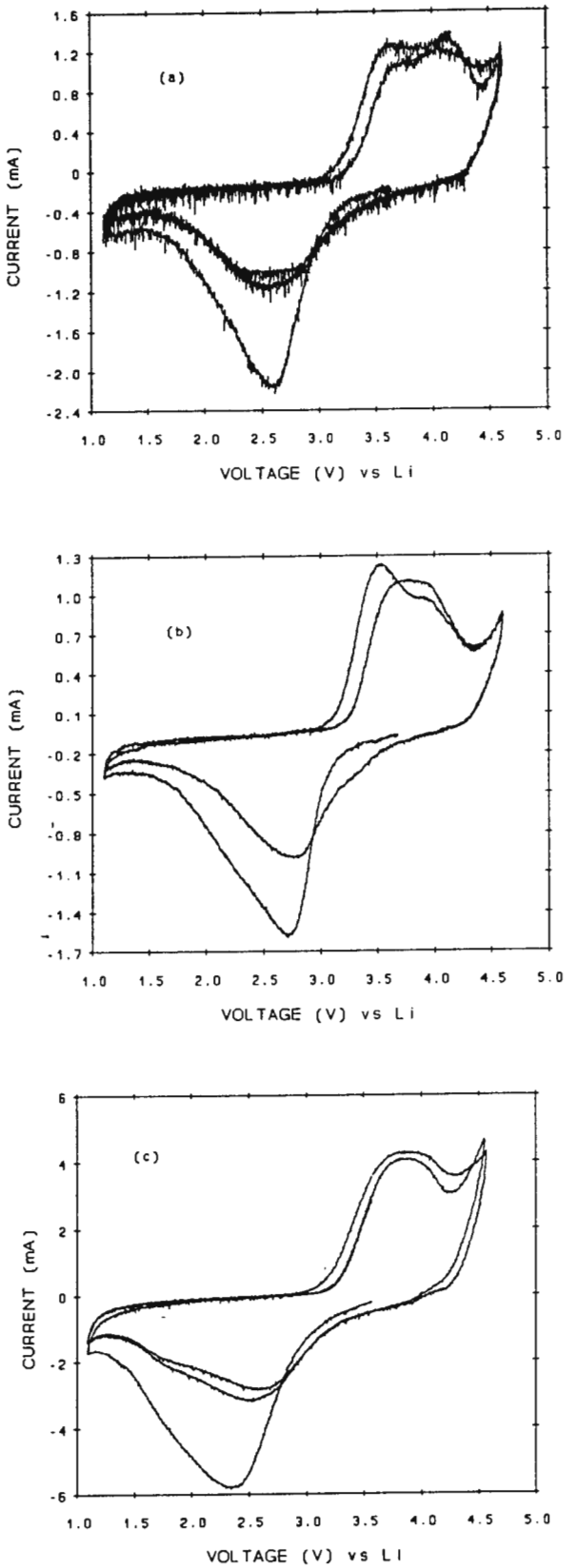

Fig. 6.18 Cyclic voltammograms of R-MnO_2.

The plots in Fig. 6.19 show that the voltage limits have an influence on the capacity retention. After 5 cycles the capacity levelled out onto a plateau and the capacity loss on consecutive cycles is very small. The voltage limits seem to have an influence on the stability of the R-MnO_2 structure, and thus the capacity. For example, the electrode which was discharged to 2.2 V (Fig. 6.19a) cycled at a higher capacity than the two electrodes discharged to 2.0 V (Fig. 6.19 b and c).

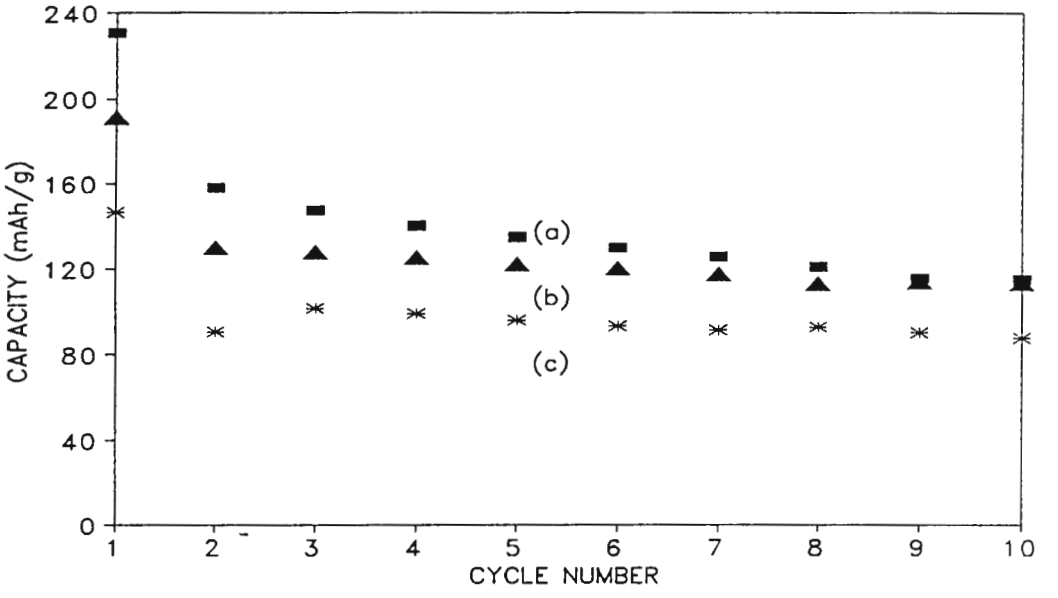

Fig. 6.19 Cycling behaviour of R-MnO_2 in a lithium cell when cycled between (a) 2.2 and 3.8 V, (b) 2.0 and 3.8 V and (c) 2.0 and 4.0 V.

In the powder X-ray diffraction pattern of the cycled R-MnO_2 electrode, in the charged state (Fig. 6.16c), the basic ramsdellite structure cannot be identified; the [1 1 0] peak at 19.8°2θ and the doublet ([2 2 1] and [4 2 0] peaks) at 52°-53°2θ are indicative of a charged R-MnO_2 electrode which has been stabilized by a small amount of lithium which is difficult to remove from the structure by electrochemical methods. The peak at 18°2θ (Fig. 6.16c) is believed to be attributed to a minor concentration of a spinel phase that is formed during the lithium insertion reactions as a result of the displacement of some manganese ions.

Chapter 7

Summary and Conclusions

Synthesis temperatures, typically between 20°C and 100°C, have been used to prepare several novel or structurally modified lithium-manganese-oxide or manganese dioxide phases from rock salt and spinel precursors. These materials are of interest as insertion electrodes for lithium batteries. The structural and electrochemical data presented in this dissertation have provided a significantly better understanding of the processes that occur during charge and discharge of lithium/manganese dioxide cells.

The rock salt phase, Li_2MnO_3, has a layered structure in which layers containing only lithium alternate with layers containing lithium and manganese in a 1:2 ratio. It can be represented in layered notation as $(Li_{1.00})(Li_{0.33}Mn_{0.67})O_2$. A novel layered $Li_{0.36}Mn_{0.91}O_2$ product was synthesized by acid leaching Li_2O at room temperature from a Li_2MnO_3 precursor synthesized at 400°C.

By acid-leaching lithium from a Li_2MnO_3 precursor, synthesized at 700°C, at temperatures between 90°C and 100°C, an α-MnO_2 product with no foreign stabilizing cations in the structure was prepared. An anhydrous α-MnO_2 was prepared by heat-treatment at 300°C; this is the first time that such a structure has been reported.

By following a similar approach, i.e. acid-leaching at temperatures above 50°C, a highly crystalline ramsdellite-MnO_2 product (R-MnO_2) was synthesized from a $LiMn_2O_4$ spinel precursor. It was also possible to lithiate R-MnO_2 with LiI without destroying the structural integrity of the R-MnO_2 framework. These highly crystalline samples have allowed, for the first time, detailed structure analysis of Li_xMnO_2(R) samples.

Summaries of the synthesis routes, physical properties and the crystallographic data of manganese oxide materials are given in Appendix A, B and C, respectively. These appendices also include certain manganese dioxide and lithium-manganese-oxide phases that were synthesized but not discussed in this dissertation.

Processing conditions and stabilization of the structures have not yet been optimised. Further work is therefore required in this area. However, a major opportunity exists to improve these materials as active electrode materials to make them attractive for commercial exploitation in rechargeable lithium batteries.

Appendices

A. Summary of Synthesis Routes for Manganese Oxide Materials

B. Summary of Physical Properties of Manganese Oxide Materials

C. Summary of Crystallographic Data of Manganese Oxide Compounds

Summary of Synthesis Routes for Manganese Oxide Materials

Sample	Synthesis	Reference [a]
γ-MnO_2:		
CMD	chemical manganese dioxide (standard material)	IBA Handbook
EMD	electrolytic manganese dioxide (standard material)	IBA Handbook
Rock Salt:		
HT-Li_2MnO_3	Li salt and Mn salt (Li/Mn = 2) heated at 700°C for 24 h	Chapter 4
LT-Li_2MnO_3	Li salt and Mn salt (Li/Mn = 2) heated at 400°C for 3 weeks	Chapter 4
Spinel:		
$LiMn_2O_4$	Li salt and Mn salt (Li/Mn = 0.5) heated at 850°C for 24 h	Wickham (1958)
λ-MnO_2	Acid leaching of $LiMn_2O_4$ at room temperature	Hunter (1981a, 1981b and 1985)
$Li_2Mn_4O_9$	Li_2CO_3 and $MnCO_3$ (Li/Mn = 0.5) heated at 400°C for 24 h	De Kock (1990)
Layered:		
HT-*l*	Stirred Li_2MnO_3 in 2.25M H_2SO_4 for 2 days at room temperature	Lubin (1991b); Rossouw (1991); Chapter 4
LT-*l*	Stirred LT-Li_2MnO_3 in 2.25M H_2SO_4 for 3 days at room temperature	Rossouw (1993), Chapter 4
Hollandite:		
α	Refluxed HT-Li_2MnO_3 in 2.25M H_2SO_4 for 2 days	Rossouw (1992a); Chapter 5
LT-α	Refluxed LT-Li_2MnO_3 in 2.25M H_2SO_4 for 2 days	Rossouw (unpublished results)
α′(K^+)	Reduced boiling $KMnO_4$ with HCl	Parida (1981); Rossouw (unpublished data)
Ramsdellite:		
R	Refluxed $LiMn_2O_4$ in 2.25M H_2SO_4 for 1 day	Rossouw (1992b); Thackeray (1993a); Ch. 6
LT-R	Refluxed $Li_2Mn_4O_9$ in 2.25M H_2SO_4 for 1 day	Rossouw (unpublished results)
Rutile:		
ß	Decomposed $Mn(NO_3)_2 \cdot 4H_2O$ at 200°C in air	McKenzie (1971)
ß′(Li)	Refluxed Mn_2O_3 in 0.5M H_2SO_4 in the presence of Li_2SO_4 for 2 days	Rossouw (unpublished results)
ß′(N)	Refluxed Mn_2O_3 in 9M HNO_3 for 2 days	Uedaira (1985); Rossouw (unpublished results)

[a] Although several papers report on the synthesis of these compounds, only a selection is listed here.

Appendix B
Summary of Physical Properties of Manganese Oxide Materials

Material (Phase)	$[H^+]$ wt%	BET [a] m^2/g	P Size [b] microns	Tap Density [c] g/cm^3	Theoretical Capacity [d] mAh/g	Gravimetric Capacity [e] mAh/g	Volumetric Capacity [f] mAh/cm^3	% [g] Utilization
CMD	3.5 % H_2O	108.10	-	1.67	308.3	221.4	369.7	71.8
EMD	3.0 % H_2O	44.68	75.0	2.11	308.3	177.1	373.7	57.4
α	0.14-0.57	46.3	42.2	0.19-0.69	308.3	211.3	145.8	68.5
LT-α	0.60	-	-	-	308.3	161.4	-	52.4
α′(K^+)	-	-	-	-	308.3	186.1	-	60.4
ß	-	-	-	2.65	308.3	-	-	-
ß′(Li)	0.10	23.5	1.0	0.55	308.3	245.4	135.0	79.6
ß′(N)	-	13.7	1.0	1.11	308.3	196.2	217.8	63.6
$LiMn_2O_4$	-	-	42.2	-	148.2	166.5	-	112.3
R	0.16	26.6	42.2	0.55	308.3	229.9	126.4	74.6
$Li_2Mn_4O_9$	-	-	-	-	212.9	133.3	-	62.6
LT-R	0.64	57.1	1.0	0.74	308.3	196.6	145.5	63.8
HT-*l* [h]	0.65-0.89	110.7	3.7	1.70	150.7	153.7	261.3	102.0
LT-*l* [i]	0.54-1.58	64.1	1.0	1.33	199.8	193.0	256.7	96.6

[a] BET surface area
[b] Particle size, 100% of the material finer than
[c] Tap density determined by tapping a certain mass of material for a specified time in a graded measuring cylinder
[d] To a rock salt stoichiometry
[e] At a cut off voltage of 2.0 V vs lithium, average values for a selection of materials
[f] Determined by multiplying the gravimetric capacity with the tap density
[g] Determined by dividing the gravimetric capacity by the theoretical capacity
[h] Data for Li/Mn = 0.94, $Li_{0.76}Mn_{0.81}O_2$, heat treated to 300°C, apart from $[H^+]$
[i] Data obtained from $Li_{0.36}Mn_{0.91}O_2$ (Li/Mn = 0.40), apart from $[H^+]$

Summary of Crystallographic Data of Manganese Oxide Compounds

Material	Structural Notation	Space Group	Lattice Parameters	Reference
Rock Salt:				
Li_2MnO_3	$(Li_{1.00})(Li_{0.33}Mn_{0.67})O_2$	C2/c	a = 4.92(8) Å, b = 8.53(3) Å, c = 9.60(4) Å, ß = 99.5°	Jansen (1973)
		C2/m	a = 4.937(1) Å, b = 8.532(1) Å, c = 5.030(2) Å, ß = 109.46(3)°	Strobel (1988)
		C2/c	a = 4.921(6) Å, b = 8.526(3) Å, c = 9.606(5) Å, ß = 99.47(5)°	Riou (1992)
Spinel:				
$LiMn_2O_4$	$(Li_{1.00})[Mn_2]O_4$	Fd3m	a = 8.24 Å	Wickham (1958)
λ-MnO_2	$\square_{1.00}[Mn_2]O_4$		a = 8.03 Å	Hunter (1981a)
	$Li_{1.00}[Li_{0.33}Mn_{1.67}]O_4$		a = 8.19 Å	Blasse (1963)
$Li_4Mn_5O_{12}$	$Li_{1.00}[Li_{0.33}Mn_{1.67}]O_4$		a = 8.166 Å	Chapter 4
	$(Li_{0.87}\square_{0.13})[Mn_{1.71}Li_{0.29}]O_4$*		a = 8.143 Å	Thackeray (1993c)
$Li_2Mn_3O_7$ (ideal)	$(Li_{0.85}\square_{0.15})[Mn_{1.74}Li_{0.26}]O_4$*		a = 8.1605 Å	Thackeray (1993c)
$Li_2Mn_4O_9$	$(Li_{0.89}\square_{0.11})[Mn_{1.78}\square_{0.22}]O_4$		a = 8.200 Å	Vol'khin (1973)
	$(Li_{0.89}\square_{0.11})[Mn_{1.78}\square_{0.22}]O_4$		a = 8.174 Å	De Kock (1990)
Layered:				
$Li_{0.36}Mn_{0.91}O_2$	$Li_{0.27}(Li_{0.09}Mn_{0.91})O_2$	R$\bar{3}$m	a = 2.9029(5) Å, c = 13.803(5) Å	Chapter 4
$Li_{1.09}Mn_{0.91}O_2$	$Li_{1.00}(Li_{0.09}Mn_{0.91})O_2$		a = 2.8509(6) Å, c = 14.259(6) Å	Chapter 4
Hollandite:				
α-MnO_2•0.3H_2O		I4/m	$a = b$ = 9.7826(2) Å, c = 2.8573(1) Å	Chapter 5
α-MnO_2			$a = b$ = 9.7876(3) Å, c = 2.8650(1) Å	
Ramsdellite:				
R-MnO_2		Pnam	a = 9.372 Å, b = 4.471 Å, c = 2.851 Å	Chapter 6
$Li_{0.3}MnO_2$			a = 9.446 Å, b = 4.932 Å, c = 2.850 Å	
$Li_{0.5}MnO_2$			a = 9.501 Å, b = 4.985 Å, c = 2.841 Å	
$Li_{0.9}MnO_2$			a = 9.910 Å, b = 5.208 Å, c = 2.812 Å	

* composition determined by neutron diffraction

References

Abraham K M (1983) and Brummer S B, "Secondary Lithium Cells" in *Lithium Batteries*, J P Gabano (Ed.), Academic Press Inc., New York, Chapter 14, 1983.

Anderson T N (1992), "Effect of Some EMD Structural Features on Alkaline Discharge Capacity". *Prog. Batteries & Battery Materials*, **11**, 105, 1992.

Bach S (1991), Pereira-Ramos J P, Baffier N and Messina R, "Birnessite Manganese Dioxide Synthesized via a Sol-Gel Process: A New Rechargeable Cathodic Material for Lithium Batteries". *Electrochim. Acta*, **36**, 1595, 1991.

Bahniuk D E (1989), "New Lithium Cells Charge Up Consumer Electronics". *Machine Design*, **Feb. 23**, 101, 1989.

Batley H (1986), "Batteries for Memory Protection". *Electronics & Power*, **Feb**, 163, 1986.

Bayer G (1966) and Hoffman W, "Complex Alkali Titanium Oxides $A_x(B_yTi_{8-y})O_{16}$ of the α-MnO_2 Structure-Type". *Am. Miner.*, **51**, 511, 1966.

Blasse G (1963), "The Structure of Some New Mixed Metal Oxides Containing Lithium". *J. Inorg. Nucl. Chem.*, **25**, 743, 1963.

Botkovitz P (1992), Deniard P, Tournoux M and Brec R, "Structural and Electrochemical Characteristics of a Hollandite Type Li_xMnO_2". *6th International Meeting on Lithium Batteries, Extended Abstract,* **III-B-31**, 385, 1992.

Brodd R J (1985), "Advanced Batteries". *Chemtech*, **Oct.**, 1985.

Brookman M (1984), "Overview of Applications, Trends for Lithium Batteries". *Electrionics*, **30**, 43, 1984.

Burns R G (1980) and Burns V M, "Recent Structural Data for Manganese(IV) Oxides". *Manganese Dioxide Symp.*, **2**, 97, 1980.

Burns R G (1985) and Burns V M, "Tunnelling through MnO_2: Covalent Bonding and Structural Linkages in Tetravalent Manganese Oxides". *Proc. Electrochem. Soc. Symp. MnO_2 Electrode Theory and Practice for Electrochemical Applications*, **85-4**, 97, 1985.

Bursill L A (1979), "Structural Relationship between ß-Gallia, Hollandite, Psilomelane, Ramsdellite and Gallium Titanate Type Structures". *Acta Cryst.*, **B35**, 530, 1979.

Buser W (1954), Graf P and Feitknecht W, "Beitrag zur Kenntnis de Mangan(II)-manganite und des δ-MnO_2". *Helv. Chim. Acta*, **37**, 2332, 1954.

Butler G (1952) and Thirsk H R, "Electron Diffraction Evidence for the Existence and Fine Structure of a Cryptomelane Modification of Manganese Dioxide Prepared in the Absence of Potassium". *Acta Cryst.*, **5**, 288, 1952.

Byström A M (1949), "The Crystal Structure of Ramsdellite, an Orthorhombic Modification of MnO_2". *Acta Chem. Scan.*, **3**, 163, 1949.

Byström A (1950) and Byström A M, "The Crystal Structure of Hollandite, the Related Manganese Oxide Minerals, and α-MnO_2". *Acta Cryst.*, **3**, 146, 1950.

Chukhrov F V (1979), Gorshkov A I, Sivtsov A V and Beresovskaya V V, "New Data on Natural Todorokites". *Nature*, **278**, 63, 1979.

Clearfield A (1988), "Role of Ion Exchange in Solid-State Chemistry". *Chem. Rev.*, **88**, 125, 1988.

Cole W F (1947), Wadsley A D and Walkley A, "An X-Ray Diffraction Study of Manganese Dioxide". *Trans. Electrochem. Soc.*, **92**, 133, 1947.

Dahn J R (1991), Von Sacken U, Juzkow M W and Al-Janaby H, "Rechargeable $LiNiO_2$/Carbon Cells". *J. Electrochem. Soc.*, **138**, 2207, 1991.

David W I F (1983), Goodenough J B, Thackeray M M and Thomas M G S R, "The Crystal Structure of Li_2MnO_2". *Rev. Chim. Miner.*, **20**, 636, 1983.

David W I F (1984), Thackeray M M, Bruce P G and Goodenough J B, "Lithium Insertion into ß-MnO_2 and the Rutile-Spinel Transformation". *Mat. Res. Bull.*, **19**, 99, 1984.

De Kock A (1990), Rossouw M H, de Picciotto L A, Thackeray M M, David W I F and Ibberson R M, "Defect Spinels in the System $Li_2O.yMnO_2$ ($y > 2.5$): A Neutron-Diffraction Study and Electrochemical Characterization of $Li_2Mn_4O_9$". *Mat. Res. Bull.*, **25**, 657, 1990.

Delano P H (1950), "Classification of Manganese Dioxides". *Ind. Eng. Chem.*, **42**, 523, 1950.

Delmas C (1989), "Alkali Metal Intercalation in Layered Oxides". *Mat. Sci. Eng.*, **B3**, 97, 1989.

Delmas C (1992) and Saadoune I, "Electrochemical and Physical Properties of the $Li_xNi_{1-y}Co_yO_2$ Phases". *Solid State Ionics*, **53-56**, 370, 1992.

De Picciotto L A (1984), Thackeray M M, David W I F, Bruce P G and Goodenough J B, "Structural Characterization of Delithiated $LiVO_2$". *Mat. Res. Bull.*, **19**, 1497, 1984.

De Picciotto L A (1985) and Thackeray M M, "Transformation of Delithiated $LiVO_2$ to

the Spinel Structure". *Mat. Res. Bull.*, **20**, 187, 1985.

De Wolff P M (1959), "Interpretation of Some γ-MnO_2 Diffraction Patterns". *Acta Cryst.*, **12**, 341, 1959.

Ewing M (1982), "Lithium Batteries - Where the Future Lies". *Electronics & Power*, Jul/Aug, 523, 1982.

Fanchon E (1991), Hodeau J L, Vicat J and Watts J A, "Three-Dimensional/One-Dimensional Transition in the Cs^+ Sublattice of the Mixed Valence $CsTi_8O_{16}$ Hollandite: Structures at 297 and 673 K". *J. Solid State Chem.*, **92**, 88, 1991.

Fernandes J B (1983), Desai B and Dalal V N K, "Studies on Electrochemically Precipitated Mn(IV) Oxides - I". *Electrochim Acta*, **28**, 309, 1983.

Fleischer M (1960), "Studies of the Manganese Oxide Minerals. III. Psilomelane". *Am. Miner.*, **45**, 176, 1960.

Fleischer M (1962), Richmond W E and Evans H T, "Studies of the Manganese Oxides. V. Ramsdellite, MnO_2, an Orthorhombic Dimorph of Pyrolusite". *Am. Miner.*, **47**, 47, 1962.

Frondel C (1960), Marvin U B and Ito J, "New Data on Birnessite and Hollandite". *Amer. Miner.*, **45**, 871, 1960.

Furukawa N (1987a), Saito T and Nohma T, "Non-aqueous Secondary Cell". *European Patent*, Application no. 87115912.5, 1987.

Furukawa N (1987b), Saito T, Teraji K, Nakane I and Nohma T, "Manganese Oxides for Lithium Secondary Battery". *Ext. Abstr. 172nd Electrochemical Society Meeting*, 557, 1987.

Furukawa N (1988), Saito T and Nohma T, "Nonaqueous Secondary Cell". *European Patent*, **0 279 235 A1**, Application no. 88101120.9, 1988.

Furukawa N (1992) and Nohma T, "Performance of a Lithium Containing Manganese Dioxide (CDMO)-Lithium Secondary Batteries". *6th International Meeting on Lithium Batteries*, Extended Abstracts, **THU-03**, 97, 1992.

Gabano J P (1983), "Lithium Battery Systems: An Overview" in *Lithium Batteries*, J P Gabano (Ed.), Academic Press Inc., New York, Chapter 1, 1983.

Giovanoli R (1980), "A Review on Structural Data of Electrolytical and Chemical MnO_2". *Manganese Dioxide Symp.*, **2**, 113, 1980.

Giovanoli R (1990), "Transformations involving γ-MnO_2". *Prog. Batteries & Solar Cells*, **9**, 1, 1990.

Goodenough J B (1982), "Fast Ion Transport in Solids", in *Synthesis, Crystal Growth and Characterization*, Krishan Lal (Ed.), North-Holland, 1982, pp. 519 - 553.

Goodenough J B (1984), Thackeray M M, David W I F and Bruce P G, "Lithium Insertion/Extraction Reactions with Manganese Oxides". *Rev. Chim. Miner.*, **21**, 435, 1984.

Goodenough J B (1989), Manthiram A, James A C W P and Strobel P, "Lithium Insertion Compounds". *Mat. Res. Soc. Symp. Proc.*, **135**, 391, 1989.

Gopalakrishnan J (1988), "Layered Oxides derived from Metal-Oxygen Octahedra: Synthesis, Structure and Properties". *Rev. Solid State Sci.*, **1**, 515, 1988.

Humbert M A (1992), Biensan Ph, Broussely M, Lecerf A, Dollé A and Ladhily H, "A High Performance Li_xMnO_y Cathodic Material for Rechargeable Lithium Cells". *6th*

International Meeting on Lithium Batteries, Extended Abstract, **III-C-06**, 397, 1992.

Hunter J C (1981a), "MnO_2 Derived From $LiMn_2O_4$". *United States Patent*, **4,246,253**, 1981.

Hunter J C (1981b), "Preparation of a New Crystal Form of Manganese Dioxide: λ-MnO_2". *J. Solid State Chem.*, **39**, 142, 1981.

Hunter J C (1985) and Tudron F B, "Nonaqueous Electrochemistry of Lambda-MnO_2". *Proc. Electrochem. Soc. Symp. MnO_2 Electrode Theory and Practice for Electrochemical Applications*, **85-4**, 444, 1985.

Ikeda H (1983), "Lithium-Manganese Dioxide Cells", in *Lithium Batteries*, J P Gabano (Ed.), Academic Press Inc., New York, Chapter 8, 1983.

Ilchev N (1989), Manev V and Hampartzumian K, "The Lithium-Manganese Dioxide Cell. II. Behaviour of Manganese Dioxide in Nonaqueous Electrolyte". *J. Power Sources*, **25**, 177, 1989.

Ilchev N (1992), Banov B and Kvachkov R, "Physicochemical Characteristics and Electrochemical Behaviour of MnO_2 in Primary Lithium Cells". *6th International Meeting on Lithium Batteries, Extended Abstracts*, **IV-A-06**, 416, 1992.

Jansen M (1973) and Hoppe R, "Zur Kennis der NaCl-Strukturfamilie: Neue Untersuchengen an Li_2MnO_3". *Z. Anorg. Allg. Chem.*, **397**, 279, 1973.

Kao W-H (1988), "Effect of Particle Size on Transformation of EMD during Digestion in Sulphuric Acid Containing Mn(II)". *J. Electrochem. Soc.*, **135**, 1317, 1988.

Kozawa A (1989), Umezu Y and Yoshio M, "Possible Explanations for Unusual Discharge Behaviour of Li/MnO_2 Cells". *Prog. Batteries Sol. Cells*, **8**, 49, 1989.

Krause R (1993), "High Energy Batteries". *Pop. Sci.*, **Feb.**, 64, 1993.

Lang G (1966), "Strukturvergleiche an Ternären und Quarternären Oxiden". *Z. Anorg. Allg. Chemie*, **348**, 246, 1966.

Lecerf A (1990), Lubin F and Broussely M, "Rechargeable Electrochemical Battery including a Lithium Anode". *United States Patent*, **4,975,346**, 1990.

Li J-B (1988), Koumoto K and Yanagida H, "EXAFS Study of Polymorphs of Manganese Dioxides". *J. Mat. Sci.*, **23**, 2595, 1988.

Li L (1991a) and Pistoia G, "Secondary Li Cells. I. A Comparison of the Behaviour of Cathodes Based on Pure and Lithiated Manganese Oxides". *Solid State Ionics*, **47**, 231, 1991.

Li L (1991b) and Pistoia G, "Secondary Li Cells. II. Characteristics of Lithiated Manganese Oxides Synthesized from $LiNO_3$ and MnO_2". *Solid State Ionics*, **47**, 241, 1991.

Lubin F (1991a), "MnO_2 et Dérivés commes Matériaux Cathodiques dans un Générateur Électrochimique Rechargeable à Anode de Lithium". *Thesis*, Institut National des Sciences Appliquées de Rennes, 1991.

Lubin F (1991b), Lecerf A, Broussely M and Labat J, "Chemical Lithium Extraction from Manganese Oxides for Lithium Rechargeable Batteries". *J. Power Sources*, **34**, 161, 1991.

Macklin W J (1991), Neat R J and Powell R J, "Performance of Lithium-Manganese Oxide Spinel Electrodes in a Lithium Polymer Electrolyte Cell". *J. Power Sources*, **34**, 39, 1991.

Manev V (1989), Ilchev N and Nassalevska A, "The Lithium-Manganese Dioxide Cell. I. Oxygen and Water Release during the Thermal Treatment of MnO_2". *J. Power*

Sources, **25**, 167, 1989.

Manev V (1992a), Momchilov A, Nassalevska A and Kozawa A, "Performance of Spinel Related λ-MnO_2 in a 4 V Rechargeable Lithium Cell". *6th International Meeting on Lithium Batteries, Extended Abstracts*, **III-B-11**, 332, 1992.

Manev V (1992b), Momchilov A, Nassalevska and Kozawa A, "Optimization of $LiMn_2O_4$ Synthesis for 4 V Rechargeable Lithium Batteries". *The Tianjin International Power Sources Symposium & Trade Show, TIPSS/TS'92*, September 22-26, 1992, Tianjin, China, Extended Abstracts, p 64, 1992.

McKenzie R M (1971), "The Synthesis of Birnessite, Cryptomelane, and Some Other Oxides and Hydroxides of Manganese". *Min. Mag.*, **38**, 493, 1971.

McMurdie H F (1944), "Microscopic and Diffraction Studies on Dry Cells and their Raw Materials". *Trans. Electrochem. Soc.*, **86**, 313, 1944.

Mendiboure A (1985), Delmas C and Hagenmuller P, "Electrochemical Intercalation and Deintercalation of Na_xMnO_2 Bronzes". *J. Solid State Chem.*, **57**, 323, 1985.

Mizushima K (1981), Jones P C, Wiseman P J and Goodenough J B, "Li_xCoO_2 ($0 < x \leq 1$): A new Cathode Material for Batteries of High Energy Density". *Solid State Ionics*, **3/4**, 171, 1981.

Moore T E (1950), Ellis M and Selwood P W, "Solid Oxides and Hydroxides of Manganese". *J. Am. Chem. Soc.*, **72**, 856, 1950.

Mukherjee B (1965), "Crystallography of Psilomelane, $A_3X_6Mn_8O_{16}$". *Min. Mag.*, **35**, 643, 1965.

Murphy D W (1978), DiSalvo F J, Carides J N and Waszczak J V, "Topochemical

Reactions of Rutile Related Structures with Lithium". *Mat. Res. Bull.*, **13**, 1395, 1978.

Murphy D W (1979) and Christian P A, "Solid State Electrodes for High Energy Batteries". *Science*, **205**, 651, 1979.

Murphy D W (1991), "Intercalation Chemistry - Useful Reactions, New Materials and Enhanced Physical Properties", in *Advances in the Synthesis and Reactivity of Solids*, 1, 237, 1991. JAI Press Ltd.

Nakamura H (1992), Isono K-I, Kuromoto H and Yoshio M, "Determination of Chemical Composition of Chemically Lithiated Manganese Dioxide by the Continuous Variation Method". *The Tianjin International Power Sources Symposium & Trade Show, TIPSS/TS'92*, September 22- 26, 1992, Tianjin, China, Extended Abstracts, p 136, 1992.

Nohma T (1989), Saito T, Furukawa N and Ikeda H, "Manganese Oxides for a Lithium Secondary Battery - Composite Dimensional Manganese Oxide (CDMO)". *J. Power Sources*, **26**, 389, 1989.

Nohma T (1990), Yamamoto Y, Nishio K, Nakane I and Furukawa N, "Lithium-Containing Manganese Dioxide (Composite Dimensional Manganese Dioxide: CDMO) as Positive Material for a Lithium Secondary Battery". *J. Power Sources*, **32**, 373, 1990.

Nohma T (1991) and Furukawa N, "Li/MnO_2 (CDMO) Rechargeable Batteries". *Proc. Electrochem. Soc.*, **91-3**, 311, 1991.

Nohma T (1992), Yamamoto Y, Nakane I and Furukawa N, "Improvement of Lithium-Containing Manganese Dioxide (Composite Dimensional Manganese Oxide: CDMO) as Positive Material for Lithium Secondary Batteries". *J. Power Sources*, **39**, 51, 1992.

Ohzuku T (1981), Tari I and Hirai T, "The Cathodic Behaviour of Microwave-Treated Manganese Dioxide in Lithium Nonaqueous Cells". *Electrochim. Acta*, **26**, 1423, 1981.

Ohzuku T (1988) and Hirai T, "Heat-Treated Electrolytic Manganese Dioxide - Its Structure, Physicochemical Properties, and Electrochemical Reactivity". *Prog. Batteries Sol. Cells*, **7**, 31, 1988.

Ohzuku T (1989a), Sawai K and Hirai T, "Preliminary Results on Synthesis and Characterization of Li_xMnO_{2-d} for Rechargeable Lithium Cell". *Chem. Express*, **4**, 777, 1989.

Ohzuku T (1989b), Kitagawa M and Hirai T, "Electrochemistry of Manganese Dioxide in Lithium Nonaqueous Cell. I. X-Ray Diffraction Study on the Reduction of Electrolytic Manganese Dioxide". *J. Electrochem. Soc.*, **136**, 3169, 1989.

Ohzuku T (1990), Kitagawa M and Hirai T, "Electrochemistry of Manganese Dioxide in Lithium Nonaqueous Cell. II. X-Ray Diffractional and Electrochemical Characterization on Deep Discharge Products of Electrolytic Manganese Dioxide". *J. Electrochem. Soc.*, **137**, 40, 1990.

Ohzuku T (1991), Kitagawa M, Sawai K and Hirai T, "Topotactic Reduction of Alpha-Manganese (Di)Oxide in Nonaqueous Lithium Cells". *J. Electrochem. Soc.*, **138**, 360, 1991.

Ohzuku T (1992), Ueda A and Hirai T, "$LiMnO_2$ as Cathode for Secondary Lithium Cell". *Chem. Express*, **7**, 193, 1992.

Parant J P (1971), Olazcuaga R, Devalette M, Fouassier C and Hagenmuller P, "Sur Quelques Nouvelles Phases de Formule Na_xMnO_2 ($x \leq 1$)". *J. Solid State Chem.*, **3**, 1, 1971.

Parida K M (1981), Kanungo S B and Sant B R, "Studies on MnO_2 - I. Chemical Composition, Microstructure and Other Characteristics of Some Synthetic MnO_2 of Various Crystalline Modifications". *Electrochem. Acta*, **26**, 435, 1981.

Post J E (1982), von Dreele R B and Buseck P R, "Symmetry and Cation Displacements in Hollandites: Structure Refinements of Hollandite, Cryptomelane and Priderite". *Acta Cryst.*, **B38**, 1056, 1982.

Post J E (1988) and Bish D L, "Rietveld Refinement of the Todorokite Structure". *Amer. Min.*, **73**, 861, 1988.

Riou A (1992), Lecerf A, Gerault Y and Cudennec Y, "Etude Structurale de Li_2MnO_3". *Mat. Res. Bull.*, **27**, 269, 1992.

Rossen E (1992), Jones C D W and Dahn J R, "Structure and Electrochemistry of $Li_xMn_yNi_{1-y}O_2$". *Solid State Ionics*, **57**, 311, 1992.

Rossouw M H (1990), de Kock A, de Picciotto L A, Thackeray M M, David W I F and Ibberson R M, "Structural Aspects of Lithium-Manganese-Oxide Electrodes for Rechargeable Lithium Batteries". *Mat. Res. Bull.*, **25**, 173, 1990.

Rossouw M H (1991) and Thackeray M M, "Lithium Manganese Oxides from Li_2MnO_3 for Rechargeable Lithium Battery Applications". *Mat. Res. Bull.*, **26**, 463, 1991.

Rossouw M H (1992a), Liles D C, Thackeray M M, David W I F and Hull S, "Alpha Manganese Dioxide for Lithium Batteries: a Structural and Electrochemical Study". *Mat. Res. Bull.*, **27**, 221, 1992.

Rossouw M H (1992b), de Kock A, Liles D C, Gummow R J and Thackeray M M, "Synthesis of Highly Crystalline Ramsdellite-MnO_2 and Its Lithiated Derivative $LiMnO_2$". *J. Mat. Chem.*, **2**, 1211, 1992.

Rossouw M H (1993), Liles D C and Thackeray M M, "Synthesis and Structural Characterization of a Novel Layered Lithium Manganese Oxide $Li_{0.36}Mn_{0.91}O_2$ and Its Lithiated Derivative $Li_{1.09}Mn_{0.91}O_2$". *J. Solid State Chem.*,

Schöllhorn R (1980), "Reversible Topotactic Redox Reactions of Solids by Electron/Ion Transfer". *Angew. Chem. Int. Ed. Engl.*, **19**, 983, 1980.

Schumm B Jr. (1990), "Pores, Structure and Battery Performance for Electrolytic Manganese Dioxide (EMD)". *Prog. Batteries Sol. Cells*, **9**, 142, 1990.

Sherman D M (1984), "The Electronic Structures of Manganese Oxide Minerals". *Am. Miner.*, **69**, 788, 1984.

Strobel P (1986) and Charenton J-C, "Influence of Foreign Cations on the Synthesis of Various Non-Stoichiometric Forms of Manganese Dioxide". *Rev. Chim. Min.*, **23**, 125, 1986.

Strobel P (1987) and Charenton J-C, "Structural Chemistry of Phyllomanganates: Experimental Evidence and Structural Models". *Rev. Chim. Min.*, **24**, 199, 1987.

Strobel P (1988) and Lambert-Andron B, "Crystallographic and Magnetic Structure of Li_2MnO_3". *J. Solid State Chem.*, **75**, 90, 1988.

Strouff P (1988) and Boulègue J, "Synthetic 10-Å and 7-Å Phyllomanganates: Their Structures as Determined by EXAFS". *Amer. Min.*, **73**, 1162, 1988.

Swinkels D A J (1992) and Hall K N, "Some Physical Properties of EMD". *Prog. Batteries & Battery Materials*, **11**, 16, 1992.

Tarascon J M (1991a), Wang E, Shokoohi F K, McKinnon W R and Colson S, "The Spinel Phase of $LiMn_2O_4$ as a Cathode in Secondary Lithium Cells". *J. Electrochem. Soc.*, **138**, 2859, 1991.

Tarascon J M (1991b) and Guyomard D, "Li Metal-Free Rechargeable Batteries Based on $Li_{1+x}Mn_2O_4$ Cathodes ($0 \leq x \leq 1$) and Carbon Anodes". *J. Electrochem. Soc.*, **138**,

2864, 1991.

Thackeray M M (1988) and De Kock A, "Synthesis of γ-MnO_2 from $LiMn_2O_4$ for Li/MnO_2 Battery Applications". *J. Solid State Chem.*, **74**, 414, 1988.

Thackeray M M (1989), de Kock A, de Picciotto L A and Pistoia G. *J. Power Sources*, **26**, 355, 1989.

Thackeray M M (1992a), de Kock A, Rossouw M H, Liles D C, Bittihn R and Hoge D, "Spinel Electrodes from the Li-Mn-O System for Rechargeable Lithium Battery Applications". *J. Electrochem. Soc.*, **139**, 363, 1992.

Thackeray M M (1992b), Rossouw M H, de Kock A, de la Harpe A P, Gummow R G, Pearce K and Liles D C, "The Versatility of MnO_2 for Lithium Battery Applications". *The 6 th International Meeting on Lithium Batteries, Extended Abstracts*, **FRI-03**, 136, 1992.

Thackeray M M (1993a), Rossouw M H, Gummow R J, Liles D C, Pearce K, de Kock A, David W I F and Hull S, "Ramsdellite-MnO_2 for Lithium Batteries: The Ramsdellite to Spinel Transformation". *Electrochim. Acta*, **38**, 1259, 1993.

Thackeray M M (1993b), Rossouw M H, de Kock A, de la Harpe A P, Gummow R G, Pearce K and Liles D C, "The Versatility of MnO_2 for Lithium Battery Applications". *J. Power Sources*, **43-44**, 289, 1993.

Tsuji M (1984) and Abe M, "Synthetic Inorganic Ion-Exchange Materials XXXVI. Synthesis of Cryptomelane-Type Hydrous Manganese Dioxide as an Ion-Exchange Material and their Ion-Exchange Selectivities towards Alkali and Alkaline Earth Metal Ions". *Solv. Extr. Ion Exchange*, **2**, 253, 1984.

Turner S (1979) and Buseck P R, "Manganese Oxide Tunnel Structures and their Intergrowths". *Science*, **203**, 456, 1979.

Turner S (1981) and Buseck P R, "Todorokites: A New Family of Naturally Occurring Manganese Oxides". *Science*, **212**, 1024, 1981.

Turner S (1988) and Post J E, "Refinement of the Substructure and Superstructure of Romanéchite". *Amer. Min.*, **73**, 1155, 1988.

Uedaira S (1985), Sameshima Y and Tamura H, "Lithium Manganese Dioxide Cell". *European Patent*, 85102480.2, 1985.

Voinov M (1982), "MnO_2: Structure and Activity". *Electrochim. Acta*, **27**, 833, 1982.

Vol'khin V V (1973), Leont'eva G V and Onorin S A, "Synthesis, Structure, and Properties of ISM-1 Ion-Sieve Cation-Exchanger". *Izv. Akad. Nauk SSSR, Neorg. Mat.*, **9**, 1041, 1973.

Wadsley A D (1953), "The Crystal Structure of Psilomelane, $(Ba,H_2O)_2Mn_5O_{10}$". *Acta Cryst.*, **6**, 433, 1953.

West A R (1984), in *Solid State Chemistry and Its Applications*, John Wiley & Sons, 1984, p. 570.

Wickham D G (1958) and Croft W J, "Crystallographic and Magnetic Properties of Several Spinels Containing Trivalent JA-1044 Manganese". *J. Phys. Chem. Solids*, **7**, 351, 1958.

Wizanski A R (1989), Rauch P E and DiSalvo F J, "Powerful Oxidizing Agents for the Oxidative Deintercalation of Lithium from Transition-Metal Oxides". *J. Solid State Chem.*, **81**, 203, 1989.

Yao Y F (1987), Gupta N and Wroblowa H S, "Rechargeable Manganese Oxide Electrodes. Part I. Chemically Modified Materials". *J. Electroanal. Chem.*, **223**, 107, 1987.

Yoshio M (1989), Nakamura H, Piao G P and Kozawa A, "A Few Preliminary Experiments of Rechargeable Manganese Dioxide for Secondary Li/MnO_2 Cells". *Prog. Batteries Sol. Cells*, **8**, 175, 1989.

Yoshio M (1990), Inoue S, Piao G and Nakamura H, "Novel Lithium-Manganese Composite Oxide for the Cathode of Lithium Secondary Batteries". *Prog. Batteries Sol. Cells*, **9**, 205, 1990.

Yoshio M (1991), Nakamura H and Noguchi H, "Lithium Manganese Rechargeable Cells". *Prog. Batteries Sol. Cells*, **10**, 1991.

Zinovik M A (1978), Balakirev V F and Chufarov G I, "The Definition of Chemical Compounds and Composition-Property Dependencies in Multicomponent, Spinel-Type, Solid Solutions". *Dokl. Akad. Nauk SSSR*, **263**, 885, 1982.